Pre-normative research for safety of hydrogen driven vehicles and transport through tunnels and similar confined spaces

Fuel Cells and Hydrogen Joint Undertaking (FCH JU)
Grant Agreement Number 826193

Deliverable D3.3
Final report on analytical, numerical and experimental studies on fires, including innovative prevention and mitigation strategies

Lead authors: DTU (F. Markert; L. Giuliani; L.S. Sørensen, W. Liu)
Contributing authors:
NCSRD (A. G. Venetsanos, G. Momferatos)
HSE (S. Bergin, M. Pursell)
KIT (Z. Xu)
PS (J. Grune)
USN (A.V. Gaathaug)
UU (D. Cirrone, V. Shentsov, S. Kashkarov, D. Makarov, V. Molkov)
CEA (G. Bernard-Michel)

Version: 220228
Delivery date for internal review: 20th February 2022
Due date: 28th February 2022
Dissemination level: Public

Deliverable administration					
Work Package	WP3. Thermal and pressure effects of hydrogen jet fires and structure integrity				
N. and title	D3.3. (D10) Final report on analytical, numerical and experimental studies on fires, including innovative prevention and mitigation strategies				
Type	Report				
Status	Draft/Working/**Released**	Due	M36	Date	28-02-2022
Comments	None				

Development and revision			
Version N.	Date	Authors	Description
220222	22-02-22	F. Markert, L. Giuliani, L.S. Sørensen, W. Liu (DTU)	Contribution; Final draft compilation
220222	01-02-22	S. Bergin; M. Pursell (HSE)	Contribution
220222	04-02-22	D. Cirrone (UU)	Contribution
220222	05-02-22	G. Momferatos (NCSRD)	Contribution
220222	05-02-22	P. Russo (URS)	Contribution
220222	16-02-22	A.V. Gaathaug (USN)	Contribution
220222	24-02-22	G. Bernard-Michel (CEA)	Contribution
220222	25-02-22	J. Grune (PS)	Contribution
220222	23-02-22	J. van den Berg (NEN)	Reviewer of deliverable
220222	25-02-22	D. Cirrone (UU)	Review of deliverable
202228	28-02-22	F. Markert (DTU)	Final version

Disclaimer

Despite the care that was taken while preparing this document the following disclaimer applies: the information in this document is provided as is and no guarantee or warranty is given that the information is fit for any particular purpose. The user thereof employs the information at his/her sole risk and liability.
The document reflects only the authors' views. The FCH JU and the European Union are not liable for any use that may be made of the information contained therein.

Acknowledgments

This project has received funding from the Fuel Cells and Hydrogen 2 Joint Undertaking (JU) under grant agreement No 826193. The JU receives support from the European Union's Horizon 2020 research and innovation programme and United Kingdom, Germany, Greece, Denmark, Spain, Italy, Netherlands, Belgium, France, Norway, Switzerland.

Summary

HyTunnel-CS project aims to conduct internationally leading pre-normative research (PNR) to close knowledge gaps and technological bottlenecks in the provision of safety and acceptable level of risk in the use of hydrogen and fuel cell cars as well as hydrogen delivery transport in underground transportation systems. Work Package 3 (WP3) of HyTunnel-CS focuses on the investigation of thermal and pressure effects of hydrogen jet fires and structure integrity.

This document presents the final deliverable (D3.3) on results of experimental, analytical and numerical studies for final report regarding ignited leaks and jet flames in tunnels and underground parking. The generated knowledge is also used to identify innovative safety strategies and solutions for the prevention and mitigation of jet fires consequences, providing recommendations for RCS and for an inherently safer use of hydrogen vehicles in underground transportation systems.

Keywords

Hydrogen, tunnel, release, jet fire, concrete spalling, structural integrity, engineering tool, numerical simulation, experiment, confined space, ignited leak.

Table of contents

Summary 4
Keywords 4
Abbreviations 9
Definitions 9
List of figures 10
List of tables 16
1. Introduction and scope 17
1.1 Work Package overview 17
1.1.1 Structure and synergy with HyTunnel-CS work plan 18
2. Analytical studies, development and validation of engineering tools (Task 3.2/UU) 19
2.1 Correlation for pressure peaking phenomenon for jet fires enclosure (ST 3.2.1, UU) . 19
2.1.1 Introduction 19
2.1.2 PPP model formulation for unignited releases and jet-fires 21
2.1.3 USN experiments 21
2.1.4 PPP for unignited hydrogen releases 22
2.1.5 PPP for ignited hydrogen releases 24
2.1.6 Conclusions 27
2.2 Hydrogen fire suppression systems by water sprays and oxygen depletion (ST 3.2.2, KIT) 27
2.2.1 Introduction 27
2.2.2 Vented tunnel section with vehicle models 28
2.2.3 Hydrogen jet fire 29
2.2.4 FDS software 30
2.2.5 Hydrogen blowdown from vessel 30
2.2.6 Suppression measures - Water spray 31
2.2.7 Simulation scenarios and result analysis 33
2.2.8 Gas temperature in case of small hydrogen mass flow rate 41
2.2.9 Gas temperature in case of large hydrogen mass flow rates 45
2.2.10 Gas temperature in case of very large hydrogen mass flow rate 45
2.2.11 Correlation between hydrogen mass flow rate and water spray flow rate 46
2.2.12 Humidity 46
2.2.13 Concluding remarks and future studies 55
2.3 Mechanical ventilation of hydrogen jet fire in underground parking (ST3.2.3, UU) ... 55

2.3.1 Compliance to BS 7346-7-2013 55
2.3.2 An analytical model: considerations and conclusions 56
2.3.3 A CFD approach to model hydrogen jet fires in underground car parks 57
2.3.4 Description of the CFD model 57
2.3.5 Results and discussion 57
2.3.6 Effect of a hydrogen jet fire on a car HRR 60
2.3.7 Concluding remarks 61
3. Numerical studies (Task 3.3/NCSRD) 62
3.1 CFD model for predictive simulation of pressure peaking phenomenon for hydrogen jet fire in confined space (ST 3.3.1, UU) 62
3.1.1 Validation experiments 62
3.1.2 Description of the CFD model 63
3.1.3 Release source modelling 63
3.1.4 Results and discussion 63
3.1.5 Time-efficient approach of the uniform cube-shaped control volumes grid 66
3.1.6 Concluding remarks 68
3.2 CFD model of hydrogen non-premixed turbulent combustion in scaled underground parking with mechanical ventilation (ST3.3.2, NCSRD) 68
3.2.1 Development of the thermal radiation module 68
3.2.2 Brief Description of the experiments 70
3.2.3 Numerical Setup of the Simulations 76
3.2.4 Validation Results 76
3.2.5 Conclusions 83
3.3 Coupled CFD/FEM modelling of the structures reaction to fire (ST 3.3.3, DTU/UU) 83
3.3.1 Object and aim of the study 83
3.3.2 Tunnel structure reaction to hydrogen fire (DTU, UU) 85
3.3.3 Accidental scenarios 86
3.3.4 CFD modelling of hydrogen jet fire in a tunnel (UU) 86
3.3.5 FE Thermal model 93
3.4 CFD model on influence of hydrogen releases to fire spread scenarios in underground transportation systems (ST 3.3.4, DTU) 98
4. Experiments (Task 3.4/CEA) 105
4.1 Pressure peaking phenomenon for hydrogen jet fires in confined spaces (ST 3.4.1, USN) 105

4.2 Thermal effects of hydrogen non-premixed turbulent combustion on a vehicle fire behaviour, structure and evacuation conditions in underground parking (ST 3.4.2, USN) 106
4.2.1 Experimental matrix and procedures 109
4.2.2 Results 109
4.3 Effect of hydrogen jet fire on structure integrity and concrete spalling (ST 3.4.3, DTU) 112
4.3.1 Introduction 112
4.3.2 Preliminary tests 112
4.3.3 Wall test setup 112
4.3.4 Concrete recipes and test specimen 113
4.3.5 Spalling tests on concrete wall elements 114
4.4 Effect of hydrogen jet fires on the erosion of tunnel road materials and lining materials (ST 3.4.4, HSE) 119
4.4.1 Introduction 119
4.4.2 Aims of testing 120
4.4.3 Test Methodology 120
4.4.4 Material samples 121
4.4.5 Experimental setup 124
4.4.6 Ignition mechanism 125
4.4.7 Measurements 125
4.4.8 Results (commissioning trial only) 131
4.4.9 Impeded jet release – sensor plates 131
4.4.10 Discussion and conclusions 132
4.5 Effect of hydrogen combustion from TPRD on vehicle fire dynamics in tunnel (ST 3.4.5, CEA) 133
4.5.1 Introduction 133
4.5.2 Test geometry 133
4.5.3 Description of the burner 138
4.5.4 Test sequence and test matrix 140
4.5.5 Test results - Reference jet-fire (200 bar, 2 mm, UP) 142
4.5.6 Effect of tank pressure for a 2 mm jet-fire 144
4.5.7 Effect of release location for a 2 mm jet fire 146
4.5.8 Effect of release diameter in case of downward 45° jet-fire 151
4.5.9 Coupling Fire/jet-fire for a 2 mm upward jet-fire 152
4.5.10 Blowdown characterization 155

4.5.11 Conclusions and recommendations 156
4.6 Effect of water sprays on mitigation of hydrogen jet fires (ST 3.4.6, PS) 158
4.6.1 Facility 158
4.6.2 Results 161
4.6.3 Conclusions and recommendations 167
5. Main conclusions and innovations 169
6. References 170

Abbreviations

ACH	Air Changes per Hour
ACV	Angular Control Volume
CFD	Computational Fluid Dynamics
CGH2	Compressed Gaseous Hydrogen
CFL	Courant–Friedrichs–Lewy number
CV	Control volume
FCEV	Fuel Cell Hydrogen Vehicle
FCHV	Fuel Cell Electric Vehicle
FDS	Fire Dynamic Simulator
FE	Finite Elements
FFFS	Fixed Fire Fighting System
FRR	Fire Resistance Rating
FVDOM	Finite Volume Discrete Ordinates Method
HPHR	High Pressure Hydrogen Rig
HPV	Hydrogen Powered Vehicle
HRR	Heat Release Rate
HTM	Hygro-Thermal-Mechanical
LES	Large Eddy Simulation
LH2	Liquid Hydrogen
LHV	Lower Heating Value
MFM	Mass Flow Meter
MFR	Mass Flow Rate
NIST	National Institute of Standards and Technology
NWP	Nominal Working Pressure
PP	Polypropylene
PPP	Pressure Peaking Phenomena
PRD	Pressure Relief Device
P&ID	Process & Information Diagram
RANS	Reynolds-Averaged Navier–Stokes
RCS	Regulations, Codes and Standards
RH	Relative Humidity
SAB	Stakeholders Advisory Board
SCV	Spatial Control Volume
SSR	Sum of Squared Residuals
ST	Sub-Task
TPRD	Thermally activated Pressure Relief Device
VLES	Very Large Eddy Simulation
WP	Work Package

Definitions

Accident is an unforeseen and unplanned event or circumstance causing loss or injury.

List of figures

Figure 1. Pressure peaking phenomenon for release of hydrogen with mass flow rate 390 g/s into the enclosure of 30.4 m^3 with a vent of typical brick size 25x5 cm compared with pressure dynamics for releases of helium, methane and propane at the same conditions (Brennan et al., 2013). 20
Figure 2. PPP for release of hydrogen into the enclosure of 30.4 m^3 with a vent of typical brick size 25x5 cm pressure dynamics for 62 L storage at pressures 700 (solid) and 350 (dashed) bar from 5.08 mm TPRD. 21
Figure 3. Explosion chamber used in PPP experiments. 22
Figure 4. Unignited PPP model validation. 23
Figure 5. PPP model validation for jet fires with hydrogen mass flow rate (1-4 g/s). 25
Figure 6. PPP model validation for jet fires with hydrogen mass flow rate (7.5-9 g/s). 26
Figure 7. PPP model validation for jet fires with hydrogen mass flow rate (~11 g/s). 27
Figure 8. Schematic representation of the tunnel cross-section: horseshoe geometry (left) (Venetsanos, 2008) and rectangular geometry (right). 28
Figure 9. Tunnel model with three cars. 28
Figure 10. Momentum-dominated, transitional, and fully buoyancy-dominated jet. 29
Figure 11. The under-expanded jet scheme: 1– Pressure vessel; 2– nozzle entrance; 3– nozzle exit; 4– effective nozzle diameter (Molkov, 2012). 30
Figure 12. Spectrum of the water droplet diameters (Granta et al., 2000). 32
Figure 13. Schematic model of simulated tunnel section. 33
Figure 14. Small hydrogen mass flow rate with orifice diameter 1.37 mm. 34
Figure 15. Large hydrogen mass flow rate with orifice diameter 1.94 mm. 35
Figure 16. Very large hydrogen mass flow rate with orifice diameter 2.74 mm. 35
Figure 17. Consideration of the integral cooling effect of the spray on H2 combustion: Tunnel exit average gas temperature with coarse and refined grids. 37
Figure 18. Downstream average gas temperature with coarse and refined grids. 37
Figure 19. Tunnel exit average gas temperature with refined or coarse grids, in cases with water spray. 38
Figure 20. Downstream average gas temperature with refined or coarse grids, in cases with water spray. 38
Figure 21. Heat release rate (HRR) comparison between the case with water spray and the case without spray, and the comparison between the hydrogen release rate decay and HRR decay. 39
Figure 22. Temperature contours of large water droplet (Case lll), with a vertically upwards jet from TPRD. 40
Figure 23. Temperature contours of small water droplet (Case lls). 40
Figure 24. Tunnel exit average gas temperature of cases with small water mass flow rate. 41
Figure 25. Downstream average gas temperature of cases with small water mass flow rate. 42
Figure 26. Tunnel section average gas temperature of cases with small water mass flow rate. 42
Figure 27. Tunnel exit average gas temperature of cases with large water mass flow rate. 43
Figure 28. Downstream region average gas temperature of cases and large water mass flow rate. 43
Figure 29. Tunnel section average gas temperature of cases with large water mass flow rate. 44
Figure 30. Tunnel exit average gas temperature of cases with water sprays. 44
Figure 31. Tunnel exit average gas temperature of very large hydrogen mass flow rate with water sprays. 45
Figure 32. Downstream average gas temperature of very large hydrogen mass flow rate with water sprays. 46
Figure 33. Tunnel section average relative humidity of small hydrogen mass flow rate with small water mass flow rate. 48

Figure 34. Tunnel section average relative humidity of small hydrogen mass flow rate with water sprays. 48
Figure 35. Tunnel section average absolute humidity of small hydrogen mass flow rate with small water mass flow rate. 49
Figure 36. Tunnel section average absolute humidity of small hydrogen mass flow rate with water sprays. 49
Figure 37. Tunnel section average absolute humidity of large hydrogen mass flow rate with water sprays. 50
Figure 38. Tunnel section average absolute humidity of very large hydrogen mass flow rate with water sprays. 51
Figure 39. Hydrogen contours of large hydrogen mass flow rate with large water mass flow rate and small water particle. 52
Figure 40. Tunnel exit average hydrogen volume fraction of large hydrogen mass flow rate with water sprays. 52
Figure 41. Tunnel section average oxygen volume fraction of large hydrogen mass flow rate with water sprays. 53
Figure 42. Velocity vector field of very large hydrogen mass flow rate without water spray. 54
Figure 43. Velocity vector field of very large hydrogen mass flow rate with large water mass flow rate and small droplet. 54
Figure 44. Case study A: real underground car park in St. Martnes Latem - Gent, Belgium; Case study B: real underground 3 storeys car park in Haarlem, The Netherlands (ArcelorMittal, 2019). 56
Figure 45. Effect of mechanical ventilation presence for a TPRD=0.5 mm, 45° angle. Ceiling height=3m, time=16 s. 58
Figure 46. Effect of TPRD inclination with respect to perpendicular to the ground for TPRD=0.5 mm, ceiling height=3m, 10 ACH. 58
Figure 47. Effect of TPRD diameter for the inclination 45° with respect to perpendicular to the ground, ceiling height=3m, 10 ACH. 59
Figure 48. Hydrogen jet fire contribution to a vehicle fire HRR. Left: results for TPRD diameters 0.5-5 mm. Right: results for TPRD diameters 0.5-2 mm. 61
Figure 49. Pressure dynamics in the enclosure for Test 14: CFD simulations with inflow boundary conditions at the notional nozzle exit versus experiments. 64
Figure 50. CFD simulation results of OH mole fraction distribution in plane x=0 perpendicular to the enclosure walls with vents: Test 14, ts=0.34ms (Cirrone et al., 2022). 64
Figure 51. CFD simulation results of temperature distribution in plane x=0 perpendicular to the enclosure walls with vents: Test 14, ts=0.34ms (Cirrone et al., 2022). 65
Figure 52. CFL convergence for volumetric source approach and effect of heat transfer (HT) versus simulation with adiabatic walls (AW) on pressure dynamics: Test 14. 66
Figure 53. Pressure dynamics in the enclosure for the unified “cube grid” approach: (a) Test No.14; (b) Test No.18; (c) Test No.19 (Cirrone et al., 2022). 67
Figure 54. Left: Subdivision of the unit sphere into non-equal angular control volumes by splitting the azimuthal angle range and the polar angle range into 6 segments. Right: Subdivision of the unit sphere into 33 equal angular control volumes using the algorithm proposed in (Leopardi, 2006). 70
Figure 55. Sketch of the vertical under-expended jet flame experiment (adapted from (Schefer et al., 2006)). 71
Figure 56. Sketch of the horizontal under-expended jet flame experiment. 72
Figure 57. Radiative Heat Flux for a) 1 mm and 340 bar b) 3mm and 325 bar c) 5mm at 320 bar. 74
Figure 58. Model of the geometry of the USN, shown with a plane of the grid and sensor positions. 75
Figure 59. Vertical jet fire experiment: numerical predictions for the radial radiative heat flux as a function of non-dimensional height. Circles: experimental measurements. Dashed line: FT_N scheme. Solid line: our new proposed scheme. 77

Figure 60. Vertical jet fire experiment: demonstration of independence of numerical results with respect to the number of ACVs. Circles: experimental measurements. Black: N = 80 ACVs. Red: N = 120 ACVs. Green: N = 168 ACVs. 77
Figure 61. Vertical jet fire experiment: demonstration of independence of numerical results with respect to number of SCVs. Circles: experimental measurements. Black line: coarse grid. Red line: medium grid. Green line: fine grid. 78
Figure 62. Horizontal jet fire experiment: comparison of the predictions of the radial radiative heat flux as a function of time given by the two different angular discretization schemes. Filled circles: experimental measurements. Dashed line: FT_N scheme. Solid line: Our new proposed scheme. Left: First radiometer, x = 2 m from the nozzle. Middle: x = 2.9 m from the nozzle. Right: x = 3.8 m from the nozzle. 79
Figure 63. Horizontal jet fire experiment: demonstration of independence of numerical results with respect to the number of ACVs. Circles: experimental measurements. Black: N = 168 ACVs. Red: N = 224 ACVs. Green: 288 ACVs. Left: First radiometer, 2 m from the nozzle. Middle: 2.9 m from the nozzle. Right: 3.8 m from the nozzle. 79
Figure 64. Horizontal jet fire experiment: demonstration of independence of numerical results with respect to the number of SCVs. Filled circles: experimental measurements. Black: coarse grid. Red: medium grid. Green: fine grid. Left: First radiometer, x = 2 m from the nozzle. Middle: x = 2.9 m from the nozzle. Right: x = 3.8 m from the nozzle. 80
Figure 65. Comparison between experimental measurements and simulation results for selected sensors of the vertical, 10ACH experiment 1. 81
Figure 66. Comparison between experimental measurements and simulation results for selected sensors of the 45 degree, 10ACH experiment 6. 82
Figure 67. Comparison of numerical and experimental time-series for the radiative heat flux sensor. position located closest to the jet fire, experiment 7. 83
Figure 68. Geometry and dimension of the tunnel section. 84
Figure 69. Details of the suspended deck and steel tendon sustaining it. 84
Figure 70. Drilled tunnel used as case study and sections of the CFD and FEM models. The main dimensions of the latter are reported, as well as the position of the bus and of the vertical axis passing through the TPRD. 86
Figure 71. Tunnel design and bus location. 87
Figure 72. Hydrogen mass flow rate during the four tanks blowdown. 88
Figure 73. Numerical grid: detail of tunnel longitudinal section where the hydrogen jet is located. ... 89
Figure 74. Temperature dynamics in the longitudinal section of the tunnel. 90
Figure 75. OH mole fraction dynamics in the longitudinal section of the tunnel. 90
Figure 76. Temperature and OH mole fraction dynamics in the transversal section of the tunnel. 91
Figure 77. Surface heat flux distribution on tunnel false ceiling. 91
Figure 78. Maximum surface heat flux on the tunnel false ceiling. 92
Figure 79. Longitudinal distribution of the hot gases cloud with temperature ≥ 70°C (343 K) at 20 s.93
Figure 80. Left: segment of the 10 m long sectional model with 10 mm mesh used for validation; Right: temperature profiles along the slab height at different times obtained from the analysis in case of standard fire exposure of the bottom part of the slab (continuous lines) and compared with the temperature profiles provided by the EN1992-1-2 (dotted lines). 93
Figure 81. Left: heat flux input vs. distance at different times (from 1 to 175 s). Right: heat flux vs. time at the fixed distance of 3.5. m from the release point and 5 m from the left end of the slab (slab mid-span). 94
Figure 82. Simplified model of the most solicited segment of slab (left) and resulting temperature histories at different depth (right). 95
Figure 83. Schematic of the boundary condition discretization of the refined slab model. Bottom..... 96

Figure 84. Mesh calibration by means of a sensitivity analysis on the average temperature around the flame centerline. 96
Figure 85. Temperatures at different depth at the end of the fire obtained from the analysis of the refined model considered as integer (top) and where the bottom 1.5 cm are removed as a consequence of spalling (bottom). 98
Figure 86. Layout and dimensions of the modelled car park (Liu et al., 2021). 99
Figure 87. Hydrogen vehicle model. 99
Figure 88. Hydrogen cars parked in the car park. Distance between cars 0.6 m. 100
Figure 89. Hydrogen mass release profile, TPRD = 4mm. 101
Figure 90. The corresponding heat release rate (HRR) for the mass release in Figure 89. 101
Figure 91. Development of hydrogen fire at 0 s of release time. 102
Figure 92. Development of hydrogen fire at 1.5 s of release time. 102
Figure 93. Development of hydrogen fire at 50 s of release time. 103
Figure 94. Burning history for the 5 mm nozzle diameter. 104
Figure 95. Beam no.4 surface temperatures for the different scenarios. 104
Figure 96. Ceiling no.2 surface temperatures for the different scenarios. 105
Figure 97. The 90-degree nozzle (left) and the 45-degree nozzle (right). 106
Figure 98. Hydrogen tank and coriolis mass flow meter; unsafe side. 107
Figure 99. Reference drawing: yellow- thermocouple TT, green- radiative heat flux RHF, brown-total heat flux THF, red- nozzle. 107
Figure 100. The discrete temperature along the container walls. All with 6 ACH. Red star: 700bar tank pressure and 0.5mm nozzle. Black circle: 350 bar tank pressure and 0.5 mm nozzle. Blue triangle 350 bar tank pressure and 1.0 mm nozzle. 111
Figure 101. Preliminary tests of gas burner on a concrete cylinder. 112
Figure 102. Test setup for tests of concrete wall elements in compression, with propane and hydrogen flame exposure. 113
Figure 103. Concrete wall elements for further gas exposure testing. Dim. W x L x T = 1000 x 1000 x 100 mm. Three test items of different concrete recipes (B, C, D) casted for tests. To the right a first test setup. 114
Figure 104. Test with a propane gas burner exposure on Wall Element 1 (WE1), w/c=0.40, concrete B, dense. To the right are shown the placements of the thermocouples. 115
Figure 105. WE1 – Temperature measurements on the concrete surface and in different depths (10 mm, 20mm, 30 mm and 80 mm) of the concrete, during propane gas flame exposure. 115
Figure 106. WE2 – Temperature measurements on the concrete surface and in different depths (10 mm, 20mm, 30 mm and 80 mm) of the concrete, during propane gas flame exposure. 116
Figure 107. WE2 – Temperature measurements on the concrete surface and in different depths (10 mm, 20mm, 30 mm and 80 mm) of the concrete, during propane gas flame exposure. 116
Figure 108. WE3 – Temperature measurements on the concrete surface and in different depths (10 mm, 20mm, 30 mm and 80 mm) of the concrete, during propane gas flame exposure. 117
Figure 109. WE3 – Temperature measurements on the concrete surface and in different depths (10 mm, 20mm, 30 mm and 80 mm) of the concrete, during propane gas flame exposure. 117
Figure 110. Wall 1 w/c=0.40- concrete B – dense. Left: during test with propane. Right: After test. 118
Figure 111. Tests of wall elements with gas flame exposure. The first results with propane flame tests. No spalling occurred, just some fine cracks. 118
Figure 112. Setup for small scale 700 bar hydrogen spalling experiment. 119
Figure 113. Concrete test samples. Dimensions 800x800x400 mm, high strength concrete. 122
Figure 114. Tarmac sample, polymer modified asphalt (PMA). 122
Figure 115. Pictures of the high pressure hydrogen facility showing (a) the two high pressure vessels and (b) a hydrogen jet fire release from a previous experimental campaign. 124

Figure 116. Simplified diagram of release system. PT = pressure transducer, TT = temperature transmitter. 124
Figure 117. Commissioning test setup - Free jet release using 2 mm nozzle (a) diagram outlining position of thermocouples relative to the release point and (b) photograph of thermocouple setup. . 126
Figure 118. (a) Stainless steel stand for sensing plates and (b) example of a plate in-situ. 127
Figure 119. Pressure sensing plate (a) front view with equispaced 3 mm diameter tapped holes and (b) rear view with water jacket and threaded sockets for pressure sensor attachment. 128
Figure 120. 700 bar blowdown, 50 L volume, 2 mm nozzle ignited release. Type 'R' thermocouple measurements along the axial direction of the jet. 131
Figure 121. General sketch of the 2021 jet/fire and fire/jet-fire interaction tests. 135
Figure 122. 2020 test series: supporting structure for the 8 Heat flux sensors. 135
Figure 123. 2021 test series: Radiative heat flux sensors: Left – structure with 4 staggered sensors, Right – Example of single sensors arrangement (tests 08 to 010). 136
Figure 124. Schematic description of the propane burner. 138
Figure 125. Picture of the propane burner before the tests. 138
Figure 126. Picture of the two zones: left – engulfing area, right – localized area. 139
Figure 127. Position of the burner in the tunnel. 140
Figure 128. Results of 2020 Test 17: a) Radiated heat flux – lower part, b) Radiated heat flux – Upper part, c) Gas temperature nearby the release d) Gas temperature along the ceiling nearby the injection (TkA and TkB are located in the middle of the tunnel above the burner). 142
Figure 129. Test 09 Shape of the jet-fire. 143
Figure 130. Test 09 Visible flame length with comparison to theory in open environment. 143
Figure 131. Test 09: a) Measured Radiated heat flux, b) Radiated heat flux computed by the point-source theory – Upper part, c) Gas temperature nearby the release d) Gas temperature along the ceiling. 144
Figure 132. Test 10 Shape of the jet-fire. 145
Figure 133. Test 10 Visible flame length with comparison to theory in open environment. 145
Figure 134. Test 10: a) Measured Radiated heat flux, b) Gas temperature along the ceiling. 146
Figure 135. 2021 Test 12 2 mm DW 45°: Jet-fire shape viewed from the rear side. 147
Figure 136. 2021 Test 12: Ground view from the side before jet-fire – the painted central line has a graduation of 0.5 m and the first one is 1.0 m far from the orifice. 147
Figure 137. Test 12: a) Measured Radiated heat flux, b) Gas temperature along the ceiling. 148
Figure 138. Hot gas cloud at -6 m close to the ceiling: a) Test 12 2 mm, b) Test 13 1 mm, c) Sensors location on M7, d) Thermocouples coordinates. 149
Figure 139. 2021 Test 18 2 mm DW 90°: Jet-fire shape viewed from the rear side. 150
Figure 140. Test 18: a) Measured Radiated heat flux, b) Gas temperature along the ceiling. 151
Figure 141. 2020 Test n°22 2 mm DW 90°: Jet-fire shape viewed from the rear side. 151
Figure 142. 2021 Test 13 1 mm DW 45°: Jet-fire shape viewed from the rear side. 152
Figure 143. Test 13: a) Measured Radiated heat flux, b) Gas temperature along the ceiling. 152
Figure 144. 2021 Test 15: Jet-fire shape viewed from the rear side. 153
Figure 145. Test 15 Visible flame length with comparison to theory in open environment. 154
Figure 146. Test 15: a) Measured Radiated heat flux, b) Gas temperature along the ceiling, c) Oxygen content close to the ceiling at -6 m, d) CO2 content close to the ceiling at -6 m. 154
Figure 147. Helium mass flow drop with TPRD of 2mm for the test of 2021. 156
Figure 148. A) Safety vessel V220 (A2) of HYKA. B) Technical drawing. C) Sketch of the set up for suppression tests of water sprays on hydrogen jet fires. 158
Figure 149. Mist nozzle head (Danfoss SEM-SAFE® Type: HNMP-5-10-1.19-00) (left), corresponding mobile professional high-pressure water mist system (Callies GmbH) (middle) and spiral full cone spray nozzle (right). 158

Figure 150. Pre-tests of a water mist spray. Left: facility to measure the quantity and uniformity of H2O-charging on the ground. Right: final design of the two nozzles head system in operation. 159
Figure 151. Example of the influence of a roof above the nozzle sprinkler system on the uniformity of H2O-charging on the ground. Left: no roof. Right: final design with roof..... 159
Figure 152. Experimental set-up (two mist nozzles head configuration) installed in the safety vessel V220 (A2). 160
Figure 153. H2-jet-fire and water mist injection. Left: start-up of water mist injection. Right: established water mist injection. 161
Figure 154. H2-jet-fire and water mist injection. Left: start-up of water mist injection. Right: established water mist injection. 162
Figure 155. Snapshot from high-speed movie (Jet-fire: H2 = 1g/s. nozzle = 4 mm). 162
Figure 156. Left, snapshot from high-speed movie. Right, stack montage of the visible flame length on the jet axis from the corresponding high-speed movie. (Jet-fire: H2 = 5 g/s. nozzle = 1 mm; dry)... 163
Figure 157. Left, snapshot from high-speed movie. Right, stack montage of the visible flame length on the jet axis from the corresponding high-speed movie. (Jet-fire: H2 = 5 g/s. nozzle = 1 mm; Mist 18 kg/min). 163
Figure 158. Average temperatures on the H2-jet-fire axis vs. distance to the nozzle. 164
Figure 159. Temperature profiles perpendicular to the axis x of the jet-fire (H2 = 1g/s. nozzle = 4 mm) in three distances to the nozzle A) 0.75 m B) 1 m and C) 1.25 m. 165
Figure 160. Left, temperature profiles perpendicular to the jet axis (y-direction) for different positions to the release nozzle (x-direction) for the jet configuration (1 g/s H2; 1 mm nozzle) for dry and mist atmospheres. Right, corresponding temperature contour plots. 166
Figure 161. Comparison of temperature contour plots of for dry and mist atmospheres for the 5 g/s H2-release configurations. 167

List of tables

Table 1. Structure of WP3. 18
Table 2. Experimental matrix - PPP for unignited hydrogen releases. A nozzle diameter of 4 mm and a volume V_{enc}. of 14.9 m^3 is applied in all experiments..... 22
Table 3. Experimental matrix - PPP for ignited hydrogen releases. A nozzle diameter of 4 mm and a volume Venc. of 14.9 m3 is applied in all experiments..... 24
Table 4. Effect of oxygen concentration (European Industrial Gases Association, 2009). 32
Table 5. Volume and mass fraction of oxygen in the gas phase. 36
Table 6. Water sprays matrix. 39
Table 7. Correlation between hydrogen mass flow rate and water sprays. 46
Table 8. USN experiments selected for CFD model validation. 62
Table 9. Notional nozzle (NN) parameters employed as inlet conditions for simulations. 63
Table 10. Matrix of experimental campaign performed by the Italian National Fire Corps in collaboration with URS. 72
Table 11. Matrix of the USN experiments. 75
Table 12. Details of the bus on-board hydrogen storage system. 87
Table 13. Material parameters for the car model. 100
Table 14. Mesh size and the total energy released. 100
Table 15. TPRD activation for the three vehicles. 104
Table 16. Data description of sensors. 108
Table 17. Sensors' location. 108
Table 18. Experimental matrix and parameters. Blowdown releases. 109
Table 19. Experimental results of temperature measurements. 110
Table 20. Concrete recipes for testing of spalling. 114
Table 21. Release characteristics. 121
Table 22. DTU and HSE concrete specification, including explanation for deviations. 123
Table 23. 77-day crush test results for concrete samples (a) without and (b) with fibres. 123
Table 24. Experimental tests matrix. 130
Table 25. Position of the 2020 Radiated heat flux sensors (0, 0, 0) corresponds to the TPRD exit in the upward position. 136
Table 26. 2021 test series: Radiated Heat Flux sensors positions. 137
Table 27. 2021 test series: Radiated Heat Flux sensors positions for the tests 09 and 010. 137
Table 28. Jet-fire and Fire/Jet-fire interaction test matrix. 141
Table 29. Summary of 2021 tests' results – Mass flow rate. 156
Table 30. Summary of 2021 tests' results – Hazard distances. 157
Table 31. Test matrix of water spray on hydrogen jet fires. 161
Table 32. Measured visible flame length of hydrogen jet fires. 164

1. Introduction and scope

The present report, deliverable D3.3, presents the results of the research performed within WP3 "Thermal and pressure effects of hydrogen jet fires and structure integrity" in the HyTunnel-CS project. The aim of WP3 is to investigate and to assess the thermal and pressure effects produced by hydrogen jet fires in tunnels and confined spaces. For instance, this is the case of an external fire heating a vehicle's hydrogen tank, leading to the opening of the thermally activated Pressure Relief Device (TPRD) to vent the compressed hydrogen gas and prevent the failure of the tank. The vented hydrogen is likely to ignite, due to the fire surrounding the tank, producing a jet fire. Hereunder, focus is posed on the effect of hydrogen jet fires on the structural integrity.

The activities reported in D3.3 follow the detailed programme and plan defined in deliverable D3.1 "Detailed research programme on hydrogen fires in confined structures" (HyTunnel-CS D3.1, 2019). Few planned activities were updated during the project course according to new developments, findings and strategic advises from the Stakeholders Advisory Board (SAB). Some experimental activities have been affected by the Covid-19 lockdowns and restrictions. Those activities that are yet in progress will be reported in HyTunnel-CS Deliverable D4.4.

A first step to the preparation of this document was given by Milestone MS7 "M3.3. Results of experimental, analytical and numerical studies for final report", which presented a first version of the report on the research outcomes. Milestone was submitted in November 2021 (Month 33).

Deliverable D3.3 reports on the developed engineering tools, numerical studies and performed experimental tests. It discusses the addressed knowledge gaps and the obtained results. The report will also present the interconnections of each activity with HyTunnel-CS work plan and the potential implementation to provide innovative prevention and mitigation strategies in recommendations for Regulations, Codes and Standards (RCS) and for inherently safer use of hydrogen vehicles in underground traffic systems. Task 3.2 comprises the analytical studies, development and validation of engineering tools. Task 3.3 reports the performed numerical investigations. Finally, the status of the experimental activities is reported (Task 3.4).

1.1 Work Package overview

The experimental campaigns, analytical and numerical studies in WP3 address those areas where the current knowledge is insufficient to calculate hazards and risks of hydrogen-powered vehicles and transport in tunnels and other confined spaces. These were defined through the critical review of the state of the art conducted in HyTunnel-CS D1.2 "Report on hydrogen hazards and risks in tunnels and similar confined spaces" (HyTunnel-CS D1.2, 2019). WP3 focuses on the scenario involving hydrogen jet fires and their interaction with a car fire dynamics and the confined space systems, whether this is the ventilation or the fire suppression systems. The analytical, numerical and experimental studies aim at improving the understanding of hydrogen jet fires effects, generating unique experimental data to support the validation of engineering and numerical models to be used in hydrogen safety engineering. The final scope is the identification of innovative safety strategies and solutions for the prevention and mitigation of jet fires consequences, providing recommendations for RCS and for an inherently safer use of hydrogen vehicles in underground transportation systems. A detailed list of the work-package objectives can be found in (HyTunnel-CS D3.1, 2019).

1.1.1 Structure and synergy with HyTunnel-CS work plan

Work Package 3 is structured in 5 tasks closely interconnected between each other and with HyTunnel-CS work plan. Task 3.1 designed the research programme on the basis of the identified knowledge gaps, current needs for hydrogen transportation in underground systems and resistance of their structure to fire exposure and strategic advice from the SAB. The detailed work plan has been described in HyTunnel-CS D3.1 and it defined the activities to be carried out in Tasks 3.2, 3.3 and 3.4. Task 3.2 focuses on the development of analytical studies and engineering tools, and their validation against experiments available in literature or performed within Task 3.4. Validated tools developed within this task support the guidelines and recommendations for RCSs developed within WP6. Task 3.3 focuses on the development and validation of numerical models to simulate scenarios not representable by the assumptions of engineering correlations and to give further insights into the dynamics and additional hazards of an accident. Task 3.4 focuses on the conduction of the experimental programme to establish a scientific basis and generate experimental data to support hazard and risk assessments. This task provides the fundamental data for validation of the engineering tools and CFD models developed in tasks 3.2 and 3.3, respectively. Thus, a close collaboration between modellers and experimentalists has been ensured to optimise and refine the design of experiments. Finally, Task 3.5 gathers the knowledge and outcomes achieved in tasks 2, 3 and 4 into the intermediate and final reports, respectively D3.2 and D3.3, on analytical, numerical and experimental studies on fires, including innovative prevention and mitigation studies. Table 1 provides an overview of the WP's structure, tasks and corresponding sub-tasks. This report will follow WP3 structure when describing the performed activities.

Table 1. Structure of WP3.

Title (leader)
Task 3.1. Programme of research (DTU)
Task 3.2. Analytical studies, development and validation of engineering tools (UU)
Sub-task 3.2.1. PPP correlation for jet fires (UU)
Sub-task 3.2.2. Fire suppression by water sprays and O_2 depletion (KIT)
Sub-task 3.2.3. Mechanical ventilation in underground parking (UU)
Task 3.3. Numerical studies (NCSRD)
Sub-task 3.3.1. Pressure Peaking Phenomenon CFD model (UU)
Sub-task 3.3.2. Fire in ventilated underground parking (NCSRD)
Sub-task 3.3.3. CFD/FEM modelling of fires effect on structures (DTU, *UU*)
Sub-task 3.3.4. Fire spread scenarios in underground spaces (DTU)
Task 3.4. Experiments (CEA)
Sub-task 3.4.1. Pressure Peaking Phenomenon for hydrogen jet fires (USN)
Sub-task 3.4.2. TPRD fire effect on vehicle, structure and evacuation (USN)
Sub-task 3.4.3. Fire effect on structure integrity and concrete spalling (DTU)
Sub-task 3.4.4. Fire effect on erosion of road materials and lining (HSE)
Sub-task 3.4.5. Effect of TPRD fire on vehicle fire dynamics in tunnel (CEA)
Sub-task 3.4.6. Effect of water sprays on mitigation of hydrogen jet fires (PS)
Task 3.5. Reports on hydrogen jet fire effects and safety strategies (DTU, All)

2. Analytical studies, development and validation of engineering tools (Task 3.2/UU)

2.1 Correlation for pressure peaking phenomenon for jet fires enclosure (ST 3.2.1, UU)

2.1.1 Introduction

The information on the pressure peaking phenomenon can be found in (Molkov, 2012) and in recent publications of Ulster University (Brennan et al., 2010, 2018; Hussein et al., 2018; Makarov et al., 2018). In vehicles, hydrogen is most commonly stored today as a compressed gas in tanks. The Commission Regulation (EU) No 406/2010 ("Commission Regulation (EU) No 406/2010 - European Environment Agency") requires that on-board compressed hydrogen storage tanks should be equipped with non-reclosing thermally activated pressure relief devices (TPRDs). The TPRD is fitted to the fuel tank and starts to release hydrogen when a temperature of about 110°C is reached inside the safety device, e.g. in fire conditions. The TPRD can provide rapid release of hydrogen if a large orifice diameter is used, thus minimising the possibility of tank explosion during too long exposure to fire. High mass flow rates from a TPRD are probably "acceptable" outdoors. However, the hazards resulting from a rapid release in room-like enclosures, e.g. garages and maintenance shops, are different and may not be acceptable with regards to life safety and property protection.

Let us consider a hypothetical scenario involving a release from a typical on-board hydrogen storage tank at 35 MPa, through a 5.08 mm diameter orifice (Brennan et al., 2010). The release is assumed to occur vertically upward in the centre, 0.5 m above the floor, of a small garage of size L x W x H=4.5x2.6x2.6 m (SAE J2579, 2009) and volume of 30.4 m^3 with a single vent equivalent in area to a typical brick L x H=25x5 cm located close to the ceiling. A conservative approach is taken, i.e. a constant mass flow rate of 390 g/s is applied (ignoring a pressure drop in the storage tank) after the TPRD opening.

Figure 1 illustrates the predicted overpressure versus time for a range of fuels with different molecular mass and the same mass flow rate of 390 g/s at the same garage (with discharge coefficient C=0.6): hydrogen, methane, propane with the molecular masses of 2, 16 and 44 g/mol, respectively. It is clearly showed how the maximum overpressure drops with increasing molecular mass. There is a small pressure peak for methane release as its molecular mass is below that of air. The pressure peaking phenomenon is absent for propane as its molecular mass is higher than air. Instead, the pressure generated by the release of hydrogen into the vented enclosure is growing monotonically to reach the maximum and then decreases to a steady state value, when only hydrogen flows out of the enclosure through the vent(s). The phenomenon must be taken into account when designing TPRDs for the use with different gases for indoor applications. Indeed, the same TPRD used for CNG or LPG should not be assumed to behave in the same way for hydrogen.

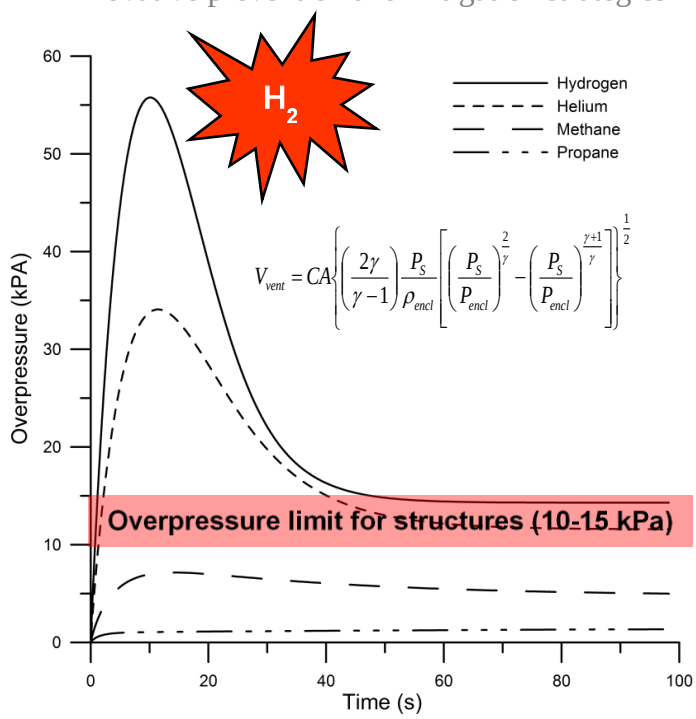

Figure 1. Pressure peaking phenomenon for release of hydrogen with mass flow rate 390 g/s into the enclosure of 30.4 m^3 with a vent of typical brick size 25x5 cm compared with pressure dynamics for releases of helium, methane and propane at the same conditions (Brennan et al., 2013).

In order to explain the phenomenon the pressure dynamics presented in Figure 1 is shown for the constant release not taking into account the blowdown from the storage tank. It shows the difference with other gases and demonstrates that PPP is applied for lighter than air gases.

Figure 2 demonstrates the difference in PPP for release from 62 L storage tank at pressures 700 (solid) and 350 (dashed) bar from 5.08 mm TPRD into the same enclosure of 30.4 m^3 and vent. It can be seen that the maximum overpressure reduced practically by 3 times for 350 bar but still poses serious hazard for civil structures. It is worth mentioning that this is an unignited release; in case of ignition the volumetric flow rate will increase by 22 times due to combustion (Makarov et al., 2018), details in section 2.1.2.

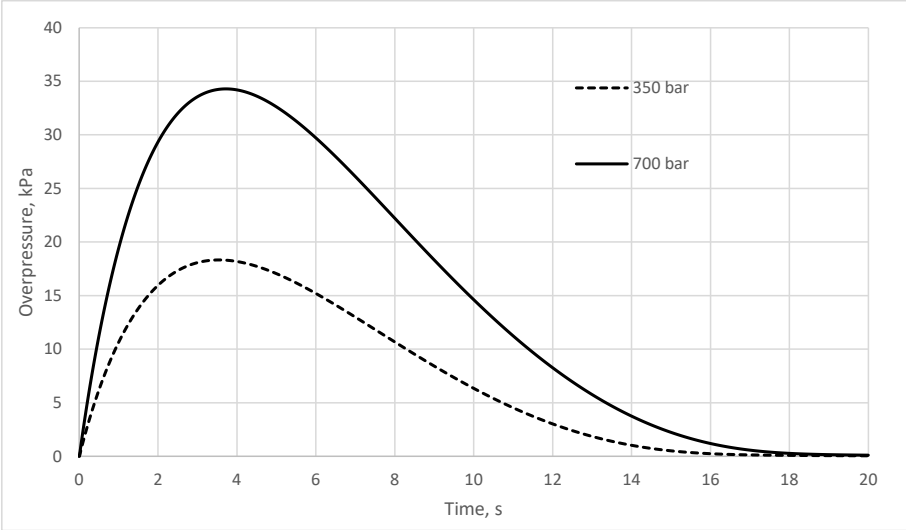

Figure 2. PPP for release of hydrogen into the enclosure of 30.4 m^3 with a vent of typical brick size 25x5 cm pressure dynamics for 62 L storage at pressures 700 (solid) and 350 (dashed) bar from 5.08 mm TPRD.

The validation of the PPP has been previously done only for the small-scale enclosure. Within HyTunnel-CS project the extensive experimental programme has been done by partner USN and model validation both for unignited and ignited tests was conducted by partner UU.

2.1.2 PPP model formulation for unignited releases and jet-fires

The system of equations to predict the overpressure dynamics in the assumption of perfect mixing for unignited releases has been previously described in detail in Deliverable D1.2 (HyTunnel-CS D1.2, 2019), whereas the model description and validation against small-scale tests has been presented in (Makarov et al., 2018).

The difference between the ignited and unignited PPP can be explained as follows. The volumetric flow rate of hydrogen into the enclosure can be written as a function of mass flow rate as $\dot{V} = \dot{m}_{\mathrm{H2}} RT / M_{\mathrm{H2}} P$. The stoichiometric reaction of hydrogen combustion in air can be written for a mole of hydrogen as $\mathrm{H_2} + 0.5(\mathrm{O_2} + 3.76\mathrm{N_2}) = \mathrm{H_2O} + 0.5 \cdot 3.76\mathrm{N_2}$. Both hydrogen and air at initial temperature T_0 are "consumed" during the combustion. As a result complete combustion of 1 mole of hydrogen would require (1+3.76)/2 moles of air and will generate one mole of water vapour and 3.76/2 moles of nitrogen both at T_{ad}, corresponding to the gas volume flow rate $\dot{V} = \dot{V}_{\mathrm{H2O}}\big|_{T_{ad}} + \dot{V}_{\mathrm{N2}}\big|_{T_{ad}} - \dot{V}_{1/2(\mathrm{O2}+3.76\mathrm{N2})}\big|_{T_0} - \dot{V}_{\mathrm{H2}}\big|_{T_0}$. For an arbitrary molar flow rate of hydrogen, $\dot{m}_{\mathrm{H2}}/M_{\mathrm{H2}}$, and assuming the absolute pressure doesn't change notably, the volume flow rate could be rewritten as:

$$\dot{V} = \frac{\dot{m}_{\mathrm{H2}}}{M_{\mathrm{H2}}}\frac{RT_{ad}}{P} + \frac{3.76}{2}\frac{\dot{m}_{\mathrm{H2}}}{M_{\mathrm{H2}}}\frac{RT_{ad}}{P} - \frac{(1+3.76)}{2}\frac{\dot{m}_{\mathrm{H2}}}{M_{\mathrm{H2}}}\frac{RT_0}{P} - \frac{\dot{m}_{\mathrm{H2}}}{M_{\mathrm{H2}}}\frac{RT_0}{P} = \frac{\dot{m}_{\mathrm{H2}}}{M_{\mathrm{H2}}}\frac{RT_0}{P}\left(\frac{T_{ad}}{T_0} + \frac{3.76}{2}\frac{T_{ad}}{T_0} - \frac{1+3.76}{2} - 1\right).$$

Thus, the difference between the flow rate of the unignited release defined and the ignited release (jet fire) from the same source is given by the factor in the brackets in red on the right-hand side of the equation. Value of the factor is α_c=22±1.

2.1.3 USN experiments

The hydrogen experiments were performed in an explosion chamber shown in Figure 3, which was placed approximately 15 m from the controlling setup. The explosive chamber has inner

dimensions: 2000x2980x2500 mm, giving a total volume of 14.9 m^3. The explosion chamber has two plates installed with 50 screws each, around the plate. The back plate has assembled a door. The explosion chamber's walls in total have five vents of 80 mm diameter each. Four of them are located in the lower corners (two vents at the wall) whereas the 5th is located in the middle of the front wall coming out inside of the chamber floor.

Figure 3. Explosion chamber used in PPP experiments.

Further details on the experimental facility and methodology are available in Lach et al. (2020) and Lach and Gaathaug (2021a).

2.1.4 PPP for unignited hydrogen releases

The experimental matrix of 10 unignited releases is shown in Table 2, while the comparison of the model results with experimental data is shown in Figure 4.

Table 2. Experimental matrix - PPP for unignited hydrogen releases. A nozzle diameter of 4 mm and a volume V_{enc}. of 14.9 m^3 is applied in all experiments.

Exp no	Vent area, [cm^2]	Vent size, [mm]	$\dot{m}_{H2}$, [g/s]	P_{tank}, [bar]	P_{peak}, [kPa]	t_{peak}, [s]	t_r, [s]
2	12	9x ∅13	1.9	26.8	0.42	10	90
3	20	1x ∅51.6	3.5	40	0.51	10	120
4	20	1x ∅51.6	9.05	104	2.86	17	120
5	14	1x ∅42	9.9	110	6.45	37	120
6	14	1x ∅42	10.1	117.5	6.74	37	120
7	6	4x ∅13	3.05	36	4.07	80	180
8	6	4x ∅13	3.05	39.7	3.96	77	180
9	6	4x ∅13	4.75	58.5	8.05	89	200
10	6	4x ∅13	4.2	52.6	6.70	89	200
11	6	4x ∅13	blowdown	49.6	7.00	64	1000

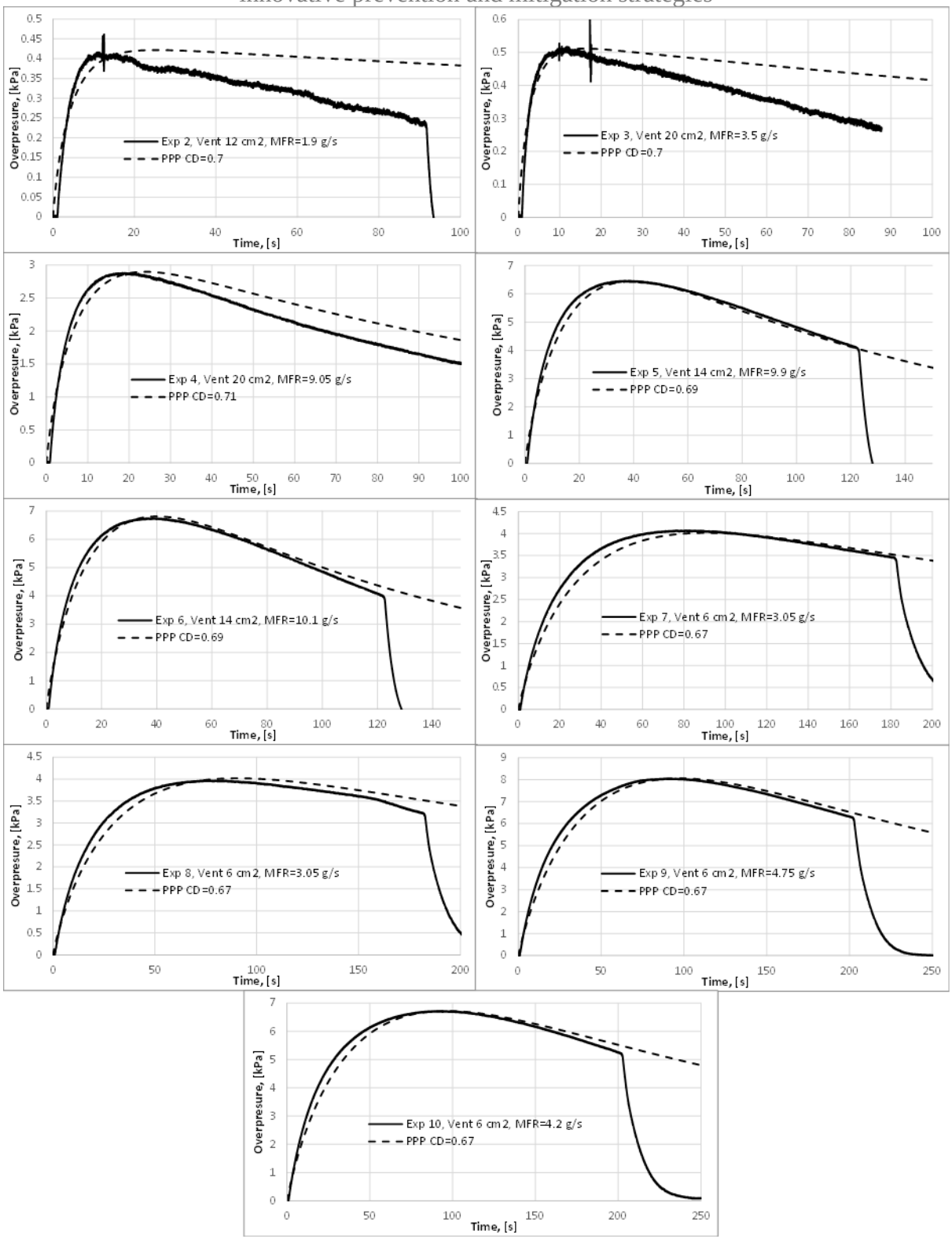

Figure 4. Unignited PPP model validation.

It can be seen that for all tests the model shows very good agreement both in dynamics and magnitude of the pressure peak. Contrary to the previous study (Makarov et al., 2018) where the discharge coefficient C_D had a big scatter due to enclosure "breathing", i.e. creation of "additional" vents due to enclosure walls deformation under internal pressure, in this set of

tests the discharge coefficient value is in a narrow range C_D=0.67-0.71 across all experiments and peak pressures.

2.1.5 PPP for ignited hydrogen releases

The experimental matrix of 31 ignited releases is shown in Table 3. Calculations were conducted using a discharge coefficient value in the range C_D=0.7-0.8. Model comparison against selected experiments is given in Figure 5 - Figure 7.

Table 3. Experimental matrix - PPP for ignited hydrogen releases. A nozzle diameter of 4 mm and a volume Venc. of 14.9 m3 is applied in all experiments.

Setup					Measured					
Exp nr	T_0 in enclosure [K]	H_2 release time	Open vent	Mass flow rate [g/s]	Experimental overpressure [kPa]	Experimental underpressure [kPa]	Temperature [°C]			
							T1	T2	T3	T4
1	281	5*	1	1.45	4.8	-0.1	9	45	86	85
2	282	10*	1	1.37	4.5	-0.3	14	81	128	125
3	283	5*	1	3.38	16.7	-0.6	69	119	171	164
4	285	10*	1	3.15	15.8	-2.8	141	175	251	225
5	288	10*	2	3.14	5.3	-1.1	93	175	270	230
6	288	10*	2	3.04	5	-1.1	86	176	258	223
7	276	6*	2	7.90	22	-2.5	166	209	353	319
8	277	6*	2	7.50	20.6	-2.3	142	207	348	287
9	279	6*	3	8.37	13.9	-2.9	194	242	403	345
10	279	6*	3	8.35	13.7	-2.8	192	243	389	332
11	280	7.5	3	8.63	14.7	-3.3	204	249	416	358
12	282	6	3	8.90	15.1	-2.3	176	215	372	322
13	281	6	3	11.72	21.7	-4.3	244	288	458	408
14	277	6	3	11.37	21.1	-3.8	241	274	430	352
15	277	6	3	4.00	4.3	-0.5	40	129	202	194
16	277	6	3	4.07	4.5	-0.5	45	130	209	190
17	278	6	2	11.52	33.3	-3.2	211	263	415	367
18	278	6	2	11.47	33	-3.4	205	267	414	367
19	278	6	1	8.62	48.1	-5.7	194	205	359	300
20	278	7.5	1	8.50	46.5	-8.2	243	247	383	332
21	280	6	2	8.52	23.7	-2	166	223	333	294
22	280	6	2	2.60	4.1	-0.3	12	98	142	139
23	279	15	2	2.36	3.5	-1.1	87	174	275	238
24	280	25	3	2.38	1.82	-0.95	195	240	368	331
25	278	25	3	3.87	4.1	-2.2	315	339	481	435
26	282	20	3	6.70	10.1	-4.6	384	467	603	568
27	281	10	3	6.65	9.9	-2.7	213	259	433	391
28	282	10	2	6.56	16.8	-3.5	219	247	419	369
29	281	20	2	6.55	16.7	-8.7	375	474	578	531
30	283	10	1	6.65	35.9	-14.1	246	259	392	349
31	282	20	1	6.56	35.3	-25.3	366	444	556	522

Figures also show mass flow rate dynamics as recorded during the experiment. For each experiment two simulations were conducted – for a constant mass flow rate of hydrogen (as stated in Table 3) and for transient hydrogen mass flow rate as demonstrated in Figure 5-Figure 7. As can be seen, the account of mass flow rate dynamics provides better agreement with experimental pressure dynamics. Maximum pressure peak value depends on the absolute value of hydrogen mass flow rate and not on the mass flow rate dynamics, which is, probably, due to the short transitional processes in the considered experiments.

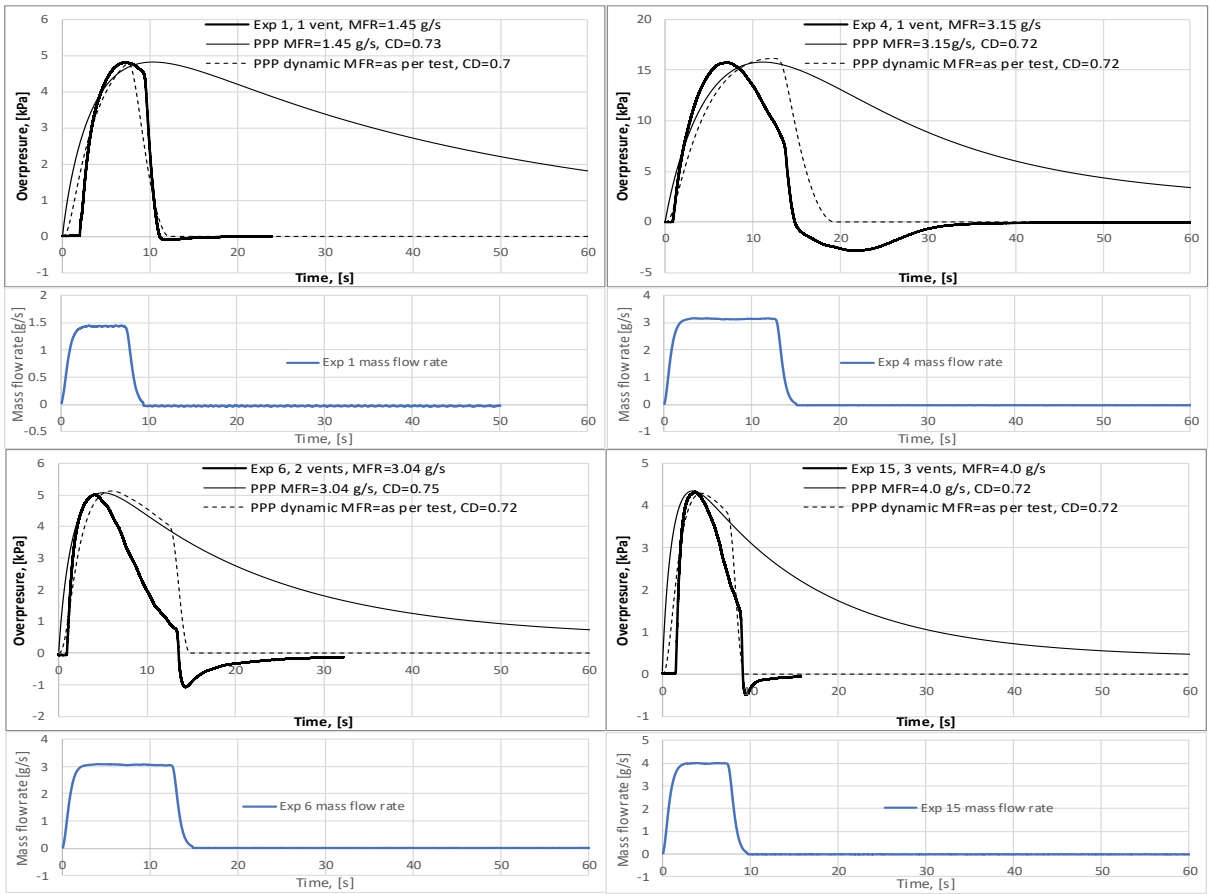

Figure 5. PPP model validation for jet fires with hydrogen mass flow rate (1-4 g/s).

Experimental pressure records for all performed tests demonstrate some underpressure developing after termination of hydrogen supply. This is in line with previous experimental observations in HyIndoor project (HyIndoor D4.4, 2014), where the hazards associated with under-pressure after termination of hydrogen supply or extinction of the flame due to oxygen depletion were noticed and discussed. This high level of under pressure could result in the civil structure implosion and should also be considered while doing hydrogen safety engineering. It should be noted that this effect is due to heat losses and condensation of the combustion products (water), which are currently not taken into account in the model, hence, cannot be seen in simulated pressure dynamics.

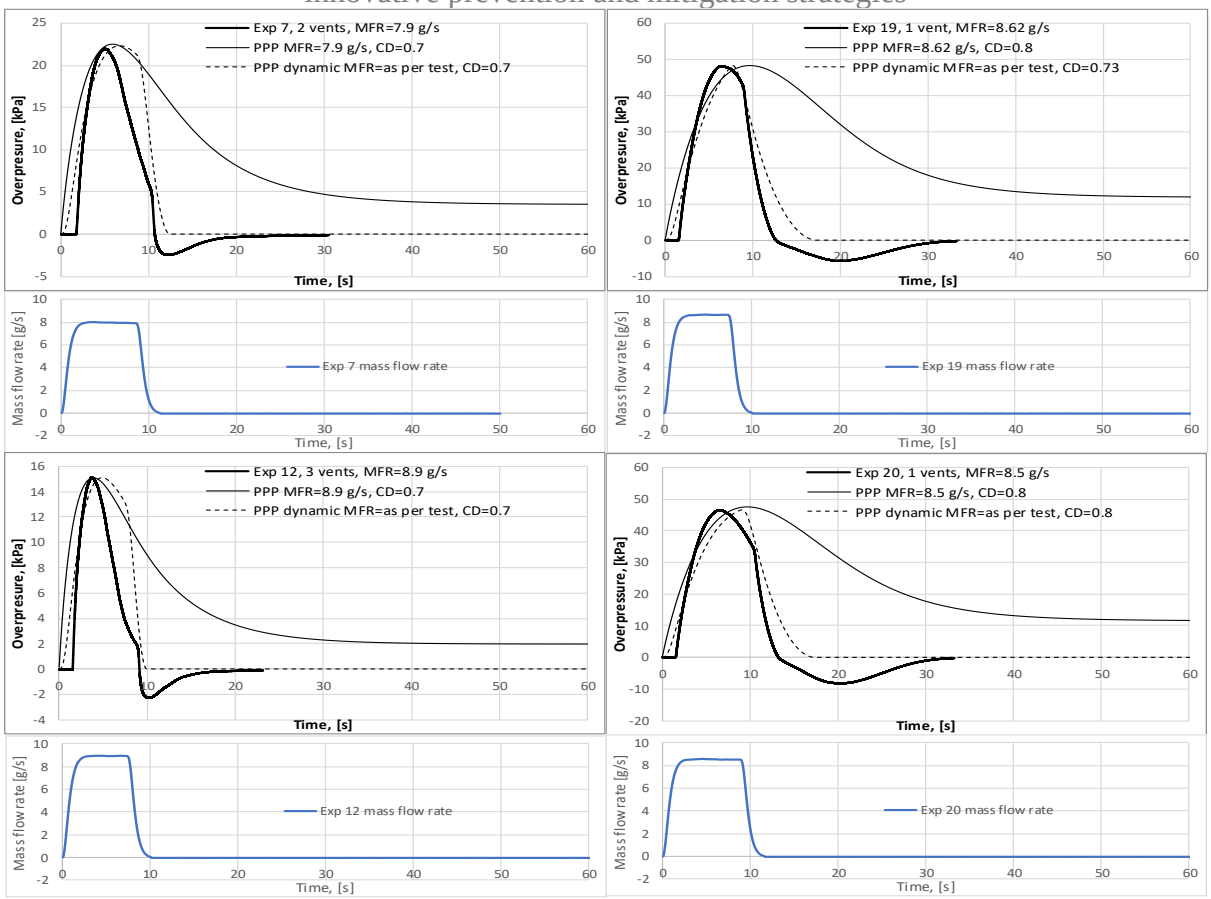

Figure 6. PPP model validation for jet fires with hydrogen mass flow rate (7.5-9 g/s).

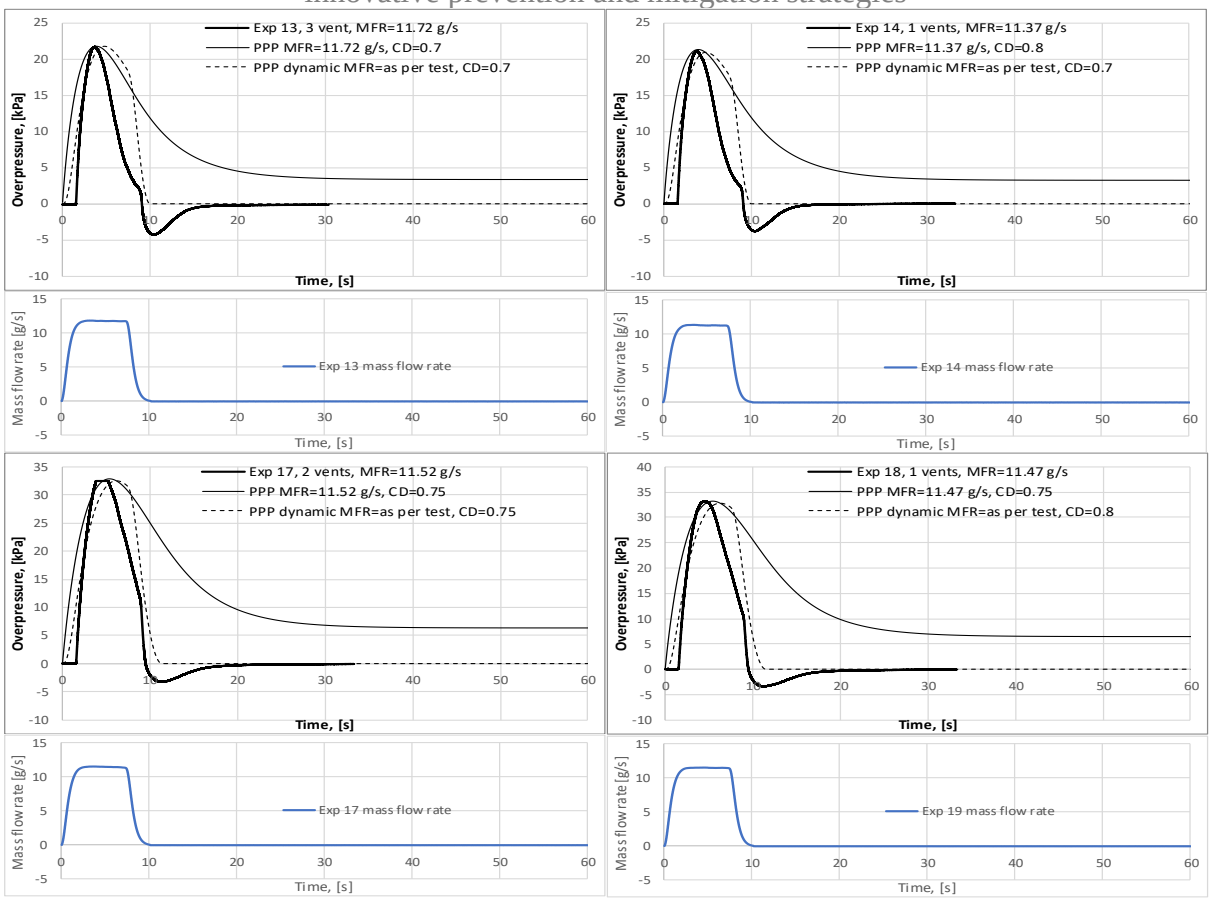

Figure 7. PPP model validation for jet fires with hydrogen mass flow rate (~11 g/s).

2.1.6 Conclusions

The experiments carried out by the USN were used for pressure peaking phenomena model validation for ignited and unignited hydrogen releases in large-scale scenarios. Nine experiments were selected for unignited PPP with discharge coefficient C_D in range 0.67-0.71 and 12 experiments for ignited PPP with the accounting of hydrogen combustion factor α=22 and discharge coefficient C_D in the range 0.7-0.8. The model provided very good agreement with both experimental pressure peak magnitude and experimental pressure peak arrival time. Pressure dynamics was reproduced both for constant and variable mass flow rates for all ignited tests. The phenomenon of under pressure in ignited PPP has been confirmed and should be treated carefully in the design of ventilation. The PPP tool will therefore be an excellent design tool that will be part of recommendations for the inherently safer use of hydrogen vehicles.

2.2 Hydrogen fire suppression systems by water sprays and oxygen depletion (ST 3.2.2, KIT)

2.2.1 Introduction

The effects of hydrogen fire suppression by water spray and oxygen depletion are studied by CFD numerical simulations of the interaction between the ignited hydrogen release from a fuel cell hydrogen vehicle (FCHV) and water spray installed in the traffic tunnel. A general tunnel section geometry is set up with some FCHV models inside, and the FDS code is applied to

make the simulations of hydrogen fires in conditions of water spray or oxygen depletion. The suppression effects are evaluated based on the simulation results.

2.2.2 Vented tunnel section with vehicle models

The EU Directive 2004/54/EC identifies the design features of the road tunnel, which encompass the following elements (EU, 2004):

- Tunnel length
- Number of tubes and lanes
- Lane width
- Traffic direction
- Cross-section shape, diameter or area
- Horizontal and vertical alignment

The accident scenario is assumed to take place in the two-way two-lane single-tube tunnel. Based on the shape of horseshoe tunnel cross-section, the cross-section in the simulation is simplified into rectangular geometry, the length of this straight tunnel section is 20 meters, the width is 9 meters, and the height is 5.8 meters, as shown in Figure 8. The tunnel model contains three cars, as shown Figure 9.

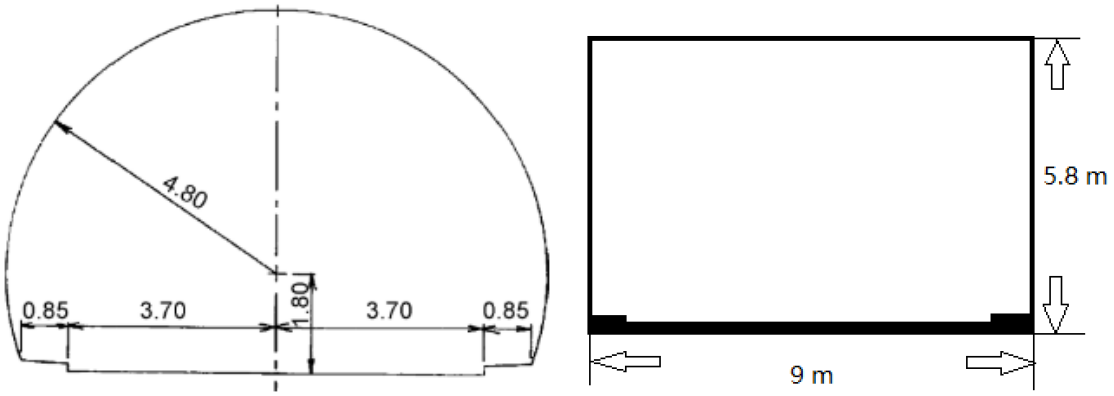

Figure 8. Schematic representation of the tunnel cross-section: horseshoe geometry (left) (Venetsanos, 2008) and rectangular geometry (right).

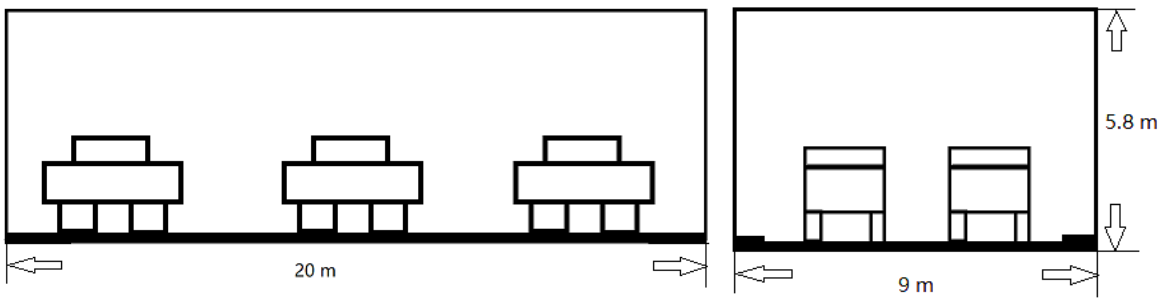

Figure 9. Tunnel model with three cars.

As a common mitigation measure, ventilation of tunnel is modelled in the study. The reference velocity of longitudinal ventilation is defined as 3 m/s, according to previous investigations

(Król et al., 2017; Zhang et al., 2019). In some cases, the ventilation direction is reversed for sensitivity analysis.

Some relevant phenomena are introduced to preset related parameters appropriately in the software to simulate different scenarios. Hydrogen release rate, oxygen volume fraction and water mist density need to be considered. In addition, the turbulence model, combustion model, mass and heat transfer model in the simulation code are required to be determined.

2.2.3 Hydrogen jet fire

The following steps summarize the evolution of ignited pressurized hydrogen release. When the FCHV is involved in a fire accident, the TPRD is activated immediately to avoid overpressure in the vessel. Then hydrogen blowdown occurs at the TPRD orifice. Therefore, the hydrogen jet fire is assumable as a result (HyTunnel-CS D1.3, 2019).

Prediction of hydrogen flame length and jet fire shape is critical to deal with issues related to hydrogen hazard. Jet fire scaling is provided by scientist Molkov for instance (Molkov and Saffers, 2011). They are buoyancy-dominated jet fires (laminar flames), transitional jet fires (subsonic, transitional expanded flame) and momentum-dominated jet fires (choked and under-expanded jet flame).

Figure 10 presents the shape of horizontal hydrogen jet flame in three phases:

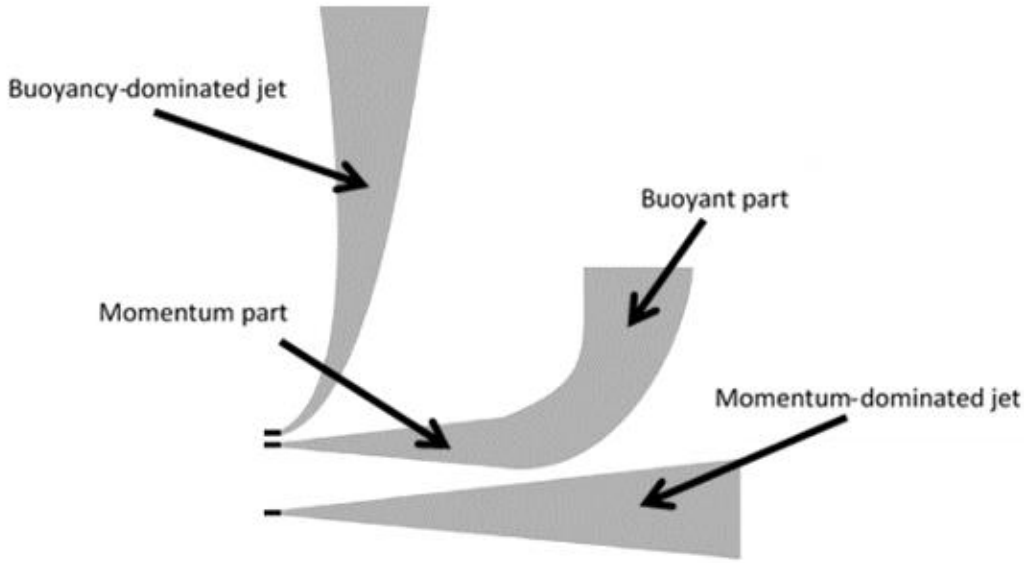

Figure 10. Momentum-dominated, transitional, and fully buoyancy-dominated jet.

For horizontal hydrogen fire, momentum-dominated jet is the most relevant phenomenon. There are three crucial criteria of straight flames to describe harm of injury or death as below (Molkov and Saffers, 2013; LaChance et al., 2011):

- No harm limit, 70 °C
- Pain limit for 5 min exposure, 115 °C
- Third degree burns for 20 seconds, 309 °C

The relationship between TPRD diameter and hydrogen flame length is proportional. In the past, the orifice diameter was up to about 6 mm, which is nowadays reduced down to 2 mm for typical FCHV scenario (HyTunnel-CS D1.3, 2019).

2.2.4 FDS software

Several programs are available to conduct fire simulation, such as SMARTFIRE, FLUENT, SOFIE, FDS and so on (Glasa and Valasek, 2014). Two computational software are used in this work. The first one is the Fire Dynamic Simulator (FDS), which is developed by the National Institute of Standards and Technology, USA (NIST, User Guide). FDS focuses on heat transfer and combustion process, and uses Navier-Stokes equations to appreciate thermally-driven flow at low Mach number, resolve parameters like temperature, chemical composition, species concentration, relative humidity, velocity inside every grid unit at an individually discrete time step (NIST, User Guide). The second is the PyroSim program, which is a Graphical User Interface (GUI) for the FDS tool (Thunderhead Engineering, PyroSim Manual).

In FDS, different turbulence models are available. For the following simulations, the Very Large Eddy Simulation (VLES) is selected. The VLES model is developed on a hybrid methodology, which is a compromise of efficiency and precision between conventional Reynolds-Averaged Navier–Stokes (RANS) model and Large Eddy Simulation (LES) model (Han and Krajnovic, 2013; Liu and Shih, 2006; Labois and Lakehal, 2011). This model calculates the very large scales of turbulence, and the remaining scales are solved by an eddy viscosity model (NIST, User Guide). Liquid droplets of water spray in this study are modelled as Lagrangian particles in the FDS code. Lagrangian particle model focuses on the bi-directional coupling between the gas phase and particles, specifically, on momentum transfer between the particles and the surrounding conveying gases.

2.2.5 Hydrogen blowdown from vessel

The total hydrogen mass in the tank is 5 kg; the overall volume of three onboard tanks is about 125 Liter, and the pressure is 70 MPa. The blowdown of hydrogen uses the adiabatic model. More specifically, CGH2 is rapidly released from the high pressure vessel, and heat transfer influence on the released hydrogen temperature is negligible and ignored.

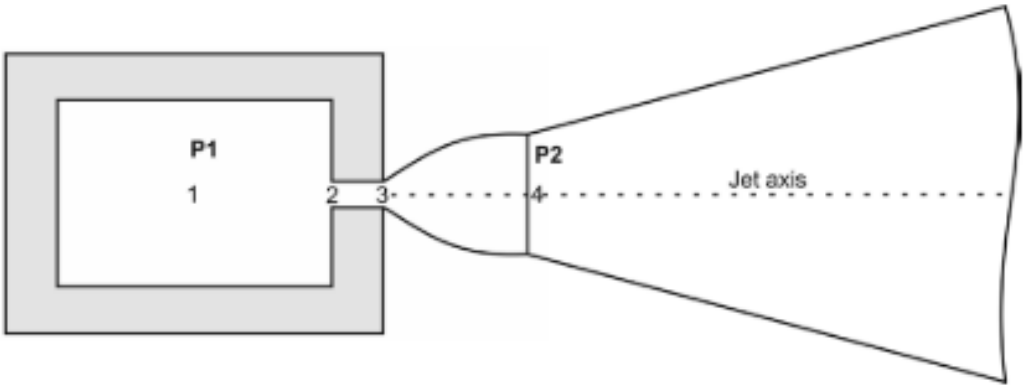

Figure 11. The under-expanded jet scheme: 1– Pressure vessel; 2– nozzle entrance; 3– nozzle exit; 4– effective nozzle diameter (Molkov, 2012).

In the blowdown process, the shape of the hydrogen jet transits from under-expanded to expanded (Molkov, 2012), as shown in Figure 11. CGH2 is released from the orifice at cross-section 3 with higher pressure. Cross-section 4 is assumed as the effective nozzle, because the pressure of hydrogen has dropped to atmospheric pressure until this location.

The decay from the maximum initial hydrogen mass flow rate down to 10% of this rate is simulated.

2.2.6 Suppression measures - Water spray

Installation of the water suppression system, hydrogen detection device, temperature and smoke sensors is important to improve tunnel safety (Till and Coon, 2019). When fire is detected in the tunnel, the water suppression system is activated at the proper time. The water mass flow rate and/ or spray angle can be adjusted based on detected information and diagnose outcomes.

Fixed Fire Fighting System (FFFS) is a water injection system, but the application of FFFS in tunnels is worldwide uncommon. FFFS has been written in the law only in Japan and Australia (HyTunnel-CS D1.1, 2019). There are different extinguishing agents in FFFS (CETU, 2010), such as inert gas, foam, water, water with tenso-active, etc. Although water suppression is not most efficient for gas fire (HyTunnel-CS D1.1, 2019), it may still adopted to suppress hydrogen fire in tunnel due to the low cost and easy availability.

The mitigation mechanisms of water can be summarized as direct cooling, evaporative cooling, and the oxygen displacement. Smaller water droplets have a larger surface-to-volume ratio of liquid phase, and therefore a better dispersion character. The control features of water mist system are given as follows and are discussed in the report (CETU, 2010):

- manual control
- operated by section and by remote control
- length of water mist section of 30 – 50 m.

The estimated cost for a water mist system approximates 2 million Euro per km of tunnel, and the maintenance cost is circa 40000 Euro per km of tunnel per year (HyTunnel-CS D1.1, 2019).

2.2.6.1 *Droplet size of water mist*

Water spray differ according to the different droplet sizes, as shown in Figure 12. Smaller droplet is chosen due the following three reasons (AbdRabbo et al., 2016). Firstly, small droplet has large surface area to enhance surface heat transfer, which is beneficial for vaporization and gas temperature reduction. Secondly, water mist can bring inerting effects by reducing oxygen fraction and local fire extinguishing. Thirdly, the water mist can limit the thermal radiation effect.

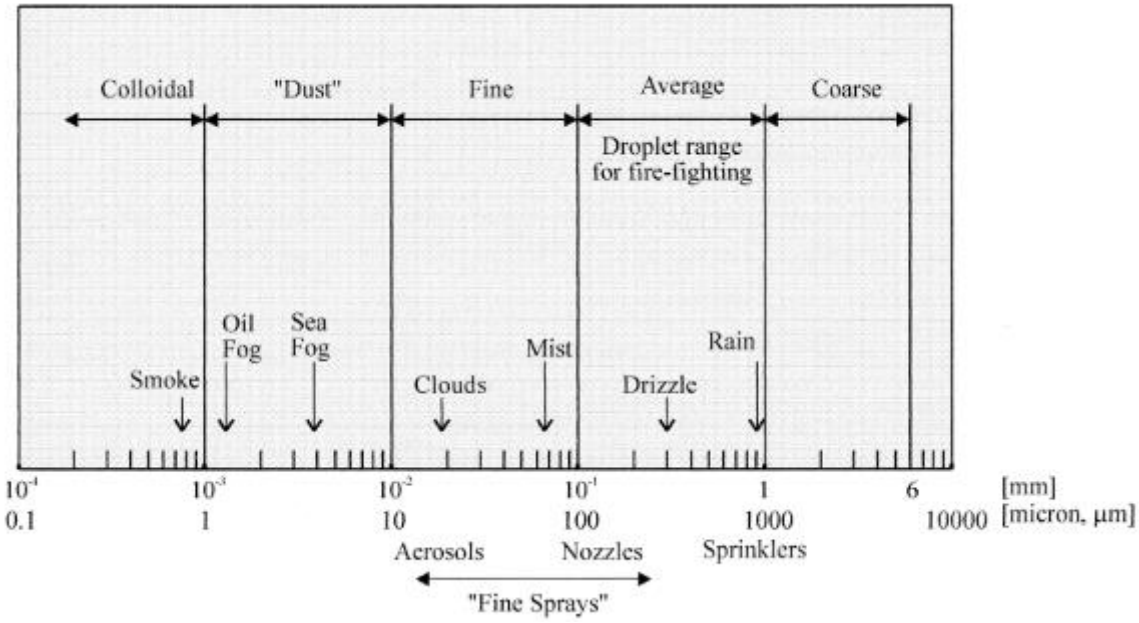

Figure 12. Spectrum of the water droplet diameters (Granta et al., 2000).

2.2.6.1.1 Spray nozzle flow rate

For different purposes, water spray mass flow rate can vary very much for extinguishing fires in different scales and fuels. According to the Pyrosim handbook (Thunderhead Engineering, PyroSim Manual), there are four types of water spays available:

- Generic commercial spray: flow rate 56.1 L/min
- Generic industrial spray: flow rate 80.13 L/min
- Generic residential spray: flow rate 49.05 L/min
- Generic storage spray: flow rate 164.59 L/min

2.2.6.2 *Oxygen depletion*

Based on the different effects and symptoms of oxygen depletion on human being, the oxygen depletion is divided into five classes, as indicated in Table 4.

Table 4. Effect of oxygen concentration (European Industrial Gases Association, 2009).

O_2 (vol. %)	**Effects and Symptom**
18 - 21	**The individual can detect no discernible symptoms**. It is safe to continue working.
11 - 18	Reduction of physical and intellectual performance **without the sufferer being aware**.
8 - 11	Possibility of fainting within a few minutes without prior warning. **Risk of death below 11%**.
6 - 8	Fainting occurs after a short time. **Resuscitation possible** if carried out immediately.
0 - 6	Fainting almost immediate. **Brain damage**, even if rescued.

2.2.7 Simulation scenarios and result analysis

2.2.7.1 *Geometry model and boundary conditions*

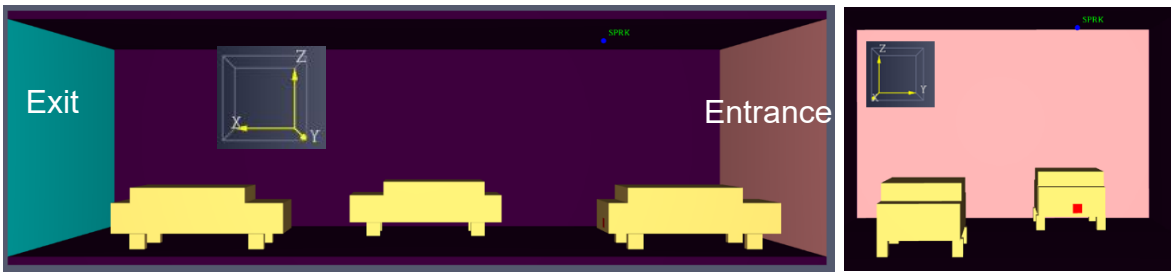

Figure 13. Schematic model of simulated tunnel section.

The model in Figure 13 is built with the following settings for the FDS simulations:

- Tunnel geometry: length 20 m, width 9 m, height 5.8 m.
- Vents of the tunnel: the cross-section on the right hand side as tunnel entrance (inlet); the cross-section on the left hand side as tunnel exit (outlet).
- Ventilation: 3 m/s, with a positive direction from right to left.

Exterior dimensions of car model in simulation scenario:

- Length: 4500 mm
- Width: 1800 mm
- Height: 1600 mm
- Ground clearance: 400 mm

Environment parameters:

- Ambient temperature: 20 °C
- Ambient pressure: 101325 Pa
- Ambient oxygen volume fraction: 0.21
- Relative humidity: 40 %
- Maximum visibility: 30 m
- Gravity: - 9.81 m/s^2 along Z-axis

Spray models:

- Location: sprinkler coordinates (5 m, 2 m, 5.5 m)
- Operation pressure: 0.5 bar (default in FDS model)
- Particle velocity: 5 m/s
- Spray angle: 60 to 75°
- Jet stream type: Conical
- Injected particles per second: 10000

Water droplet:

- Drag option: Sphere
- Density volume fraction: 1E-5
- Minimum diameter: 20 µm
- Maximal diameter: Infinity

2.2.7.2 *Parameter configurations*

The scenarios of hydrogen release, distribution and combustion in the tunnel section are simulated in this section. Moreover, the mitigation measures suppressing hydrogen fire are an activated water mist system and limited oxygen volume fraction. The maximal hydrogen mass flow rate is controlled as 0.05 kg/s, 0.1 kg/s, and 0.2 kg/s. The hydrogen pressure in the reservoir is 70 MPa, the temperature of the reservoir is 293 K, the total hydrogen mass is circa 5 kg, and the volume of the onboard tank is 124.77 L.

Hydrogen mass flow rate decay curve

The decaying curves of hydrogen blowdown are assumed as caused by adiabatic process and are calculated by using the model in https://elab-prod.iket.kit.edu/. The blowdown decay curves of hydrogen mass flow rate and the remaining hydrogen mass in the tank are shown in the following figure.

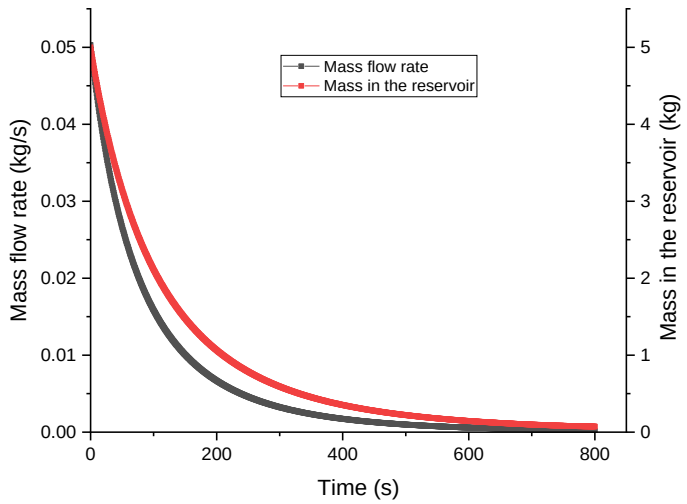

Figure 14. Small hydrogen mass flow rate with orifice diameter 1.37 mm.

Figure 14 shows the decay of the hydrogen mass flow rate with the initial maximum rate of 0.0503 kg/s. In this condition, the orifice diameter is 1.37 mm, the decay duration from beginning to the one-tenth of the maximal mass flow rate is 237.6 s.

For another hydrogen blowdown assumption, the maximal hydrogen mass flow rate is 0.1009 kg/s, the corresponding orifice diameter is 1.94 mm, and it takes 118.8 s from the maximum hydrogen mass flux to 10 % of the initial hydrogen release rate. The hydrogen blowdown curve is shown in Figure 15.

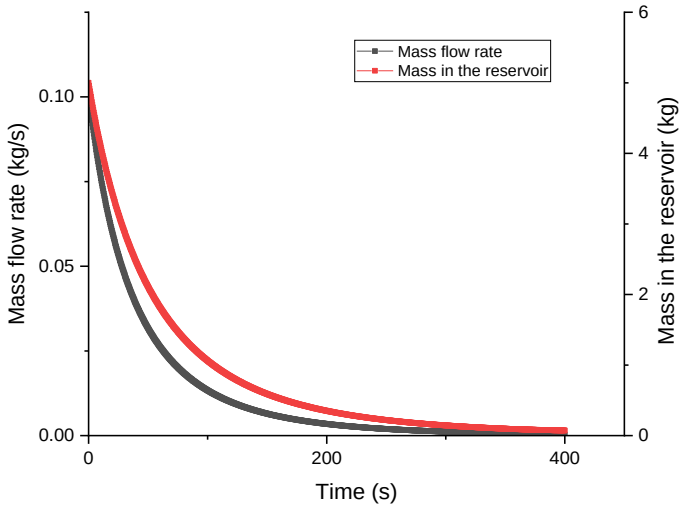

Figure 15. Large hydrogen mass flow rate with orifice diameter 1.94 mm.

According to the sub-task description of the HyTunnel-CS project, the third case with a maximal hydrogen injection mass flow rate of 0.2 kg/s is also computed, the flow rate decay curve is shown in Figure 16. The corresponding opening diameter is about 2.74 mm, and the simulation time for injection is 59.4 seconds.

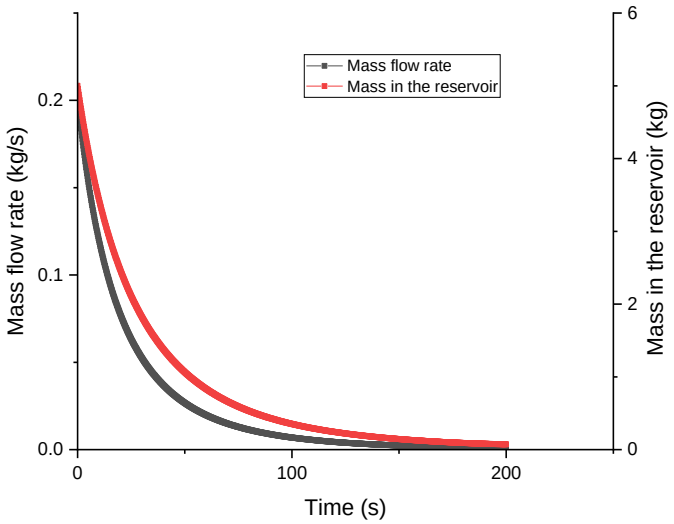

Figure 16. Very large hydrogen mass flow rate with orifice diameter 2.74 mm.

<u>Water injection</u>

One of the major mitigation measures to suppress hydrogen fire is water spray. In the configuration of the Pyrosim (GUI), two representative sprinklers are assumed (Thunderhead Engineering, PyroSim Manual):

- Generic industrial spray: 80.13 L/min
- Generic storage spray: 164.59 L/min

Another critical parameter is the size of water droplets, which are the median volumetric droplet diameter injected from the sprinkler. In the study, three types of median diameter (Wang et al., 2016) are defined:

- Small droplet size: 100 μm
- Middle droplet size: 200 μm
- Large droplet size: 300 μm

Oxygen volume fraction

The concentration of oxygen affects not only human health, but influences also the combustion of hydrogen. In the simulation scenarios, different oxygen depleted situations are defined as follows:

- Normal concentration: 21 vol. % (reference case)
- Medium depletion of oxygen: 15 vol. %
- Serious depletion of oxygen: 11 vol. %

Human cannot survive if the surrounding air contains less than 11 vol. % oxygen. Therefore, lower oxygen concentration is not considered in the study.

Table 5. Volume and mass fraction of oxygen in the gas phase.

Volume fraction of oxygen in the gas phase	Mol mass of air (g/mol)	Mass fraction of oxygen in the gas phase
0.21	28.62	0.2324
0.15	28.6	0.1678
0.11	28.44	0.1238

Ventilation

The minimum ventilation speed is defined as 3 m/s, as recommended in the (HyTunnel-CS D1.1, 2019). When analyzing the effect of water spray, only the ventilation from the tunnel section entrance to exit is configured. In case of oxygen depletion simulations, the reverse ventilation direction is considered additionally, in order to make comparison between variant cases.

Grid convergence check

Grid sensitivity is determined by comparing the result of the same case by using the finer grid and coarser grid, respectively. This step is to check the stability and the robustness of the grids (AbdRabbo et al., 2016). The two grid options are:

- Grid 1: average mesh size circa 0.459 m, cell number 11160
- Grid 2: average mesh size circa 0.344 m, cell number 26496

The comparisons are made between the average gas temperatures at the exit of the tunnel section and the temperature at the fire downstream region, i.e., X+Z+ zone, because they are significant parameters to evaluate the effectiveness of fire suppression.

According to the simulation case "alpha" (small hydrogen mass flow rate, without water injection, without oxygen depletion), the concerned temperatures are presented in Figure 17 and Figure 18.

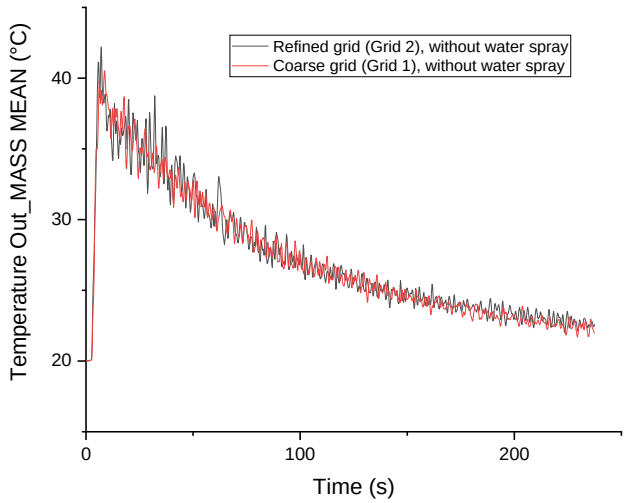

Figure 17. Consideration of the integral cooling effect of the spray on H2 combustion: Tunnel exit average gas temperature with coarse and refined grids.

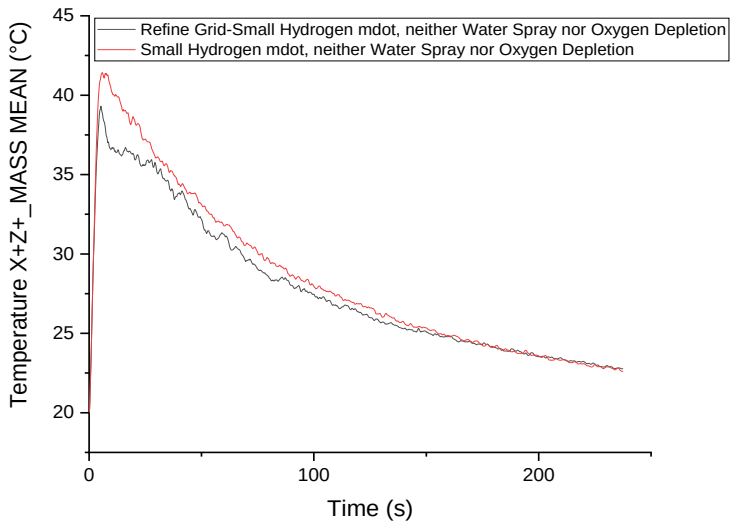

Figure 18. Downstream average gas temperature with coarse and refined grids.

Figure 17 shows a good consistency between the two simulated average gas temperatures at the tunnel exit. Figure 18 presents also a good agreement between the two temperature curves, except a little discrepancy between about 5-30 s. It can be determined that the coarse grid can be chosen for a better computing efficiency.

The same analysis procedure is done to the simulation case "sll" with water spray, to show the performance of the coarse grid and the refined grid.

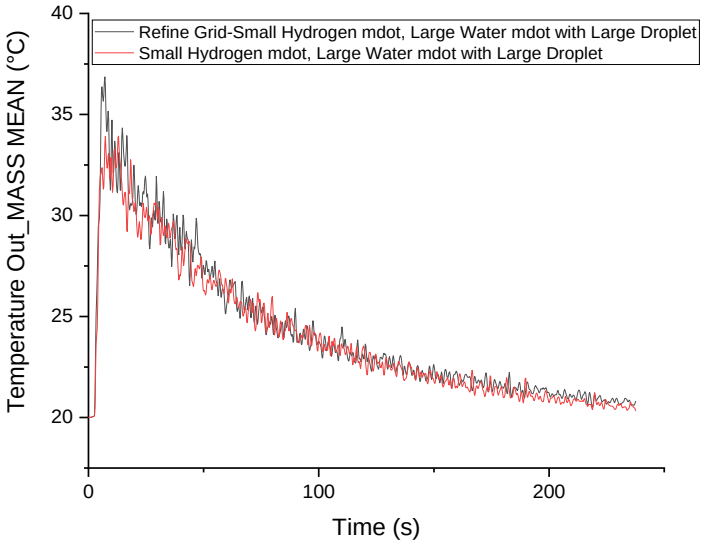

Figure 19. Tunnel exit average gas temperature with refined or coarse grids, in cases with water spray.

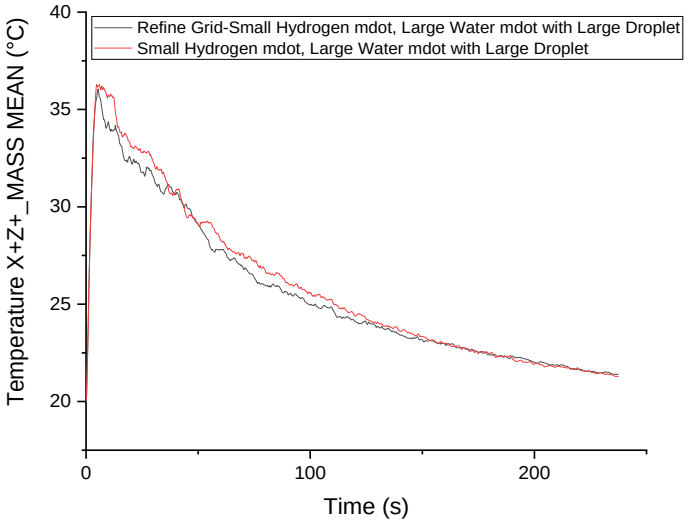

Figure 20. Downstream average gas temperature with refined or coarse grids, in cases with water spray.

Both Figure 19 and Figure 20 show good consistency between the concerned temperatures.

However, the computing time efficiency of Grid 1 (coarse mesh) is much higher than that of Grid 2 (refined mesh). The computing time (CPU time) for case “alpha” is 4 h by using Grid 1, and 14 h by using Grid 2; the computing time for case “sll” is 13 h by using Grid 1, and 38 h by using Grid 2. Due to time efficiency consideration, the coarse grid (Grid 1) with an average cell size of 0.459 m is chosen for all the simulation cases.

<u>Water spray scenarios</u>

Table 6. Water sprays matrix.

	Water spray						Without water spray
	Small mass flow rate of water (80.13 L/min)			Large mass flow rate of water (164.59 L/min)			
	Small droplet (100 µm)	Middle droplet (200 µm)	Large droplet (300 µm)	Small droplet (100 µm)	Middle droplet (200 µm)	Large droplet (300 µm)	Pos. ventilation (3 m/s)
Small mass flow rate of H_2 (max.0.05 kg/s)	sss	ssm	ssl	sls	slm	sll	alpha
Large mass flow rate of H_2 (max.0.1 kg/s)	lss	lsm	lsl	lls	llm	lll	beta
Very large mass flow rate of H_2 (max.0.2 kg/s)	xlss	xlsm	xlsl	xlls	xllm	xlll	epsilon

The 21 simulation scenarios, listed in Table 6, are simulated by using the FDS code. Representative output parameters like gas temperature, humidity and gas volume fraction in certain regions are computed as results to analyze suppression effect of water spray in different cases.

<u>Heat release rate</u>

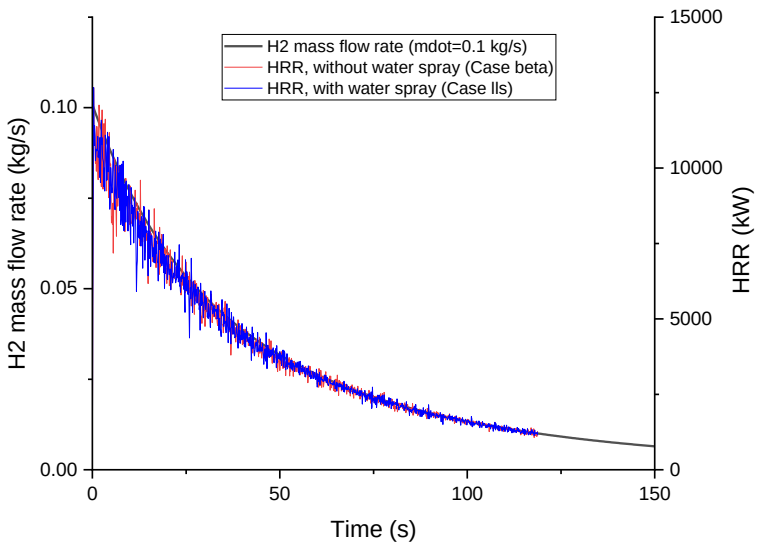

Figure 21. Heat release rate (HRR) comparison between the case with water spray and the case without spray, and the comparison between the hydrogen release rate decay and HRR decay.

The two heat release rate (HRR) curves in case of with/ without water spray, as shown in Figure 21, coincide with each other. It implies that all the hydrogen is burned in the simulation domain.

Temperature

Temperature contours

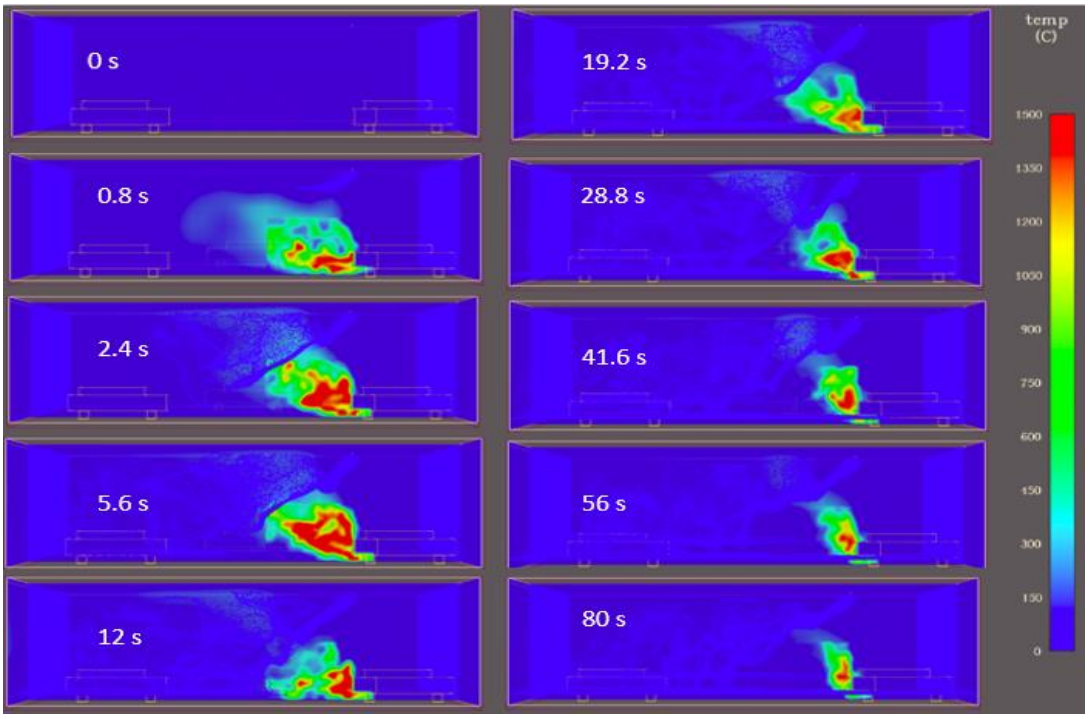

Figure 22. Temperature contours of large water droplet (Case lll), with a vertically upwards jet from TPRD.

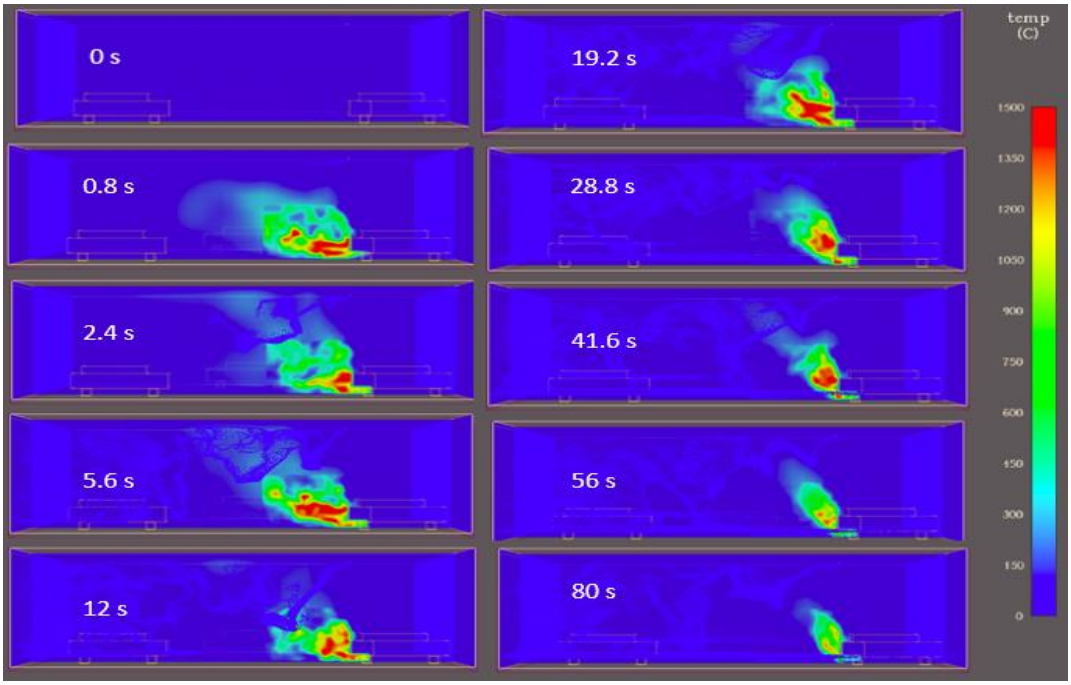

Figure 23. Temperature contours of small water droplet (Case lls).

Temperature contour plots are shown in Figure 22 and Figure 23, for the plane which cuts through the hydrogen injection location along the longitudinal direction of the tunnel. The two plots present similar hydrogen flame evolution processes with interaction with the water spray. However, by comparing the two plots at the two times of 2.4 s and 5.6 s, the hydrogen fire dimension shown in Figure 23 is smaller than that in Figure 22. It is because the spray with smaller water droplets of case "lls" has a better suppression effect on fire than that of case "lll".

2.2.8 Gas temperature in case of small hydrogen mass flow rate

Figure 24 expresses the suppression effect of water injection with different droplet sizes. Without water spray system, the average gas temperature at the exit reaches 40 °C, as shown in the curve in black in Figure 24. However, due to the mitigation effect of water injection (80.13 L/min), the peak temperature decreases by at least 5 °C. When the droplet diameter decreases from 300 μm to 100 μm, the average gas temperature at the exit decreases to about 32 °C.

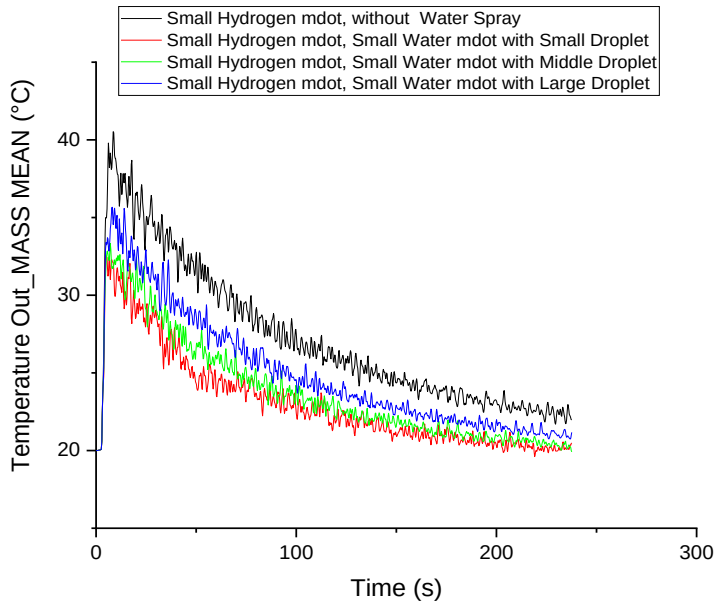

Figure 24. Tunnel exit average gas temperature of cases with small water mass flow rate.

The mean gas temperature in the downstream region from Figure 25 is about 2-3 °C higher than the tunnel exit average gas temperature from Figure 24. Meanwhile, the average gas temperature in the volume of the X+Z+ region (Figure 25) appears smoother than the average gas temperature at the tunnel exit plane (Figure 24).

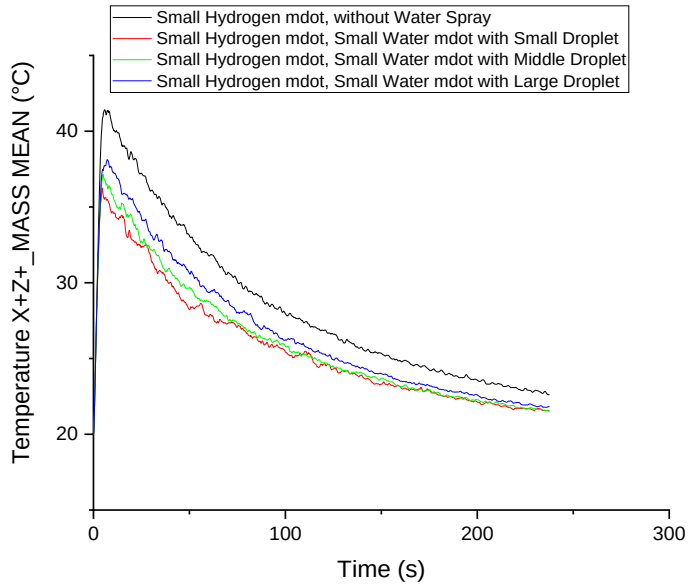

Figure 25. Downstream average gas temperature of cases with small water mass flow rate.

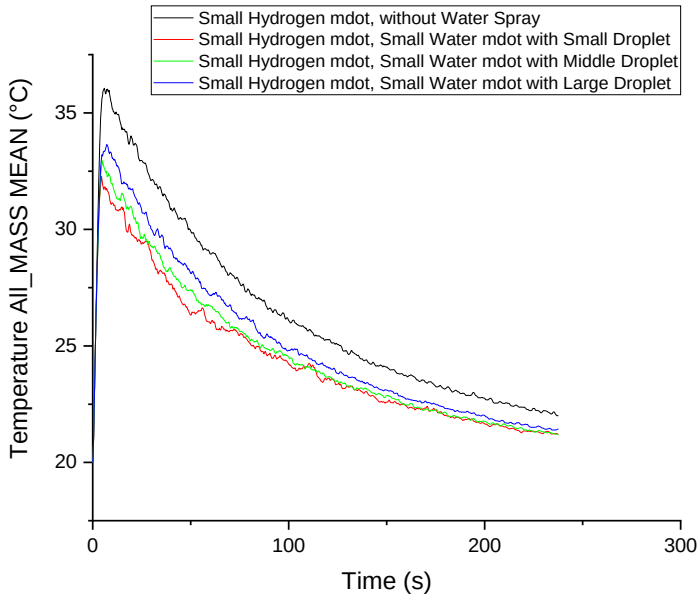

Figure 26. Tunnel section average gas temperature of cases with small water mass flow rate.

The average gas temperature in the entire domain is shown in Figure 26, which is lower than that of the downstream region (Figure 25). The reason is that the fresh air in the upstream region has the lower ambient temperature. That is to say, the upstream region is barely influenced by the heat release from hydrogen fire due to the ventilation effect. By focusing on the effect of different droplet sizes in Figure 26, it can be concluded that the small water droplets bring better suppression effect than the large droplets. The peak value of the average gas temperature is reduced by about 4 °C by the water spray, if the curve in black (no spray) is compared to the curve in red (with water spray).

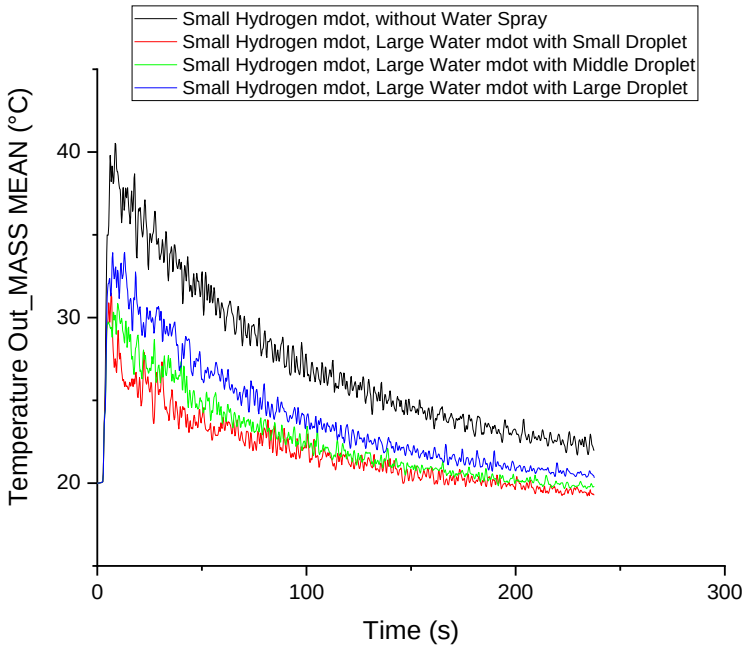

Figure 27. Tunnel exit average gas temperature of cases with large water mass flow rate.

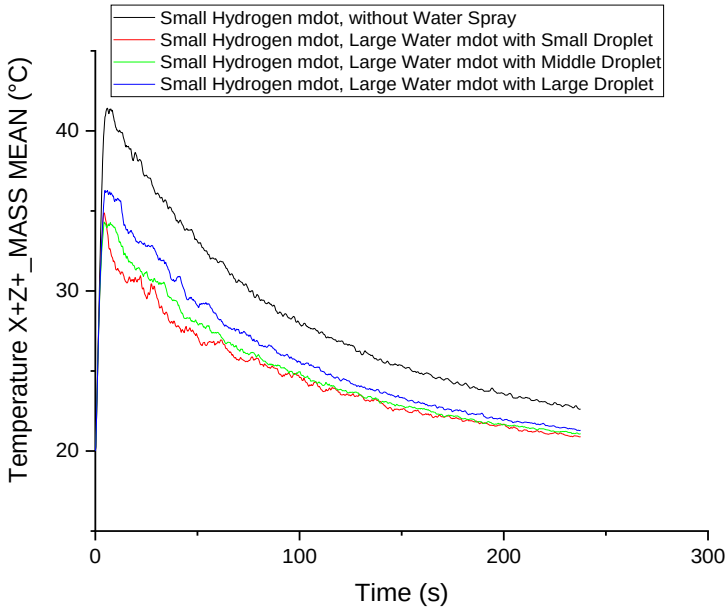

Figure 28. Downstream region average gas temperature of cases and large water mass flow rate.

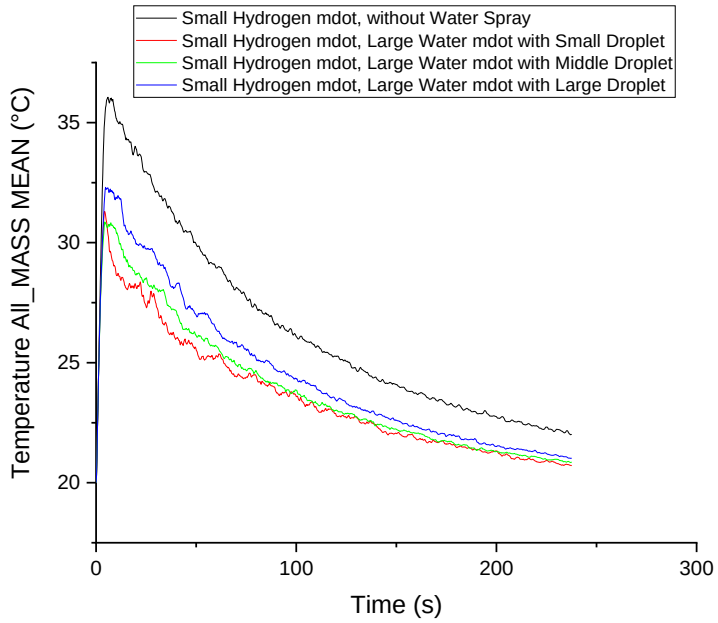

Figure 29. Tunnel section average gas temperature of cases with large water mass flow rate.

In case of large mass flow rate of water spray, the average gas temperatures at the tunnel exit, in the downstream region and in the whole tunnel section, are shown in Figure 27, Figure 28 and Figure 29, respectively. They show similar features as in Figure 24 through Figure 26.

The suppression effect of different water spray flow rate is compared in Figure 30. It can be concluded that water spray can cool down the thermal effect of hydrogen fire, and the larger water flow rate (164.59 L/min) has a better cooling effect than that of 80.13 L/min.

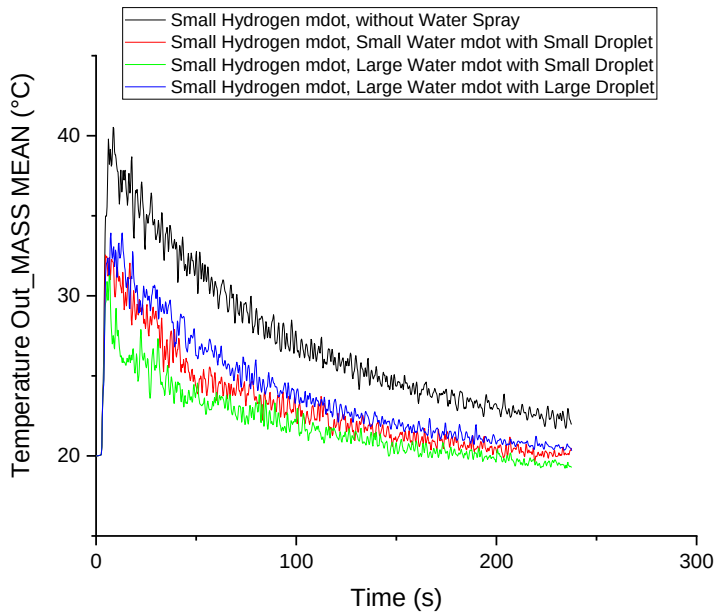

Figure 30. Tunnel exit average gas temperature of cases with water sprays.

2.2.9 Gas temperature in case of large hydrogen mass flow rates

The same simulations have been done for the case of large hydrogen mass flow rate (0.1 kg/s). The simulation results on the gas temperature features are very similar to the previous case with smaller hydrogen flow rate, except a temperature increase in the gas due to the larger heat release rate of hydrogen combustion.

2.2.10 Gas temperature in case of very large hydrogen mass flow rate

In cases of very large hydrogen mass flow rate (0.2 kg/s), the peak value of average gas temperature at tunnel exit is over 70 °C, which exceeds the no-harm temperature limit to human beings, but it is only in the short duration, as shown in Figure 31.

Figure 31 also shows that the suppression effect of small water spray mass flow rate with small droplets is roughly equivalent to the effect of large water spray mass flow rate with large droplets, by comparing the curves in red and in blue in Figure 31. Similar conclusion can be drawn in the previous cases of small and large H_2 mass flow rates. The useful conclusion may supply a good guidance for the water spray system design in practice.

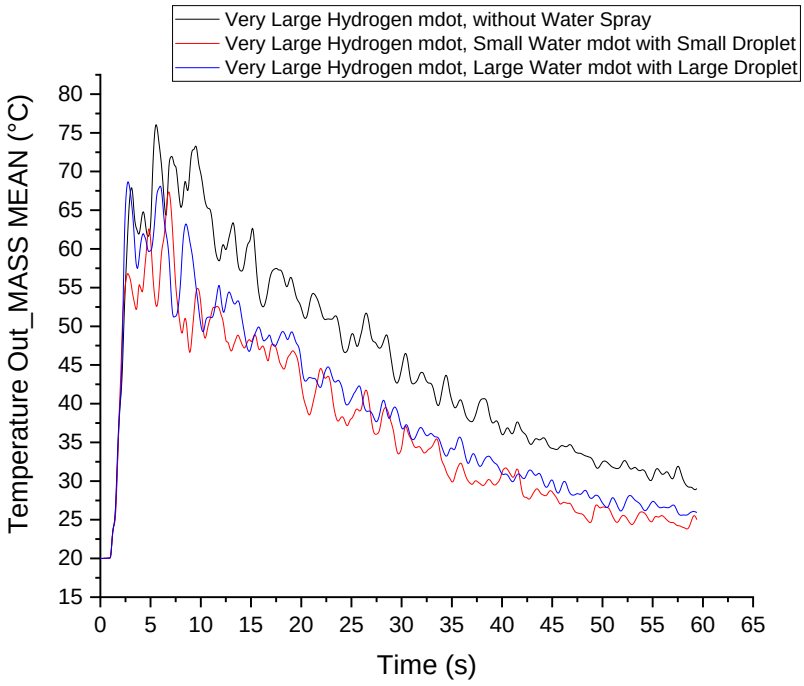

Figure 31. Tunnel exit average gas temperature of very large hydrogen mass flow rate with water sprays.

Water injection can generate turbulence (Wingerden, 1995). The reason is the momentum exchange between the injected water and the conveying gas phase. The generated turbulence can intensify hydrogen combustion in some circumstance (Thomas, 2000). This phenomenon is observed in Figure 32, which shows the average gas temperature in the downstream region. Generally, the gas temperature in case of larger water spray mass flow rate is lower than that of smaller water flow rate. However, the temperature values are inversed at the moment of 2-3 s, as shown in Figure 32. It is thought to be caused by the water injection induced turbulence.

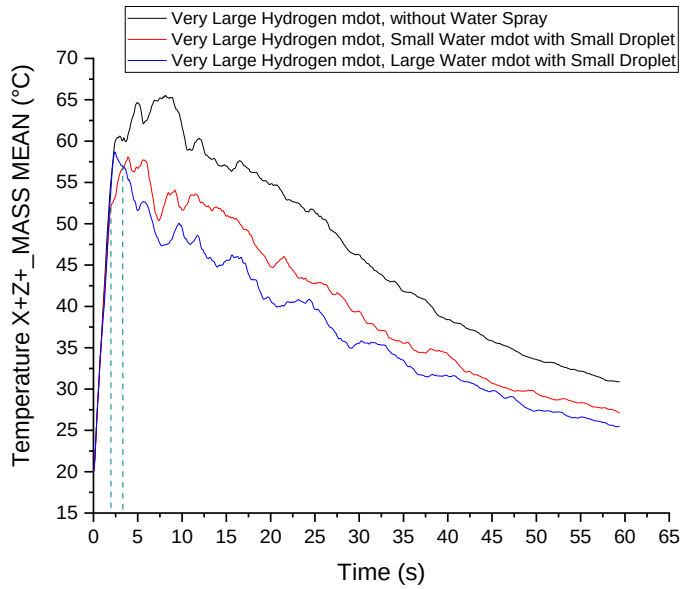

Figure 32. Downstream average gas temperature of very large hydrogen mass flow rate with water sprays.

2.2.11 Correlation between hydrogen mass flow rate and water spray flow rate

In view of thermodynamics, a larger mass flow rate of water spray is needed to cool down the hydrogen fire with a larger hydrogen mass injection rate, to the same level of gas temperature. Therefore, a series of simulations with increasing H_2 mass flow rate from 0.05 kg/s to 0.13 kg/s are simulated with increasing water mass flow rate, as shown in Table 7. In the five simulation cases, the peak value of average gas temperature in the whole tunnel section is cooled down to 33 °C; the droplet size is 100 μm.

Table 7. Correlation between hydrogen mass flow rate and water sprays.

Hydrogen mass flow rate (kg/s)	Water mass flow rate (L/min)
0.05	80
0.1	690
0.11	1600
0.12	3100
0.13	6000

2.2.12 Humidity

Humidity is associated with human metabolism. Thus, too high or too low humidity can cause health problem. By definition, the relative humidity is the ratio of absolute humidity relative to a maximum humidity given in the below formula (Wexler, 1965):

$$\varphi = \frac{\rho_\omega}{\rho_{\omega,max}} * 100\% = \frac{e}{E} * 100\%$$

with φ: relative humidity; ρ_ω: absolute humidity $\left[\frac{g}{m^3}\right]$; $\rho_{\omega,max}$: max. absolute humidity $\left[\frac{g}{m^3}\right]$; e: vapor pressure[Pa]; E: saturated vapor pressure[Pa].

Compared with relative humidity, absolute humidity is used preferentially because it describes the water content of air:

$$\rho_\omega = \frac{e}{R_\omega * T}$$

with R_ω: gas constant of water, 461.25 $\left[\frac{J}{kg*K}\right]$; T: temperature [K].

To convert the relative humidity into the absolute humidity, the saturated vapor pressure is required to be determined in advance, which is in the industry mostly approximated by formula, for example (Wexler, 1965):

$$P = \exp\left(20.386 - \frac{5132}{T}\right)$$

with P: vapor pressure [mmHg]; T: the temperature[K].

$$E = \frac{P}{760} * 101325$$

Besides, the Antoine equation and many other approximate formulas are used to calculate the saturated vapor pressure with different accuracy.

Consequently, the connection between the above parameters is

$$\varphi * E = e = \rho_\omega * R_\omega * T$$

The absolute humidity expresses as below:

$$\rho_\omega = \frac{\varphi * E}{R_\omega * T}$$

There is a comfortable requirement about relative humidity, when the relative humidity is between 30 % to 70 %, man feels comfortable (Gilmore, 1992). Lower relative humidity can result in dry mouth, nosebleed, and dry cracked skin. A higher relative humidity can inhibit the heat dissipation of the human body.

Water droplets are generated by spray system and interact with hydrogen fire. Due to the vaporization of water, the relative humidity increases. As shown in Figure 33, smaller water droplets have stronger evaporation effect. The relative humidity-time curves go through a decreasing-increasing evolution process. The range of relative humidity of water injection cases keep in 28% - 43%. Water sprays improve relative humidity and the value of relative humidity quickly return to the comfortable range for human.

According to Figure 34, the larger water spray mass flow rate produces a higher relative humidity than that of smaller water mass flow rate, certainly because the evaporation amount is increased due to the larger amount of injected water.

Relative humidity

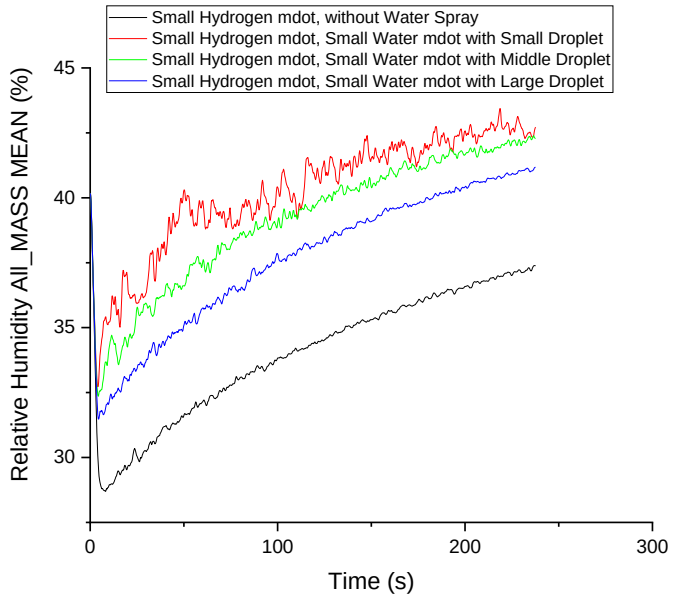

Figure 33. Tunnel section average relative humidity of small hydrogen mass flow rate with small water mass flow rate.

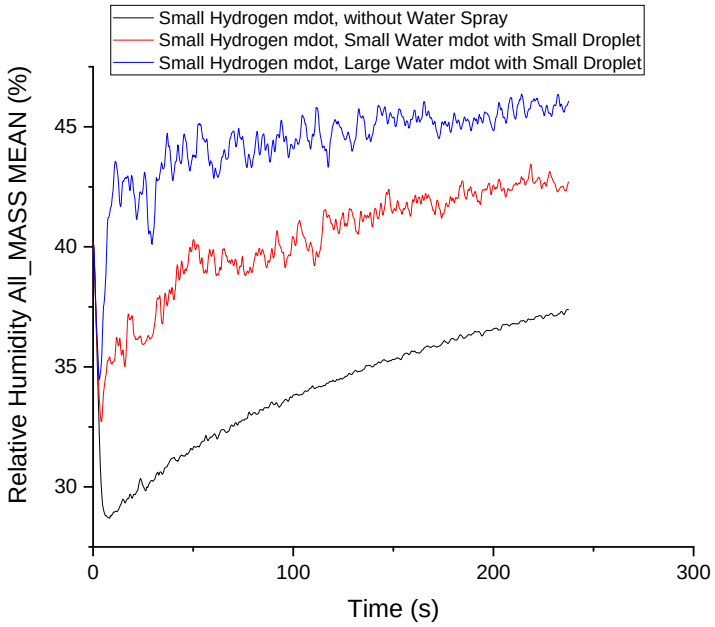

Figure 34. Tunnel section average relative humidity of small hydrogen mass flow rate with water sprays.

Absolute humidity

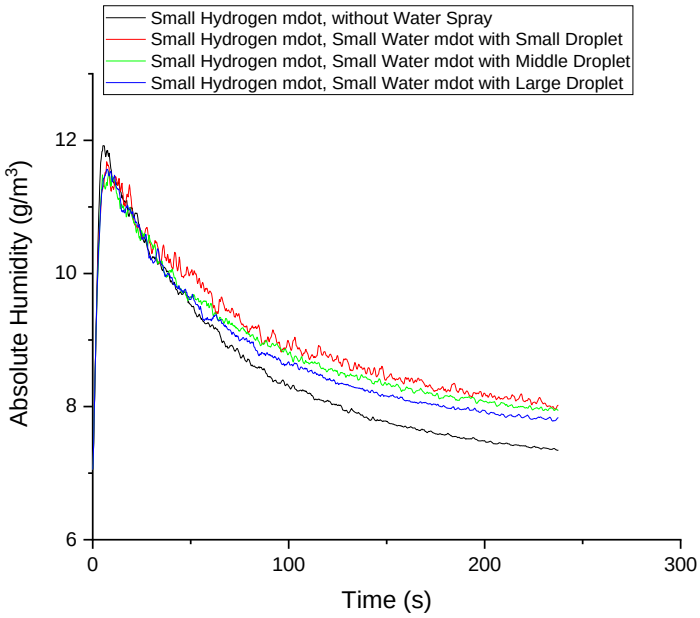

Figure 35. Tunnel section average absolute humidity of small hydrogen mass flow rate with small water mass flow rate.

Evaporation of water droplets increases absolute humidity. Especially in the later stage of simulation in Figure 35, the absolute humidity in the case of smaller water droplet is higher than in other cases. It indicates that smaller droplets are prone to evaporate, due to a large surface-to-volume ratio.

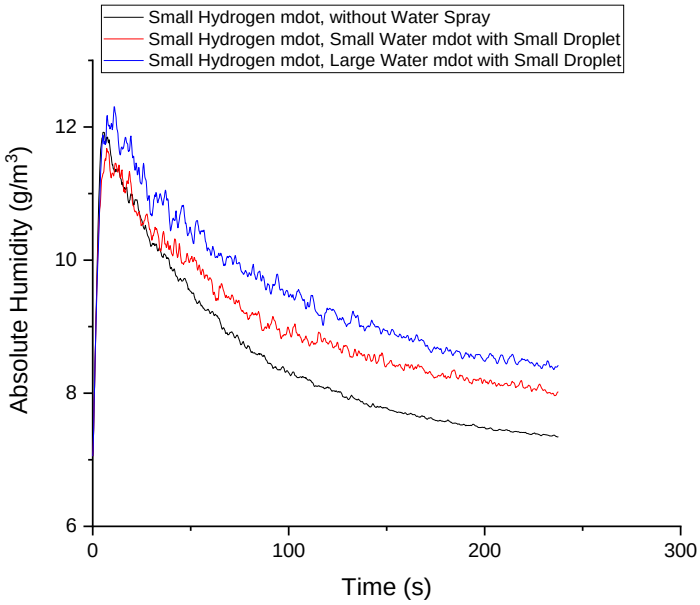

Figure 36. Tunnel section average absolute humidity of small hydrogen mass flow rate with water sprays.

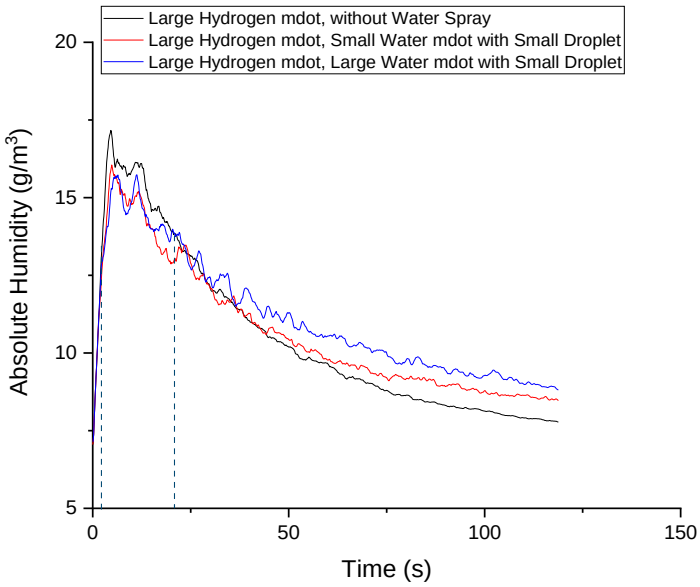

Figure 37. Tunnel section average absolute humidity of large hydrogen mass flow rate with water sprays.

The absolute humidity time evolution curve in Figure 36 shows that the water injection increases steam fraction in air, thus, increases the absolute humidity. However, in case of a large H_2 mass flow rate, as shown in Figure 37, the water spray results in a decrease of the absolute humidity at the earlier stage of about 20 seconds. On one hand, the absolute humidity is increased by the water evaporation; on the other hand, the maximum (saturated) absolute humidity is decreased due to the gas temperature decrease. Therefore, the real absolute humidity is a compromise between the two competing effects. In case of small H_2 release rate, the former effect (evaporation) dominates the phenomena, but the latter effect (decrease of maximum absolute humidity) prevails the phenomena at the earlier 20 seconds in the case of large H_2 release rate.

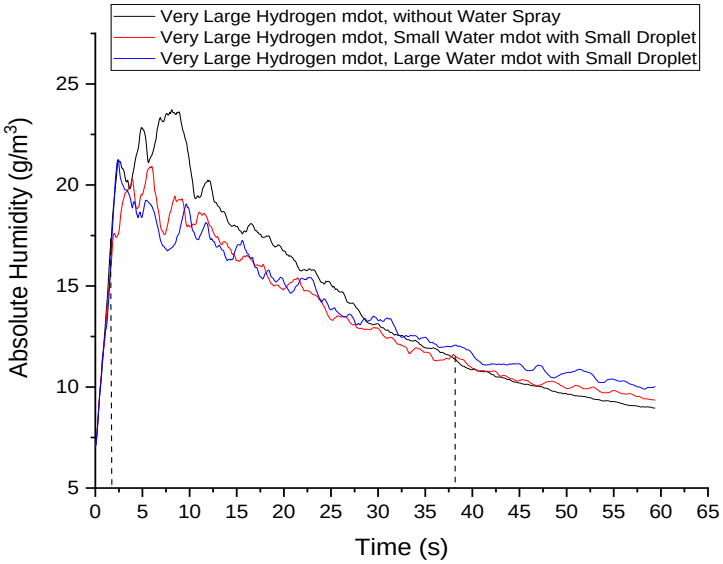

Figure 38. Tunnel section average absolute humidity of very large hydrogen mass flow rate with water sprays.

The curves of absolute humidity in Figure 38 have similar features compared to the curves in Figure 37. In case of very large hydrogen mass flow rate (0.2 kg/s), the decrease of saturated absolute humidity due to the cooling effect of spray, plays a dominant role in the first half minute. Thus, the absolute humidity of the case with water spray before 37 s is smaller than that of the case without spray.

Hydrogen volume fraction contours

The following hydrogen contours in Figure 39 shows the transient evolution of the hydrogen jet fire. The state of hydrogen jet fire is a momentum-dominated jet flow before 5.6 s, because, as can be seen from the Figure 39, the flame extends mainly in horizontal direction. Due to the decay of the injected hydrogen mass flow rate, the flame shape later looks like a buoyancy-dominated jet, which develops vertically. The flame development process is consistent with the description in Section 2.2.3.

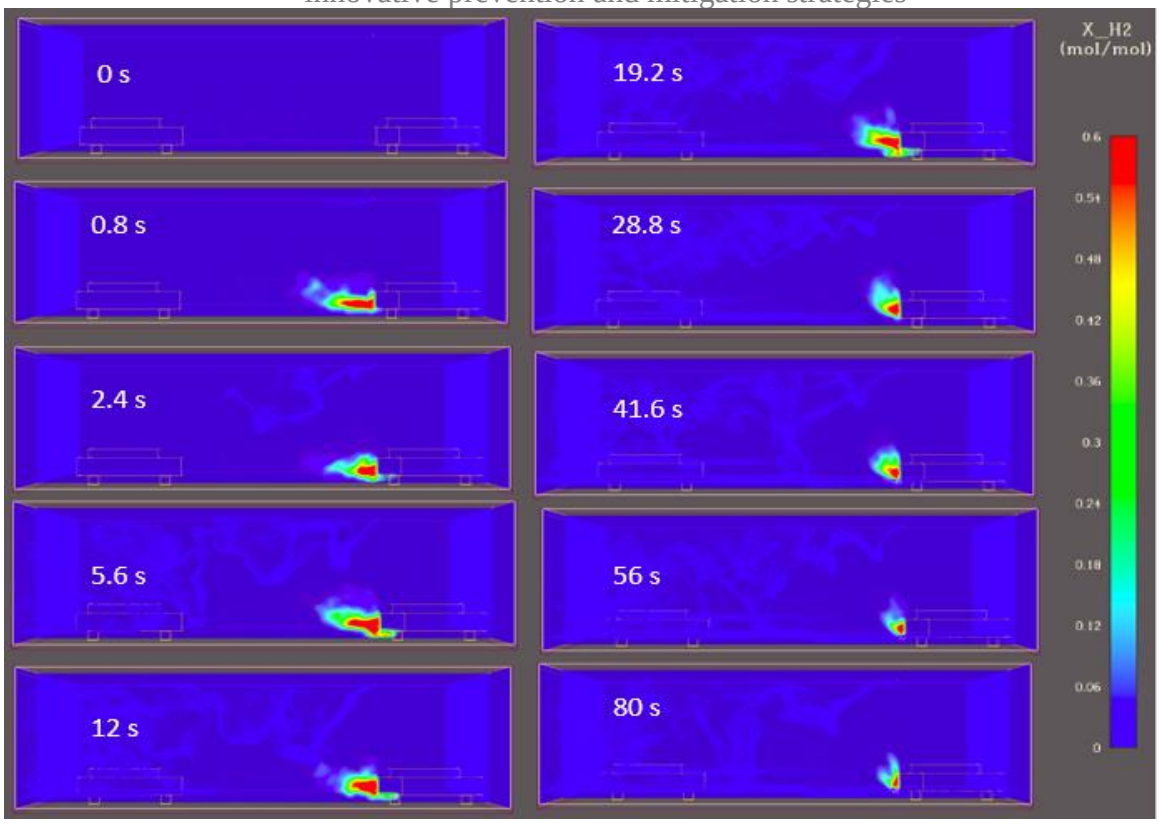

Figure 39. Hydrogen contours of large hydrogen mass flow rate with large water mass flow rate and small water particle.

Hydrogen volume fraction

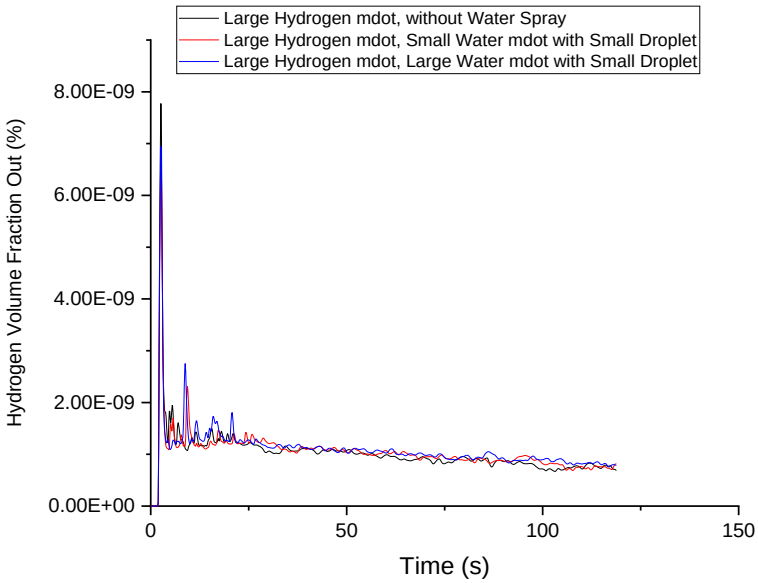

Figure 40. Tunnel exit average hydrogen volume fraction of large hydrogen mass flow rate with water sprays.

Figure 40 illustrates that water injection makes no difference to the amount of escaped hydrogen from the tunnel exit. Unburned hydrogen remains at negligible level (below 4 vol. %, LFL), and it does not bring risk to the external space.

As the result of hydrogen combustion and water evaporation, the oxygen concentration in tunnel section decreases at the beginning period, as shown in Figure 41. The oxygen concentration returns the ambient level afterwards, due to the vented fresh air and the decaying of injected hydrogen amount. The oxygen concentration in case of larger water mass flow rate is smaller than that of smaller spray flow rate, because of the stronger evaporation effect in the former case.

Oxygen volume fraction

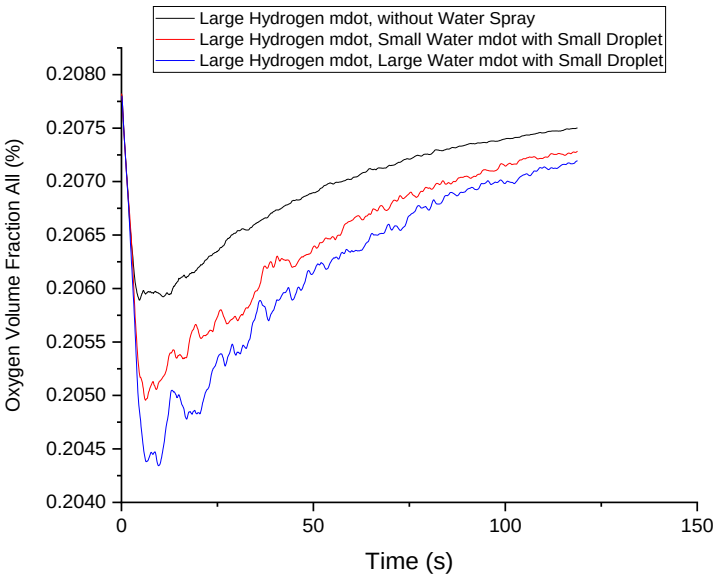

Figure 41. Tunnel section average oxygen volume fraction of large hydrogen mass flow rate with water sprays.

Velocity flow field

The momentum transfer between water droplets and the gas phase is enhanced in case of larger water injection rate. Water sprays can generate turbulence in some circumstances. Thus, plotting velocity fields is helpful to observe the flow patterns. Figure 42 and Figure 43 display vector fields of the reference case without spray (Case beta) and the case with water spray under 0.2 kg/s hydrogen mass flow rate (Case lls).

In Figure 42, the velocity vector of gas phase is related to the hydrogen mass flow rate. In the time around 2 s, the flow field near the injection location of TPRD is similar to a momentum-dominated jet. The hydrogen jet flame extends quite a long distance horizontally without water spray.

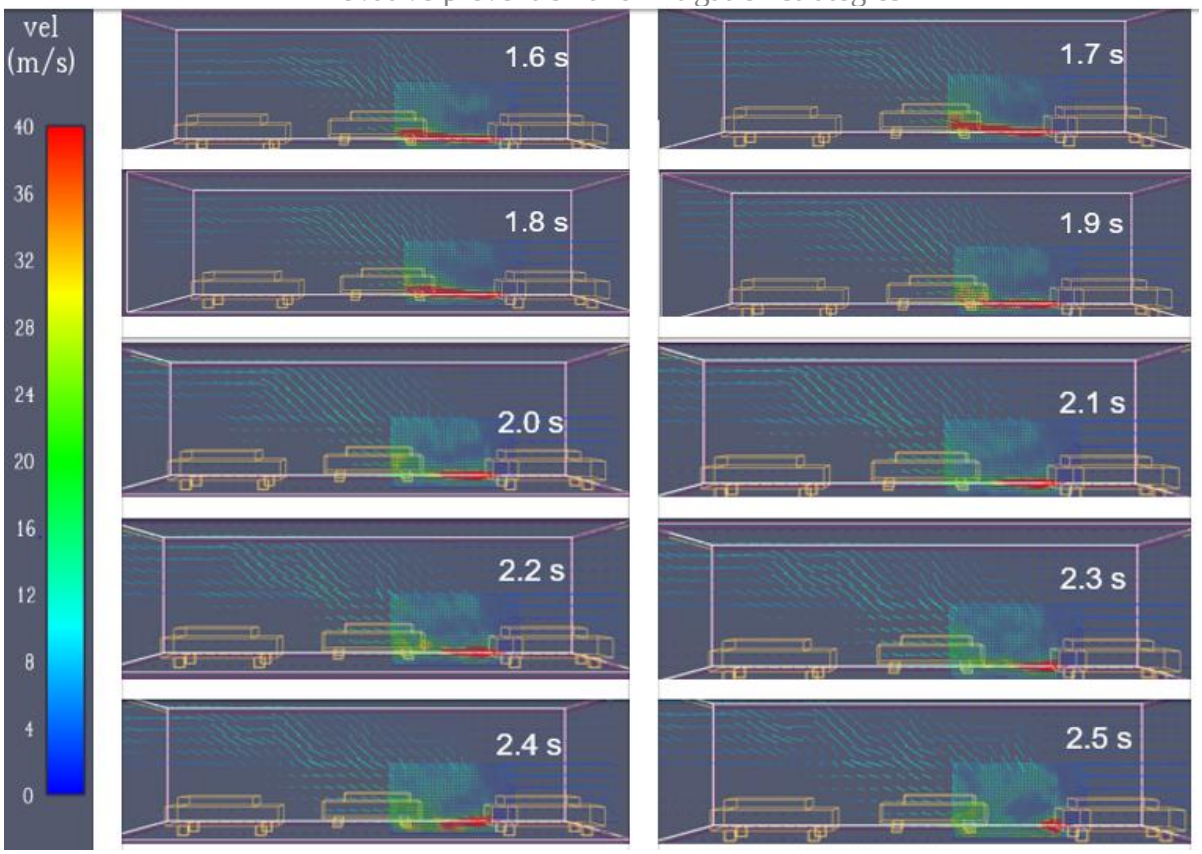

Figure 42. Velocity vector field of very large hydrogen mass flow rate without water spray.

At the early stage (2 s to 3 s) from Figure 43, the length of the hydrogen jet flame is significantly influenced by the interaction between the water spray droplets and the flame, especially as shown at 2.4 s in Figure 43. According to the picture, the hydrogen jet flame develops a little in the downwards direction, due to the downwards momentum of the water injected and due to its entrainment effect.

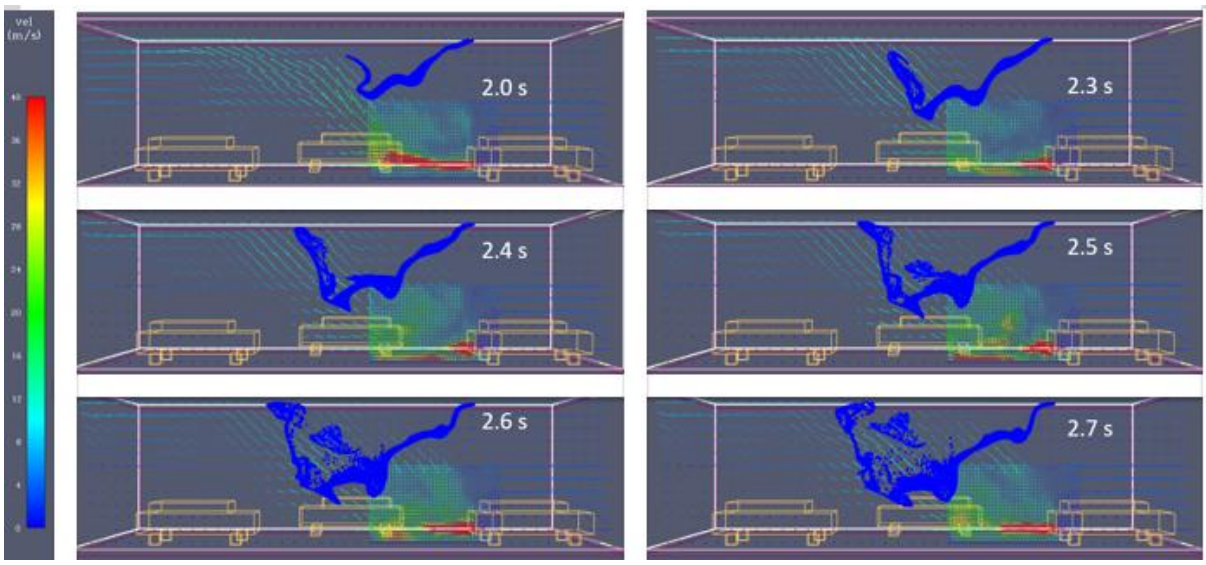

Figure 43. Velocity vector field of very large hydrogen mass flow rate with large water mass flow rate and small droplet.

2.2.13 Concluding remarks and future studies

The scope of this subtask is to predict the interaction between hydrogen fires and water sprinkling in tunnels. The details of this multi-physics phenomena can only be studied by CFD simulations. Therefore, the Fire Dynamic Simulator code (FDS code) was chosen to investigate the dynamics between water sprays and hydrogen flames. The presented results were further developed and used to build a correlation using a zero-dimensional lump parameter code for simplified assessments.

2.3 Mechanical ventilation of hydrogen jet fire in underground parking (ST3.2.3, UU)

The aim of the task is the development of a model to assess the effect of a hydrogen jet fire on the mechanical ventilation system of an underground parking. The model should be capable to assess whether the current ventilation standards for underground parking in case of a vehicle fire are still applicable in the event of hydrogen jet fire from a vehicle TPRD. The results of the preliminary studies via the analytical modelling are shortly summarized in Section 2.3.2. It was concluded that CFD modelling would be required to assess complex scenarios beyond the capabilities and assumptions of the reduced model. Therefore, the initial plan of the sub-task was updated to include numerical simulations. The study analyses as well the heat release rate (HRR) from the jet fire through the TPRD of an on-board storage tank, as it may aggravate the vehicle fire consequences.

2.3.1 Compliance to BS 7346-7-2013

The British Standards defining the code of practice for underground car parks are used as a reference for the mechanical ventilation requirements (BS 7346-7:2013, 2013). In the event of a fire, the main requirements are:

- Clear the smoke produced by the fire to facilitate the occupants escape and the first responders' intervention.
- Provide at least 10 Air Changes per Hour (ACH).

Thus, 10 ACH will be used as a reference scenario for the ventilation flow rate in the underground car park. In order to assess if a hydrogen jet fire from TPRD would meet the standard ventilation requirements, the study verifies the compliance to BS 7346-7-2013 performance recommendations for equipment:

"All fans intended to exhaust hot gases used within a car park ventilation system should be tested in accordance with BS EN 12101-3 to verify their suitability for operating at 300 °C for a period not less than 60 minutes (class F300)."

Temperature of 300 °C will be used as the limit that can be recorded at ventilation ducts for an inherently safer operation of the mechanical ventilation system in the event of a hydrogen jet fire. This is a conservative assessment as the duration of hydrogen jet fires will be shorter than 60 minutes.

2.3.2 An analytical model: considerations and conclusions

In a first stage of the task development, an analytical model has been proposed to assess the effect of hydrogen jet fires on a mechanical ventilation system in an underground car park. Hydrogen ignited releases in the underground park are assumed to be steady state. The model considers that only one extraction duct is present in the enclosed space. Five scenarios of releases from different thermally activated Pressure Relief Device (TPRD) diameters (0.5 - 5.0 mm) and storage pressures (350-700 bar) are considered for the study.

The model assumes an isobaric and adiabatic combustion with perfect mixing of the total fresh air provided by the mechanical ventilation and combustion products produced by the hydrogen jet fire, i.e. N2 and H2O. The model allows to estimate the temperature of the resulting mixture expected at the entrance of extraction ducts and that should be lower than the identified limit of 300°C. Details on the procedure and equations are given in (Makarov et al., 2018).

The model has been applied to assess the effect of hydrogen jet fires on the mechanical ventilation system for two real underground car parks, hereby indicated as case A and case B. The underground car park A is located in Gent, Belgium. The layout is represented in Figure 44 and main dimensions are 45x3x23 m (ArcelorMittal, 2019). The case study B involves a larger car park with dimensions 100.8x2.6x75.6 m (ArcelorMittal, 2019), shown in Figure 44.

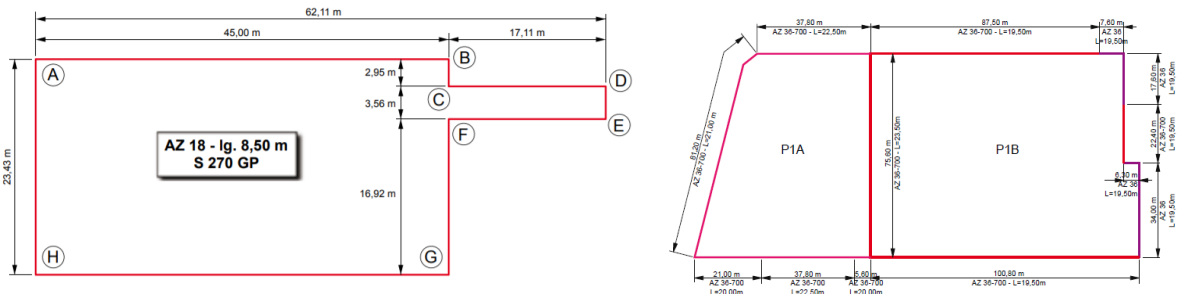

Case study A Case study B

Figure 44. Case study A: real underground car park in St. Martnes Latem - Gent, Belgium; Case study B: real underground 3 storeys car park in Haarlem, The Netherlands (ArcelorMittal, 2019).

For the underground carpark A, a TPRD diameter equal to 0.5 mm leads to an acceptable temperature at the extraction duct, being below 100 °C for the 10 ACH. A diameter of 1 mm leads to acceptable conditions for 15 ACH, whereas it leads to temperature slightly above 300 °C for 10 ACH. TPRD diameters equal and above 2 mm lead to a temperature significantly larger than 300 °C, thus categorised as unacceptable.

For the underground carpark B, it was observed that TPRD diameters in the range 0.5-2 mm lead to an acceptable temperature level at the extraction duct, whereas TPRD diameter of 5 mm leads to a not acceptable temperature. Results showed that the acceptability of a hydrogen jet fire effect on the ventilation system strictly depends on the dimensions of the underground garage. For instance, at 10 ACH, a 2 mm TPRD is demonstrated to result in acceptable temperature at the extraction duct for the larger car park in case B, but not for the car park in case A. TPRD diameters of 0.5 and 1 mm showed acceptable or close to acceptable temperatures for both car park layouts.

The model assumed one extraction vent, along with a perfect and adiabatic mixing of combustion products and fresh air provided by the mechanical ventilation system. However, in

real applications with multiple extraction vents and large volume enclosures, the simplified model at the present state may not well reproduce the temperature expected at the entrance of the ventilation system. Furthermore, a hydrogen ignited release from a FCEV onboard storage may lead to highly non-uniform and transient hydrogen distribution, which usually violate assumptions of the reduced model and may lead to loss of results accuracy. CFD avoids assumptions typical for the reduced models and may be recommended as a reliable tool for analysis of unignited and ignited hydrogen release hazards and their interaction with mechanical ventilation system in underground parking. CFD allows to take into account highly dynamic release character (i.e. blowdown of the storage tank), downwards direction of the TPRD, a large volume of parking, presence of obstacles, position of the vehicle, presence and location of ventilation ducts and losses in them. For this reason, the simplified model performances should be assessed through comparison with CFD simulations of hydrogen jet fires in an underground parking with multiple extraction vents, similarly to the study conducted in Task 2.2 for unignited releases of hydrogen (see HyTunnel-CS D2.3, 2022).

2.3.3 A CFD approach to model hydrogen jet fires in underground car parks

This work investigates numerically the scenario involving an ignited hydrogen release through the TPRD of a hydrogen-powered vehicle in an underground parking. The study follows the tracks of Task 2.2 investigating unignited releases in an underground parking with mechanical ventilation (see HyTunnel-CS D2.3, 2022). The selected underground car park is that showed in Figure 44 - case A, as having smaller size and thus leading to a more conservative assessment. Hydrogen is assumed to be released during blowdown of a storage tank with volume equal to 62.4 L and 700 bar as initial storage pressure. Fourteen simulations were conducted for different release scenarios and height of the underground car park:

- TPRD diameters: 0.5, 0.6, 0.75, 1.0, 2.0 mm,
- TPRD release angles: 0°, 30°, 45°, 60°,
- Ventilation rate: ACH= 0, 10 (for considered car park),
- Car park ceiling height: 2.1 and 3 m.

2.3.4 Description of the CFD model

The CFD model is based on an implicit pressure-based solver with incompressible ideal gas flow. A RANS approach is employed for turbulence modelling, with realizable κ-ε sub-model for solving turbulent kinetic energy and turbulent dissipation rate respectively (Shih et al., 1995). The Eddy Dissipation Concept was used for combustion (Magnussen, 1981). It includes detailed chemical mechanisms of 9 species and 18 reactions by a subset of Peters and Rogg's mechanisms (Peters and Rogg, 1993). The Discrete Ordinates model is implemented to take into account heat radiation losses (Murthy and Mathur, 1998).

2.3.5 Results and discussion

The effect of different parameters and characteristics of the TPRD release, ventilation rate and car park were assessed systematically and in sequence. The results are reported in the following sections.

2.3.5.1 *Effect of mechanical ventilation presence*

The effect of mechanical ventilation for the combustion products cloud with temperature equal or above 573 K (300° limit) is shown in Figure 45. Distribution is shown for the time 16 s and

release with TPRD ∅0.5 mm and 45° inclination with respect to perpendicular to the ground. It could be observed that ventilation presence does not affect the hot products distribution. Mechanical ventilation should be maintained according to current BS requirements (10 ACH).

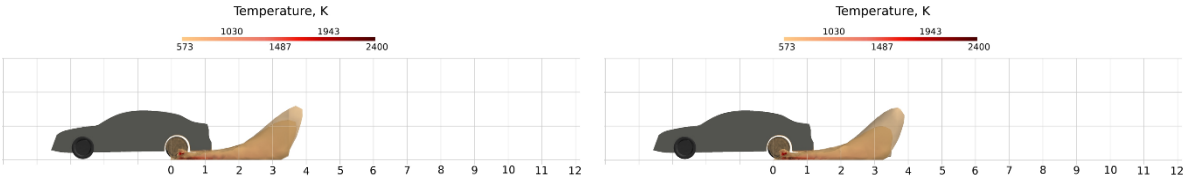

0 ACH 10 ACH

Figure 45. Effect of mechanical ventilation presence for a TPRD=0.5 mm, 45° angle. Ceiling height=3m, time=16 s.

2.3.5.2 *Effect of TPRD inclination*

The second analysis focuses on the effect of the jet inclination for a TPRD diameter equal to 0.5 mm. Figure 46 shows the simulated distribution of the cloud with temperature ≥300°C at the time the maximum height is achieved for each TPRD inclination. It can be observed that all TPRD inclinations comply to BS for a car park ceiling height of 3 m. However, it was observed that in the case of the TPRD direction with 0° angle, the cloud with T≥300°C reaches a maximum height of 2 m, even if for a short time. The hot combustion products with temperature corresponding to fatality harm criteria (309°C, third-degree burns for 20 s exposure - LaChance, 2010) envelop the vehicle and may prevent escape of the occupants. For a 30° angle, the T≥300°C cloud reaches a maximum height of 2.1 m for a short time. For both 45° and 60° angles, the T≥300°C cloud reaches a maximum height lower than 2 m. A further analysis has been conducted on hazard distances for people, according to the "no-harm" criteria in LaChance (2010) - 70°C for any exposure duration. It was observed that the "no-harm" distance from the vehicle is the lowest for a 0° TPRD angle. However, it has been observed that hot combustion products surround the vehicle, reaching the fatality harm level, and may prevent escape of the occupants. For a 30° angle, "no-harm" distance is lower than 5 m, but as mentioned earlier the cloud with T≥300°C would reach the ceiling in car parks with a height of 2.1 m. For a release with 45° TPRD angle the "no-harm" distance is calculated as 6.2 m, which is lower than distance for 60° angle. Combining the conclusions reached for compliance to BS for the mechanical ventilation and harm criteria for people, a TPRD with 45° inclination represents the best choice and will be used for the assessment on the effect of a TPRD diameter.

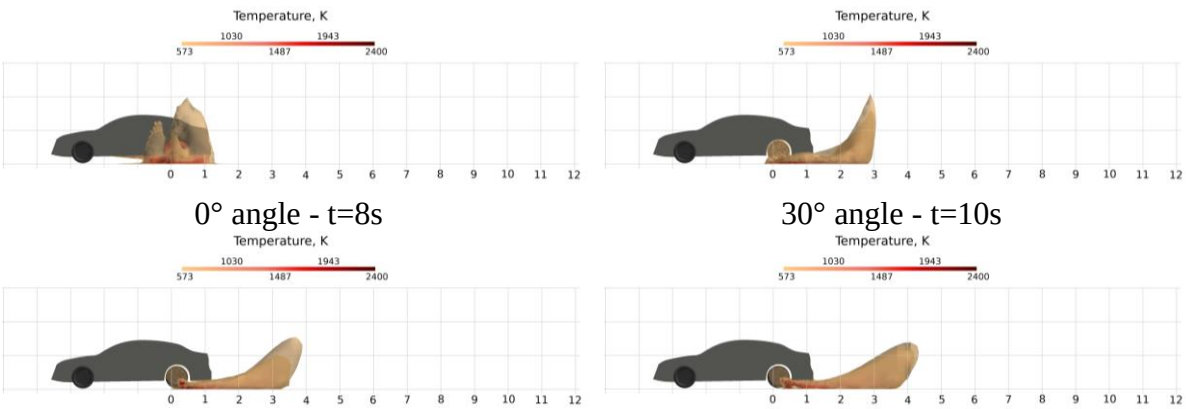

0° angle - t=8s 30° angle - t=10s

45° angle - t=16 s 60° angle - t=10s

Figure 46. Effect of TPRD inclination with respect to perpendicular to the ground for TPRD=0.5 mm, ceiling height=3m, 10 ACH.

2.3.5.3 *Effect of a TPRD diameter*

The effect of a TPRD size on the compliance of a hydrogen jet fire to the BS has been assessed by changing diameter in the range 0.5-2.0 mm. Figure 47 shows the distributions of the cloud with T≥300°C at the time of maximum height of the cloud for each case. It can be observed that for the case TPRD ∅0.5 mm, the T≥300°C cloud does not reach the ceiling. Temperature of 300°C is reached at a maximum height equal to 1.6 m. For a TPRD ∅0.6 mm, the T≥300°C cloud does not reach the 3 m ceiling, but reaches a 2.5 m height. Simulation for a ceiling height of 2.1 m shows that the T≥300°C reaches the ceiling, which could undermine the safety for these car parks. For both releases with TPRD ∅0.75-1.0 mm, a temperature ≥ 300°C under the ceiling is reached within 8 s. This time is decreased to 5 s when a TPRD ∅2.0 mm is employed. In this case the hot products cloud reaches the wall at approximately 12 m behind the rear of the vehicle. The "no-harm" distances from the back of the vehicle is below 6.5 m for TPRD ∅0.5-0.6 mm, whereas this reaches the wall of the car park at 12 m behind the vehicle for TPRD ∅0.75-1.0 mm.

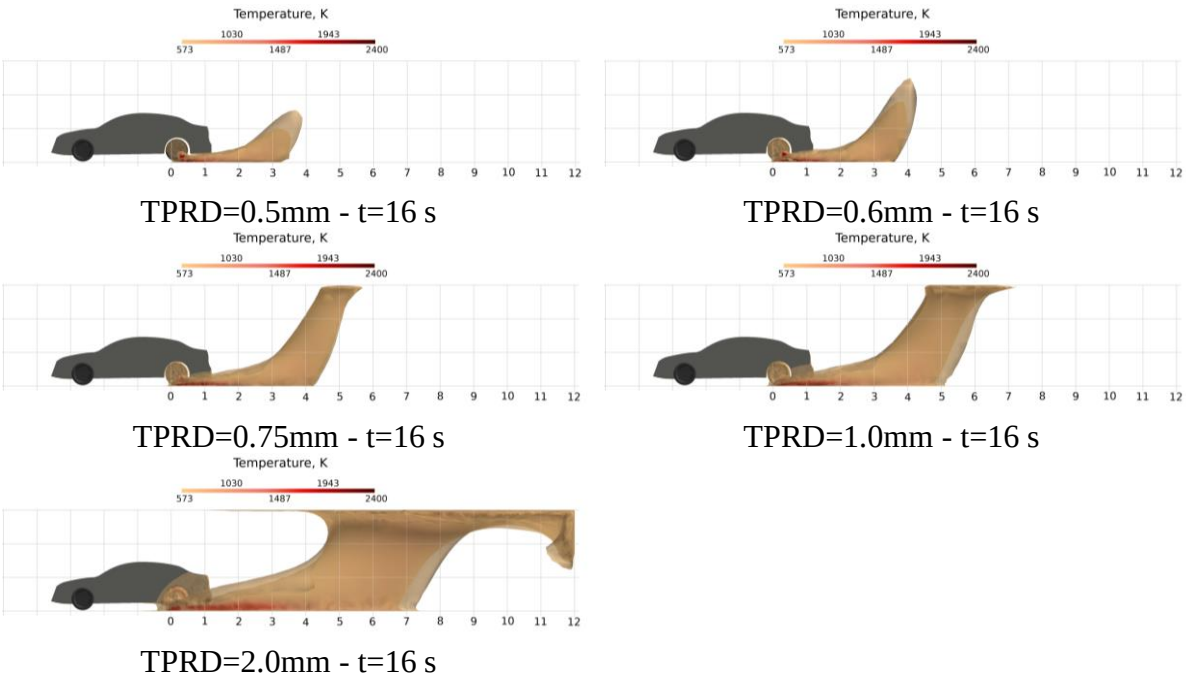

Figure 47. Effect of TPRD diameter for the inclination 45° with respect to perpendicular to the ground, ceiling height=3m, 10 ACH.

Results of the numerical model are in agreement with the observations in Hussein (2019) on naturally ventilated covered car park with dimensions LxHxW=30x28.4x2.6 m. The downward direction of the jet fire was seen to significantly decrease the dangerous zone for the ventilation system. The ceiling was yet reached by the T> 300°C cloud for a 2 mm TPRD diameter with jet inclinations of either 0°, 30° or 45°. On the other hand, a TPRD diameter equal to 0.5 mm and jet inclination of 45° did not produce a dangerous cloud at the ceiling during the tank blowdown duration, i.e. 1h 40 min for a 117 l tank at initial pressure 70 MPa. It should be remarked that natural ventilation may provide a lower amount of fresh air compared to mechanical ventilation.

The CFD modelling is observed to provide insights into the dynamics of unsteady jet fires with downward direction in underground car park with multiple extraction vents. As supposed,

results obtained for such a detailed modelling are seen to not fully agree with results of the simpler reduced analytical tool. For the car park with dimensions 45x3x23 m, the analytical model suggested that a TPRD with diameter of 1.0 mm could still be acceptable providing a temperature of 302°C at the extraction vent. However, CFD modelling showed that such a TPRD diameter would be not acceptable as per a size of 0.75 mm. It is concluded that in elaborate scenarios with multiple extraction vents, downward and unsteady jet fires, CFD modelling should be used as a reliable tool for hydrogen safety engineering. Furthermore, CFD modelling allows to assess more accurate hazard distances and consequences for certain TPRD designs. The exception may be given by vertical free jet fires, as it is considered that the dimensionless flame correlation could yet be used to assess temperature decay along the jet flame ant when it reaches the ceiling. E-laboratory platform developed within NET-Tools can be used for such assessments.

2.3.6 Effect of a hydrogen jet fire on a car HRR

A final analysis was performed to assess the effect of hydrogen jet fires on the Heat Release Rate (HRR) of a burning vehicle. The British Standard BS 7346-7:2013 (7346-7:2013, 2013) suggests the following design options when considering HRR in underground car parks:

- Steady-state design fires: "*The design fire should either use the appropriate value of heat release rate and other parameters from Table 1 or an alternative appropriate in the circumstances of the particular design…*". Given values of HRR vary from 4 MW for an indoor car park with a sprinkler system to a maximum of 8 MW for an indoor car park without a sprinkler system.
- Time-dependent design fires: "*The design fires should be based on an experimental test fire…*"

The HRR of a hydrogen jet fire was calculated based on the mass flow rate dynamics in time and the hydrogen gas heat of combustion 119.93 MJ/kg. A realistic hydrogen tank of 62.4 L volume and 700 bar storage pressure (Yamashita et al., 2015) were considered along with TPRD diameters 5, 2, 1 and 0.5 mm. The resulting hydrogen jet fire HRR was combined with a real car fire HRR curve as given in (Okamoto et al., 2013). Figure 48 (left) shows the effect of a hydrogen jet fire HRR on a vehicle HRR for all the considered diameters. HRR associated with TPRD diameter 5 mm reaches a peak of approximately 80 MW, which is significantly larger than either a steady state or time-dependent design fire, even if for such a short release duration as 32 s. Figure 48 (right) presents a reduced scale graph for TPRD release diameters in the range 0.5-2 mm. HRR for a 2 mm TPRD reaches a peak of 13 MW during the 3 min 20 s release. On the other hand, HRR for a 1 mm TPRD results in a negligible contribution to a time-dependent vehicle HRR for a release duration of 13 min 20 s. Furthermore, it does not significantly exceed the minimum steady state design fire HRR of 4 MW. Even lower contribution is recorded for a 0.5 mm TPRD, which would require 53 min 20 s for emptying the tank. It may be concluded that for a TPRD diameter ≤ 1 mm, the hydrogen jet fire contribution to a vehicle fire HRR may be negligible at the cost of a longer duration of the tank blowdown.

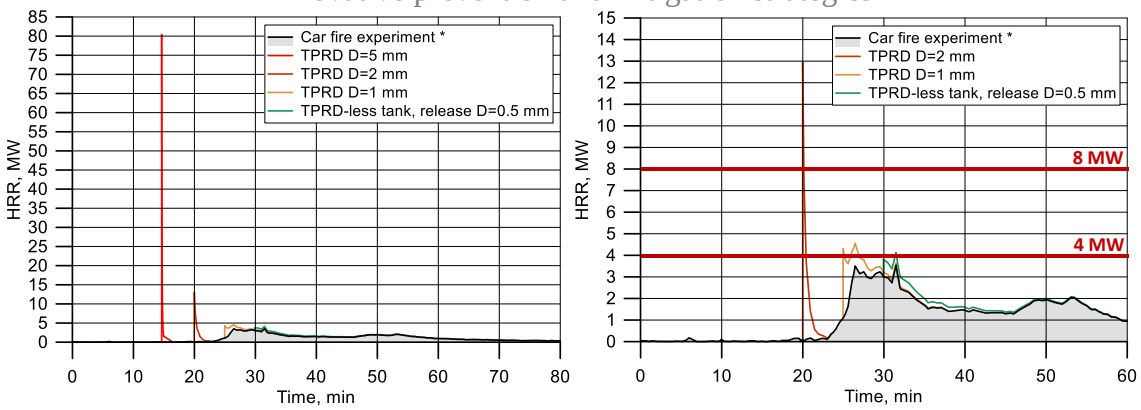

Figure 48. Hydrogen jet fire contribution to a vehicle fire HRR. Left: results for TPRD diameters 0.5-5 mm. Right: results for TPRD diameters 0.5-2 mm.

2.3.7 Concluding remarks

The following conclusions and recommendations can be withdrawn for downwards hydrogen jet fires directed backwards a FCHV in an underground car park of dimensions 45x3x23 m, onboard tank volume of 62.4 L and 700 bar NWP:

- Mechanical ventilation should be maintained according to current BS requirements (10 ACH). Ventilation is demonstrated to not affect the hot products distribution and associated hazard distances for TPRD ∅0.5 mm.
- A release angle of 45° through a TPRD ∅0.5 mm is recommended to not obstruct the vehicle evacuation and reduce the hot combustion products height compared to angles 0-30°, and to reduce hazard distances compared to angle 60°.
- A release with angle 45° with TPRD diameter of 0.5 mm is found to comply with current ventilation requirements in underground car parks with height 2.1-3.0 m and to not significantly affect a FCHV heat release rate (+15%).
- It should be remarked that the used damage criterion is conservative and that jet fires will have much shorter duration compared to the resistance time (at least 60 minutes) and a general car fire.

3. Numerical studies (Task 3.3/NCSRD)

3.1 CFD model for predictive simulation of pressure peaking phenomenon for hydrogen jet fire in confined space (ST 3.3.1, UU)

The aim of this work is to develop and validate a CFD model to assess the overpressure hazards generated from Pressure Peaking Phenomenon for hydrogen jet fire in a large scale enclosure with dimensions similar to those of a garage. The reasons to have a validated CFD model together with the engineering tool presented in Section 2.1 are the following:

- to simulate those scenarios that cannot be represented by the engineering tool assumptions;
- to expand the range of applicability of the engineering model by using CFD simulations as a verification tool;
- to calculate the thermal load on the enclosure surfaces;
- to calculate hazard distances based on pressure and thermal effects in the external surroundings of the enclosure.

A CFD model to predict pressure peaking phenomenon for hydrogen jet fire in confined space was developed by (Hussein et al., 2018) and validated against experiments performed at KIT facility in Germany within HyIndoor project. Enclosure had a volume of 1 m^3 and release of hydrogen had mass flow rates in the range 0.55-1.1 g/s. The same CFD model will be employed in this task and its performances will be analysed against larger scale experiments performed by USN within HyTunnel-CS project. These experiments are characterised by an enclosure with volume 15 m^3. Hydrogen mass flow rate was varied up to 11.5 g/s, which is approximately 10 times the mass flow rate used for validation in (Hussein et al., 2018). Simulated pressure dynamics within the enclosure is compared to experimental results to assess the predictive capabilities of a CFD model. Ansys Fluent platform is used for simulations. A novel approach is suggested to improve the time efficiency of calculations. Furthermore, the CFD model application is expanded to the scenarios involving cryogenic releases to assess the effect of storage temperature on the PPP magnitude. It will be shown that conclusions of the numerical study and validity of the CFD model can be expanded to pressure hydrogen sources up to 700 bar. This research has been published in (Cirrone et al., 2022), which reports full details of the numerical study and its validation process.

3.1.1 Validation experiments

Three experiments from the set of 31 tests performed by USN within subtask 3.4.1 are used for validation of the CFD model. The three tests selected were those having higher mass flow rate and pressure for the scenarios with either 1, 2 or 3 vents open. Table 8 reports the pressure and mass flow rate for the selected tests. The release diameter was 4 mm for all the tests. The enclosure had dimensions 2.98x2.50x2.00 m. Details of the experimental set up are given in description within Section 2.1.3.

Table 8. USN experiments selected for CFD model validation.

Test	Hydrogen storage pressure, bar	Mass flow rate, g/s	N. of vents
14	117.8	11.37	3
18	124.6	11.47	2
19	89.3	8.62	1

3.1.2 Description of the CFD model

The CFD model is based on an implicit pressure-based solver. A compressible ideal gas flow was considered for simulations. A RANS approach is employed for turbulence modelling, with realizable κ-ε sub-model for solving turbulent kinetic energy and turbulent dissipation rate respectively (Shih et al., 1995). The Eddy Dissipation Concept was used for combustion (Magnussen, 1981). It includes detailed chemical mechanisms of 9 species and 18 reactions by a subset of Peters and Rogg's mechanisms (Peters and Rogg, 1993). The Discrete Ordinates model is implemented to take into account heat radiation losses (Murthy and Mathur, 1998).

3.1.3 Release source modelling

Release pressure is included in the range 89.3-124.6 bar. At such pressure, an under-expanded jet is expected, which would lead to strong expansion shock waves in the zone outside the nozzle where the pressure decreases to ambient. The notional nozzle approach is used to model the under-expanded hydrogen jet in simulations (Molkov et al., 2009). A discharge coefficient, C_d, was implemented in calculations to match the experimental mass flow rate. Table 9 presents the calculated notional nozzle parameters that will be used to model the release sources.

Table 9. Notional nozzle (NN) parameters employed as inlet conditions for simulations.

Test	Mass flow rate, g/s	C_d	D_{NN}, mm	T_{NN}, K	U_{NN}, m/s
14	11.37	0.13	11	230.8	1154.5
18	11.47	0.12	11	231.7	1156.6
19	8.62	0.12	9.5	231.7	1156.6

A second approach was considered to model the hydrogen release source in order to reduce the calculation time. Previous numerical work by (Molkov et al., 2009) found that a volumetric source (VS) with size four times the notional nozzle diameter correctly reproduced experiments on unignited hydrogen jets. The present study employed a cubic volumetric source with length four times the hydraulic notional nozzle diameter. The source terms for mass, momentum and energy were calculated from the mass flow rate, velocity and temperature for the notional nozzle reported in Table 9. The description of the computational domain and numerical details for the two release source modelling approaches is reported in (Cirrone et al., 2022).

3.1.4 Results and discussion

A first analysis is focused on the pressure dynamics within the enclosure for experimental Test 14. Figure 49 shows the comparison between experimentally measured pressure and CFD simulation results for time steps (ts) 0.17 and 0.34 ms, corresponding to CFL of about 25 and 50, respectively. Simulations well predict the experimental overpressure peak (21.1 kPa) with an accuracy of 3% for ts=0.17 ms (20.5 kPa) and 5% for ts=0.34 ms (20.1 kPa). Overall, it can be observed that the experimental overpressure dynamics in the enclosure is well reproduced by both CFD simulations. Given the negligible difference in the obtained pressure up to 6 s, it is concluded that a time step equal to 0.34 ms provides a converged solution. Simulation was then continued only for ts = 0.34 ms, given the associated saving of computational time.

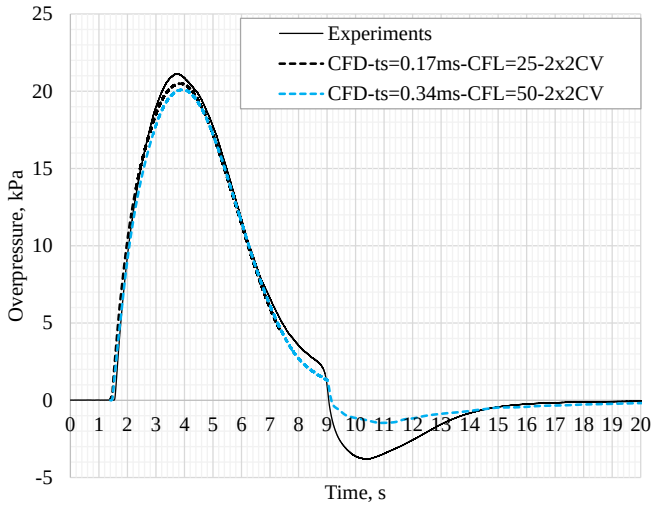

Figure 49. Pressure dynamics in the enclosure for Test 14: CFD simulations with inflow boundary conditions at the notional nozzle exit versus experiments.

Figure 50 shows the distribution of OH mole fraction on the plane x=0 perpendicular to the enclosure walls where vents are located. This distribution gives insights into the location of the combustion zone, i.e. the jet fire. It can be observed that the jet fire touches the enclosure ceiling. With time, the jet fire increases in width and the maximum OH mole fraction decreases, indicating a lower reaction rate due to a lower availability of air in the enclosure.

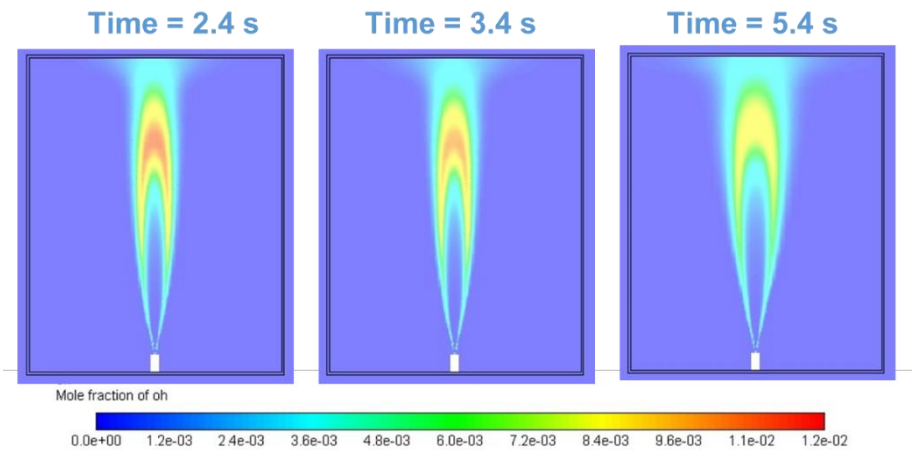

Figure 50. CFD simulation results of OH mole fraction distribution in plane x=0 perpendicular to the enclosure walls with vents: Test 14, ts=0.34ms (Cirrone et al., 2022).

Figure 51 shows the temperature distribution in the enclosure with time. The jet fire impinges on the ceiling and the hot combustion products move beneath it and finally descends along the enclosure side walls. By the time 5.4 s, the enclosure starts to be filled up with hot combustion products. Simulations employed a hexahedral mesh with inclusion of heat transfer effect at the enclosure walls. A CFD assessment conducted on a polyhedral mesh led us to conclusion that if it may give a more accurate reproduction of the jet impingement on a surface, it could lead to inaccurate results in case the heat transfer is not included in the model (up to twice pressure peak) for reproducing PPP with compressible flows and enhanced wall functions. Thus, a hexahedral mesh was maintained for the analysis.

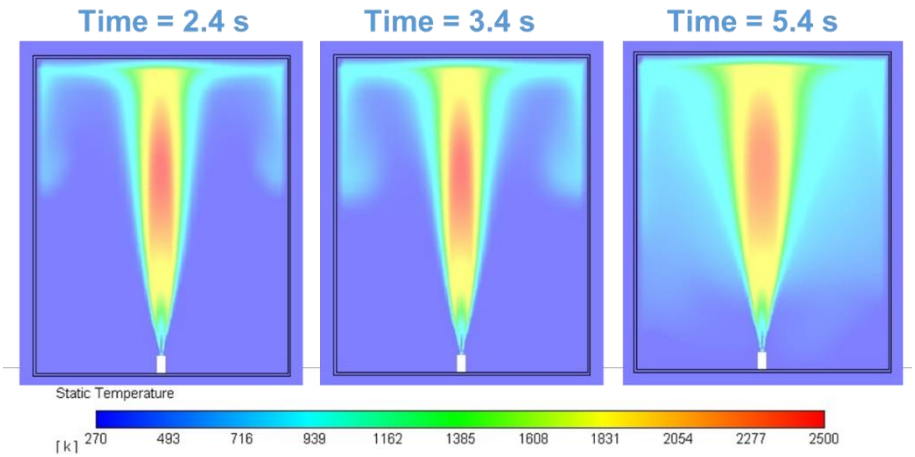

Figure 51. CFD simulation results of temperature distribution in plane x=0 perpendicular to the enclosure walls with vents: Test 14, ts=0.34ms (Cirrone et al., 2022).

Experimental measurement equipment included four thermocouples located close to the enclosure walls to assess the thermal load on the structure. The thermocouples were coated with Inconel; thus, it is considered that temperature recordings are affected by the transmission through the Inconel layer. This value is considered to not be comparable to recordings of simulated temperature in the gas, unless experimental records are further processed to consider heat transfer and estimate the temperature in the gas. However, this process may be affected by significant inaccuracies rendering the comparison not reliable.

Calculation time for simulations was significant, requiring approximately 45 h for calculating 1 s of release with a time step of 0.34 ms on a 60 parallel processors machine. In an effort to reduce calculation time, a second numerical grid employing one cell to discretise the notional nozzle is used, which, given the larger cell size at the release point, allows to use a larger time step while maintaining CFL=50 (ts = 0.5 ms). The maximum variation in the pressure peak was about 0.5%, confirming independence of the grid. The calculation time reduced to only 30 hours for calculating 1 s, which is not yet sufficient to have efficient calculations.

To further reduce the calculation time without affecting accuracy of solution, a volumetric source approach to model the release source was considered. The CFL was changed in the range 0.37-50 (ts= 0.12-16 ms) to find convergence of a solution. Figure 52 shows the resulting overpressure dynamics for CFL in the range 0.12-1 ms. It can be observed that variation in pressure dynamics decreases with the decrease of CFL. The calculated pressure peaks were 20.86 kPa and 21.00 kPa for CFL of 0.75 and 0.37 respectively. The corresponding relative difference is 0.7%, which is considered to be acceptable for engineering applications. Thus, a CFL=0.75 was deemed sufficient to reach convergence of results while maintaining an acceptable calculation time (12 h to simulate 1 s of hydrogen release). With this approach, a simulation of a test can be completed in 4 days, which is a significant decrease in calculation time from the case employing the notional nozzle approach. The calculated pressure peak is 20.86 kPa, which well agrees with experimentally measured 21.1 kPa. The pressure dynamics is well reproduced, despite a slight difference towards the descending phase of the curve.

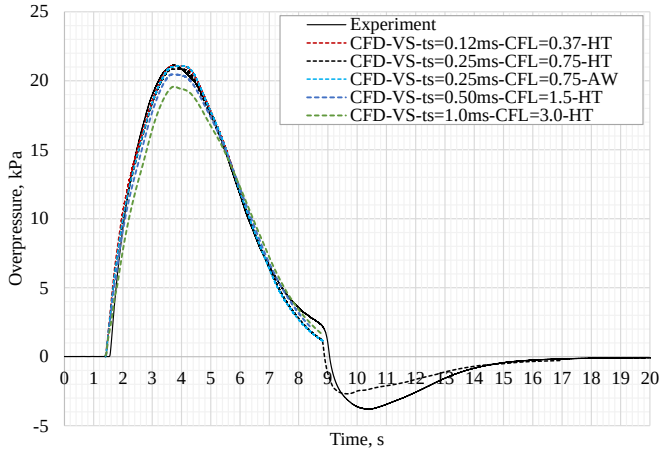

Figure 52. CFL convergence for volumetric source approach and effect of heat transfer (HT) versus simulation with adiabatic walls (AW) on pressure dynamics: Test 14.

The effect of heat transfer on pressure dynamics was assessed by modelling the enclosure walls as adiabatic. Figure 52 compares results of simulation modelling heat transfer through the enclosure walls (curve HT) and simulation considering the enclosure walls as adiabatic (curve AW, i.e. adiabatic walls) for CFL=0.75. Pressure peak slightly increased from 20.86 kPa to 21.05 kPa when heat transfer through the walls was not included in the model, which is considered to be a negligible effect on the pressure peak and dynamics. These results confirm conclusions by (Hussein et al., 2018).

The CFD model was employed to model experimental tests 18 and 19. Figure 53 shows comparison between the experimental and simulated overpressure dynamics (VS3.8cm) in the enclosure for Test 18 (b) and Test 19 (c). Simulated pressure peak for Test 18 was 35.10 kPa, which conservatively predicts the experimentally measured 33.22 kPa within 7% accuracy. On the other hand, simulated overpressure in the enclosure for Test 19 reached a maximum value of 42.21 kPa, which slightly underpredicted the experimental pressure peak (48.1 kPa).

3.1.5 Time-efficient approach of the uniform cube-shaped control volumes grid

The use of a volumetric source model is found, as demonstrated above, to reduce significantly the calculation time by approximately a factor of 3. In this section, a novel and simplified approach is developed to further enhance the time efficiency of calculations while maintaining an acceptable solution accuracy. This is based on the building of a uniform hexahedral grid throughout the calculation domain with the same size as the vent (7 cm square opening). The volumetric source is modelled as a cube with a 7 cm side. The approach is noted as VS7.0cm.

Figure 53a shows the pressure dynamics for Test No.14. A larger volumetric source results in a 8% larger simulated pressure peak (22.66 kPa), whereas the negative phase is simulated similarly. This variation could be associated with the lower resolution of the numerical grid for the highly non-uniform burning hydrogen-air mixture. A CFL sensitivity study for Test 14 showed that the pressure dynamics is not affected by the CFL number decrease from 0.75 to 0.50. Thus, the CFL=0.75 was maintained for the simulations using the “cube grid”. Figure 53b and 10c show the overpressure dynamics for Test No.18 and Test No.19 respectively. Maximum pressure for Test No.18 demonstrates variation by +5.8%, i.e. the increase from 35.03 kPa for a VS size 3.8 cm to 37.20 kPa for VS size 7.0 cm, and the difference of maximum

overpressure simulated for VS=7.0 cm from the experimentally measured value is +11% (conservative). For Test 19, the simulated overpressure peak with VS=7.0 cm differs from experiments by only -7.4%. Conversely to what is observed for Test 14, the negative pressure in Tests 18 and 19 is affected by the change of VS modelling approach.

The simplified uniform "cube grid" VS=7.0 cm approach is seen to reduce significantly the calculation time by approximately 3 times compared to the VS=3.8 cm approach, and by approximately 7.5 times compared to the previously used notional nozzle exit approach. The accuracy of the maximum simulated overpressure is found to be ±11%. This is well within the acceptable engineering accuracy for such complex phenomenon. It can be concluded that the unified "cube grid" VS=7.0 cm approach is a valuable hydrogen safety engineering tool for the assessment of the pressure peaking phenomenon.

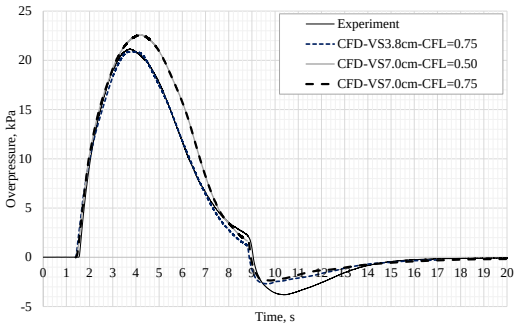

(a) Test No.14

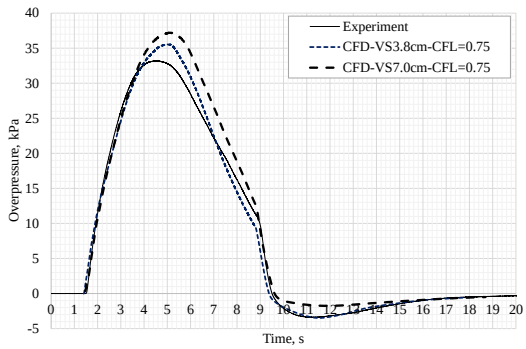

(b) Test No.18

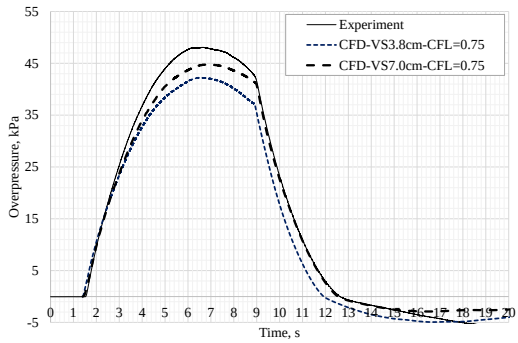

(c) Test No.19

Figure 53. Pressure dynamics in the enclosure for the unified "cube grid" approach: (a) Test No.14; (b) Test No.18; (c) Test No.19 (Cirrone et al., 2022).

A CFD assessment was conducted on the effect of hydrogen storage temperature on the magnitude of PPP. This study has been performed in conjunction with PRESLHY project activities. Test 14 has been considered for the comparison. Temperature in the storage, T_S, was decreased down to 100 K and the same storage pressure, pipe diameter of 4 mm and discharge coefficient as per Test 14 were considered. The decrease of temperature causes an increase of released hydrogen mass flow rate (MFR) from 11.37 g/s for T_S=277 K, to 14.11 g/s for T_S=200 K and 23.16 g/s for T_S=100 K. The pressure peak recorded for a storage temperature T_s=200 K and MFR=14.11 g/s is 26.95 kPa. The pressure peak increases up to 42.82 kPa for the case with T_s=100 K and MFR=23.16 g/s. The higher is the positive pressure peak the higher is the negative pressure peak, which reaches -5.36 kPa.

3.1.6 Concluding remarks

CFD simulations on hydrogen low pressure ignited releases in an enclosure were performed to validate a CFD model for predicting Pressure Peaking Phenomenon. The use of a volumetric source approach to model hydrogen releases was found to significantly reduce calculation time while maintaining a good accuracy of the solution. Simulations were compared against large scale experiments performed by USN within HyTunnel-CS (Subtask 3.4.1). Performed simulations showed that a CFD model agrees well with the experimentally measured pressure peak and dynamics in the enclosure. A time-efficient approach based on the uniform cube-shaped control volumes grid was proposed to further reduce calculation time. This approach allowed to reduce by approximately 7.5 times the computational time compared to the previously used notional nozzle exit approach, while maintaining the accuracy of the maximum simulated overpressure equal to ±11%.

The CFD model is seen to represent well experiments with storage pressure up to 12.5 MPa and hydrogen mass flow rate up to 11.5 g/s. The validation domain of the CFD model is not limited by storage pressure but is defined by the released mass flow rate, being this the key input for PPP. A release of hydrogen from a storage with pressure 12.5 MPa and TPRD diameter of 4 mm would be equivalent to a release from a 70 MPa storage and 0.65 mm TPRD diameter, as calculated through e-Laboratory developed within NET-Tools project (11.5 g/s for conservative C_d=1). Thus, the conclusions of the present study are valid for current onboard storage systems with such TPRD diameter and the CFD model can be applied for the associated safety assessments.

3.2 CFD model of hydrogen non-premixed turbulent combustion in scaled underground parking with mechanical ventilation (ST3.3.2, NCSRD)

The aim of this this subtask is to develop a numerical model for the prediction of thermal hazards from under-expanded hydrogen jet fires in confined vented spaces such as underground parking stations and maintenance garages. The NCSRD in-house ADREA-HF computational fluid dynamics (CFD) code was further developed and validated for this purpose. In particular, a new thermal radiation module was implemented and numerical results were compared with results from three different hydrogen jet fire experiments. The first two were free under-expanded hydrogen jet fire experiments, while the third involved impinging under-expanded jet fires in a confined vented space.

3.2.1 Development of the thermal radiation module

The ADREA-HF CFD code (Venetsanos, Papanikolaou and Bartzis, 2010) was further developed for the simulation of radiative transfer in non-premixed turbulent combustive flows. In addition to the P1 method, which is also available in the code, the finite volume discrete ordinates method (FVDOM) was implemented from scratch as a new module. The FVDOM method is a more accurate alternative to the P1 method, however it is also more computationally demanding. The main advantage of the FVDOM method is its superior performance in optically thin regions (Modest, 2013). In hydrogen combustion, where the only

radiatively participating species is H_2O, the presence of optically thin regions can greatly reduce the accuracy of the P1 model, especially near solid boundaries.

The P1 and FVDOM methods both solve the radiative transfer equation

$$\hat{n} \cdot \vec{\nabla} I(\vec{r}, \hat{s}) = \kappa(\vec{r}) I_b(\vec{r}) - \beta(\vec{r}) I(\vec{r}, \hat{s}) + \frac{\sigma_s(\vec{r})}{4\pi} \int_{4\pi} I(\vec{r}, \hat{s}) \Phi(\vec{r}, \hat{s}, \hat{s}') d\Omega',$$

where $I(\vec{r}, \hat{s})$ is the radiative intensity (units: W/m^2/sr), $\kappa(\vec{r})$ is the absorption coefficient (units: m^{-1}), $I_b(\vec{r}) = \frac{\sigma T^4(\vec{r})}{\pi}$ is the blackbody emission at temperature T (units: W/m^2/sr), $\beta(\vec{r}) = \kappa(\vec{r}) + \sigma_s(\vec{r})$ is the extinction coefficient (units: m^{-1}), $\sigma_s(\vec{r})$ is the scattering coefficient (units: m^{-1}) and $\Phi(\vec{r}, \hat{s}, \hat{s}')$ is the non-dimensional scattering phase function. In the above definitions, $\vec{r}$ is the spatial coordinate vector while $\hat{s}$ is the unit vector in the direction of the propagating ray. In hydrogen combustion, scattering is negligible because of the absence of soot in the combustion products, so that the scattering coefficient $\sigma_s(\vec{r})$ can be taken equal to zero. The absorption coefficient as a function of the local temperature is calculated using the recent, improved model of (Chmielewski and Gieras, 2015), which is based on absorption line data from the HITEMP experimental database. The older, alternative model of (Barlow et al., 1999), which is based on results from the RADCAL code (Grosshandler, 1993) is also available in the ADREA-HF code.

On a solid surface, the radiative transfer equation satisfies the boundary condition

$$I(\vec{r}_w, \hat{s}) = \varepsilon(\vec{r}_w) I_b(\vec{r}_w) + \frac{\rho(\vec{r}_w)}{\pi} \int_{\hat{n} \cdot \hat{s} < 0} I(\vec{r}_w, \hat{s}') |\hat{n} \cdot \hat{s}| d\Omega',$$

where $\varepsilon(\vec{r}_w)$ is the surface emittance and $\rho(\vec{r}_w)$ is the surface reflectance. On an open boundary, the boundary condition is

$$I(\vec{r}_b, \hat{s}) = 0, \hat{n}_b \cdot \hat{s} > 0$$

where $\hat{n}_b$ is the unit normal on the boundary, pointing into the domain. On symmetry planes, the specular reflective boundary condition that was recently proposed by (Cai and Modest, 2016) was implemented.

In the FVDOM method, the radiative transfer equation is discretized by integrating over angular and spatial control volumes:

$$\int_{\Omega_i} \int_{A_k} I \hat{s} \cdot \hat{n} \, dA d\Omega = \int_{\Omega_i} \int_{V_p} (\kappa I_b - \beta I) dV d\Omega + \int_{\Omega_i} \int_{V_p} \frac{\sigma_s}{4\pi} \int_{4\pi} \Phi(\hat{s}', \hat{s}) d\Omega d\Omega dV$$

Here Ω_i is an angular control volume, A_k is a spatial control surface and V_p is a spatial control volume. A novel feature of our implementation is the use of the algorithm presented in (Leopardi, 2006) for the definition of the angular control volumes. In other FVDOM implementations, the unit sphere is subdivided into control volumes by splitting the azimuthal angle range in N segments and the polar angle range in M segments, resulting in great variation of the angular control volume size and possibly very small angular control volumes near the poles. Our implementation subdivides the unit sphere in an arbitrary number of equal angular control volumes, using spherical caps on the poles. The difference between the subdivisions resulting by the two methods is presented in Figure 54.

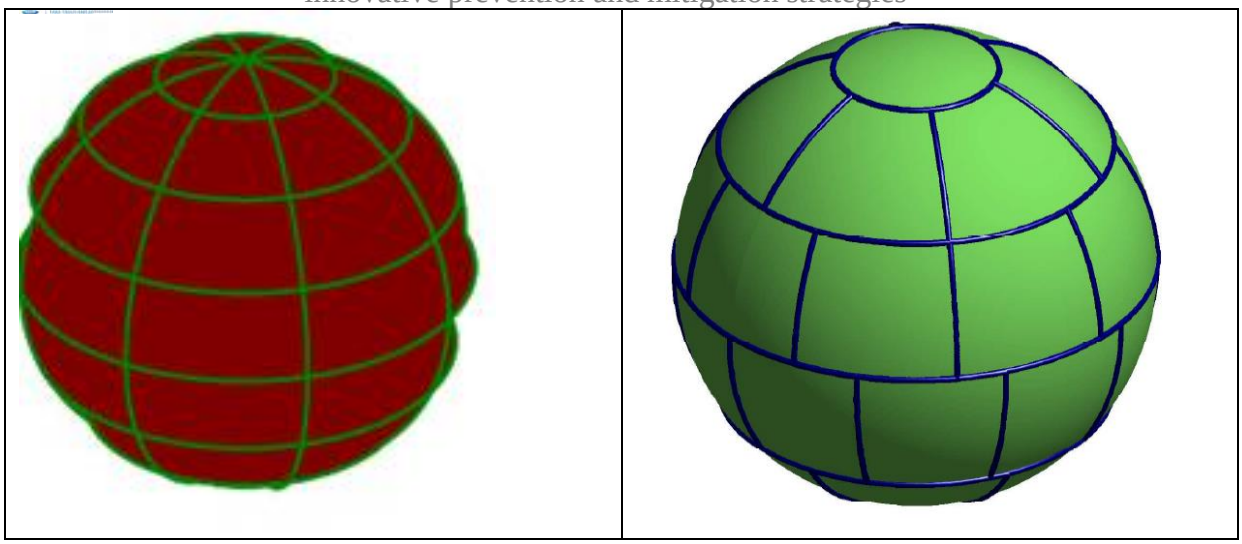

Figure 54. Left: Subdivision of the unit sphere into non-equal angular control volumes by splitting the azimuthal angle range and the polar angle range into 6 segments. Right: Subdivision of the unit sphere into 33 equal angular control volumes using the algorithm proposed in (Leopardi, 2006).

After the integrations are performed in the last equation, the discretized equation reads

$$\sum_k I_{ki}\,(\hat{s}_i \cdot \hat{n}_k)A_k = \beta_p\left(S_{pi} - I_{pi}\right)V_p\Omega_i,$$

where subscript i refers to an angular control volume centre, subscript p refers to a spatial control volume centre and subscript k refers to a spatial control volume face centre. Solution of the above equation is achieved using the step scheme (Modest, 2013). Our implementation is capable of solving the equation of the step scheme using an explicit iterative procedure, or alternatively by using the collection of implicit solvers available in the code ADREA-HF. The FVDOM method was implemented in a module of about 2000 lines of Fortran 90 code, which includes both OpenMP and MPI parallel routines. Future development goals include the implementation of the more accurate, second order CLAM scheme (Jessee and Fiveland, 1997). A GPU-accelerated version of the explicit radiation solver using OpenACC directives is also under development, with promising preliminary results in terms of GPU speedup.

3.2.2 Brief Description of the experiments

3.2.2.1 *Sandia Experiment*

The first experiment considered is a vertical under-expanded jet fire at 170 bar (Schefer et al., 2006, 2007). A sketch of the experimental setup is shown in Figure 55. The diameter of the nozzle is equal to 1.91 mm. Blowdown was initiated from a set of 6 hydrogen tanks at a pressure of approximately 2500 psia. During the experiment, the flame length L_{vis} was measured at various time instants and a set of radiometers was accordingly placed at an axial distance equal to $L_{vis}/2$. This makes the radial radiative heat flux at this fixed non-dimensional radial distance available as a function of height, at various time instants. In this study, we select the first recorded time instant at 5 s after ignition for validation against our numerical results.

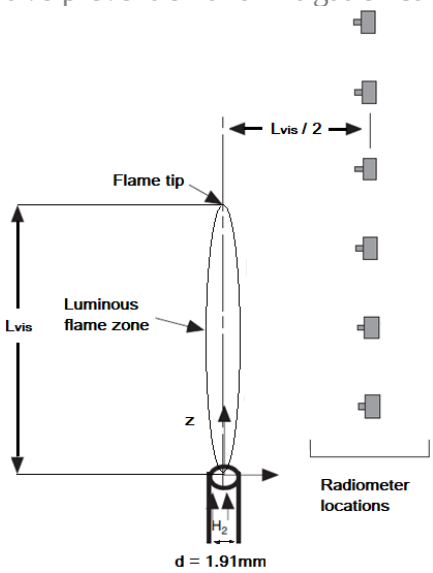

Figure 55. Sketch of the vertical under-expended jet flame experiment (adapted from (Schefer et al., 2006)).

3.2.2.2 *URS Experiment*

In the second experiment, a horizontal under-expanded jet fire at 340 bar was studied. This large scale hydrogen jet-fires tests (see Table 10) experiment were carried out by the University of Rome "La Sapienza" in collaboration with the Italian Fire Corps within the framework of the HyTunnel-CS project (Russo et al., 2020). In Figure 56, we present a sketch of the experimental setup. The diameter of the nozzle is equal to 1 mm. Neither blowdown curves nor flame lengths were measured during the experiment. Three radiometers were positioned at the horizontal plane passing through the nozzle (z = 1.05 m). This configuration makes the value of the radiative heat flux available as function of time at three different fixed locations. As seen in Figure 56, this experiment included several thermocouples, however temperature measurements are not considered in this study, which focuses on the radiative heat flux.

Hydrogen jet-fires tests were conducted in open space at various hydrogen pressures (up to 450 bar) and orifice diameters (1-7 mm). Hydrogen was provided by a storage tube trailer supplied by Linde. The trailer consisted of 16 high-pressure hydrogen storage tubes. The volume of each tube was 50 L at a nominal pressure of 450 bar. The tube trailer was connected to the orifice (1-7 mm bore hole) via a 12 m pipe with a constant internal diameter of 7 mm in order to minimize head losses. The jet was directed horizontally at approximately 1 m above the ground level. The igniter was a continuous propane air burner.

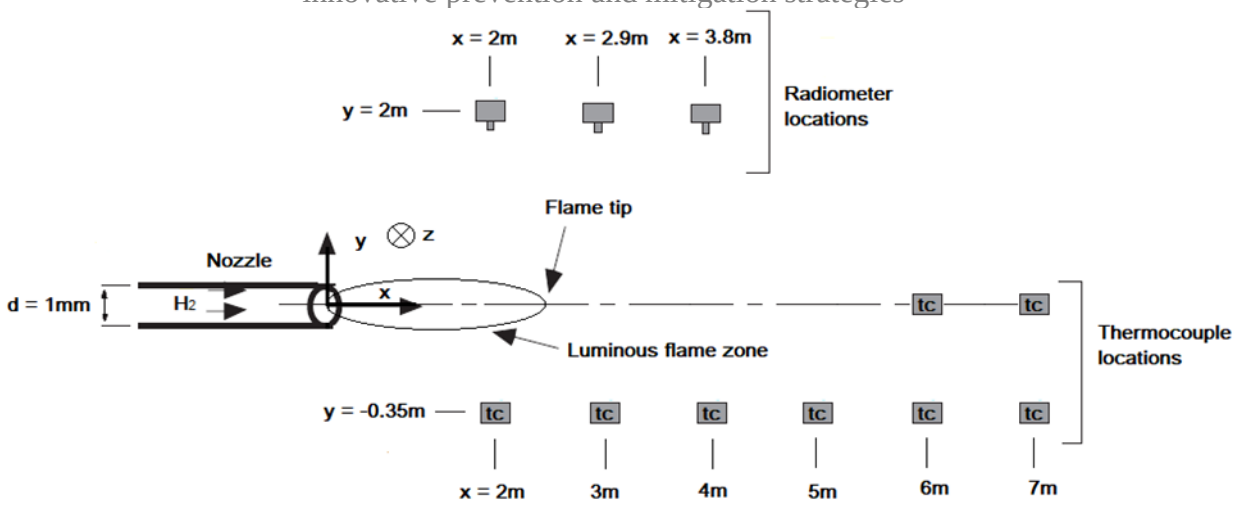

Figure 56. Sketch of the horizontal under-expended jet flame experiment.

The temperatures downstream the orifice were measured by K-type thermocouples that were installed in a stainless wire gauze. The thermocouples were located at different distances (up to 8 m) along the jet-axis, at 0.35 m distance (by the jet-axis) in perpendicular direction, and at height of 0.4 m, 1.03 m and 2.10 m (Figure 56).

Three radiant flux meters were installed (CAPTEC: sensing element of 30 x 30 mm, sensitivity 3 μV/(W/m^2) at a radial distance of 2 m from the jet centreline and at an axial distance of 2, 2.9 and 3.8 m from the orifice, see Figure 56. The radiometers were mounted on a tripod and orientated towards the projected flame centre.

A LWIR camera (FLIR A655SC) which streams full-frame 16-bit data at 50 Hz was installed at about 10 m from the jet centreline so as to visualize the flame.

Table 10. Matrix of experimental campaign performed by the Italian National Fire Corps in collaboration with URS.

Test	Orifice diameter [mm]	Initial release Pressure [bar]	Final release Pressure [bar]	Release time [s]	Wind velocity [m/s]	Wind direction
TEST 1	1	410	340	20	8	SO
TEST 2	1	340	330	30	8	SO
TEST 3	1	345	340	20	10	OSO
TEST 4	1	340	330	25	10	OSO
TEST 5	1	330	320	25	10	OSO
TEST 6	3	360	325	8	8	SO
TEST 7	3	325	280	16	8	SO
TEST 8	3	280	225	17	8	SO

TEST 9	3	225	140	60	8	SO
TEST 10	5	320	270	20	10	OSO
TEST 11	5	270	240	20	10	OSO
TEST 12	5	240	200	20	10	OSO
TEST 13	7	200	180	20	10	OSO
TEST 14	7	180	80	100	10	OSO
TEST 15	7	180	150	20	10	OSO
TEST 16	7	150	130	20	10	OSO

The emissivity coefficient of hydrogen flame is smaller than that of other gaseous fuel flames. However, it cannot be ignored the fact that radiation from a hydrogen flame affects its surroundings in the case of a large flame. Therefore, the thermal radiation from the flame was measured to investigate its thermal effect on its surroundings as reported in Russo et al. (2020). Moreover, they were also used to validate a newly-developed thermal radiation module of the ADREA-HF computational fluid dynamics (CFD) code (Momferatos et al., 2021).

As an example, radiative heat flux measurements for 1, 3 and 5 mm orifice at a pressure of about 320 bar are reported in Figure 57 a-c. For 1 mm orifice a maximum radiative heat flux of about 2 kW/m^2 is measured at a radial distance of 2 m from the jet centerline and at an axial distance of 2 m from the orifice along the jet axis. This value decreases to 1.5 and then to 1 kW/m^2 increasing the axial distance to 2.9 m and 3.8 m. These values are similar to the value of solar radiation. Therefore, it is not expected harm for long exposure to humans to these values of radiative heat flux.

On the contrary for 3 mm orifice the radiative heat flux reaches a maximum value of 10 kW/m^2 at 2 m axial distance, and decreases to about 9 kW/m^2 at 2.9 and 3.8 m distance. Increasing the orifice size to 5 mm, radiative heat fluxes as high as 16 kW/m^2 were measured at 2.9 and 3.8 m, values higher than that measured at 2 m (13 kW/m^2) indicating a shift of the flame center along the x-axis.

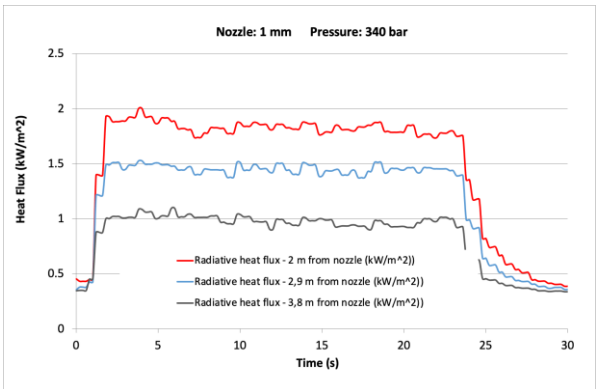

a)

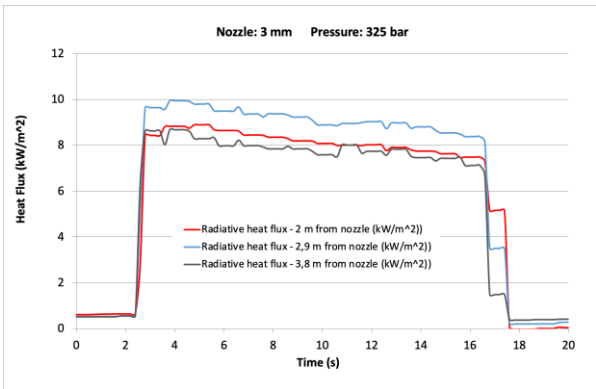

b)

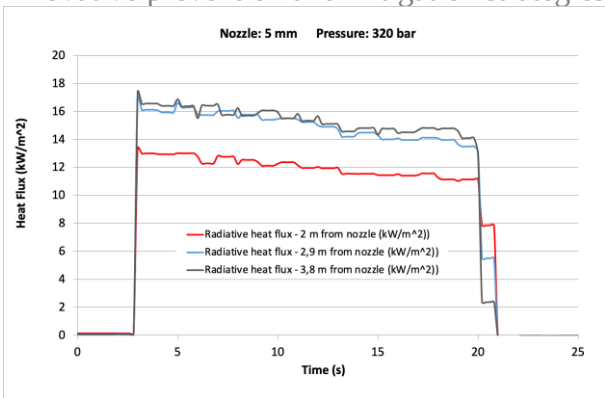

c)

Figure 57. Radiative Heat Flux for a) 1 mm and 340 bar b) 3mm and 325 bar c) 5mm at 320 bar.

3.2.2.3 *USN Experiment*

The experiment conducted by USN considers the thermal hazards resulting from jet fires originating from the bottom of a vehicle model located inside a container and impinging on the ground. The experiment takes place inside a container which acts as a model of a confined vented space such as an underground parking station or a maintenance garage. The basic experimental setup is identical with that published in (Lach and Gaathaug, 2021b). The model of the experiment, together with a plane of the numerical grid and sensor positions is shown in Figure 58. The experimental matrix is shown in Table 11.

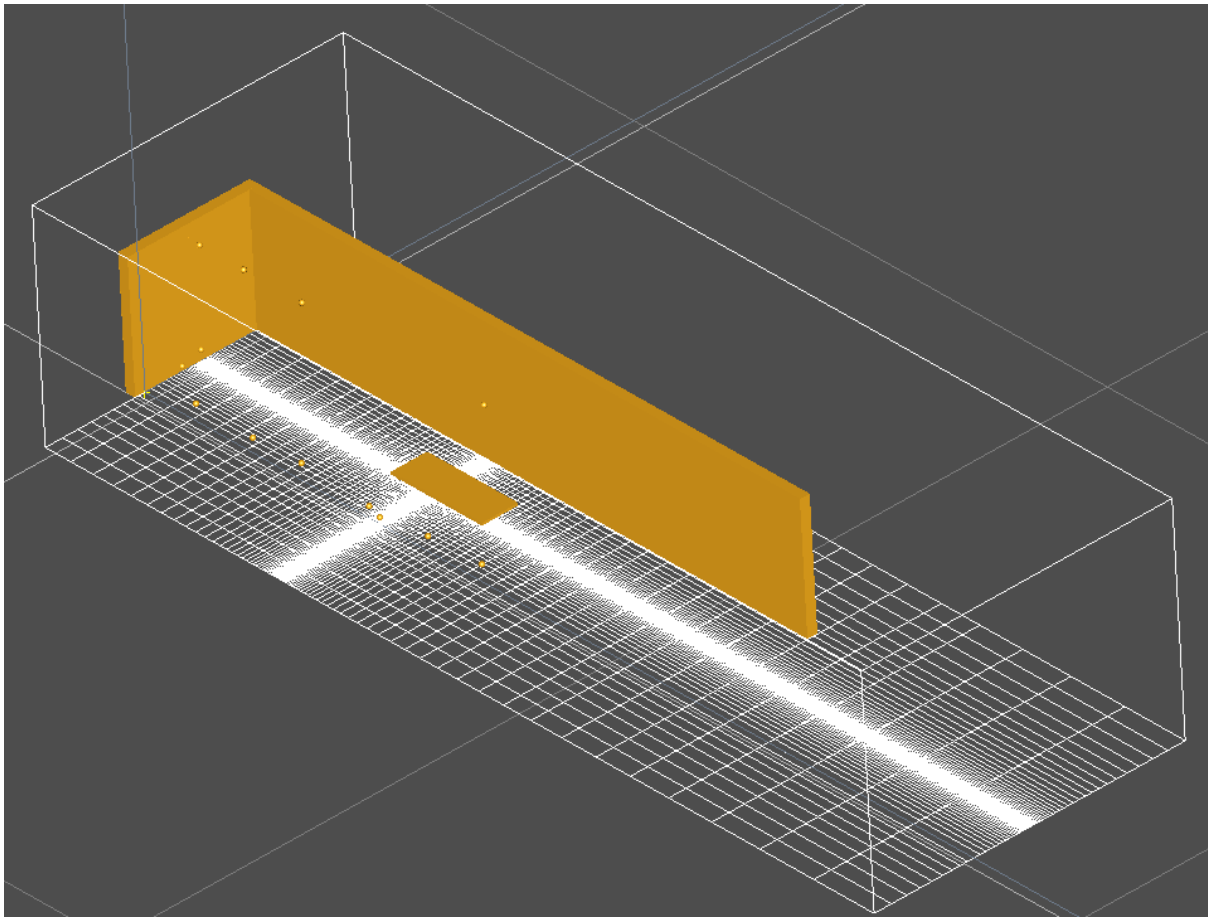

Figure 58. Model of the geometry of the USN, shown with a plane of the grid and sensor positions.

Table 11. Matrix of the USN experiments.

Exp nr	**Nozzle angle [º]**	**Nozzle diameter [mm]**	**Air change per hour [ACH]**	**Ambient temp [º C]**	**H_2 release duration [s]**
1	90	0.5	10	22	450
2	90	0.5	6	19	80
3	45	0.5	6	23	500
4	45	0.5	6	22	500
5	45	0.5	10	22	500
6	45	0.5	10	19	500
7	45	0.5	6	19	500
8	45	1.0	6	15	500

3.2.3 Numerical Setup of the Simulations

3.2.3.1 *Sandia Experiment*

In all simulations presented for this experiment, the simulation domain was extended 3.5 m away from the nozzle in x and y directions, and 12 m in the z direction. The grid remained uniform up to 0.13 m in the x and y directions and 0.26 m in the z direction, consisting of cubical spatial control volumes (SCVs) of side equal to 0.026, 0.0173 and 0.0144 m for the coarse, medium and dense grid respectively. Outside the aforementioned limits, the sides of the SCVs expanded with a ratio equal to 1.12 for all three space directions.

3.2.3.2 *URS Experiment*

For the simulations relevant to this experiment the computational domain extended 3 m away from the jet axis in the positive and negative y direction. In the x direction, it extended 3 m upstream and 10 m downstream, while in the z direction it extended 4 m above the jet. The grid remained uniform in a region of dimensions (x, y, z) = (0.4, 0.012, 0.012) m located in front of the nozzle. There, all SCVs were cubical with a side equal to 0.04, 0.02 and 0.0133 m for the coarse, medium and dense grid respectively. Outside this region the sides of the SCVs were expanded with a ratio equal to 1.12 in all spatial directions.

3.2.3.3 *USN Experiment*

In the case of validation against the USN experiment, only one spatial grid (the one shown in Figure 58) and only one number of ACVs (equal to 80) was considered. When satisfactory results are obtained, a detailed grid independence study will be performed, which will include both the effects of spatial and angular discretization.

3.2.4 Validation Results

3.2.4.1 *Sandia Experiment*

In comparing our numerical results with the vertical under-expanded jet fire experiment of (Schefer et al., 2006, 2007), our main objective is to answer the following question: how well can our radiation model predict the spatial distribution of the radiative heat flux at a fixed time instant? In Figure 59 we present a comparison of the predictions of the radial radiative heat flux q_x at a radial distance equal to $L_{vis}/2$ and t = 5 s, as a function on non-dimensional height, for two different angular discretization schemes: the FT_N scheme of (Kim and Huh, 2000) and our new proposed scheme. The number of ACVs is equal to N = 80 and the spatial grid is composed of approximately 162,000 SCVs. The experimental visible flame length L_{vis} at t = 5.0 s is equal to 4.3 m, whereas our simulations predict a value between 4.7 and 4.9 m which does not vary with angular discretization scheme, angular or spatial resolution. The lower value corresponds to the distance of the furthest T = 1500 K temperature contour from the nozzle, whereas the upper limit corresponds to the distance to the furthest T = 1300 K temperature contour. For all curves, the non-dimensional height is normalized by dividing with the experimental visible flame length. We observe that both angular discretization schemes capture the curve of the radial radiative heat flux rather accurately, especially for small values of non-dimensional height, and that the new scheme performs marginally better overall. The discrepancy at the right tail of the curve can be attributed to the influence of boundary conditions, as well as, to some extent, the difference between the experimental and numerical flame length.

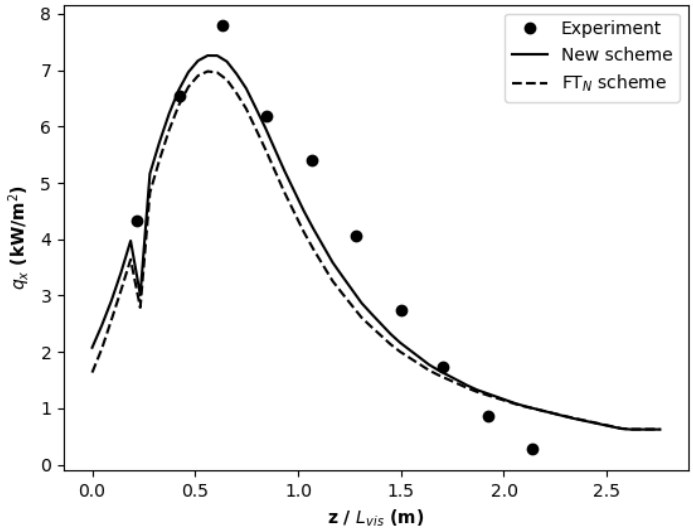

Figure 59. Vertical jet fire experiment: numerical predictions for the radial radiative heat flux as a function of non-dimensional height. Circles: experimental measurements. Dashed line: FT_N scheme. Solid line: our new proposed scheme.

In Figure 60, we consider the independence of our new angular discretization scheme with respect to the number of ACVs. For this purpose, we present again the predictions for the radial radiative heat flux as above but for three different angular discretizations: a coarse one with 80 ACVs, a medium one with 120 ACVs and a fine one with 168 ACVs. The spatial grid is the same as in Figure 59, consisting of 162,000 SCVs. It is evident that the new scheme demonstrates excellent convergence properties, as the three curves corresponding to the coarse, medium and fine angular discretizations are very close to each other.

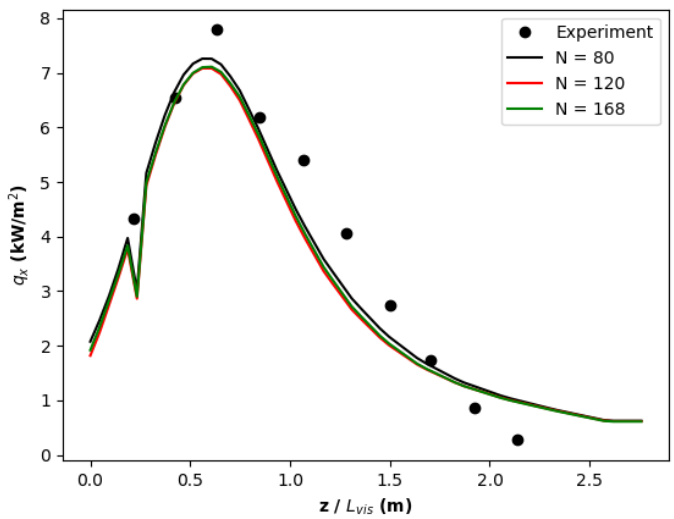

Figure 60. Vertical jet fire experiment: demonstration of independence of numerical results with respect to the number of ACVs. Circles: experimental measurements. Black: N = 80 ACVs. Red: N = 120 ACVs. Green: N = 168 ACVs.

Figure 61 presents a spatial grid independence study for our new angular discretization scheme. In all curves the number of ACVs is equal to N = 80. The coarse grid is the same as in the

previous two figures (162,000 SCVs), the medium grid is composed of approximately 272,000 SCVs and the fine grid is composed of approximately 358,000 SCVs. As the spatial resolution changes from coarse to medium, the peak of the curve is more accurately captured, whereas the predictions for small values of non-dimensional height remain excellent. As the spatial resolution changes from medium to dense, the peak of the curve is slightly under-predicted. Comparing the coarse grid with the two denser ones, predictions are significantly improved for intermediate values of non-dimensional height (1-1.5), while for higher values the discrepancy remains. This suggests that the source of this disagreement between experiment and simulation is due to boundary conditions and numerical/experimental visible flame length differences.

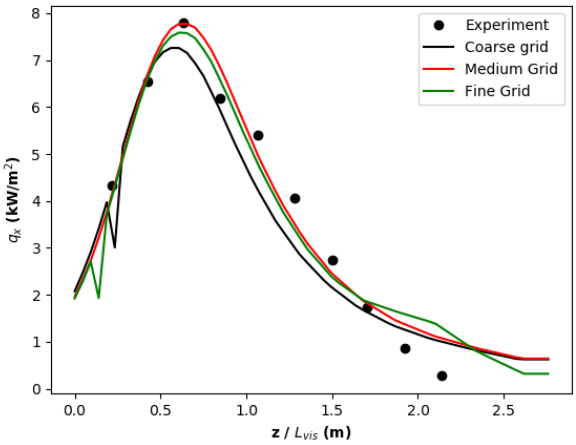

Figure 61. Vertical jet fire experiment: demonstration of independence of numerical results with respect to number of SCVs. Circles: experimental measurements. Black line: coarse grid. Red line: medium grid. Green line: fine grid.

3.2.4.2 *URS Experiment*

The horizontal under-expanded jet fire experiment provides an opportunity to test our radiation model's predictions of the radiative heat flux as a function of time, at three different fixed points in space. In Figure 62 we present the predictions of the radial radiative heat flux as a function of time given by the two different angular discretization schemes. The number of ACVs is equal to N = 168, whereas the number of SCVs is approximately equal to 129,000. Both schemes are able to capture the values given by all three radiometers during the whole duration of the experiment.

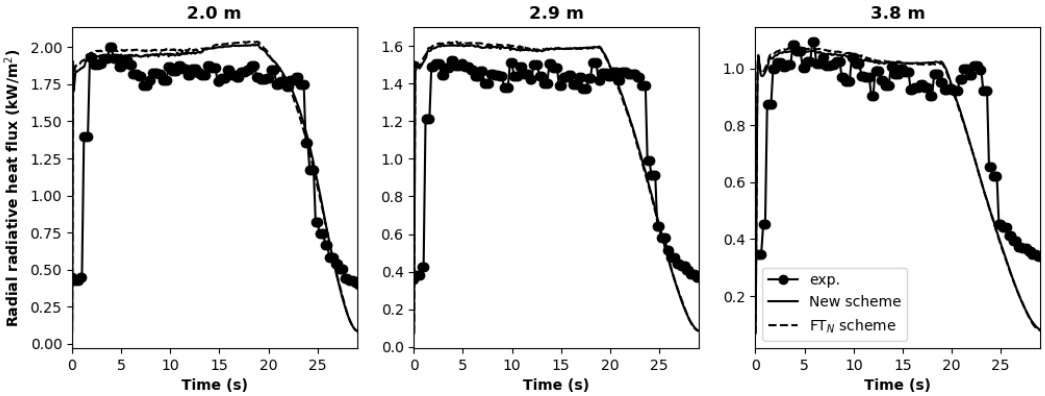

Figure 62. Horizontal jet fire experiment: comparison of the predictions of the radial radiative heat flux as a function of time given by the two different angular discretization schemes. Filled circles: experimental measurements. Dashed line: FT_N scheme. Solid line: Our new proposed scheme. Left: First radiometer, x = 2 m from the nozzle. Middle: x = 2.9 m from the nozzle. Right: x = 3.8 m from the nozzle.

Figure 63 demonstrates the independence of the numerical predictions for the radial radiative heat flux with respect to the angular discretization, for the horizontal jet flame experiment. Results corresponding to three different angular discretizations are presented: the coarse one corresponds to N = 168 ACVs, the medium to N = 224 ACVs and the fine one to N = 288 ACVs. The number of SCVs is again approximately equal to 129,000. Even though the predictions corresponding to the coarse and medium angular discretizations are closer to the experimental curves than the prediction corresponding to the fine angular discretization, all numerical curves remain close to the experimental ones for all radiometer positions. This is, overall, a more demanding problem than the vertical jet fire, as is evidenced by the increased number of ACVs which is necessary to reproduce the experimental curves.

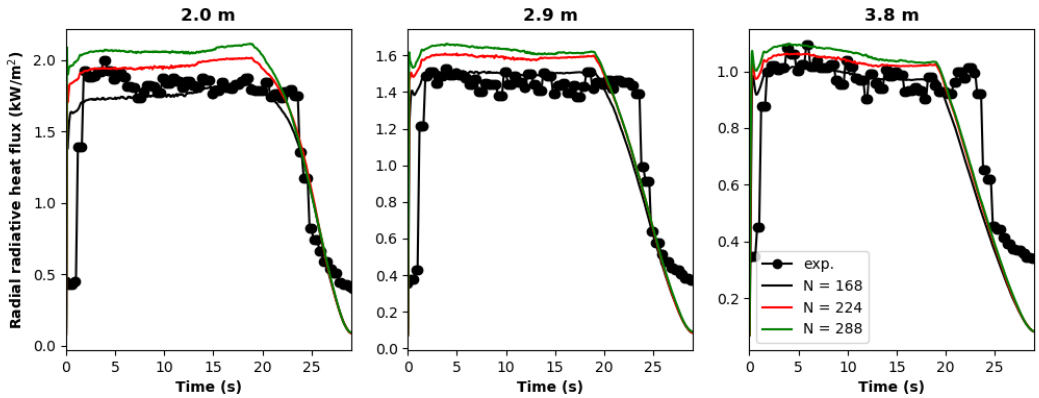

Figure 63. Horizontal jet fire experiment: demonstration of independence of numerical results with respect to the number of ACVs. Circles: experimental measurements. Black: N = 168 ACVs. Red: N = 224 ACVs. Green: 288 ACVs. Left: First radiometer, 2 m from the nozzle. Middle: 2.9 m from the nozzle. Right: 3.8 m from the nozzle.

Finally, in Figure 64 we present a spatial grid independence study for the horizontal jet flame experiment. Again, we consider the radial radiative heat flux as a function of time at the same three different positions. The coarse grid is the same as in the previous two figures, consisting of approximately 129,000 SCVs, the medium grid consists of approximately 365,000 SCVs spatial control volume and the fine grid of approximately 650,000 SCVs, whereas the number

of ACVs is equal to 224 in all cases. Numerical convergence is satisfactory overall, since all curves remain close to the experimental measurements for the whole duration of the experiment and the numerical predictions of the two finer grids are improved, especially for the radiometers located at x = 2.9 m and y = 3.8 m (middle and right sub-figures in Figure 64). As the spatial resolution is increased, the spurious trend observed in Figure 63 (i.e. the coarse and medium angular discretizations being closer to the experimental curves than the fine one) is remedied.

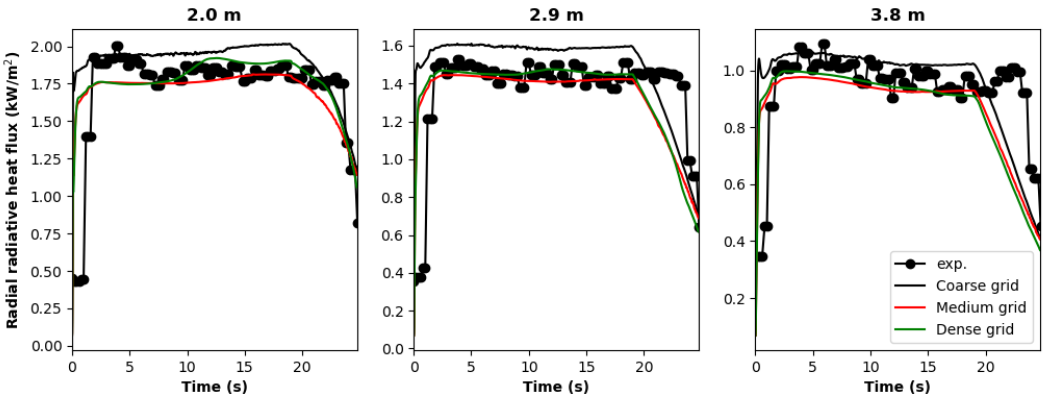

Figure 64. Horizontal jet fire experiment: demonstration of independence of numerical results with respect to the number of SCVs. Filled circles: experimental measurements. Black: coarse grid. Red: medium grid. Green: fine grid. Left: First radiometer, x = 2 m from the nozzle. Middle: x = 2.9 m from the nozzle. Right: x = 3.8 m from the nozzle.

In an extrapolation from the available experimental data, we also explored a larger diameter horizontal jet fire case with a setup in all other respects identical with the jet fires presented in this subsection. As a simple validation test, we compared the numerically predicted visible flame length with the one predicted by the NET e-laboratory online tool (NET e-laboratory). The numerically predicted visible flame is in the range [4.92, 6.05] m while the engineering model predicts a larger visible flame length equal to 6.23 m. The numerically predicted radiative heat fluxes at the three sensor positions (x = 2.0, 2.9 and 3.8 m) stabilize early at the quite elevated values of 13.73, 17.31 and 18.24 kW/m^2. Numerical convergence of the radiative heat flux curves versus time with respect to the same numbers of ACVs as above (not shown) was found to be excellent.

3.2.4.3 *USN Experiment*

In this section we will present selected validation results for the USN experiment. In Figure 65, we present a comparison of numerical and experimental time-series for four temperature sensors and one radiative heat flux sensor in experiment 1. This experiment has a vertical nozzle and a ventilation rate of 10ACH. We observe that in all these cases the simulation accurately captures the dynamics of the experiment.

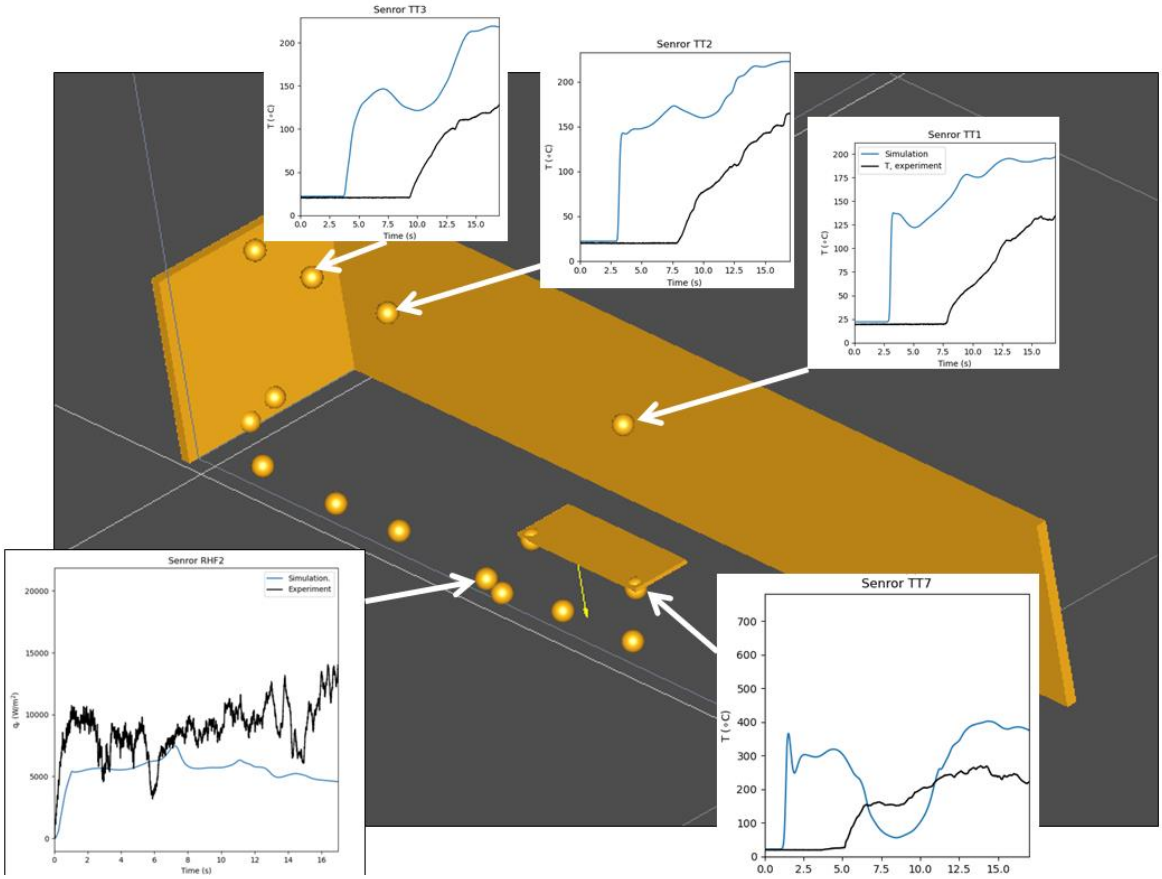

Figure 65. Comparison between experimental measurements and simulation results for selected sensors of the vertical, 10ACH experiment 1.

In particular, for the temperature sensors TT1, TT2 and TT3 (shown at the top of Figure 65, from right to left) which are located near the ceiling, the simulation results reproduce the experimental measurements overall satisfactory, although there is a premature increase in the numerical temperature time-series in all cases. The maximum temperature, which is of obvious interest for safety engineering, is in all cases slightly over-predicted. For temperature sensor TT7 (shown at the bottom right corner of Figure 65) which is closer to the nozzle, there is again satisfactory overall agreement. Even though there is an overshoot in the predicted numerical temperature early-on, the maximum predicted numerical temperature remains close to the experimental value. Finally, for the radiative heat flux sensor RHF2 (shown at the bottom left corner of Figure 65) the agreement between experimental measurement and numerical prediction is qualitatively good, although the maximum value of the radiative heat flux, another quantity of obvious importance for safety engineering purposes, is under-predicted.

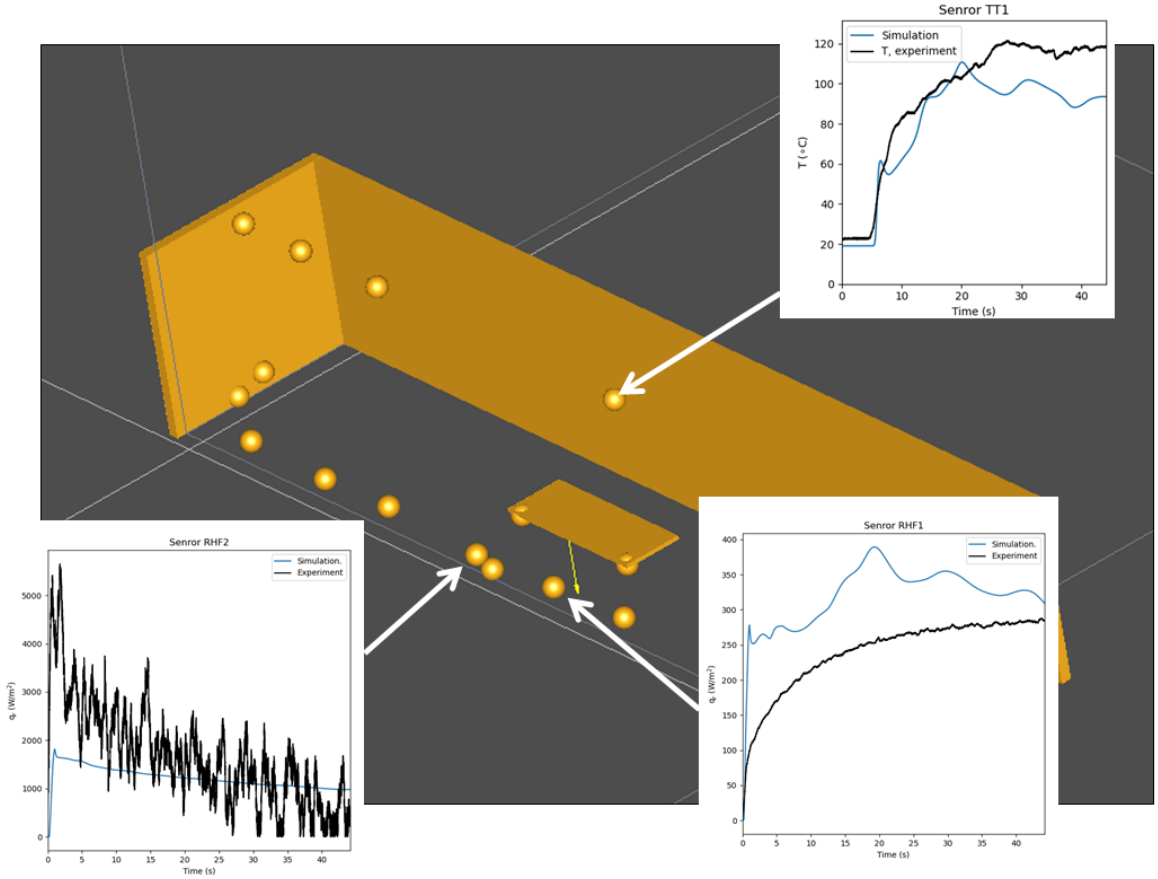

Figure 66. Comparison between experimental measurements and simulation results for selected sensors of the 45 degree, 10ACH experiment 6.

In Figure 66 we compare experimental measurements taken from experiment 6 with our numerical results. Experiment 6 has a nozzle inclined by 45 degrees towards the back of the vehicle model, and a ventilation rate of 10ACH, which is the same as experiment 1. Again, the simulation is able to capture the time evolution of both temperature and radiative heat flux, at least close to the nozzle and near the ceiling.

As far as the temperature is concerned, we compare once more the experimental values recorded by sensor TT1 (shown at the upper-right corner of Figure 66) with our numerical results. The numerical time-series follows the experimental data quite closely, although now the maximum value of the temperature is slightly under-predicted. For the radiative heat flux, we present comparisons between experimental and numerical time-series for sensors RHF1 and RHF2 (shown at the bottom of Figure 66, from right to left) which are located quite close to the nozzle. For sensor RHF1, the agreement in the time evolution is very good even though the maximum value of the radiative heat flux is over-predicted. The experimental data for sensor RHF2 are quite noisy, but again there is agreement in the time evolution, although the maximum value of the radiative heat flux is under-predicted.

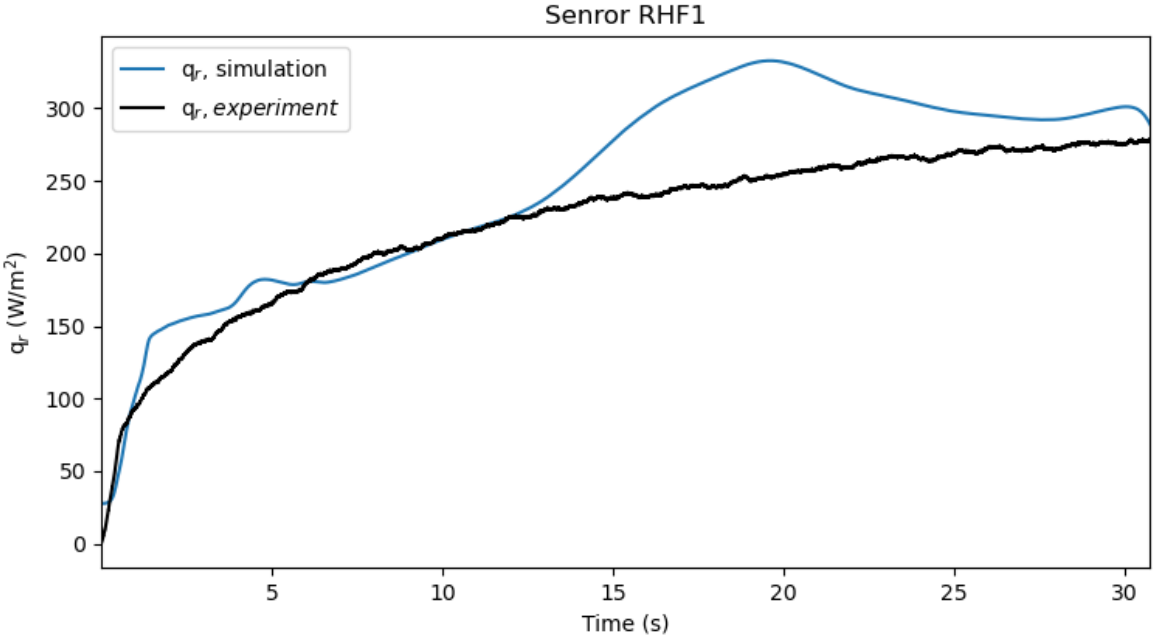

Figure 67. Comparison of numerical and experimental time-series for the radiative heat flux sensor. position located closest to the jet fire, experiment 7.

3.2.5 Conclusions

The goal of this subtask is the development of a predictive numerical model for the thermal hazards of under-expanded hydrogen jet fires in confined vented spaces, such as underground parking stations and maintenance garages. For this purpose, a thermal radiation module was developed for out in-house ADREA-HF CFD code. This module was validated against three different experiments. The first two were a vertical horizontal and a horizontal jet fire respectively. In both of these cases the agreement between experiment and simulation was excellent. In the much more important and difficult third case, which is a model of an underground parking station or maintenance garage, there is reasonable agreement for sensors located near the jet or at the ceiling but for the rest of the sensors, the numerical model needs to be improved. Current work in this direction focuses on the improvement of thermal and radiation boundary conditions, which may greatly influence the values of the temperature and the radiative heat flux in extended regions of space.

3.3 Coupled CFD/FEM modelling of the structures reaction to fire (ST 3.3.3, DTU/UU)

3.3.1 Object and aim of the study

Sub-task 3.3.3 is aimed at investigating the effects of a hydrogen-fuelled vehicle fire on the tunnel structure.

The tunnel assumed as a case study is a circular drilled tunnel of 13.3 m diameter with concrete linings and a 350 mm thick concrete suspended deck that is carrying the ventilation ducts and creating a separate from the road area (see Figure 68 left).

The geometry and dimension of the tunnel are reported in Figure 68 (right), while the materials used are concrete C30/35 for the wall linings and the deck and steel with characteristic strength of 500 MPa for the deck reinforcement. The reinforcement of the deck is made by slack bars of diameter 16 mm and spaced 150 mm, placed both at the bottom and at top of the deck, with a concrete cover of 55 mm and 35 mm from the bottom and top surface, respectively.

The slab is anchored to the side walls and, at some locations, also sustained in the middle by a series of HEB140 tendons, which are made of steel S235, as shown in Figure 69.

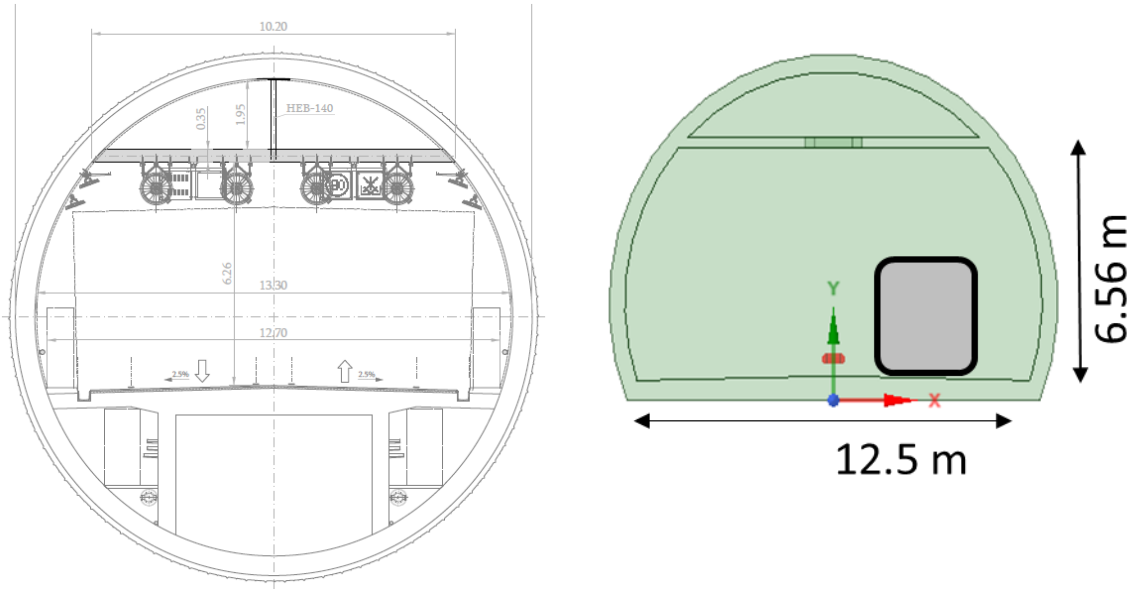

Figure 68. Geometry and dimension of the tunnel section.

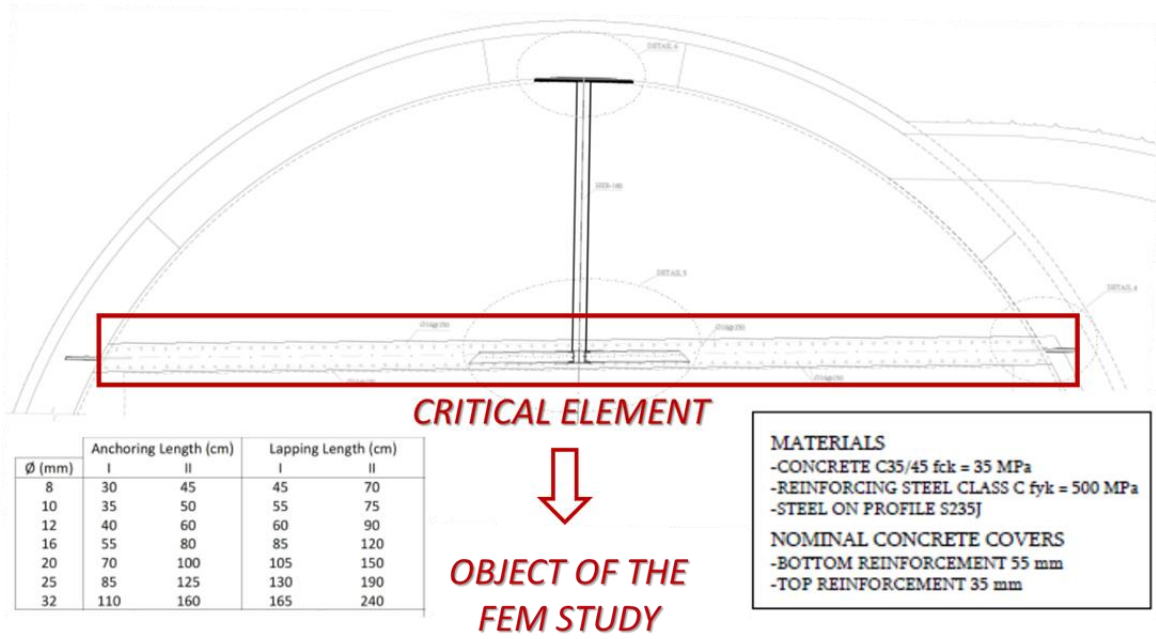

	Anchoring Length (cm)		Lapping Length (cm)	
Ø (mm)	I	II	I	II
8	30	45	45	70
10	35	50	55	75
12	40	60	60	90
16	55	80	85	120
20	70	100	105	150
25	85	125	130	190
32	110	160	165	240

Figure 69. Details of the suspended deck and steel tendon sustaining it.

The investigation of the tunnel response to jet fire will be limited to a 2D-analysis of the tunnel cross-section at the point where the accident is occurring. In particular, the accidental scenario

will be based on the jet fire triggered by a hydrogen-fuelled bus accident, as better explained in the following section.

The analysis will be a one-way coupled thermal and mechanical analysis, which will consider both the pressure and thermal effect of the jet fire. The thermal analysis will take input from the temperature obtained by the CFD analysis carried out in the present subtask on the same tunnel structure and based on the same accidental scenario. The mechanical analysis will take as input the nodal temperature history obtained by the thermal analysis and also the pressure history obtained by CFD investigation of jet fire impinging concrete tunnel walls. The analysis will take into account the thermo-plastic degradation of the materials and resort a nonlinear transient or dynamic algorithm for the solution. Results will be presented and discussed in term of deflections, plastic zone, and possible element failure. Local phenomena such as spalling or anchorage failures will not be explicitly modelled, but some qualitative consideration based on the thermal analysis result will be given.

3.3.2 Tunnel structure reaction to hydrogen fire (DTU, UU)

As explained in paragraph 3.3.1, the reaction of concrete structural elements to fire is related to i) spalling and ii) loss of resistance. The prediction of either phenomena is quite complex, as it requires:

1. an advanced CFD analysis capable of predicting the behaviour of the hydrogen fire in terms of incident heat flux or temperatures at the element surface
2. a thermal FE model capable of describing the heat penetration into the concrete and render a thermal map of the concrete element that extend long after the duration of the fire (as the heat takes much longer to penetrate the concrete)
3. a mechanical FE model capable of accounting for the softening and cracking of the concrete, thermal degradation of the concrete stiffness, strength, and ductility, as well as identifying possible local or global failures.

Prediction of spalling is in particular very challenging, as it would require also a fully coupled hygro-thermal-mechanical (HTM) analysis and is characterized by several aleatory and epistemic uncertainties, which would affect the reliability of the results. For this reason, the modelling of spalling is often tackled in a simplified way, based on pre-defined spalling criterion evaluated against the thermal map of concrete. In some cases, a mechanical analysis can follow, where layer of concrete is removed, when the spalling criteria are met (Deeny, et al., 2008).

This procedure has been applied to the case study of a drilled tunnel with concrete pre-fabricated wall linings and a 35 cm thick reinforced concrete slab placed at 6.5 m distance from the floor and carrying the ventilation system. The slab is 10 m wide and is assumed to be simply supported on the tunnel walls. The assumed fire scenario consists in a hydrogen-fuelled bus that has an accident: the TPRD (placed on the top of the bus) activates, releasing a hydrogen jet fire that hits the concrete slab just above the bus. The centreline of the flame is assumed to be at 3 m from the left support of the slab.

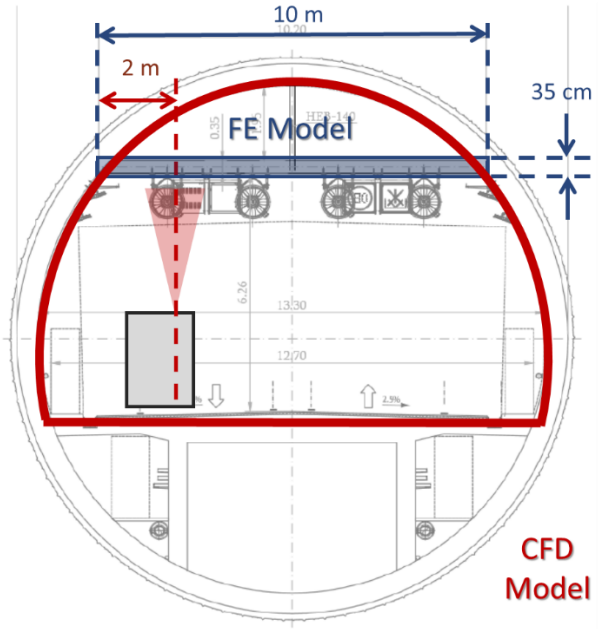

Figure 70. Drilled tunnel used as case study and sections of the CFD and FEM models. The main dimensions of the latter are reported, as well as the position of the bus and of the vertical axis passing through the TPRD.

3.3.3 Accidental scenarios

The scenario assumed in this investigation is based on the assumption of a hydrogen-fuelled bus accident. As a consequence of the accident, the hydrogen tank is overheated and a jet fire is released from the hydrogen tank TPRD.

This scenario is complementary to the accidental scenario investigated in WP4.3 on the same structure, where it is assumed that, due to a failure of the TPRD, the hydrogen is not released in a controlled way and the tank explodes.

Although the local solicitation due to pressure peak and impinging flame are unlikely to endanger the structural integrity of the tunnel, unless a concomitant vehicle fire is also considered, they could have an effect on the tunnel suspended ceiling and possibly cause local permanent damages to the concrete impinged by the hydrogen flame.

3.3.4 CFD modelling of hydrogen jet fire in a tunnel (UU)

Previous numerical study performed by Sandia National Laboratories showed that the impingement on a tunnel ceiling of a hydrogen jet fire from a 70 MPa tank and release diameter 2.5 mm may lead to concrete spalling (Anleu et al., 2017). The present study analyses the scenario of a hydrogen-powered bus involved in an accident in a tunnel. Following the accident, the thermally activated Pressure Relief Device (TPRD) on the storage tank opens. The released hydrogen ignites, producing a jet fire impinging on the tunnel ceiling. The aim of the study is to model the resulting hydrogen jet fire by CFD simulations to assess the thermal load on a tunnel infrastructure. These results were then passed into a suitable format to DTU for the FEM modelling of the thermal load effect on the integrity of a tunnel structure. The analysis of the CFD simulation results include the assessment of hazards distances for the tunnel occupants.

3.3.4.1 *Definition of a scenario*

The scenario details were defined thanks to the advice and suggestions from HyTunnel-CS SAB members to represent realistic situations. The study considers a hydrogen release from the storage tank on a hydrogen powered bus. The design of a typical bus employed in the London bus fleet is considered for the study. Bus dimensions are 13.2x3.4x2.6 m. The bus has a total of 4 storage tanks on-board operating at 350 bar pressure. Table 12 shows the parameters of the storage systems. The study assumes that the four tanks open in sequence every 60 s and release hydrogen into the tunnel through a TPRD diameter equal to 5 mm. Hydrogen is directed upwards as in typical designs of hydrogen powered buses. The hydrogen source is located on the bus top surface, specifically at 0.5 m from the side of the bus and in central position with respect to the bus length.

Table 12. Details of the bus on-board hydrogen storage system.

Storage of hydrogen	
N. of tanks	4
Pressure (at 288K)	350 bar
Tank volume	322 l
Mass of hydrogen	7.7 kg

A typical design of a road tunnel was considered for the study. Technical details on the infrastructure and operating modes of the ventilation system were provided by HyTunnel-CS SAB member IDOM. A 500 m long tunnel was considered. The tunnel has width 12.5 m and height 6.6 m. It is assumed that during fire all the openings along the tunnel for fresh air injection are closed. Five extraction vents (1.8x1.4m) are placed each 100 m along the tunnel. Ventilation system generally activates two minutes after an accident. Two more minutes are generally required to reach 100% performances of the fans. The bus is located at 300 m from the left end of the tunnel and 200 m from the right end. The bus is located in the middle of two extraction ducts V3 and V4, as showed in Figure 71. The traffic zone is separated from the ventilation duct by a concrete false ceiling with 35 cm thickness.

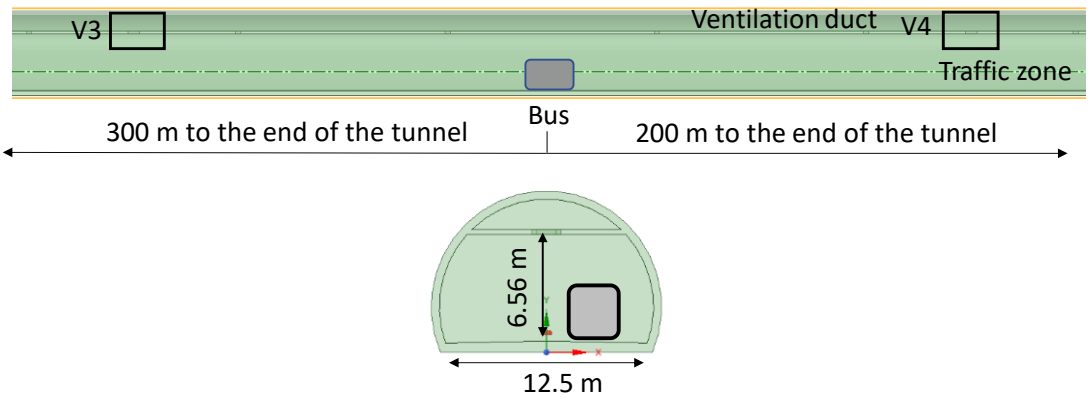

Figure 71. Tunnel design and bus location.

3.3.4.2 *Release source modelling*

A hydrogen release from a 350 bar storage tank produces an under-expanded jet. Furthermore, hydrogen properties in the storage system change in time due to the blowdown of the tank,

leading to a change in release conditions as well. Figure 72 shows the dynamics of storage pressure and hydrogen mass flow rate through the TPRD. The adiabatic-to-isothermal blowdown formulation is selected to model the release. In this formulation, the temperature within the tank stabilises at 215K once this temperature has been reached as observed in (Proust et al., 2011). The Ulster notional nozzle approach is applied to simulate the under-expanded jet properties dynamics during the tank blowdown through implementation of a volumetric source (Molkov et al., 2009). This approach is based on defining source terms for mass, momentum, energy and turbulence in a volume with size comparable to the notional nozzle at the beginning of the release. It is assumed that the four tanks open in sequence and every 60 s. At 60 s the mass flow rate has decreased by approximately 10 times from the initial value of 0.38 kg/s. In real buses, all TPRDs are connected to a unique vent line releasing upwards from the roof of the bus. Therefore, the jet fire originated by the different TPRDs in reality will be originated at the same location. Thus, the release source was the same for the hydrogen releases from the four tanks opening in sequence, each after 60 s.

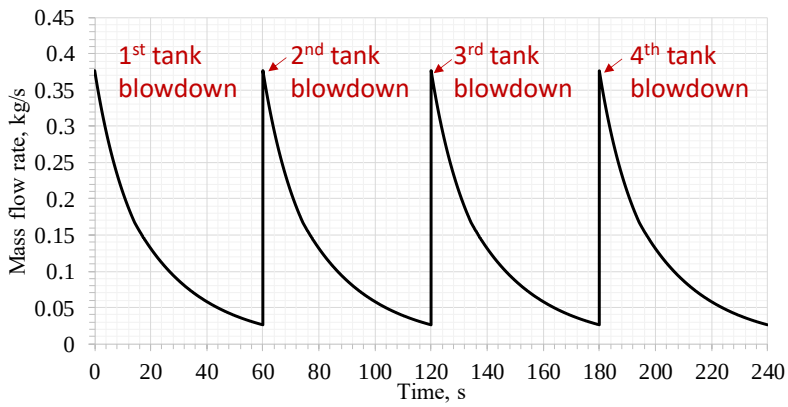

Figure 72. Hydrogen mass flow rate during the four tanks blowdown.

3.3.4.3 *CFD model*

The CFD model is based on an implicit pressure-based solver. The flow was considered as an incompressible ideal gas. RANS approach is employed for turbulence modelling, with realizable κ-ε sub-model for solving turbulent kinetic energy and turbulent dissipation rate respectively (Shih et al., 1995). The Eddy Dissipation Concept was used for combustion (Magnussen, 1981). It includes detailed chemical mechanisms of 9 species and 18 reactions by a subset of Peters and Rogg's mechanisms (Peters and Rogg, 1993). The Discrete Ordinates model is implemented to take into account radiation (Murthy and Mathur, 1998). The CFD simulations are conducted on the ANSYS Fluent platform.

3.3.4.4 *Calculation domain and numerical details*

A numerical domain with dimensions 600x40x40 m was considered for simulations. This includes the entire 500 m long tunnel and a portion of open atmosphere to ensure a sufficient distance to the domain external boundaries. A polyhedral mesh was employed, as this provides better resolutions of jets impinging on surfaces. A first assessment conducted on the opening of only one tank was used to refine the problem formulation, in particular to well represent the jet fire impingement zone on to the tunnel ceiling and the heat transfer through it.

The thickness of the tunnel ceiling was 35 cm as in designs of a real tunnel provided by the project advisor IDOM. The tunnel false ceiling was included in the numerical grid. Based on the assessment of simulation for one tank release, the numerical grid in the concrete ceiling was refined by using twenty layers increasing in size with a growth ratio of 1.1 to enhance resolution of heat transfer across the solid. The portion of ceiling within 25 m distance from the release source was subject to a refinement of the mesh with the following characteristics. A minimum cell thickness of 4 mm was imposed on the layer of solid cells adjacent to the impingement surface, and a minimum cell height of 3 cm on the adjacent layer of fluid cells. A maximum cell width of 12 cm was imposed at the tunnel ceiling up to a distance of 25 m from the release location. A maximum cell width of approximately 5 cm was imposed in the proximity of the release source, the jet area and the zone of impingement on the ceiling surface. The release volumetric source was modelled as a cube with length 6.3 cm, corresponding to the notional nozzle diameter at the start of the release. The tunnel walls were modelled as coupled, allowing heat transfer through them. The concrete properties were defined as a function of temperature according to (EN1992.1.2004). Pressure outlet conditions were imposed at the domain external boundaries with normal air composition. In order to aid solution convergence in the initial stage of the release, the time step was progressively increased from 0.001s to 0.02 s, which then was maintained for the rest of the simulation. Figure 73 shows the mentioned zone along the longitudinal section of the tunnel. The resulting numerical grid had an overall number of control volumes equal to 1,435,153.

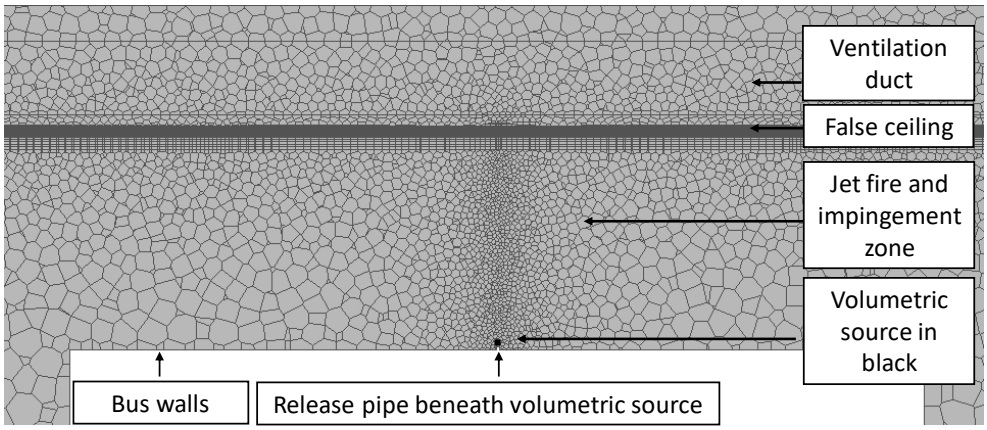

Figure 73. Numerical grid: detail of tunnel longitudinal section where the hydrogen jet is located.

3.3.4.5 *Results and discussion*

Results of CFD simulations are firstly shown as distribution of temperature and hydroxyl mole fraction to give insights into the jet fire dynamics. Figure 74 shows the temperature dynamics in the longitudinal plane of the tunnel where the hydrogen jet fire is located. At 10 and 20 s, it can be observed that the jet fire impinges on the ceiling broadening in width. The higher temperature zone of the jet fire beneath the ceiling is located in the surroundings of the jet axis, due to the flame impingement. This zone progressively decreases with time, due to the tank blowdown. The minimum width of the jet is reached at 60 s. The hot combustion products, corresponding to the zone of temperature lower than 1300K, are seen to move along the ceiling due to the buoyancy effect. A stratification of temperature along the vertical direction is formed with time, reaching the lowest height at 20 s. Similar temperature stratification can be observed as well during the sequential opening of the other three storage tanks, as shown by temperature

distributions at 90 and 150 s. Figure 75 shows the OH mole fraction distribution providing an indication of the combustion zone. The jet fire impingement zone is seen to be approximately 6 m at 10 s. This zone decreases with time reaching an extension of approximately 1 m at 60 s.

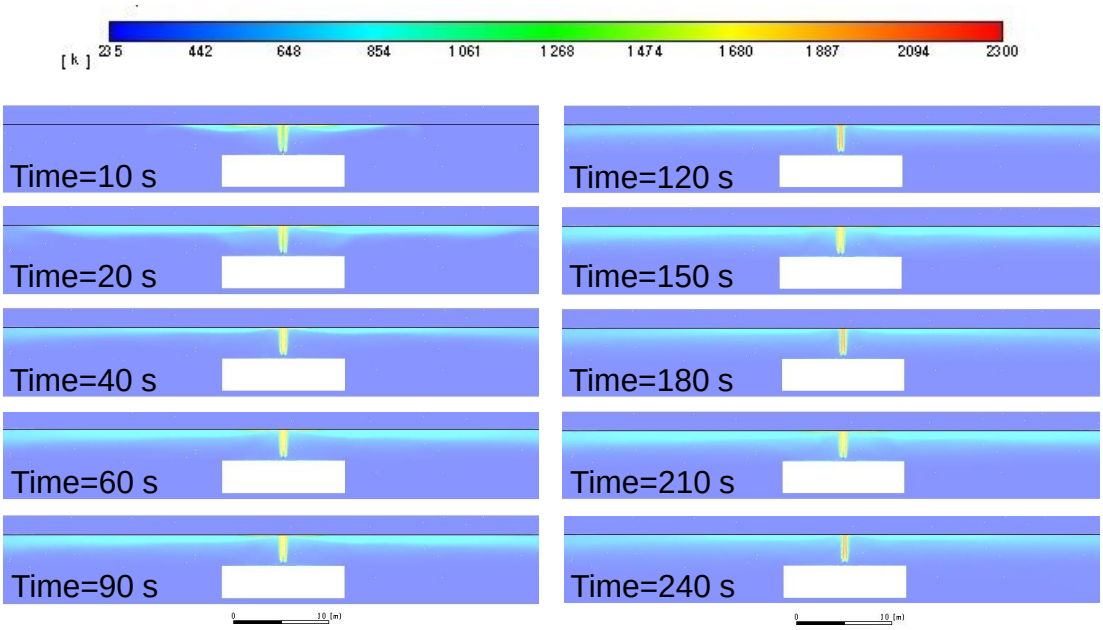

Figure 74. Temperature dynamics in the longitudinal section of the tunnel.

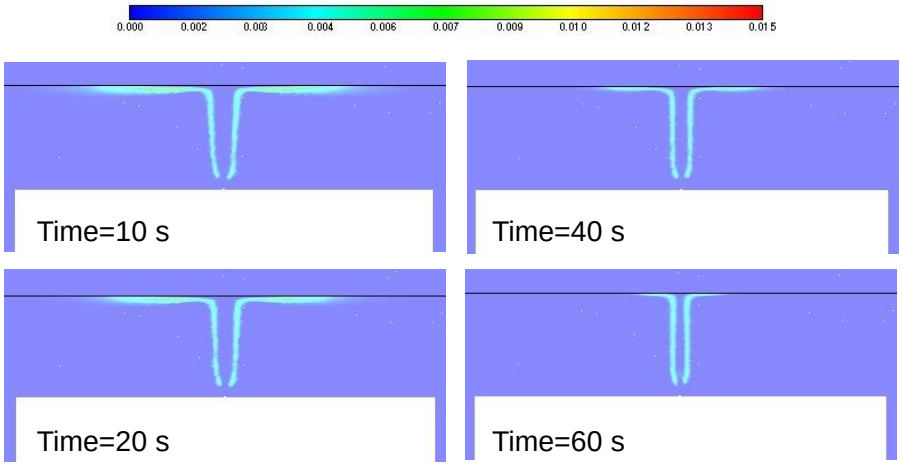

Figure 75. OH mole fraction dynamics in the longitudinal section of the tunnel.

Figure 76 shows the distribution of temperature and OH mole fraction on the transversal section of the tunnel. It can be observed that the jet fire impinges the ceiling close to the left wall. The jet fire impinging zone broadens freely in right direction. However, in the left direction, the flame moves beneath the ceiling and descends along the tunnel left side wall, due to the high momentum of the jet. This effect is visible up to 20 s, whereas it disappears at time 40 s. Occupants of the tunnel will be in the bottom part of the tunnel. Figure 76 shows how the tunnel left side may be more dangerous for people due to the greater descent of high temperature zone towards the ground.

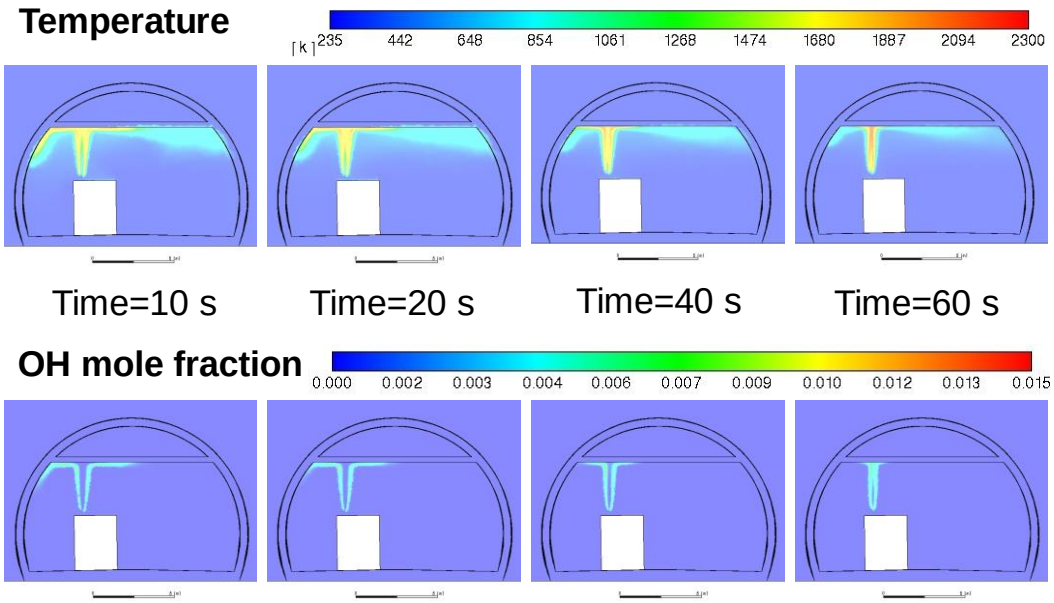

Figure 76. Temperature and OH mole fraction dynamics in the transversal section of the tunnel.

Figure 77 shows the time distribution of heat flux on the portion of the tunnel false ceiling where the jet fire impinges. At 2 s, the zone characterised by the higher heat flux is delimited to a circular zone of approximately 2 m in diameter. This zone progressively enlarges in time up to 12 s and then it starts to reduce in size to reach a minimum at 60 s.

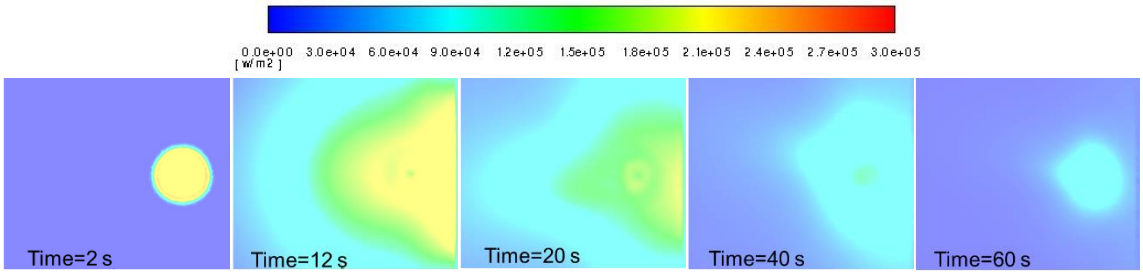

Figure 77. Surface heat flux distribution on tunnel false ceiling.

Figure 78 shows the maximum heat flux value recorded at the ceiling. A maximum surface heat flux of approximately 300 kW/m^2 is reached at 2 s, and it is seen to steeply decrease to 210 kW/m^2 in around 5 s. Afterwards the maximum surface heat flux reaches a second peak of 240 kW/m^2, to then progressively decrease reaching a minimum of 120 kW/m^2 at 60 s. Similar cycles, but with peaks of lower entities are observed during the opening of the remaining three tanks.

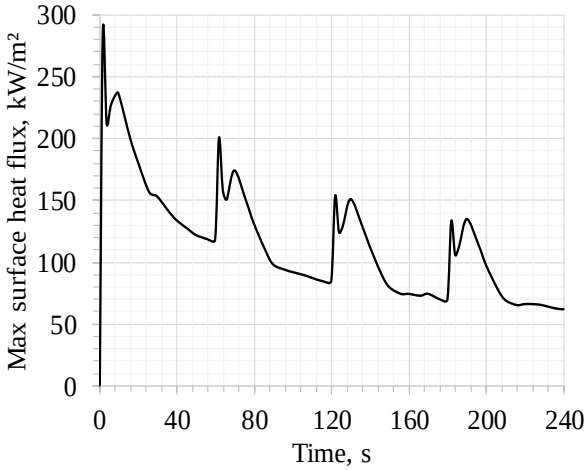

Figure 78. Maximum surface heat flux on the tunnel false ceiling.

A further analysis was conducted on the distribution of temperature along the jet axis. Focus was posed on the temperature in proximity to and across the concrete tunnel false ceiling. It was observed that the temperature in the fluid zone increases with time from approximately 1100 K at 5 s to 2100 K at 60 s. This is a consequence of the storage tank blowdown, which causes a reduction of the jet impinging zone and a movement of the high temperature zone towards the jet axis from the sides of the broaden zone, as shown in Figure 74. Temperature within the false ceiling was seen to increase in time due to the increasing temperature of the gas adjacent to the wall and due to the thermal load applied on the false ceiling wall. A maximum of approximately 1000 K is reached in the layer of 4 mm solid concrete cells closer to the surface. However, the specific FEM modelling is needed to assess the effect of the jet fire on integrity of the tunnel false ceiling.

3.3.4.5.1 Hazard distances for humans

Hydrogen-air combustion influences the temperature distribution in its surroundings and leads to the production of hot air/combustion products currents that could be dangerous for the exposed people. The following harm criteria for people, as suggested in (LaChance, 2010), are considered to assess hazard distances by temperature:

- “No harm” limit: 70°C for any exposure duration;
- “Pain” limit: 115°C for 5 minutes exposure;
- “Death” limit: 309°C, third degree burns for 20 s exposure.

Figure 79 shows the longitudinal distribution of the cloud with a temperature ≥ 70°C (343 K) at time equal to 20 s. It can be observed that the dangerous hot gases cloud is concentrated beneath the ceiling. A height of 2 m is considered as a limit for the zone where tunnel occupants may move. No harmful temperature is reached at this height, indicating that occupants may escape without harm according to the temperature thresholds. It must be highlighted that a ventilation system is not active, thus, this appears as the worst conditions scenario.

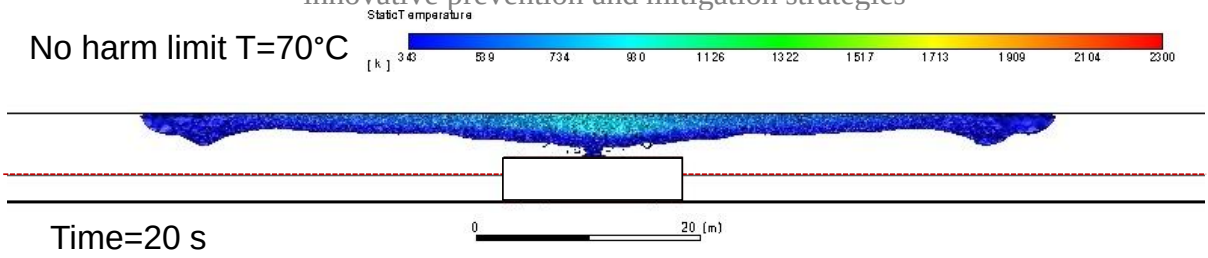

Figure 79. Longitudinal distribution of the hot gases cloud with temperature ≥ 70°C (343 K) at 20 s.

3.3.4.6 *Conclusions of the study*

The study presented the CFD modelling of a jet fire from a hydrogen powered bus in a tunnel. It gave insights into the jet fire and hot gases cloud dynamics within the tunnel. It was observed that the high temperature zone following the jet fire is concentrated in close proximity of the ceiling and moves along with it. No harmful temperatures were reached at a height equal to 2 m for a 60 s release duration, whereas harm thresholds by thermal radiation were recorded. CFD results are used in FEM modelling for a comprehensive assessment of the tunnel structure response to the jet fire.

3.3.5 FE Thermal model

A 2-dimensional FE thermal model of the cross-section of the concrete slab just above the flame has been implemented in Abaqus (Simulia, 2014) and transient thermal analyses have been carried out, with the aim of identifying the maximum heat penetration depth in the slab, an accurate thermal map of such depth, and the maximum temperature of the steel bars. Such outcomes have been used to give some probable indication of the extent of concrete damage, the possible occurrence of spalling, and the structural response of the slab.

The model has first been validated under the assumption of standard fire against results available in literature (EN1992-1-2, 2004) and sensitivity analyses on the uncertain variables (such as heat transfer coefficient, concrete conductivity and specific heat capacity) have been conducted to assess the effect of such uncertainties and calibrate the model.

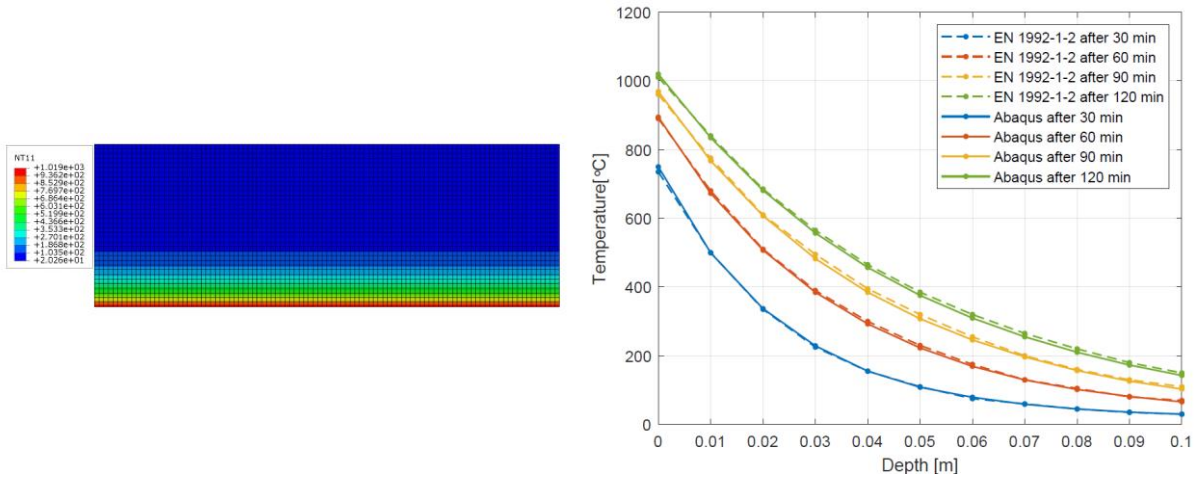

Figure 80. Left: segment of the 10 m long sectional model with 10 mm mesh used for validation; Right: temperature profiles along the slab height at different times obtained from the analysis in case of standard fire exposure of the bottom part of the slab (continuous lines) and compared with the temperature profiles provided by the EN1992-1-2 (dotted lines).

After this validation, the thermal model has been used to predict the temperature in the concrete slab exposed to the hydrogen fire resulting from the bus accident scenario. In particular, the FE thermal model takes input from the CFD model in the form of incident heat flux on the exposed surface of the concrete elements or in the form of gas temperature close to the concrete surface. Such heat input has a duration of 279 s, after which the flame is extinguished and the heat flux drops to zero and is assigned to the model in the form of boundary condition for the transient thermal analysis.

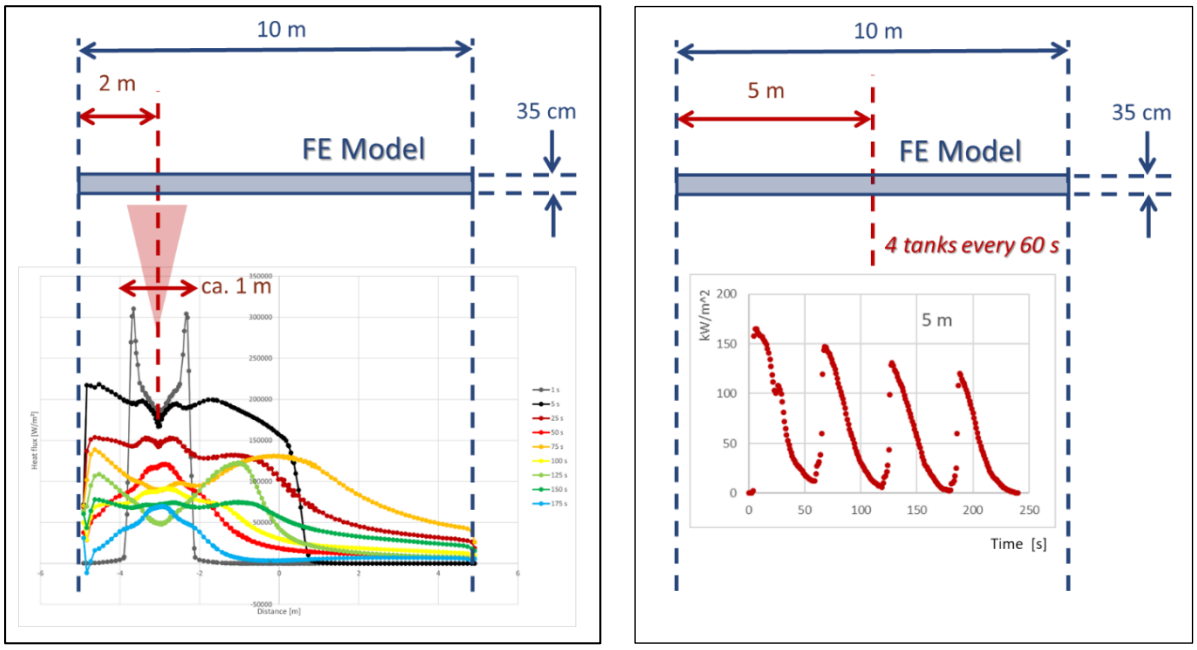

Figure 81. Left: heat flux input vs. distance at different times (from 1 to 175 s). Right: heat flux vs. time at the fixed distance of 3.5. m from the release point and 5 m from the left end of the slab (slab mid-span).

The thermal analysis is run for 400s, in order to take into account that, due to the low conductivity of the concrete, the heat transfer into the concrete section continues also after the heat solicitation has ceased and gives as output the temperature of the concrete at each instant and at each node of the mesh. Such temperature histories are then passed to the mechanical models. Although relatively coarse data are needed for the mechanical analysis, the mesh in the thermal model needs to be very fine, as a consequence of the small time step needed to model the high temperature and heat flux variations of hydrogen fires. This is something that does not occur in case of cellulosic or hydrocarbon fires typically assumed in structural fire analyses and implies that a coupled thermal-mechanical analysis cannot be done, as it is not possible to use the same mesh and model for both analyses.

Due to the very high refinement of the mesh, a preliminary simplified model has been developed, with the twofold scope of identifying:

i. the maximum penetration depth of the heat, in order to reduce the dimension of the final model
ii. the time at which the steel bars reaches the highest temperature, in order to identify the relevant running time of the analysis

The simplified model consists in a small segment of the slab just above the release point (see Figure 82). The sides of the model have been assumed to be adiabatic, while the bottom and top sides are assumed to have free convection and radiation to the fire and ambient temperature respectively, assigned as sink temperatures. The fire temperature has been taken as the gas temperature close to the surface in the considered release point provided by the CFD analysis, while the ambient temperature above the slab has been assumed equal to 20 °C.

The results of this analysis, which are expected to be conservative, due to the assumption of adiabatic sides and the most severe location of the fire, are shown in Figure 82. It is possible to see that only the first 5 cm of the concrete are interested by a relevant heating (>100 °C) and only the first 2-3 cm reach temperature close to or higher than 300 °C, which could cause permanent damage in the concrete. The steel bars, positioned at a depth of 55 mm, reaches a maximum temperature of ca. 100 °C about 30 min later the start of the fire. Such temperature is not significant from the point of view of the mechanical degradation of the steel and, as consequence, the slab is not expected to experience a reduction of the load bearing capacity as a direct consequence of the heating from the hydrogen fire.

However, the very rapid heat of the first 2 cm of the slab suggests that explosive spalling of the outermost concrete is possible. In this case, the concrete cover of the steel could be reduced and the heating of the steel could become more significant.

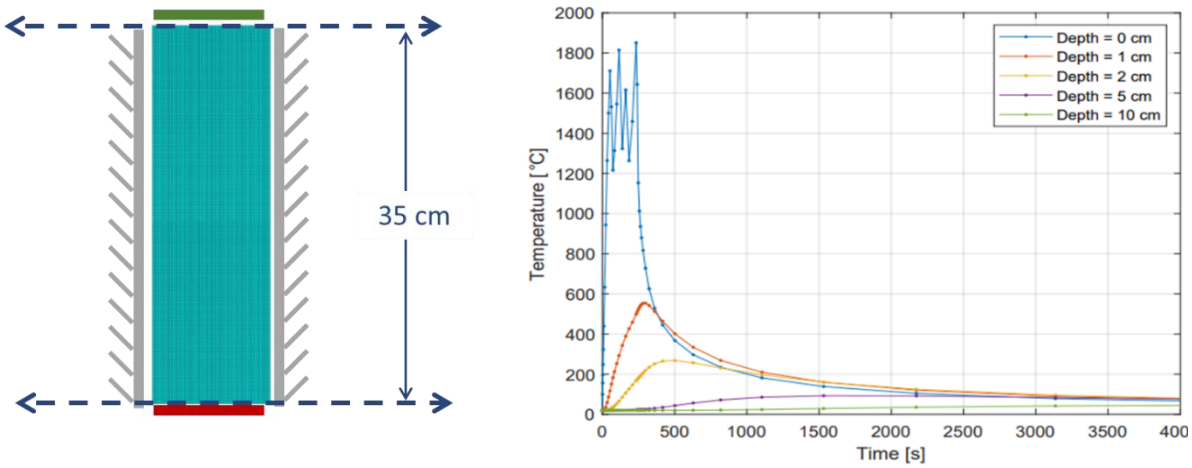

Figure 82. Simplified model of the most solicited segment of slab (left) and resulting temperature histories at different depth (right).

In order to better evaluate the possibility of spalling and the extent of it and effect on the temperatures, a more refined slab model is developed, where the full length of the slab is considered, as well as the variation of the input temperature on the bottom surface of the slab. As shown in the schematic of the model reported in Figure 83 such variation has been accounted by discretizing the boundary conditions at the bottom surface into 168 segments. Such discretization follows the discretization of the thermal input, which had been provided with the same discretization from the CFD analysis, but is much larger than the mesh size of the model, which has been set to 5 mm after a mesh calibration analysis shown on Figure 84. The use of such refined mesh has been made possible by the consideration of a reduced height of the slab to 5 cm and assumption of an adiabatic surface at the top of the slab. Such reduction

is justified by the results of the simplified model, which show an insignificant heating of the concrete at a depth of 5 cm and higher.

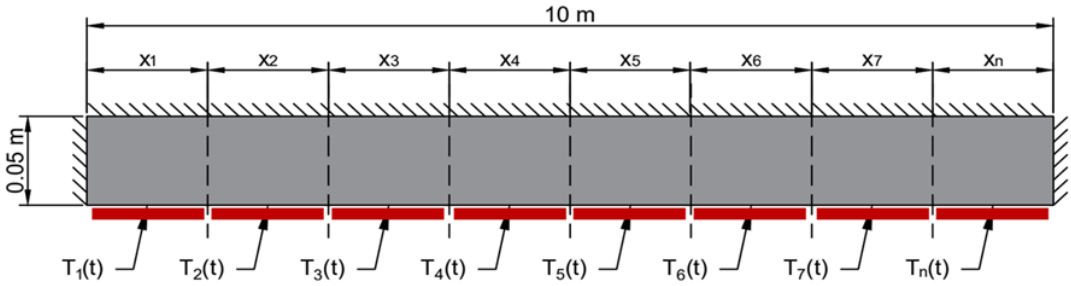

Figure 83. Schematic of the boundary condition discretization of the refined slab model. Bottom.

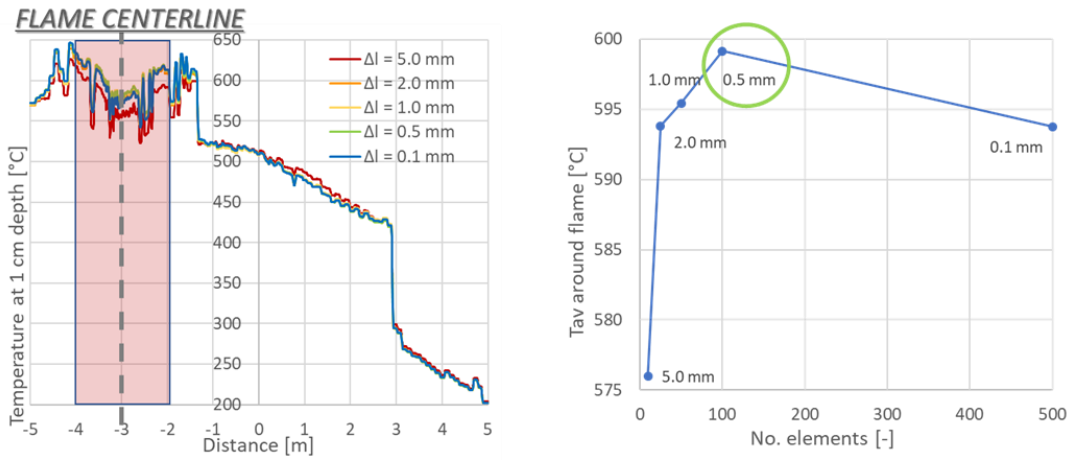

Figure 84. Mesh calibration by means of a sensitivity analysis on the average temperature around the flame centerline.

The results of the analysis of the more refined model are shown in the top chart of Figure 85 and represents the temperature at different depth in the slab at the end of the fire (279 s). It is visible that the hydrogen fire affects the concrete most severely up to 1 cm depth. The maximum concrete temperature in the surface layer and at 1 cm depth is 871°C and 644°C, respectively, while it is just 232 °C at 2 cm. This means that the concrete depth exposed to temperature higher than 300 °C is less than 2 cm. This is the temperature limit assumed for permanent damage of the concrete, according to literature (Hertz, 2018). The steel is located at 5.5 cm depth relative to the bottom surface and is still completely cold (ca. 20 °C) at the end of the fire. This temperature does not corresponds to the maximum temperature of the steel, which is reached at a much later time, but still does not exceed 100°C. At this temperature, both the 0.2% proof strength and the 2.0 % effective yield strength are not reduced and, as a consequence, the load bearing capacity of the slab is unaffected.

It is here relevant to notice that the rebar cover of regular slabs is often smaller than this specific slab and often equal to 30 mm only. However, even a slab where the steel reinforcement is placed at such reduced depth would not suffer a significant reduction of the load capacity, as visible from the fact that the temperature at 3 cm is just 87°C at the end of the fire.

By analysing the results, it is also possible to see that the critical spalling temperature of 375°C is reached at a depth of ca. 1.5 cm from the bottom surface. This temperature is used as criterion for spalling, in accordance with literature results (Hertz, 2018) and with a study on spalling criterion that is reported in full in a DTU report (Vivanni, 2021).

On the basis of this result, a new model is implemented, where the bottom 1.5 cm of concrete are removed and a new thermal analysis is conducted. The results are shown on the bottom chart of Figure 85. The temperature of the steel at the end of the fire is increased to 55°C, but is still very low and not expected to reach a heating temperature that could significantly decrease its strength and therefore reduce the capacity of the slab. The temperature at 3 cm (usual rebar cover) increases instead to 385 °C. This temperature is close to 400°C, which is the temperature at which even the effective (ultimate) yield strength is reduced and therefore indicate that the capacity of a slab with a regular cover rebar could be reduced in case of a hydrogen jet fire that induce spalling in the bottom concrete.

From the results of this study, it is concluded that, in case spalling is avoided, the structural resistance of concrete slabs exposed to hydrogen jet flame is not expected to be at risk, due to the short duration of the flame and limited time let for heat penetration into the concrete. In case of spalling, the structural resistance of a slab with a usual rebar cover of ca. 30 mm is at risk. It is therefore recommended to avoid spalling in the concrete elements that may be exposed to hydrogen fire and to ensure a high rebar cover of at least 50 mm, in order to limit the heating of the steel reinforcement if spalling should occur.

It is important to underline that these conclusions only refer to the action considered in this fire scenario and analyzed in the CFD model, that is a hydrogen jet flame triggered by the activation of the TPRD. It is however unlikely that this activation is not triggered by a previous car fire or other accidents that result in larger fire. In such cases, the heating of the concrete slab would be much longer and result in much higher temperatures of the steel and decrement of the load bearing capacity. Furthermore, the effect of the spalling possibly caused by the hydrogen flame would not be the same, as the reduction of the concrete cover in a longer fire would lead to much higher maximum steel temperature and likely failure of the slab during the longer broader fire event.

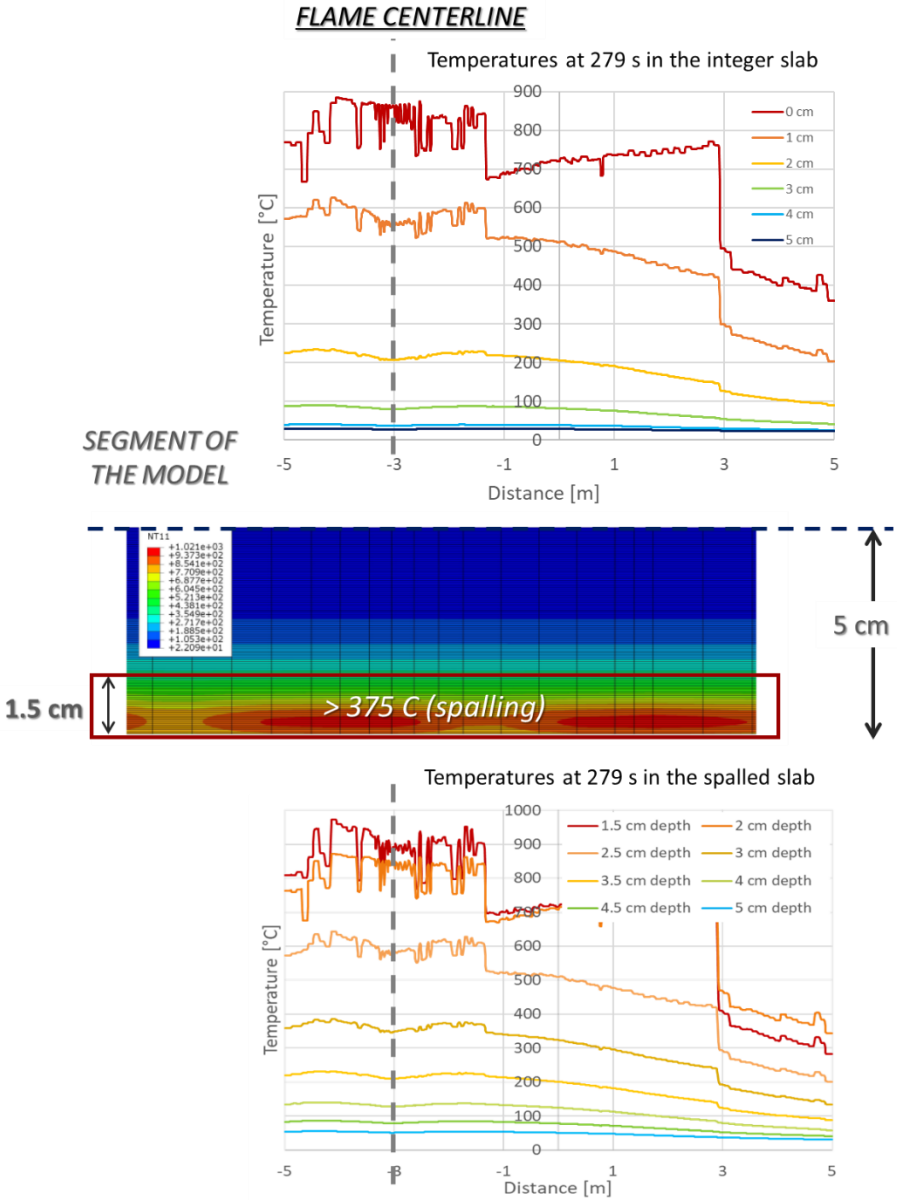

Figure 85. Temperatures at different depth at the end of the fire obtained from the analysis of the refined model considered as integer (top) and where the bottom 1.5 cm are removed as a consequence of spalling (bottom).

3.4 CFD model on influence of hydrogen releases to fire spread scenarios in underground transportation systems (ST 3.3.4, DTU)

To assess vehicle fires, some tests with burning cars have been carried out concerning the fire safety of car parks. Mangs et al. (1994) designed three full-scale fire experiments with passenger cars. The cars were tested, including oil, petrol, and ordinary passenger cabin materials. The experiments obtain the heat release rate (HRR) curve for a car fire. Dayan et al. (2017) used two 4-door sedan passenger cars to design the full-scale vehicle fire tests, which can obtain the burning behaviour and describe the spread of fire to the adjacent car by the measured temperatures, radiant heat flux and photo images. In this test, the flame spread from

the engine compartment to the car cab through the air-conditioning vents. Katsuhiro et al. (2013) carried out four full-scale car fire tests to establish the burning behaviour of minivan passenger cars under different conditions, such as door window opening and ignition point. The results indicated that the breaking of the windows could affect the fire behaviour directly.

Tamura et al. (2014) investigated the fire spread between the hydrogen-fuelled vehicles by two-vehicle fire tests. The test results indicated that the flames spreading from the interior and exterior materials of the fire origin vehicle is the direct reason for the ignition of the adjacent vehicles.

The layout of the modelled car park is shown in Figure 86, details in Liu et al. (2021):

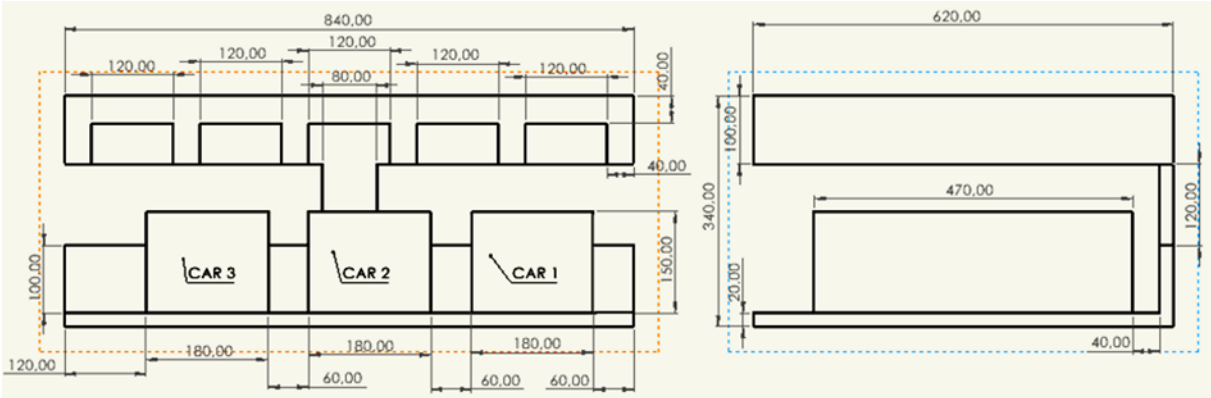

Figure 86. Layout and dimensions of the modelled car park (Liu et al., 2021).

The car model (see Figure 87) comprises different sub-models, such as tires, seats, interior material and fuel. The material parameters can be seen in Table 13. The position of the cars in the car park model is indicated in Figure 88 together with the specific locations of the structural components in the car park.

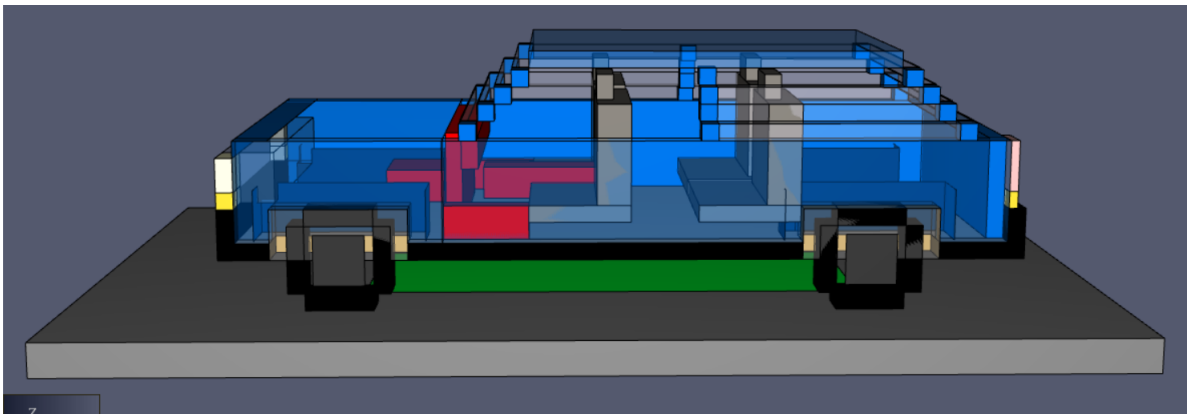

Figure 87. Hydrogen vehicle model.

Table 13. Material parameters for the car model.

Submodel	Material	Specific Heat Capacity [KJ/kg · K]	Thermal Conductivity [W/m · K]	Density [kg/m^3]
Tire (Hurley et al., 2016)	Rubber	2.01	0.13	650
Seat (Krüger et al., 2016)	Foam, PUR	1	0.05	65
	Fabric	1	0.1	100
Interior material (Krüger et al., 2016)	Polypropylene, PP	2.16	0.2	960

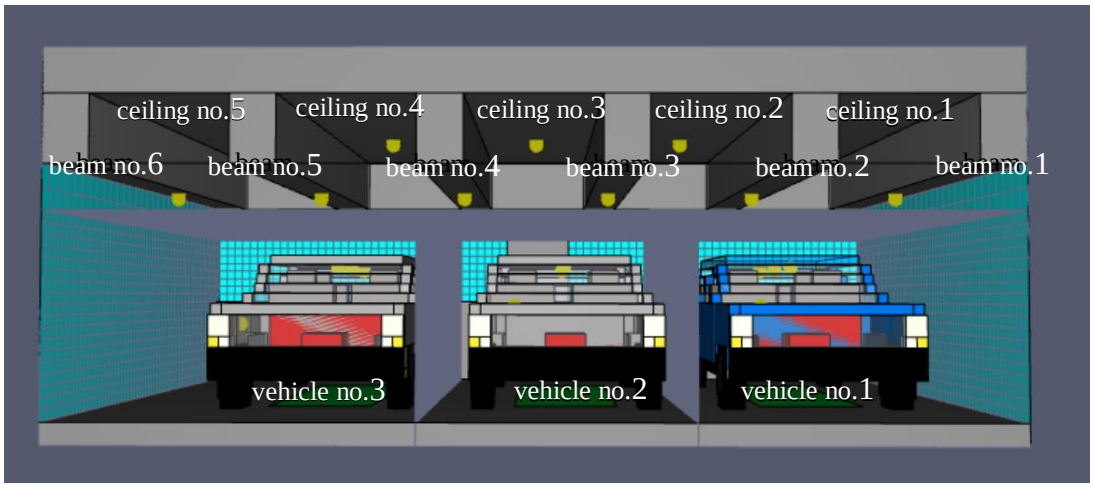

Figure 88. Hydrogen cars parked in the car park. Distance between cars 0.6 m.

The fuel is hydrogen, and the amount the hydrogen tank contains is 5 kg. The TPRD nozzle diameter applied in this study are 0.5mm, 1mm, 2mm, 3mm, 4mm and 5mm. A sensitivity analysis has been done for a 4 mm diameter. The release profiles can be seen in Figure 89 and Figure 90. The assumption for the hydrogen model is a vertical downwards jet that impinges the floor after a short distance. Therefore, the release of the hydrogen is modelled as a burner, as FDS can't simulate gas flows which speed is higher than 0.3 Mach number. The hydrogen gas is released from the burner surface (3 m^2 area) with a variable mass flow rate placed underneath the car. When the temperature near the gas cylinder reaches 110℃, the TPRD in the hydrogen vehicle will be activated, and the hydrogen will be released. Therefore, the simulated thermocouple temperature at 110℃ parameter will be used to trigger this in the FDS simulation. The hydrogen module is tested in a domain of 560 m^3, and the mesh size has been varied with $0.2\text{m} \times 0.2\text{m} \times 0.2\text{m}$, $0.1\text{m} \times 0.1\text{m} \times 0.1\text{m}$ and $0.05\text{m} \times 0.1\text{m} \times 0.2\text{m}$. The total energy released is shown in Table 14.

Table 14. Mesh size and the total energy released.

Mesh Size [m]	No. of cells	Total Energy Release [MJ]	LHV reference calculation [MJ]	Deviation from LHV calculation [%]
0.20×0.20×0.20	70000	612.445	600	2.07
0.10×0.10×0.10	560000	608.897	600	1.48
0.05×0.10×0.20	4480000	615.116	600	2.52

In the Table 14, the LHV reference calculation is obtained by multiplying the material mass and heat of combustion. The total energy release is obtained from the FDS simulation results. It can be seen from this table that $0.1\text{m} \times 0.1\text{m} \times 0.1\text{m}$ mesh size is closer to the theoretical calculation. The deviation from LHV is minimal among the three mesh sizes, and it is just 1.48%. Therefore, in the subsequent hydrogen model, the mesh size will adopt $0.1\text{m} \times 0.1\text{m} \times 0.1\text{m}$. When the mesh size is $0.1\text{m} \times 0.1\text{m} \times 0.1\text{m}$, the result of the HRR and the hydrogen releases for a 4mm TPRD can be seen in Figure 89 and Figure 90, respectively. In Figure 90, the maximum HRR is about 54000KW. After ignition, the HRR value reaches the highest value very soon.

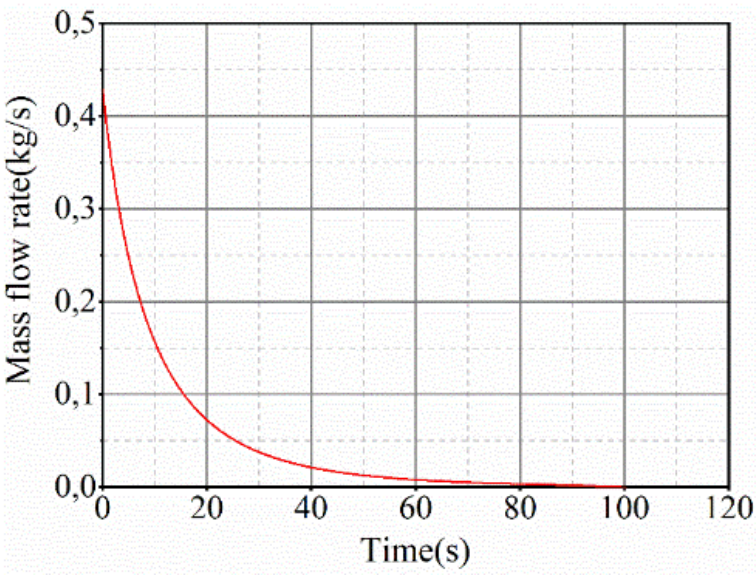

Figure 89. Hydrogen mass release profile, TPRD = 4mm.

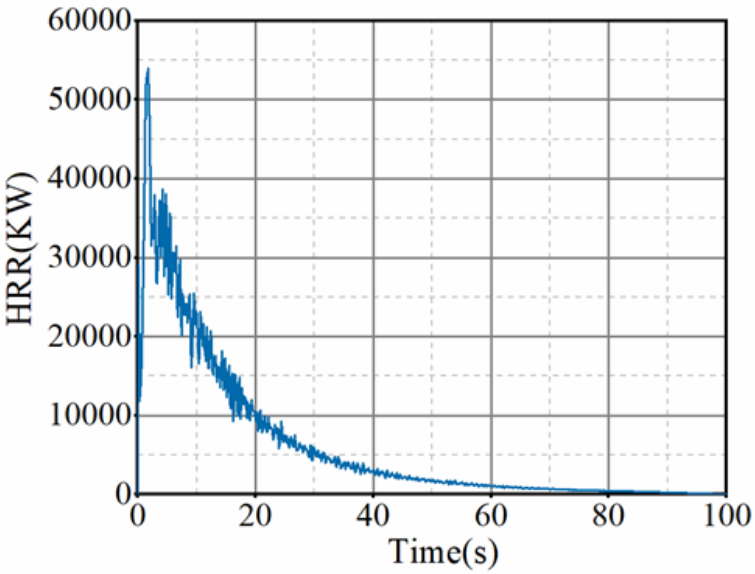

Figure 90. The corresponding heat release rate (HRR) for the mass release in Figure 89.

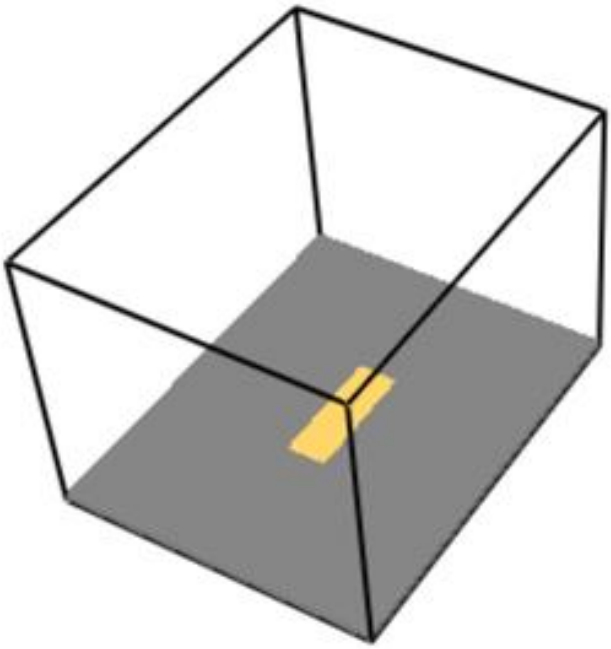

Figure 91. Development of hydrogen fire at 0 s of release time.

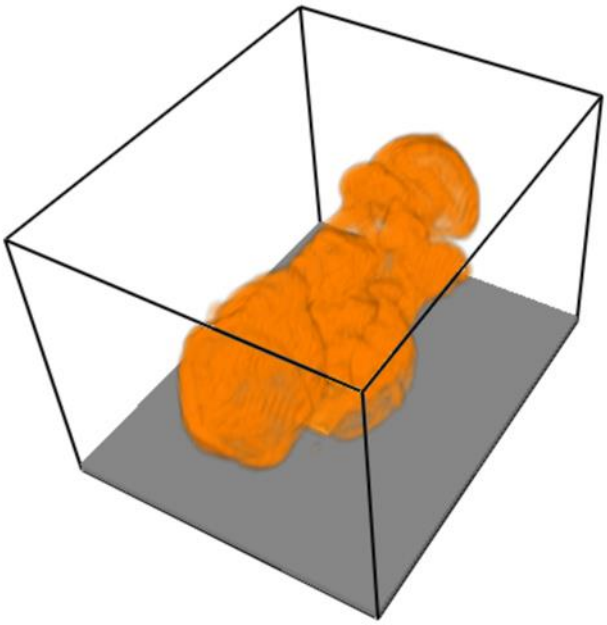

Figure 92. Development of hydrogen fire at 1.5 s of release time.

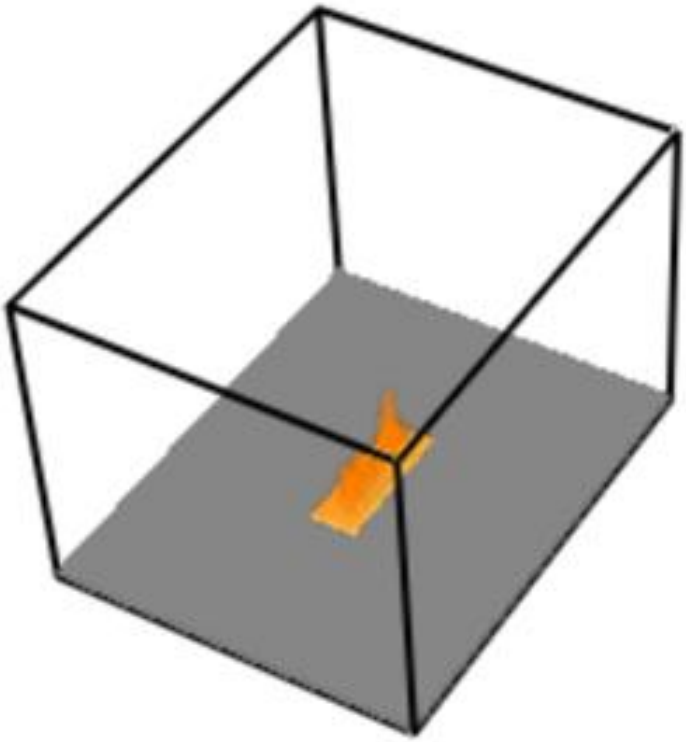

Figure 93. Development of hydrogen fire at 50 s of release time.

Figure 94 shows the hydrogen vehicle fire spread simulation results using the 5 mm TPRD nozzle diameter. It can be seen that the ignition location is in vehicle no.1 and the fire spread between the adjacent vehicles is very quick. The biggest possible flame of H_2 blowdown captured escaping the bottom of the first car right after TPRD activation occurs at 425s, and the biggest possible flame of H_2 blowdown captured escaping the bottom of the three cars occurs right after the TPRD activations at 430s. From the first vehicle's TPRD activation to the third vehicle's, it only takes about 5s. Figure 94(e) shows the time when vehicles no.1 and no.2 completely are on fire and the third vehicle showing only a little fire spread after H_2 runs out. From Figure 94(f), it is seen that for the third vehicle, the fire starts spreading through the car's back left wheel; at 609s, the fire fully developed through the third vehicle. Finally, fire self-extinguished in the car park when the time is about 3680s.

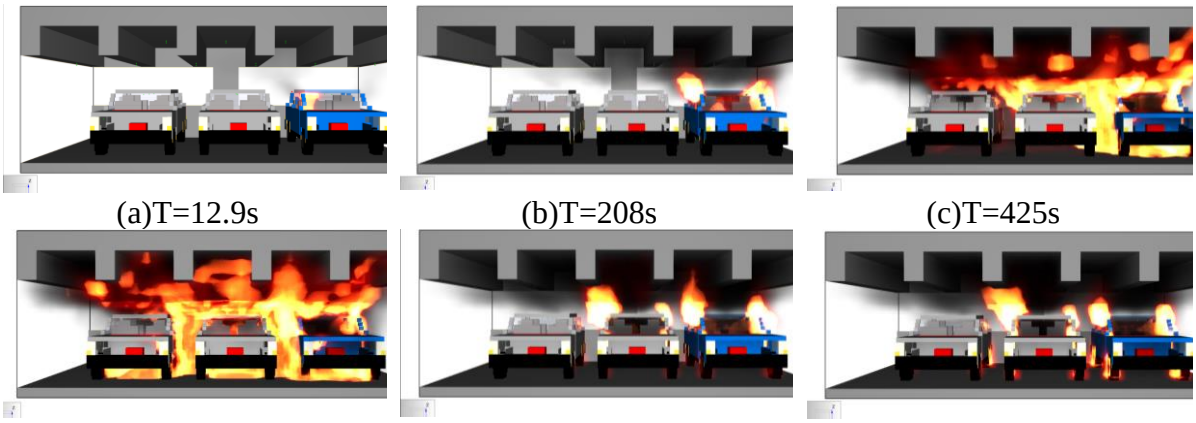

(a)T=12.9s (b)T=208s (c)T=425s

(d)T=430s (e)T=505s (f)T=551s

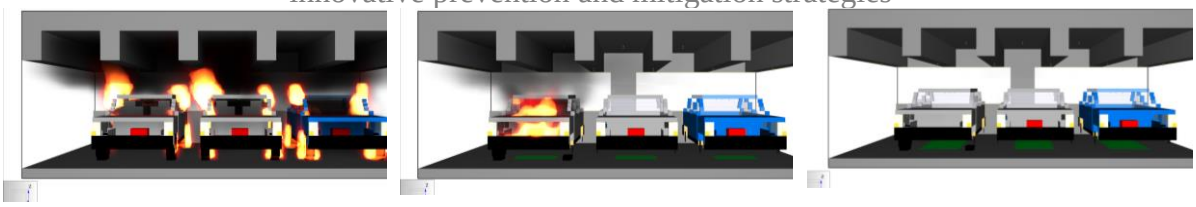

(g)T=609s (h)T=2799s (i)T=3680s

Figure 94. Burning history for the 5 mm nozzle diameter.

In Table 15 it is seen that the TPRD diameter has a little effect on the TPRD activation time of the no.1 vehicle when the amount of H2 in the tank is the same. And three vehicles' TPRD are activated almost simultaneously when the TPRD nozzle diameter is 5 mm. However, when the vehicle's TPRD nozzle diameters are 0.5mm, 2mm and 3mm, the remaining vehicle's TPRD is not activated. In the 4 mm and the 1 mm simulations, fire takes time to propagate from car nº2 to car nº3. In the 4 mm simulation, 960 seconds pass between their TPRD activations, and in the 1 mm, 1260 seconds pass. This behavior could indicate that a steady heat outcome is more likely to propagate the fire slower between FCHVs rather than a shorter but higher heat release.

Table 15. TPRD activation for the three vehicles.

TPRD diameter [mm]	TPRD activation vehicle no.1 [s]	TPRD activation vehicle no.2 [s]	TPRD activation vehicle no.3 [s]
0.5	490	None	None
1	430	600	1690
2	427	None	None
3	426	None	None
4	425	430	1385
5	425	430	430

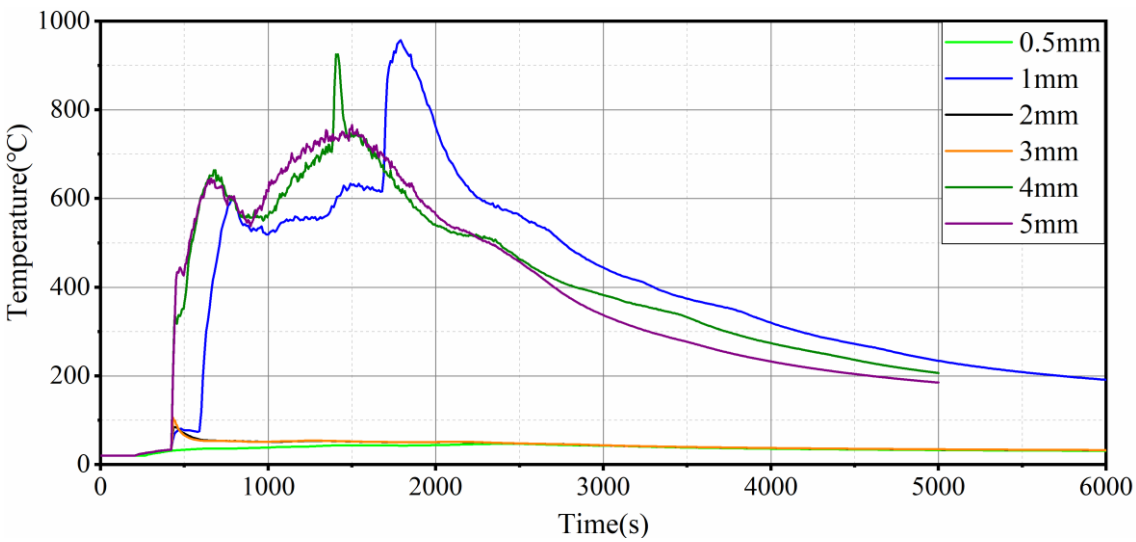

Figure 95. Beam no.4 surface temperatures for the different scenarios.

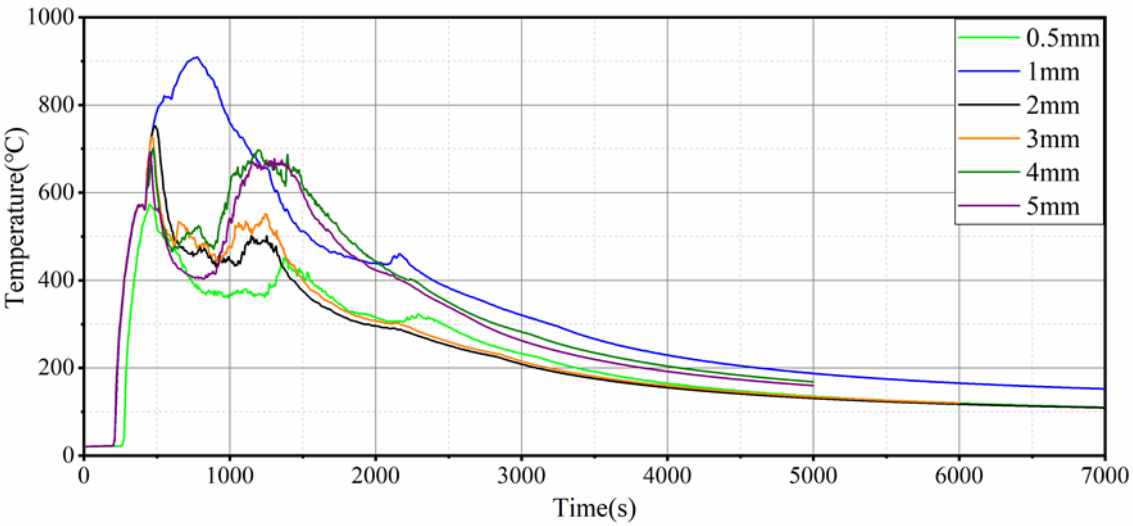

Figure 96. Ceiling no.2 surface temperatures for the different scenarios.

The Figure 95 and Figure 96 show the development of the ceiling beams and ceiling no.2 located above the burning initial car (no.1). In the 5 mm diameter scenario, the highest temperature reaches almost 950ºC. This beam reaches a higher temperature because it is right in the middle of vehicles no.2 and no.3. The flames escaping the vehicle cabin through the windows hit the concrete beam directly when they are burning. In this curve, there are two rising stages. Stage *a* indicates that the temperature raises super-fast when all the TPRDs activate in a very short time. In stage *b*, once vehicles no.2 and no.3 are completely on fire temperature starts rising again, almost reaching a peak of 800ºC. There is only one rising stage in these temperature curves for 0.5mm, 2mm and 3mm diameter scenarios. The temperature is much lower than that of other scenarios because vehicles no.2 and no.3 are not completely on fire in the simulation.

4. Experiments (Task 3.4/CEA)

4.1 Pressure peaking phenomenon for hydrogen jet fires in confined spaces (ST 3.4.1, USN)

The experimental campaign on Pressure Peaking Phenomenon (PPP) for ignited hydrogen releases in a large-scale enclosure involved approximately 30 tests for hydrogen mass flow rate up to 11.7 g/s. As expected, experimental results provided essential insights into the PPP for large scale enclosure and validation data for modelling. The experimental facility has been already described in Section 2.1.3, whereas the experimental matrix and results in Section 2.1.5 along with comparison against predictions by the analytical model for PPP by UU. Hence, they are not repeated in this chapter. A selection of tests has been used for validation of a CFD model by UU, see Section 3.1. Further details on the experimental campaign have been published in Lach and Gaathaug (2021a). The experimental data are openly available and accessible at USN Open Data Repository, doi: 10.23642/usn.17934047.

4.2 Thermal effects of hydrogen non-premixed turbulent combustion on a vehicle fire behaviour, structure and evacuation conditions in underground parking (ST 3.4.2, USN)

The experimental investigations of thermal effects from non-premixed turbulent combustion aim to assess the scenario of FCH vehicles in garages and car parks. In more detail, the study investigated the temperature field and heat flux generated close to the car in case of an ignited release from the TPRD. The potential visibility reduction due to combustion products was also investigated.

The experiments were designed to imitate the ignited release from a FCH car TPRD with storage pressure of 35 and 70 MPa. The nozzle diameter investigated was mostly 0.50 mm, but also one with 1.00 mm nozzle. A 40" ISO container was set up to simulate a car park. Two airflow ventilation rates were tested and temperature in the ventilation pipe was measured to investigate if the existing ventilation system will be damaged due to high temperatures in ventilation resulting from 'sucking out' the combustion products and hot air from the container.

The 40 ft ISO container with isolated walls, was used for all experiments with both open exit doors. Its inner dimension LxWxH: 11885 x 2240 x 2285 mm gives a total volume of 60.8 m^3. The isolation thickness was approximately 0.07 m. The real-scale parking house/underground parking has the standard 2.25 m minimum free height (Statens Vegvesen, 2019). On the floor were mounted cement-based, non-combustible building plates, 6mm thick.

The table imitating hydrogen car was scaled against the Toyota Mirai with a scaling factor of 0.4 resulting in dimensions: LxWxH: 1965 mm x 730 mm x 250 mm. The table further called 'car' consists of steel legs and a 1 mm steel plate. The hydrogen outlet was mounted vertically through the steel plate. For the first two experiments, hydrogen was vertically discharged (90 degrees) with nozzle 25 cm above the floor (see Figure 97, left). For the rest of experiments, hydrogen was discharged with 45 degrees nozzle (see Figure 97, right), 18 cm above the floor.

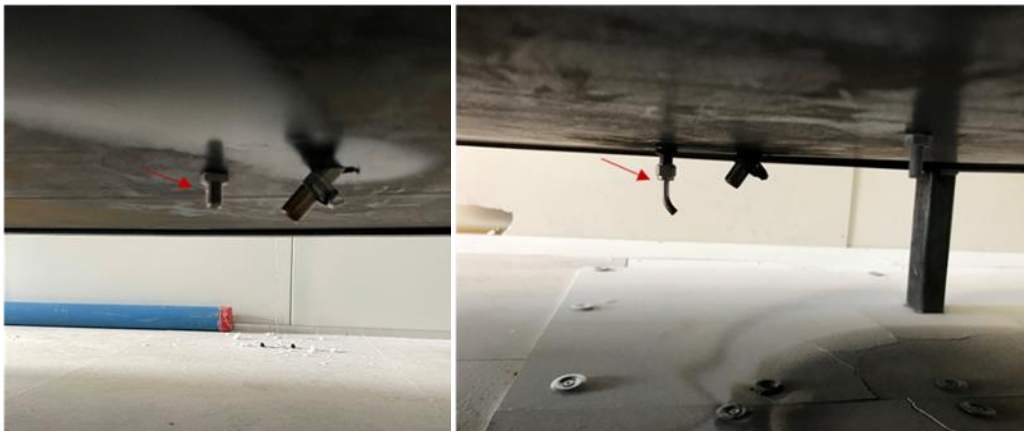

Figure 97. The 90-degree nozzle (left) and the 45-degree nozzle (right).

The hydrogen tank and Coriolis mass flow meter were placed behind the container (see Figure 98).

Figure 98. Hydrogen tank and coriolis mass flow meter; unsafe side.

The total pipe length from the hydrogen tank to the nozzle was 3.86 m. At the tank outlet a pressure transmitter was installed. The same type of pressure transmitter was mounted at the outlet of Coriolis mass flow meter.

The ventilation duct outlet with ID 0.315 m was located 0.05 m from the ceiling (0.2075 m from the ceiling to centre) on the ventilation wall (Figure 99). The pipe consists of ~2 m with 0.315 diameter pipe and ~2 m with 0.2 m diameter. The air fan model vented the air with voltage controller. The air flow rate was measured by IRIS 200. The air change per hour (ACH) for the experiments were according to British standard 10 ACH and 6 ACH. For the container geometry that means:

10 ACH: $V = ACH \cdot V_{conatıner} = 10\frac{1}{h} \cdot 60.8\, m^3 = 608\frac{m^3}{h}$

6 ACH: $V = ACH \cdot V_{conatıner} = 6\frac{1}{h} \cdot 60.8\, m^3 = 365\frac{m^3}{h}$

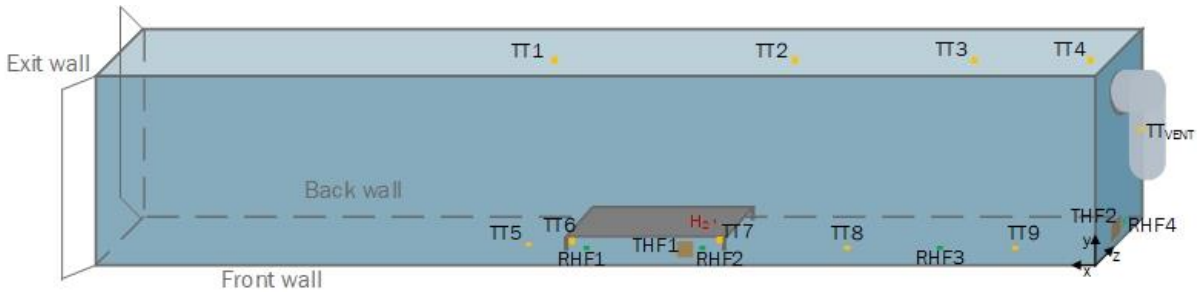

Figure 99. Reference drawing: yellow- thermocouple TT, green- radiative heat flux RHF, brown-total heat flux THF, red- nozzle.

Sensors – Type and setup

Three synchronized oscilloscopes were used to record data measured from sensors and transmitters. The recording was done with a sample rate 0.0005 s per sample for most of the experiments and sensors. The thermocouples 1-9 were sampled with rate 0.02 s per sample (50 Hz). The different sensors are explained in Table 16.

Table 16. Data description of sensors.

Scope 1	Scope 2	Scope 3
TT_{HFT1} - total heat flux from sensor 1 **TT_{HFT2}** - total heat flux sensor 2 **TT_{vent}** - temp in the ventilation pipe **RHF1**- radiative heat flux from sensor 1 **RHF3**- radiative heat flux from sensor 2 **RHF3** - radiative heat flux from sensor 3 **RHF4** - radiative heat flux from sensor 4	**P_{tank}** – pressure at the tank outlet **$P_{\dot{m}}$** - pressure at the Coriolis outlet **$\dot{m}$**- mass flow rate **DP** – differential pressure **TT_t** – temp from the tank **$T_{\dot{m}}$** - temp from the Coriolis mass flow meter	**TT1-TT9**- temp from the thermocouples type K

The location of the sensors is given in Table 17, reference to Figure 99.

Table 17. Sensors' location.

Location parameters [mm]			
	y	x	z
TT1	2105	6250	1120
TT2	2105	2320	1120
TT3	2105	1060	1120
TT4	2105	110	1120
TT5	235	7200	80
TT6	198	6330	868
TT7	200	4600	860
TT8	235	3310	74
TT9	235	1030	80
RHF1	235	6080	40
RHF2	220	4850	0
RHF3	235	2300	40
RHF4	235	40	1100
THF1	75	5020	50
THF2	95	0	750
nozzle 45	180	4980	1120
nozzle 90	230	5000	1120
TTvent	510		130 inside

4.2.1 Experimental matrix and procedures

The hydrogen tank was filled with nitrogen (10-20 bars, up to 4 times), before filling with hydrogen. The inertization process was needed to extract oxygen from the tank and pipe system. The hydrogen was pumped from a 200 bar hydrogen bottle pack through booster pump (the same as for Mechanical ventilation experiments in WP2).

Before the hydrogen ignition, a propane pilot flame was initialized. The hydrogen was released into the propane pilot flame and hence automatically ignited. The thermal effect from the propane flame was tested to be negligible (propane flame was shut down seconds after hydrogen ignited).

4.2.1.1 *Test parameters*

The releases inside the container were performed from 350 bar and 700 bar tank with 6 and 10 ACH each. The 90 degree vertical, towards the floor nozzle was used in first 2 experiments (700 bar with both ACH). For experiments 3-8 the nozzle was mounted 45 degrees downwards, towards the ventilation wall. In Table 18 the parameters of the flow in the tank and mass flow meter (MFM) are presented:

- the pressure in the tank at the moment of release of hydrogen,
- the mass flow rate and pressure at the exit of the mass flow meter (MFM) was measured and initial parameters (2 s after the release),
- the initial temperature measured in the tank, which does not include heat transfer through the steel walls of the bolt,
- the maximum and minimum temperature measured at the MFM during whole experiment.

Table 18. Experimental matrix and parameters. Blowdown releases.

Exp nr	Nozzle angle [°]	Nozzle diameter [mm]	Air change per hour [ACH]	Ambient temp [C]	Tank pressure [bar]	Pressure at MFM_{exit} [bar]	Initial MFR [g/s]	Gas temp in the tank at t_0 [C]	Max gas temp at MFM [C]	Min gas temp at MFM [C]	H_2 release duration [s]
1	90	0.5	10	22	708	683	7.3	44	34	-7	450
2	90	0.5	6	19	695	680	7.5	35	29	12	80
3	45	0.5	6	23	357	347	4.0	42	30	5	500
4	45	0.5	6	22	698	678	7.4	45	33	-8	500
5	45	0.5	10	22	690	671	7.3	39	28	-13	500
6	45	0.5	10	19	357	345	4.1	36	26	-2	500
7	45	0.5	6	19	360	349	4.0	38	27	4	500
8	45	1.0	6	15	357	315	13	33	21	-17	500

4.2.2 Results

The maximum values of temperature measured during experiments are presented in Table 19.

Table 19. Experimental results of temperature measurements.

Angle	Tank pressure [bar]	ACH	Under the car (°C)		On the wall (°C)			Under the ceiling (°C)				In the pipe (°C)	Exp nr
			T6	T7	T5	T8	T9	T1	T2	T3	T4	TVENT	
45°	700	10	30	110	30	405	245	200	220	225	230	195	5
		6	47	115	45	390	240	180	200	210	200	175	4
	350	10	30	110	30	270	140	120	-	140	140	120	6
		6	35	120	35	280	150	125	-	145	145	125	7
	350	10	30	225	25	330	535	260	-	325	315	270	8
90°	700	10	490	755	-	-	-	200	220	220	210	190	1
		6	490	270	-	325	160	205	220	205	190	175	2

The analysis of the temperature effect showed that a 45° nozzle direction did not increase the temperature in front of the car. The thermocouple mounted close to the leg of the table (what would be closer than the tires of the car) did not exceed 110 °C.

The highest temperatures were recorded with the highest mass flow of hydrogen. The temperature in the ventilation duct did not exceed 300 °C, but the experiments only burn hydrogen and the effect of a burning car is not included.

The visibility inside the container (12m long) during the experiments was not reduced due to combustion products from the hydrogen fire.

To illustrate the temperature distribution along the wall, Figure 100 shows the temperature at discrete positions of sensors. The figure illustrates 5 different time instances during the experiments. It is clearly visible how the temperature in front of the table/car is quite low, while the high temperature is recorded far behind the table/car. The highest mass flow (1.0 mm nozzle) also gave the highest temperatures.

The experimental data are openly available and accessible at USN Open Data Repository, doi: 10.23642/usn.17695082.

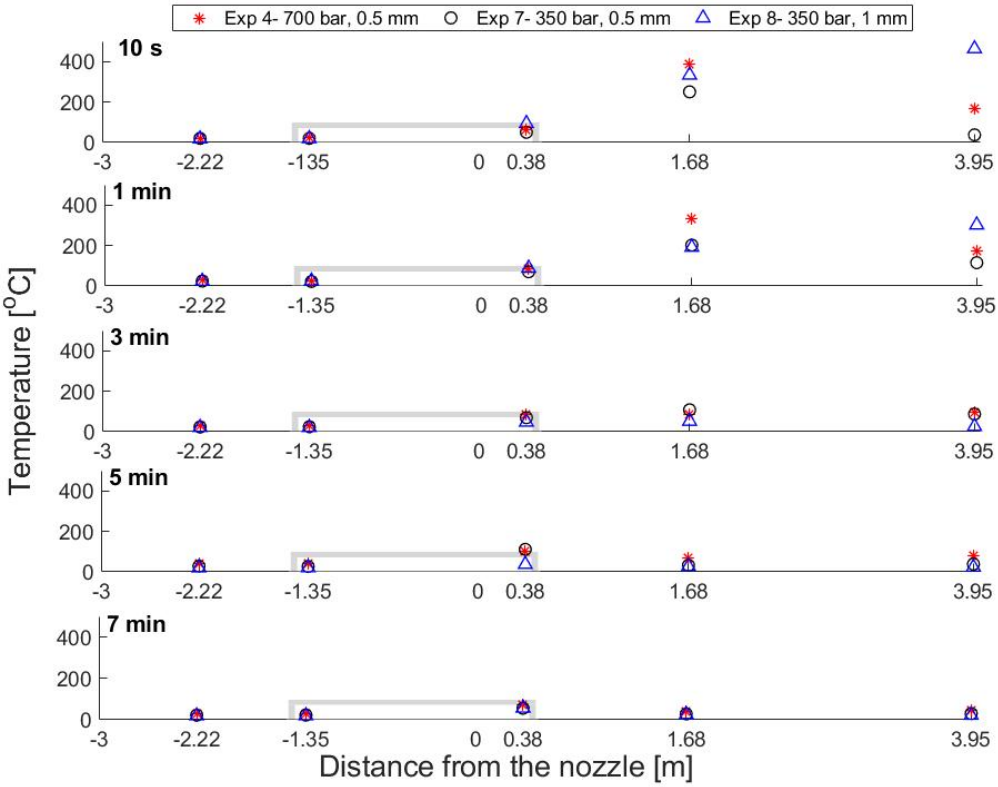

Figure 100. The discrete temperature along the container walls. All with 6 ACH. Red star: 700bar tank pressure and 0.5mm nozzle. Black circle: 350 bar tank pressure and 0.5 mm nozzle. Blue triangle 350 bar tank pressure and 1.0 mm nozzle.

4.3 Effect of hydrogen jet fire on structure integrity and concrete spalling (ST 3.4.3, DTU)

4.3.1 Introduction

A test method for gas flame exposure of concrete wall element surfaces. Wall element specimen are forced into a compression state, prior to the tests, in order to ensure that concretes susceptible for spalling in fact will show continuous spalling

4.3.2 Preliminary tests

Before conducting the hydrogen tests, some tests were made in a standard concrete cylinder test setup (Hertz & Sørensen, 2005), in which a sudden exposure to 1,000 °C for 30 minutes results in a $T_{SURFACE}$=800 °C. During these cylindrical tests, it was found which concretes were not susceptible for spalling (Zaineb, 2020). Next step was to make a preliminary gas burner test. One reason of this preliminary test was to control and adjust the gas burner valve, the balance and the amount of released gas (burning rate). See Figure below.

Figure 101. Preliminary tests of gas burner on a concrete cylinder.

4.3.3 Wall test setup

The setup for the hydrogen exposure tests, consist of a frame made of a top and bottom C-profile and four threaded rods (two in each side). The frame is placed on a platform made of timber. The system is levelled in place and supported by wedges etc. for achieving a stable system. A concrete wall element (specimen) ready for testing is placed in the frame, and adjusted horizontally and vertically to ensure the desired placement in the setup, see

Figure 102. The threaded rods are tightened using a torque wrench. Each steel rod is supplied with two locknuts (one in each end). The applied tension adjusted according to the size of the specimen, for instance the wall thickness, for reaching a desired compression in the concrete.

When the specimen is in place, the gas burner is placed in front of the concrete surface, with the gas burner head at 50 mm distance from the concrete surface. The type and amount of gas (hydrogen, propane etc.), i.e. the burning rate, is selected by the valve according to the test plan. A balance is part of the test setup for measuring the mass loss of gas during the test. In this way, the energy release rate can be calculated. The setup ensures that the gas flame

exposure is made on a concrete specimen of a certain size, compression, representing a small but realistic part of an enclosure or tunnel. The setup includes a data logger for sampling of temperatures via thermocouples (type K). Thermocouples are placed in different distances from the concrete surface, and one on the surface as well.

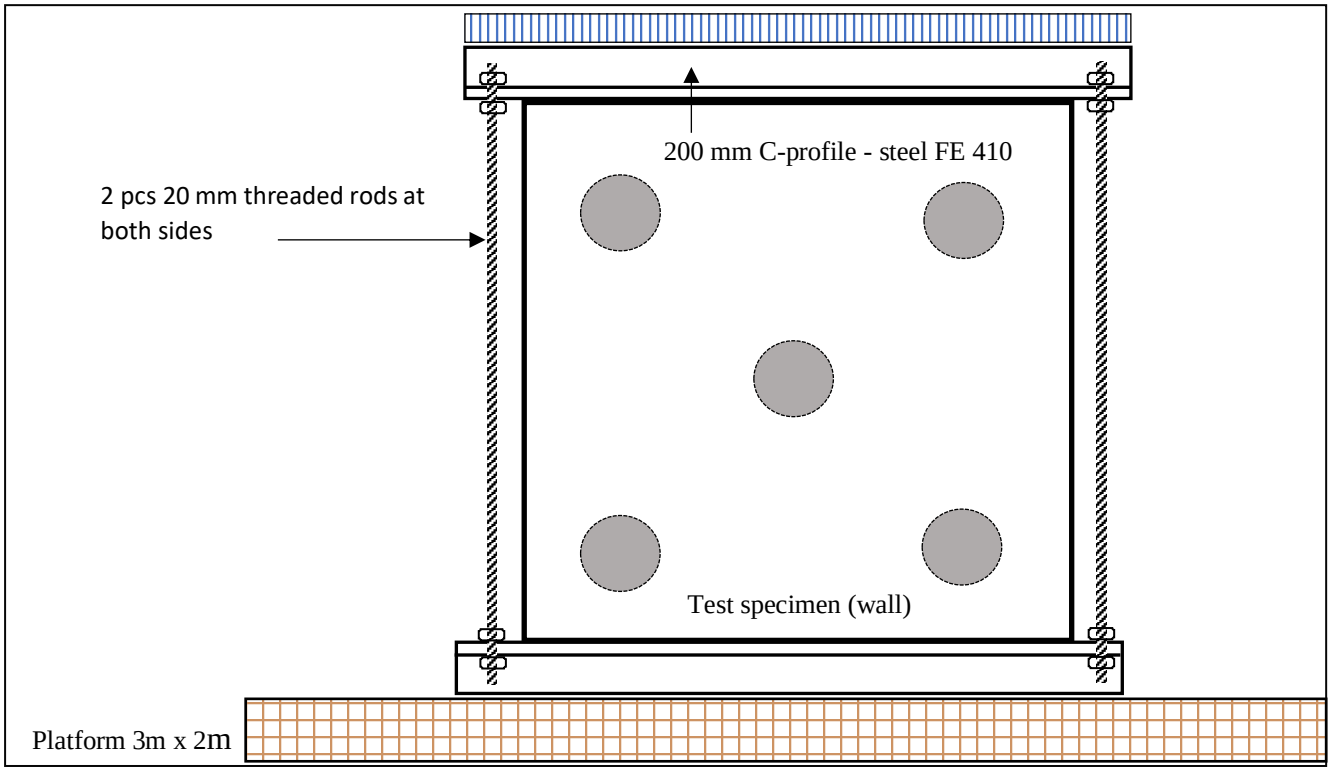

Figure 102. Test setup for tests of concrete wall elements in compression, with propane and hydrogen flame exposure.

4.3.4 Concrete recipes and test specimen

After the initial standard cylinder tests, three types of concretes, all added PP-fibers, were tested as wall elements.

Concrete recipes B, C, D (all including PP-fibers):

B: Dense concrete. Probably not susceptible to spalling, at least when PP-fibers added.

C: Dense + concrete. Could be susceptible to spalling, but the amount of fillers are on a relatively low level, so adding of PP-fibers will probably remove the risk.

D: Dense + high-strength concrete. Experience has shown susceptible to spalling, but reducing of moisture level, and adding of PP-fibers can probably remove the risk.

Table 20. Concrete recipes for testing of spalling.

Concrete	Characteristic	w/c-ratio	Microcilica	Fly ash	Plastizicer	PP-fiber	Aggregates
A	Reference	0.45	0%	0%	0	0%	Sea
B	Dense	0.40	1%	0%	+	0% / 1%	Sea
C	Dense +	0.35	2%	2%	+	0% / 1%	Sea
D	Dense + High strength	0.30	4%	0%	+	0% / 1%	Sea

The percentages in the table are by cement weight.

It is the three concretes with PP-fibers (concrete B, C, D) that is going to be further tested with propane and hydrogen, because none of them showed sign of spalling in the preliminary 1000 ºC exposure on standard cylinder corresponding to a heat flux of approximately 45 kW/m^2.

Curing should be at least 28 days, however longer is better and even more realistic, and we had a curing time of at least 60 days. A water bath (40 ºC) is used for accelerated curing for the previously casted and tested standard cylinders, but not for the current "wall specimen". It is relatively important to reach the same moisture level just before the tests, in order to get comparable results. The compressing should be at least 1.2 MPa, ensuring that the concretes susceptible to explosive spalling in fact *are* spalling continuously. If this compression is released, then it is often seen that the spalling stop. For each of the three test items (wall elements) a number of 4 gas burning exposures were performed, 2 with propane gas and 2 with hydrogen. The propane gas tests are completed, however not yet the hydrogen tests. The concrete elements for tests by exposure of gas are presented below in the figure.

Figure 103. Concrete wall elements for further gas exposure testing. Dim. W x L x T = 1000 x 1000 x 100 mm. Three test items of different concrete recipes (B, C, D) casted for tests. To the right a first test setup.

4.3.5 Spalling tests on concrete wall elements

The tests of the three wall elements presented are not yet finalized. The hydrogen tests are going to be made during February-March 2022. However, the propane gas flame exposure tests on the wall elements are complete.

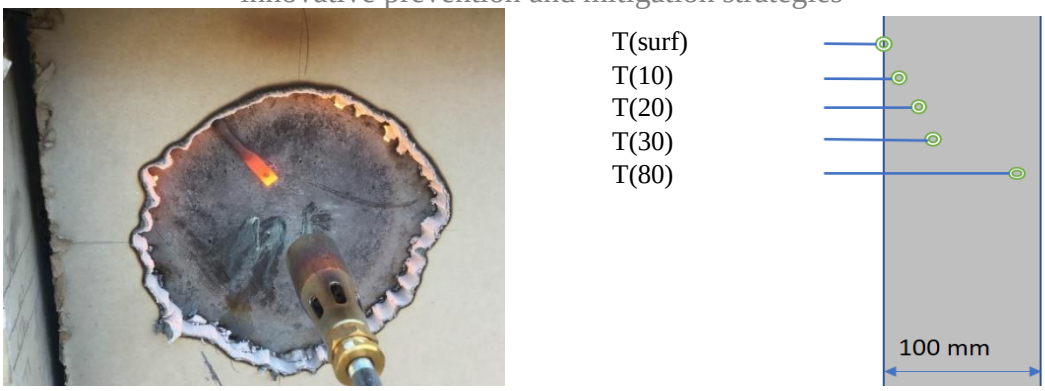

Figure 104. Test with a propane gas burner exposure on Wall Element 1 (WE1), w/c=0.40, concrete B, dense. To the right are shown the placements of the thermocouples.

The temperatures were measured by thermocouples placed at different distances from the concrete surface, see the figure above. The measurements during the tests are presented on the next figures. It is seen that the concrete surface reaches temperatures of 950-1,000 deg. C, whereas the temperature inside the concrete varies, depending on the depth, however with a quite steady temperature increase per time unit. The maximum temperature in 10 mm depth is about 450 deg. C, and that is above the (critical) triple state of water, at which temperature level spalling is often seen for concretes susceptible for spalling.

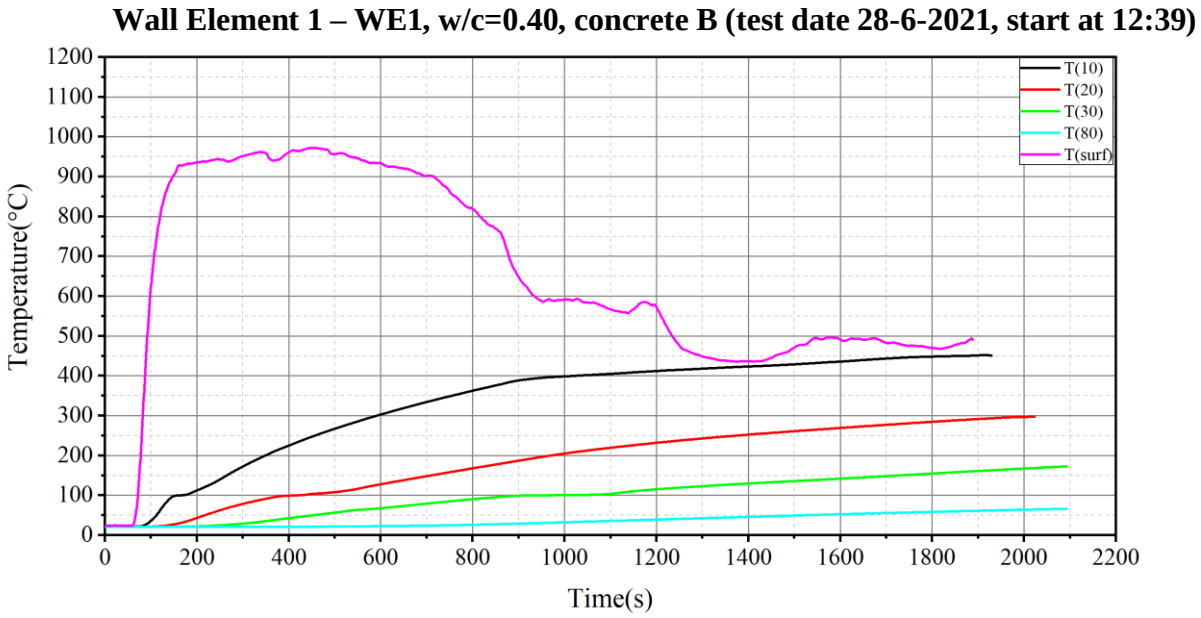

Figure 105. WE1 – Temperature measurements on the concrete surface and in different depths (10 mm, 20mm, 30 mm and 80 mm) of the concrete, during propane gas flame exposure.

Wall Element 2 – WE2, w/c=0.35, concrete C (test date 29-6-2021, start at 11:29)

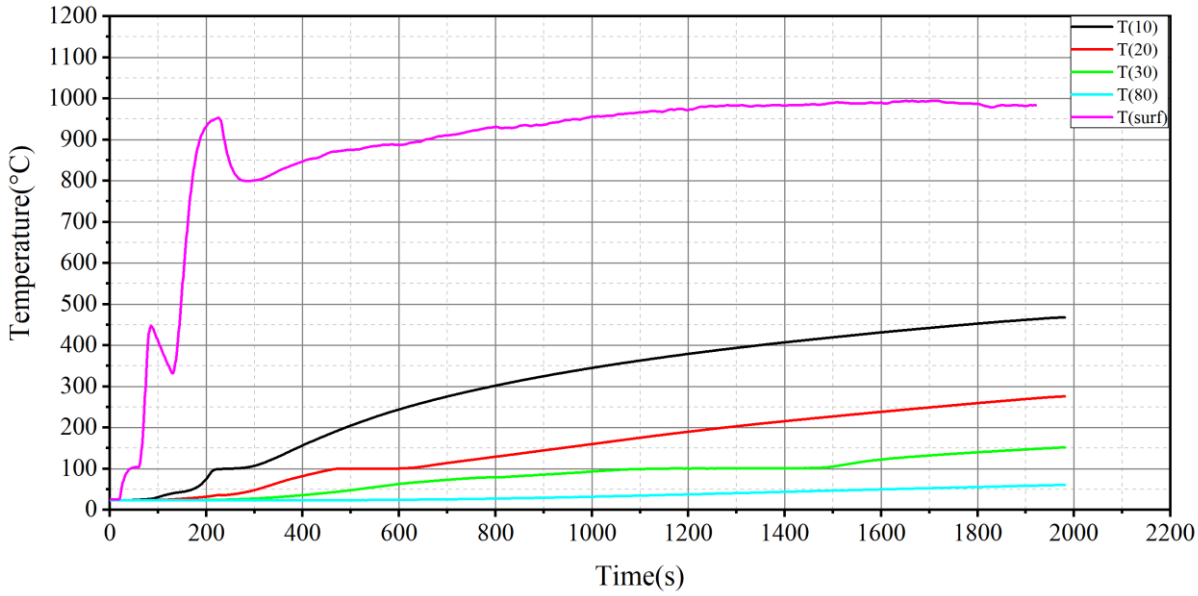

Figure 106. WE2 – Temperature measurements on the concrete surface and in different depths (10 mm, 20mm, 30 mm and 80 mm) of the concrete, during propane gas flame exposure.

Wall Element 2 – WE2, w/c=0.35, concrete C (test date 29-6-2021, start at 13:28)
(failure in some of the data points for T(30))

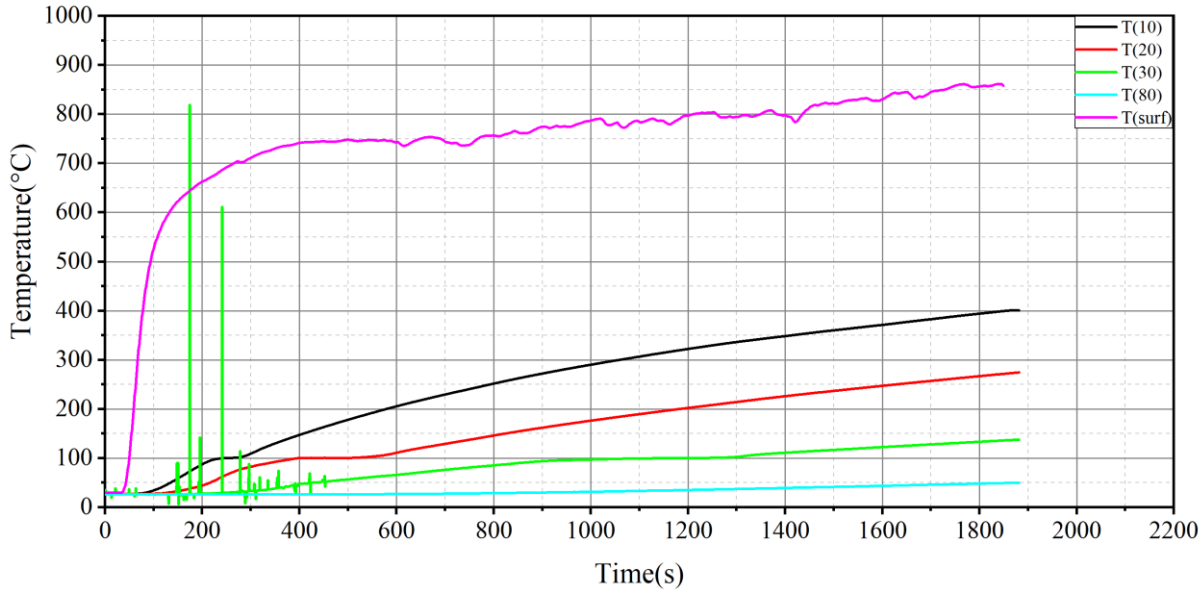

Figure 107. WE2 – Temperature measurements on the concrete surface and in different depths (10 mm, 20mm, 30 mm and 80 mm) of the concrete, during propane gas flame exposure.

Wall Element 3 – WE3, w/c=0.30, concrete D (test date 1-7-2021, start at 11:03)

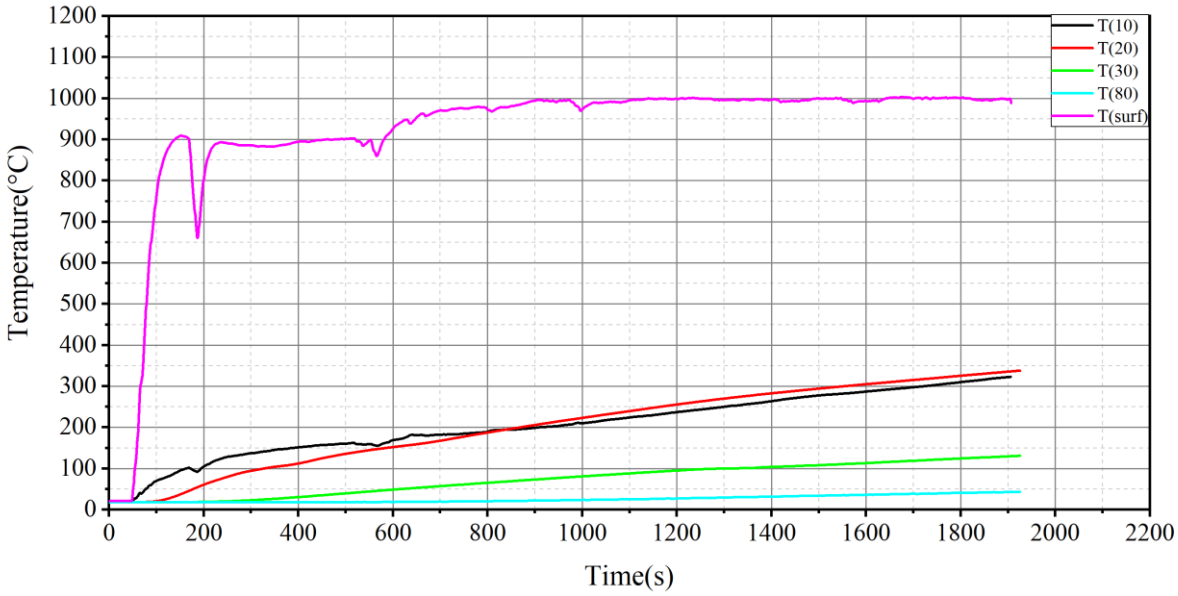

Figure 108. WE3 – Temperature measurements on the concrete surface and in different depths (10 mm, 20mm, 30 mm and 80 mm) of the concrete, during propane gas flame exposure.

Wall Element 3 – WE3, w/c=0.30, concrete D (test date 1-7-2021, start at 12:52)

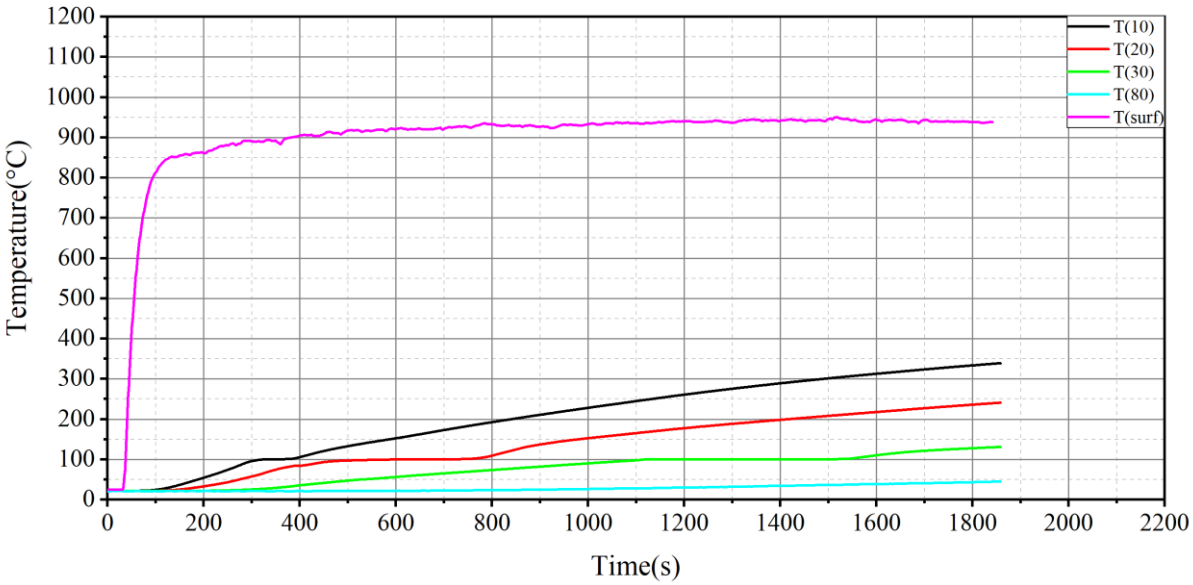

Figure 109. WE3 – Temperature measurements on the concrete surface and in different depths (10 mm, 20mm, 30 mm and 80 mm) of the concrete, during propane gas flame exposure.

Below is a photo of the conducted propane gas exposure test, during and after the test.

Figure 110. Wall 1 w/c=0.40- concrete B – dense. Left: during test with propane. Right: After test.

3.4.3.6 Initial results

Wall Element	w/c (-)	PP-Fibre yes/no	Expo-sure	Gas flow (g/min)	HRR (kW)	Spalling (yes/no)	Cracks
WE1	0.40	yes	Gas flame	16.50	12.65	no	fine cracks
WE2	0.35	Yes	Gas flame	17.75	13.53	no	fine cracks
WE3	0.30	yes	Gas flame	17.60	13,49	(no)*	fine cracks

Figure 111. Tests of wall elements with gas flame exposure. The first results with propane flame tests. No spalling occurred, just some fine cracks.

The above-described reference experiments are made in order to predict more reliable any effects that may arise from hydrogen jet flame impingements. Some additional hydrogen tests in small scale are foreseen in February/March 2022 using an experimental setup provided by USN. The principal setup from these tests is shown in the following Figure 112.

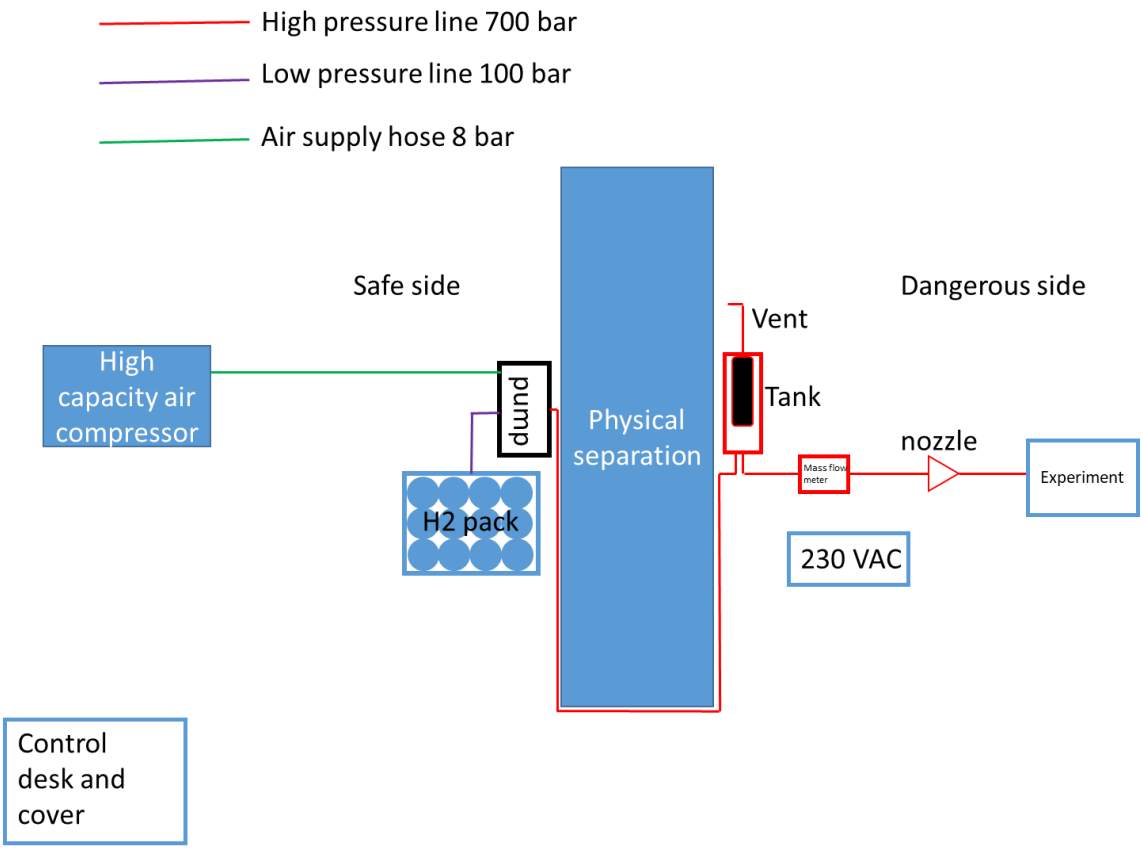

Figure 112. Setup for small scale 700 bar hydrogen spalling experiment.

3.4.3.7 Conclusions

The tests in the first standard cylinder tests (Hertz & Sørensen, 2005) found the types of concrete recipes showing spalling or not. The concretes without spalling went to the next level of tests, which was a propane flame exposure in the test setup. None of these propane gas flame tests showed sign of spalling and therefore all 3 concretes will be further tested with a hydrogen flame exposure, planned in March 2022. Outcomes and conclusions from this set of experiments will be included in HyTunnel-CS D4.4.

4.4 Effect of hydrogen jet fires on the erosion of tunnel road materials and lining materials (ST 3.4.4, HSE)

4.4.1 Introduction

"Most precast concrete tunnel segments these days and for the imminent future are fibre reinforced, with steel fibres for strength and durability and polypropylene for fire resistance" (Herrenknecht, 2020). Over the last few decades, the phenomenon of explosive spalling in concrete has received increasing attention, in particular when looking at dense concrete, e.g. >60MPa, where greater incidences of spalling have been observed (Hertz, 2003).

Explosive spalling of concrete can occur through a number of mechanisms related to the properties and load conditions of the concrete in question (McNamee & Jansson, 2015). Designs of precast concrete tunnel segments typically incorporate a 50 – 100 mm sacrificial layer on the inside of the tunnel, so once explosive spalling is mitigated; fire cannot affect the structural concrete behind (Herrenknecht, 2020).

It is envisaged that hydrogen as a fuel will play an essential role alongside battery technologies in the attempts to decarbonise transport. With the introduction of hydrogen fueled vehicles onto the road network, safety risks specific to hydrogen will need to be considered and ultimately these vehicles should not contribute an additional risk level to that of fossil fuels.

The experimental work in this subtask aims to look at the effect of a hydrogen jet impingement on materials that are representative of those used in tunnel structures. The overall purpose of Sub-Task 3.4.4 is to bring together experience of existing material standards for erosive burning and begin to define elements that could form part of a materials test for protective materials from a representative burning hydrogen jet to feed in to the recommendations for relevant Regulations, Codes, and Standards (RCS). The releases carried out for this subtask aim to mimic those potential releases that could occur in the event of blowdown of a hydrogen fueled vehicle.

4.4.2 Aims of testing

Two aspects are being tested; the first aspect aims to understand the nature of the jet release itself e.g. blowdown characteristics, temperature at various positions along the flame length, magnitude of the pressure at various stages of the blowdown. Temperature measurements in both radial and axial orientations of the jet flame will be carried out as well as pressure monitoring. During these releases, thermal and visible imaging of the flame will be performed.

The second aspect of the test programme aims to investigate the effects of the jet flame impinging on concrete, e.g. spalling, thermal effects, potential structural degradation. Post-test analysis of the sample will be carried out, investigating changes in concrete properties, namely compressive strength, thermal conductivity and pore structure. A real-time measurement will be made for one concrete impingement, where thermocouples are embedded in a sample of concrete at various depths within the sample, to look at the heat transfer through the sample as it is impinged upon by a flame.

4.4.3 Test Methodology

4.4.3.1 *Testing parameters*

Following a review of the characteristics of FCH vehicles and potential accident scenarios that could occur (HyTunnel-CS D1.3, 2019) the experimental parameters of the hydrogen jet fire testing are given in Table 21. The design of the high pressure hydrogen rig (HPHR) at the HSE facility lends itself to simulating jet fires that will result from FCH cars. The test facility can easily achieve the typical fill pressure found in FCH car storage vessels and the pressure vessels have a volume which is comparable to those found in FCH cars. A typical FCH car has a thermal pressure relief device TPRD vent line diameter of 2 mm, therefore this orifice size will be examined. Other HyTunnel sub-tasks in WP 2 and 4 are assessing the effectiveness of reducing the TPRD diameter to 0.5 mm at mitigating other hazards, such as pressure peaking

phenomena (PPP) and the formation of flammable atmospheres in confined spaces. Therefore, an orifice diameter of 0.5 mm will also be examined.

Table 21. Release characteristics.

Parameter	Value	Notes
Vessel Pressure	700 bar	700 bar is maximum fill pressure for storage vessel for a car
Hydrogen mass / Vessel Volume	50 and 100 litre	50 L is approx. size of a single vessel in a car. Typically will have 2 vessel or up to 120 L / 4.5 kg of hydrogen
Release orifice	0.5 mm, 2 mm	Cars currently use a 2 mm orifice, HyTunnel-CS proposal to reduce orifice size to 0.5 mm to mitigate PPP hazard
Flame length, Lf / Sample Stand off	Lf = 1.5 m – 2 m (d = 0.5 mm) Lf = 4.4 m - 6.6 m (d = 2 mm) Stand-off at 0.7 L_f	Correlations give range of flame lengths, Lf Hottest flame temperature at 0.7 L_f for free jet fire Commissioning test to inform sample location
Jet flame width, Wf / Sample Size	Wf ≈ 0.25 m (d = 0.5 mm) Wf ≈ 0.90 m (d = 2 mm)	Correlations relate flame width Wf (at end of flame) to length: Wf = 0.17Lfvis

4.4.4 Material samples

A review of tunnel structural material was undertaken to identify materials that are present in UK and European transportation infrastructure. Due to the limited scope of the test programme, the focus will be on assessing the effect on high strength concrete. Concrete is known to be subject to explosive spalling where the design strength is greater than 60 MPa or greater than 3% moisture content. It has been shown (Shuttleworth, 2001) that the addition of polypropylene (PP) fibres can mitigate the occurrence of spalling.

HyTunnel project partners (DTU and UU) are developing a CFD/FEM model of jet fire and blast effects on tunnel structures. To support this work, the depth and rate of heat transfer to concrete exposed to a jet fire will be assessed. A single test will be performed on a cast concrete slab with embedded thermocouple.

A demonstration test will be undertaken to show the visual effect of a hydrogen jet fire on a road covering material (tarmac). The purpose of this test is to provide visual reference material for first responder education and training, e.g. could highlight a potential indicator as to whether a vehicle's hydrogen storage system is still pressurised and venting, in an accident scenario.

The materials that will be examined are:

1. High strength concrete
2. High strength concrete with PP fibres
3. Tarmac

For this body of research, given the size and weight of precast tunnel segments, it was decided that it would be impractical to acquire a "miscasting" piece as originally intended. Instead, a set of smaller concrete samples were cast as shown in Figure 113; the concrete composition aimed to mimic some of the tunnel lining segment properties (within the limitations of what the concrete supplier could provide) e.g. high strength, presence of polypropylene fibres.

Figure 113. Concrete test samples. Dimensions 800x800x400 mm, high strength concrete.

Project partners at DTU provided a suggested sample composition that included more detailed specifications for these parameters and it was intended to recreate this as closely as possible. Table 22 provides the DTU specification, the actual specification used by HSE and an explanation where a deviation occurred. The samples were cured in open air with no specific weather protection implemented.

The tarmac sample was made using typical road surfacing material i.e. asphalt based with hot cure bitumen and poured into a mould, giving a sample with dimensions 800x800x45 mm, as shown in Figure 114.

Figure 114. Tarmac sample, polymer modified asphalt (PMA).

Table 22. DTU and HSE concrete specification, including explanation for deviations.

	DTU composition **Dense + High strength**	**HSE composition** **High strength**	**Deviations due to manufacturer capability**
Concrete Grade	C85 (85 MPa)	C40/50 (50 MPa)	Unable to cast to C85 strength. To date, 77 day crush test result has sample strength ≈ C70
water/cement (w/c) ratio	0.30	0.45	Unable to achieve lower moisture content
Microsilica	Yes	No	Not licensed to use microsilica
Fly ash	No	No	Ground Granulated Blast-furnace Slag (GGBS) used instead, cement substitute to improve strength and reduce porosity
Plasticiser	Yes	Yes	Water reducing admixture used
PP fibres	Yes	Yes (12 mm)	One sample with and one sample without
Aggregates	Sea (0-16 mm)	Land (0-20 mm)	Sea aggregates not available. Limestone used

As at day 77 of curing, crush tests, see Table 23, gave a compressive strength of 67.5 N/mm^2 for the sample without fibres and 54.8 N/mm^2 for the sample with fibres.

Table 23. 77-day crush test results for concrete samples (a) without and (b) with fibres.

	Lab ref.	Date tested	Age days	Density kg/m^3	Failure load kN	Compressive Strength N/mm^2	Specified strength N/mm^2
HSE test Mix details: 40/50 CEM I Remarks: Degree of saturation uncertain							
	51239778	01/07/2021	77	2470	675	67.5	50.0
HSE test Mix details: 40/50 CEM I Fibres Remarks: Degree of saturation uncertain							
	51239780	01/07/2021	77	2400	548	54.8	50.0

A further strength test will be carried out around the time that the concrete samples are being impinged upon so that the strength at time of testing is known. The samples will not be tested under load conditions i.e. no additional restraint will be placed around the sample

4.4.5 Experimental setup

4.4.5.1 *High Pressure Hydrogen Rig (HPHR)*

The experimental program will be undertaken using the existing High Pressure Hydrogen Rig (HPHR) facility at the HSE Science and Research Centre, as shown in Figure 115. It comprises:

- Two 50 L storage vessels with 1000 bar working pressure which are suitable for hydrogen service and ½" bore pipework.
- A gas booster compressor to charge the vessels from a hydrogen delivery pack pressure of <175 bar up to 1000 bar
- A remote operation, release timing and firing control system to perform, monitor and record test sequence data, including temperatures and pressures within the pipework and vessels during blowdown.

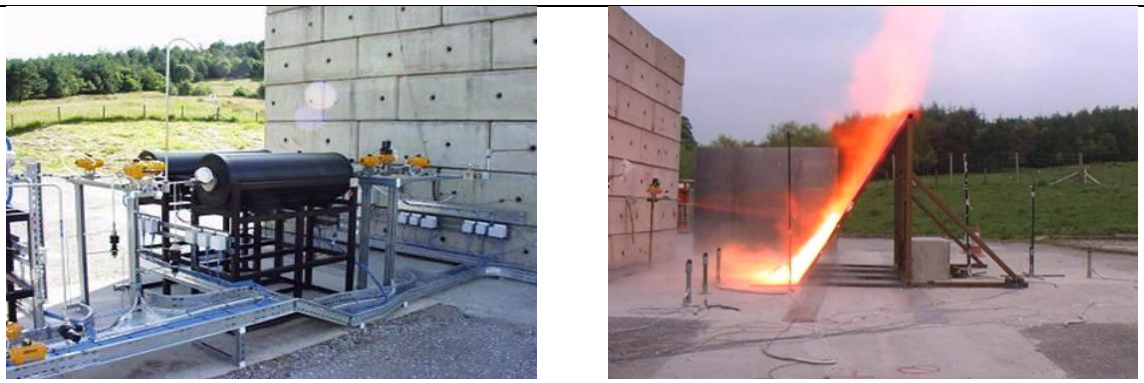

(a) (b)

Figure 115. Pictures of the high pressure hydrogen facility showing (a) the two high pressure vessels and (b) a hydrogen jet fire release from a previous experimental campaign.

A simplified process and information diagram (P&ID) of the release system is shown in Figure 116.

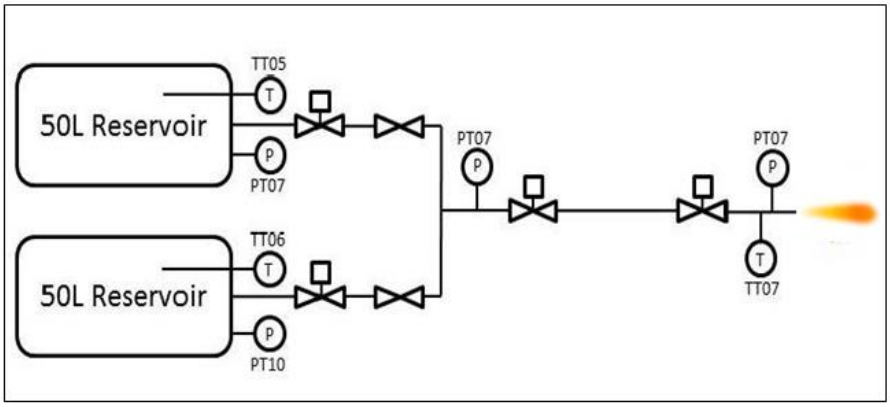

Figure 116. Simplified diagram of release system. PT = pressure transducer, TT = temperature transmitter.

4.4.5.2 *Release conditions*

Two flow conditions will be created; 700 bar through a 2 mm nozzle (actual diameter is 2.1 mm as quoted by manufacturer (manufacturer machined)) and 700 bar through a 0.5 mm nozzle (actual diameter 0.57 mm as measured using a microscope (drilled end cap)). The nozzles will be referred to notionally, as the 2 mm nozzle and 0.5 mm nozzle. These orifices and pressures were calculated to produce flow rates of 0.11 kg/s and 0.007 kg/s hydrogen, for flow conditions/nozzle sizes of 700 bar/2 mm and 700 bar/0.5 mm respectively. The release height was fixed at 1.125 m for all horizontal releases. A section of pipework with a 90° bend will be added for the final release in order to extend and orient the release downwards onto the tarmac sample. The stand-off distance between the nozzle and tarmac surface will be 50 mm, approximately.

A series of release scenarios have been designed, where different parameters will be measured:

- Unimpeded jet release – temperature measurements along free jet;
- Impeded jet release – impinging on temperature sensing plate and subsequently, pressure sensing plate;
- Impeded jet release – impinging on concrete samples

For the impeded jet scenarios, each sample (concrete test piece and sensing plate) will be placed at the same standoff position from the release point, with the chosen distance aiming to achieve maximum flame impingement over the full duration of the release i.e. imparting as much heat as much as possible.

4.4.6 Ignition mechanism

In order to ensure an ignition is consistently achieved without the build-up of a flammable cloud, a propane pilot light (as opposed to a timed pyrotechnic head) will be used. This is positioned close to the release nozzle, beyond the lift off position of the jet. It will be lit prior to the start of each test, remaining lit for the duration of the test.

4.4.7 Measurements

A National Instruments (NI) data acquision (DAQ) system will be used for data logging of the jet release temperature and pressure measurements. Pressure sensors readings will be logged at a sampling rate of 100 Hz using an NI current input module (NI-9203). Thermocouple readings will be logged at a sampling rate of 1 Hz using a dedicated NI thermocouple input module (NI-9213).

The parameters being measured for each release scenarios, as outlined above in 4.4.5.2, are described in more detail in the subsequent sections.

4.4.7.1 *Unimpeded jet release - jet axial temperature*

The first release is a free jet release, i.e. no samples are placed in its path, using the 2 mm nozzle and subsequently the 0.5 mm nozzle. Five type ‘R’ sheathed Pt/Rh thermocouples will be positioned axially along the centreline of the jet, spaced up to a range of 6 m (based on elabs prediction of flame length). An example setup is shown in Figure 117; this data relates to a commissioning test release carried out on 11th November 2021. It is intended to take at least one thermal imaging video and high speed imaging video during the jet release. This will be

taken from a 'side on' view to allow correlation of visualised flame evolution with thermocouple measurements.

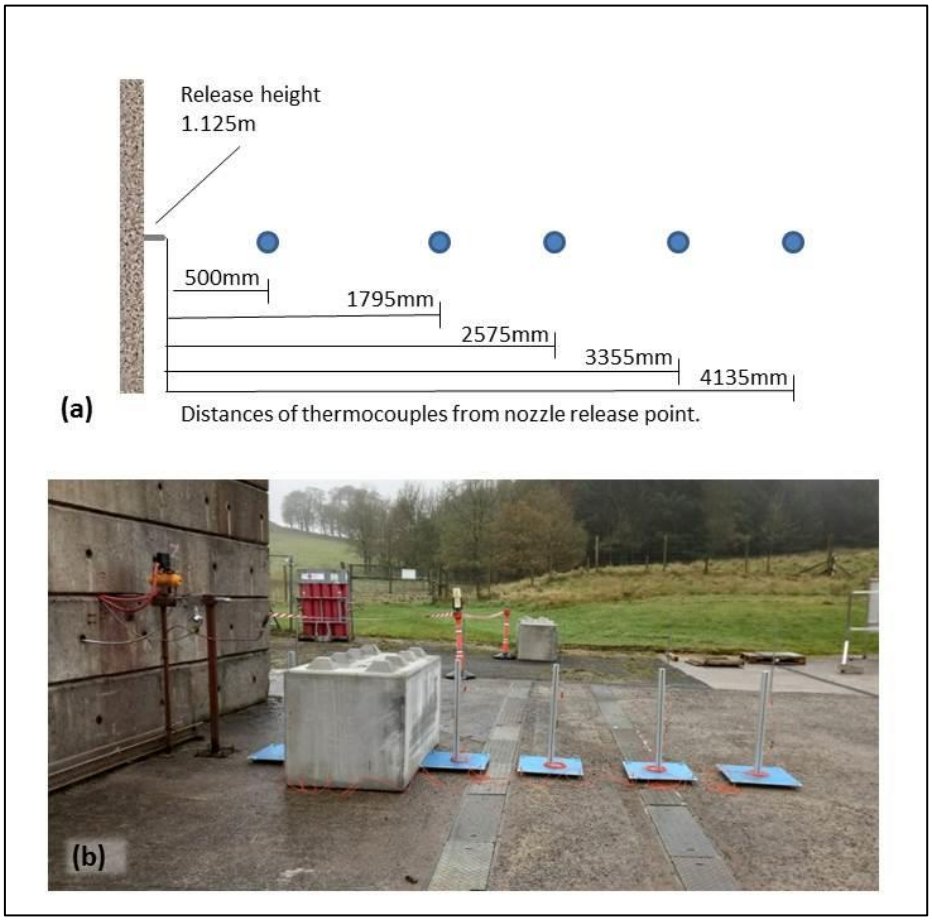

Figure 117. Commissioning test setup - Free jet release using 2 mm nozzle (a) diagram outlining position of thermocouples relative to the release point and (b) photograph of thermocouple setup.

4.4.7.2 *Impeded jet release – sensor plates*

As the release is not steady state (because the vessels have a finite volume) the pressure and temperature at any given location of the jet will change over the course of the release.

In order to understand the pressure and temperature distribution across the incident surface of the concrete samples as the jet blows down, two sensing plates have been fabricated, with the same incident surface dimensions as the concrete sample, i.e. 800x800 mm. One contains a spaced cross array of pressure sensors and the other contains the same spaced cross array of thermocouples. The spacing of the sensors on the plates aims to capture as much information across the span of the evolving jet flame, e.g. from a possible 0.7 m width flame at initial release at 700 bar, to the reducing span as the jet blows down e.g. a flame width of 0.35 m approx. at 30 bar.

A stainless steel stand has been built, onto which the two sensing plates can be bolted such that their positioning mimics that of the "interlocked" concrete test sample, as shown in Figure 118.

Figure 118. (a) Stainless steel stand for sensing plates and (b) example of a plate in-situ.

4.4.7.3 *Temperature sensing plate*

The temperature plate consists of an 8 mm thick, 800 x 800 mm, stainless steel plate. There is a centred 'cross' array of nine 1.5 mm diameter tapped holes, equispaced on a 400 mm cross, to which eight type 'N' thermocouples and one (centred) type 'R' thermocouple are potted to. The plate has been constructed from 304L standard dull finish stainless steel (emissivity ≈ 0.85). Whilst this plate is in situ, the thermal imaging camera will be mounted at a distance behind, to attempt to obtain a heat map of the plate during the release. The final standoff distance of the plate will be decided based on the initial free jet measurements made.

4.4.7.4 *Pressure sensing plate*

The pressure sensing plate consists of an 8 mm thick, 800 x 800 mm 304L, mill finish stainless steel plate as shown in Figure 119. There is a centred 'cross' array of nine 3 mm diameter tapped holes, equispaced on 400 mm cross, to which are attached stainless steel tubes, length 500 mm with inner diameter of 12.05 mm or sensing lines of 3 mm internal diameter, each terminated by an Omega PXM309-001AI 4-20mA pressure transducer. If required, the sensing lines can be cooled or temperature maintained by use of a water jacket surrounding the tubes.

Figure 119. Pressure sensing plate (a) front view with equispaced 3 mm diameter tapped holes and (b) rear view with water jacket and threaded sockets for pressure sensor attachment.

4.4.7.5 *Impeded jet release – concrete test sample*

The concrete samples were cast using commercially available "interlocking concrete block" moulds, with dividers put in the mould during casting to achieve test samples of dimension 400x800x800 mm. For the purpose of the test, these smaller test samples will be placed onto a larger, original size base block (typical dimensions of 1600x800x800 mm) see Figure 119, interlocking with it so as to secure in place.

The tests are described in more detail in the subsections below.

4.4.7.6 *Concrete test sample – post-test analysis*

It is intended to subject one of each concrete sample, i.e. one with PP fibres and one without, to a full jet blowdown from 700 bar at a standoff distance as determined by the measurements from the sensing plates. Once each blowdown test is completed, a visual assessment of the incident surface will be made. If there is visible damage on the incident surface, the sample will be 3D laser scanned to provide more detailed information as to the depth and extent of the damage. Cores (150 mm diameter) will then be extracted from both the impinged upon samples and the two un-impinged samples and all will be sent away where the same analysis will be carried out on both sets of samples.

Three measurements will be made on the cores using the methods as listed below:

- Compressive strength – crush test carried out according to BS EN 12390 standard - Testing hardened concrete.

- Thermal conductivity – The cores will be cut to a depth of 45 mm and a thermal resistance measurement made as per BS EN12664 standard – testing thermal resistance using guarded hot plate method.
- Ultrasonic testing – A pulse velocity measurement will be made of each core in order to investigate presence of cracks or voids, changes in uniformity of the concrete. The test will be carried out according to BS EN 1504 standard – determination of ultrasonic pulse velocity.

4.4.7.7 *Concrete test sample – real-time heat transfer measurements*

Given the depth of the concrete samples i.e. 400 mm, it would not have been possible to drill 1.5 mm diameter holes i.e. the thermocouple diameter, to this kind of depth in order to embed thermocouples. Larger drill bits would be required to achieve that depth and it was felt that the action of drilling holes with these larger diameters into the test samples may influence how the sample behaves from a thermal expansion point of view e.g. the presence of the holes and the potting material required to fill the holes around each thermocouple may provide a channel for pressure relief and thus the result may not be indicative of the normal behaviour of the concrete. In order to achieve some real time indication of the heat transfer through the concrete samples, it is intended to cut one of the extracted cores (from an unimpinged sample) to a shallower depth (40 mm approx.). The smaller 1.5 mm drill bits can then be used to drill five holes to a series of depths (between 0-25 mm from incident surface), and radial positions relative to the centre of the release. Once drilled, seven type 'N' thermocouples will be inserted into these holes and the core placed back into the centre hole of the original test sample. This core will be subject to a 700 bar blowdown from a 2 mm nozzle at the same standoff distance as the original samples and the heat transfer through the sample measured.

Summary of test matrix in Table 24 (overleaf) summarises the series of intended measurements.

Table 24. Experimental tests matrix.

Test ID	Notes	Conditions			Measurement	Post Test
		Volume (L)	Orifice size (mm)	Sample stand-off (m)		
1	Free Jet	50	2	n/a	Axial Temperature High speed camera VIS/IR camera	
2	Free Jet	50	0.5	n/a	Axial Temperature High speed camera VIS/IR camera	
3	Impinging Temperature Plate	50	2	1.5 (tbc)	Radial Temperature End on VIS/IR camera (heat map)	
4	Impinging Pressure Plate	50	2	1.5 (tbc)	Radial Pressure Side on VIS/IR camera (visualisation)	
5	Impinging Pressure Plate	50	0.5	1.5 (tbc)	Impingement Pressure	
6	High strength concrete	100	2	1.5 (tbc)	3D laser scan (visual assessment)	Materials analysis
7	High strength concrete with PP fibres	100	2	1.5 (tbc)	3D laser scan (visual assessment)	Materials analysis
8	High strength concrete (no impingement)	n/a	n/a	n/a	For comparison with impinged concrete samples	Materials analysis
9	High strength concrete with PP fibres (no impingement)	n/a	n/a	n/a	For comparison with impinged concrete samples	Materials analysis
10	Reinstated concrete core with thermocouples	100	2	tbc	Heat transfer through sample	
11	Reinstated concrete core with thermocouples	100	0.5	tbc	Heat transfer through sample	
12	Tarmac	50	tbc	tbc	Video	

4.4.8 Results (commissioning trial only)

4.4.8.1 *Unimpeded jet release – jet axial temperature*

The data shown in Figure 120 relates to a commissioning test carried out on 11th November 2021. The test parameters were as follows; 700 bar, 2 mm nozzle, one 50 L vessel. Five type 'R' thermocouples were positioned along the axial length of the unimpeded jet release, at a height of 1.125 m, spaced as outlined in Figure 117 and centred in the flame.

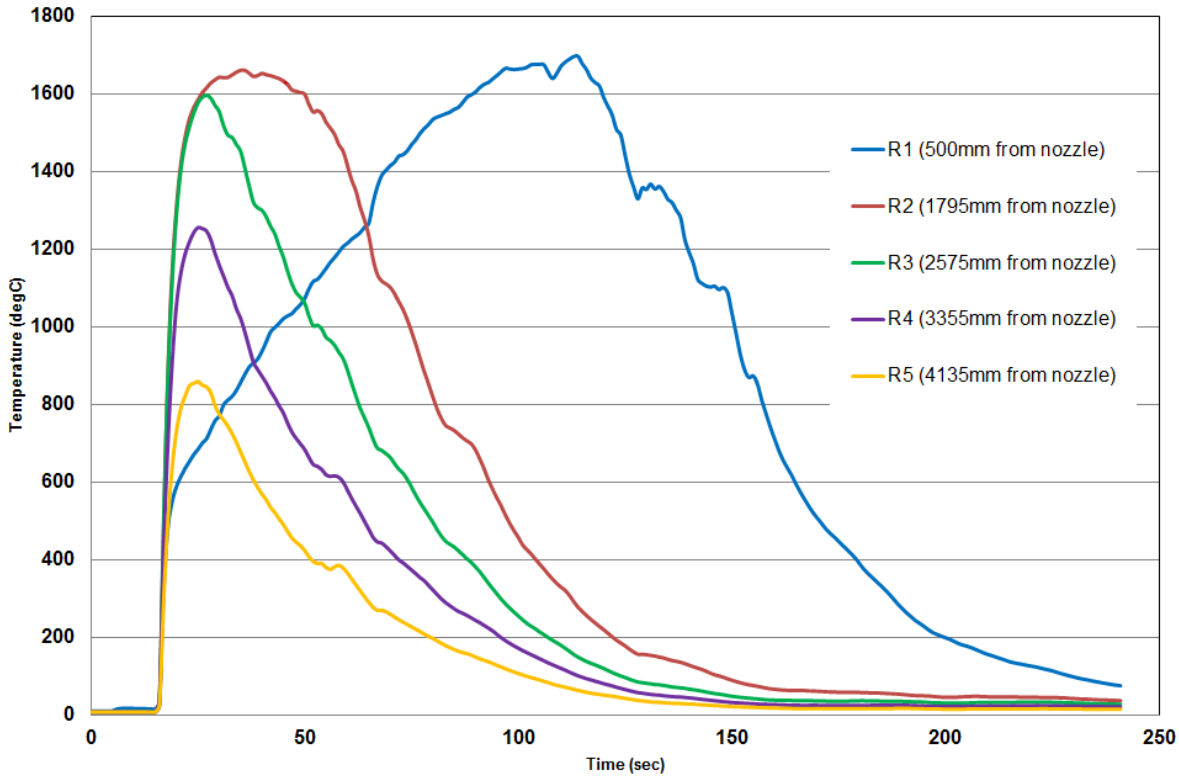

Figure 120. 700 bar blowdown, 50 L volume, 2 mm nozzle ignited release. Type 'R' thermocouple measurements along the axial direction of the jet.

R1 represents the thermocouple closest to the nozzle/release point. From the results shown in Figure 120, it can be seen that R1 does not reach higher temperatures until almost 100 seconds into the release. It is expected that this is the case, as, at the beginning of the release, R1 is in a fuel-rich portion of the higher pressure jet and thus, does not experience a stoichiometric mix.

4.4.9 Impeded jet release – sensor plates

4.4.9.1 *Temperature sensing plate*

No commissioning tests have been carried out with this plate to date. The data output is expected to show the evolution of the temperature on the incident surface of the plate across a 400 mm span in horizontal and vertical direction.

It is proposed to calculate the heat flux by relating the temperature measurements with the emissivity of the plate material.

4.4.9.2 *Pressure sensing plate*

No commissioning tests have been carried out with this plate to date. The data output is expected to show the evolution of the pressure on the incident surface of the plate across a 400 mm span in horizontal and vertical direction.

4.4.9.3 *Impeded jet release – concrete test samples*

No tests will be carried out on these samples until the jet releases listed above have been completed. Data from these tests will be used to inform on standoff distance for the concrete samples.

4.4.9.4 *Impeded jet release – Tarmac sample*

As this test requires modification of the pipework, it is intended to carry it out as the last test. It is intended to include stills from the high speed visible camera in the report, with the full video being uploaded to the consortium repository.

4.4.10 Discussion and conclusions

Typical methods for fire testing in concrete apply heating over a defined time period and temperature range (Asadi et al., 2018; Hertz & Sørensen, 2005; Rijkswaterstaat & Efectis Nederland, 2020), for example, selecting an ISO fire curve that supplies a specific heating regime. Testing in the past has aimed to identify the properties of the concrete that could be attributed as the cause for spalling. It has been found that a multitude of factors can influence whether spalling will occur, e.g. larger samples with the same concrete composition as smaller samples were found to be more likely to spall due to the added load generated by the sample bulk itself (Mcnamee & Jansson, 2015).

It is intended to correlate the temperature and pressure measurements at the incident surface of the sensing plates with the post-test material analysis of the concrete samples. The three material tests i.e. compressive strength, thermal resistance (calculate thermal conductivity from this measurement) and pulse velocity measurement (to investigate uniformity of concrete and presence of cracks) are standard methods within the building industry and it is hoped that the results from these tests may offer some insight as to whether these test methods provide a useful means of investigating erosive damage as a result of hydrogen jet impingement.

Unfortunately, due to a hydrogen shortage (attempts have been made since June 2021 to secure a hydrogen supply from a number of suppliers), the test programme has been delayed. The supply of hydrogen has been received in January 2022, and the experimental campaign is on-going. Results will be included in deliverable HyTunnel-CS D4.4.

4.5 Effect of hydrogen combustion from TPRD on vehicle fire dynamics in tunnel (ST 3.4.5, CEA)

4.5.1 Introduction

Hydrogen Fuel Cell Electric Vehicles (HFC EVs) represent an alternative to replace current internal combustion engine vehicles. The use of these vehicles with storage of compressed gaseous hydrogen (CGH2) or cryogenic liquid hydrogen (LH2) in confined spaces, such as tunnels, underground car parks, etc., creates new challenges to ensure the protection of people and property and to keep the risk at an acceptable level. Several studies have shown that confinement or congestion can lead to severe accidental consequences compared to accidents in an open atmosphere. It is therefore necessary to develop validated hazard and risk assessment tools for the behavior of hydrogen in tunnels. The HyTunnel-CS project sponsored by the FCH-JU pursues this objective. Among the experiments carried out in support of the validation, the CEA has conducted tests on Jet-Fire and Fire/Jet-Fire interaction in a full-scale tunnel geometry.

The tests were organized in two phases. The first one in October 2020 in which type II hydrogen cylinders under 200 bar were used. The second in June 2021 in which type IV tanks of 78 liters under 700 bar were used as a source of compressed gas. In these tests, in addition to the effect of the internal pressure, the effect of the diameter of the release and its orientation was studied on the jet-fire geometry, hot gases cloud transport and radiated heat fluxes in the tunnel. Additionally, effect of the presence of nearby car-fire was also investigated by the use of a propane burner.

It should be noted that for CEA tests (2021), the following definition for TPRD applies: the expression **TPRD** correspond to a manufactured TPRD with a passage aperture as a calibrated orifice and not to a commercial TPRD mounted in the hydrogen vehicle.

The relevant information regarding the test geometry, the detail of injection, the type of sensors as well as their locations are provided in some separate documents:

- For pre-tests of 2020: Sauzedde et al. (2020)
- For the tests 2021: Sauzedde et al. (2021a) and Sauzedde et al. (2021b)

The section is organized as follows. In a first paragraph, the geometry used for the test is briefly described. Then, the different phases of the test and the test matrix are detailed. Finally, the results are provided for the behavior of the jet-fire. A final section summarizes results on blowdown characterization, fully described in (Sauzedde et al., 2021b), followed by conclusions and recommendations.

4.5.2 Test geometry

The relevant information regarding the test geometry, the type of sensors as well as their locations are provided in a separate document (Sauzedde et al., 2020). A schematic description of the test arrangement is provided in Figure 121. The first configuration (a) corresponds to jet-fire tests while the second (b) describes the interaction between a car fire and the same jet-fire. The tests were performed in the tunnel du Mortier (near Autrans village, Isère, France). This disused road tunnel is a horse-shoe type geometry with a total length of about 502 m. The slope is 3.6% and the tunnel is divided in two different sections. The one located on the Autrans side

is made of a flat concrete ceiling arch and the second one on the Montaud side is raw limestone rocks. The injection device was installed in this second section for the 2021 tests whereas for the 2020 tests it was located in the concrete section.

The tunnel dimensions vary in the rocky section, an average height is close to 5.9 m, and the diameter is about 8.9 m. Two sidewalks are also present on each side of the road. The chassis representing a real car is parallel to the road. The calibrated orifice representing the thermally activated relief device (TPRD) of a real compressed gaseous hydrogen storage is located at the rear of the chassis and it can be oriented upward (UP), downward (DW) with two angles (90° and 45° to the rear). The angles are counted from the chassis which means that 90° does not correspond to the vertical because of the slope of the tunnel.

The monitoring system can be divided into two parts:

- The one related to the injection tank and the release pipes. Relative pressures and gas temperature were recorded inside the tank (P_0, T_0), at the outlet of the tank (P_1, T_1) and upstream the calibrated orifice (P_2, P_{2bis} and T_2). These are used to check the mass balance and compute the release flowrate.

- The one related to the tunnel. 10 vertical masts were used to support the main measuring devices in the upper part of the tunnel. Additional supporting structures were installed around the chassis on the lower part to monitor the radiated heat fluxes (Fx). These sensors are mainly hydrogen concentration measurement (Xe and He catharometers) and thermocouples (Tk). Oxygen concentration sensors (Ox) and CO_2 sensors (CO2) were also installed to study possible depletion of oxidizer and production of CO_2 by the propane burner. Ultrasonic wind sensors monitored the convection flow in the tunnel during the tests.

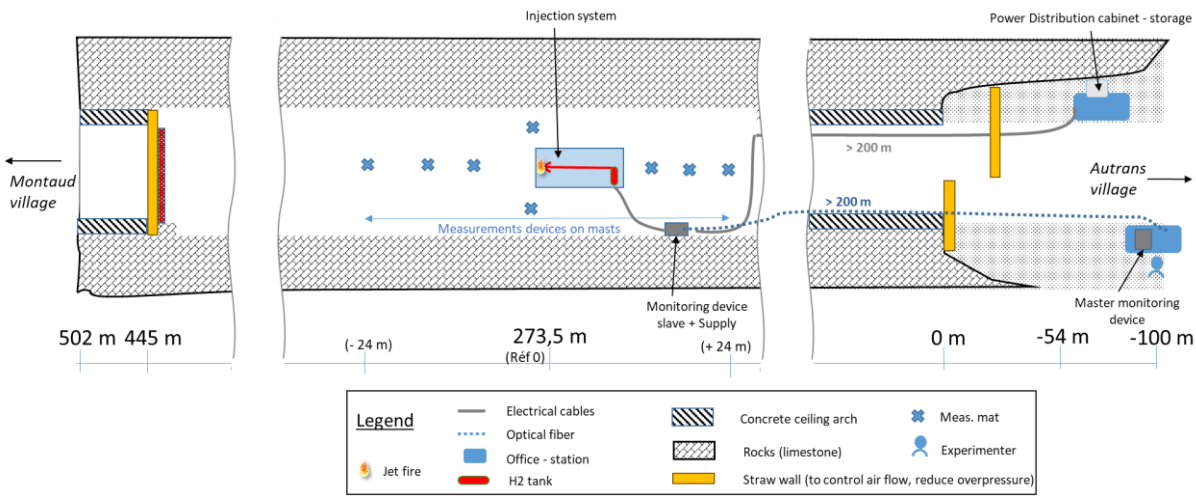

a)

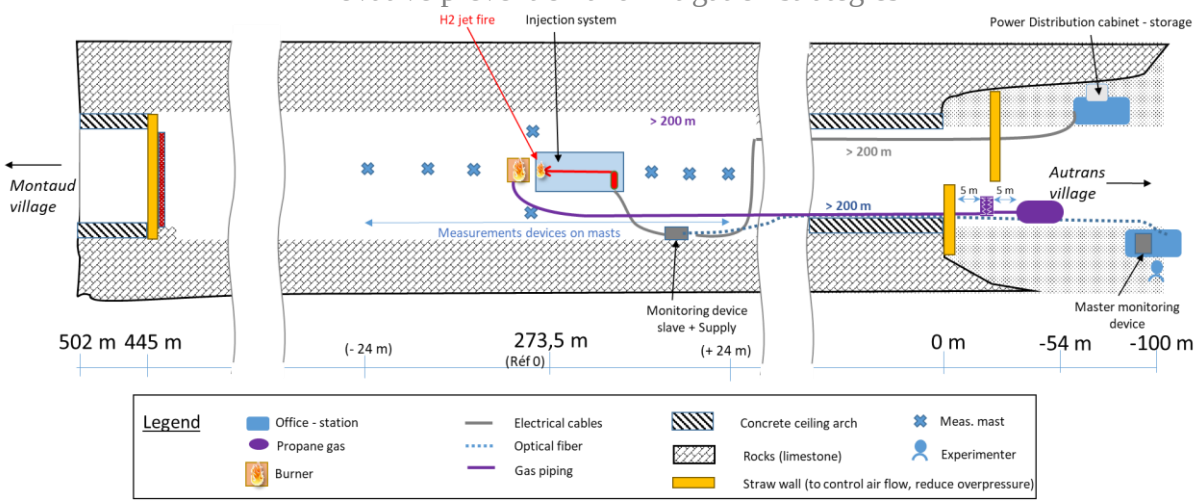

b)

Figure 121. General sketch of the 2021 jet/fire and fire/jet-fire interaction tests.

In the 2020 tests, a structure was placed facing the TPRD injection, where eight radiation heat flux sensors were installed.

Figure 122. 2020 test series: supporting structure for the 8 Heat flux sensors.

Table 25. Position of the 2020 Radiated heat flux sensors (0, 0, 0) corresponds to the TPRD exit in the upward position.

Sensor	x (mm)	y (mm)	z (mm)	Distance (mm) to a fictitious point located 2 m above TPRD
Fx1	-662	-784	1211	1294
Fx2	-852	-1029	1498	1427
Fx3	-1080	-1366	1862	1747
Fx4	-1290	-1496	2140	1980
Fx5	-1437	-1720	2347	2268
Fx6	-1631	-19760	2613	2634
Fx7	-1877	-2147	2843	2974
Fx8	-2093	-2440	3148	3414

In the 2021 test series, Captec Radiative heat flux sensors were installed during the jet-fire and the burner tests. Four of them are arranged on a structure (Figure 123 left) to look at the vertical jet-fire. The other four are arranged on single vertical masts (Figure 123 right) and can be moved from tests to tests depending on the fire location. The chosen locations are provided in Table 26 and Table 27.

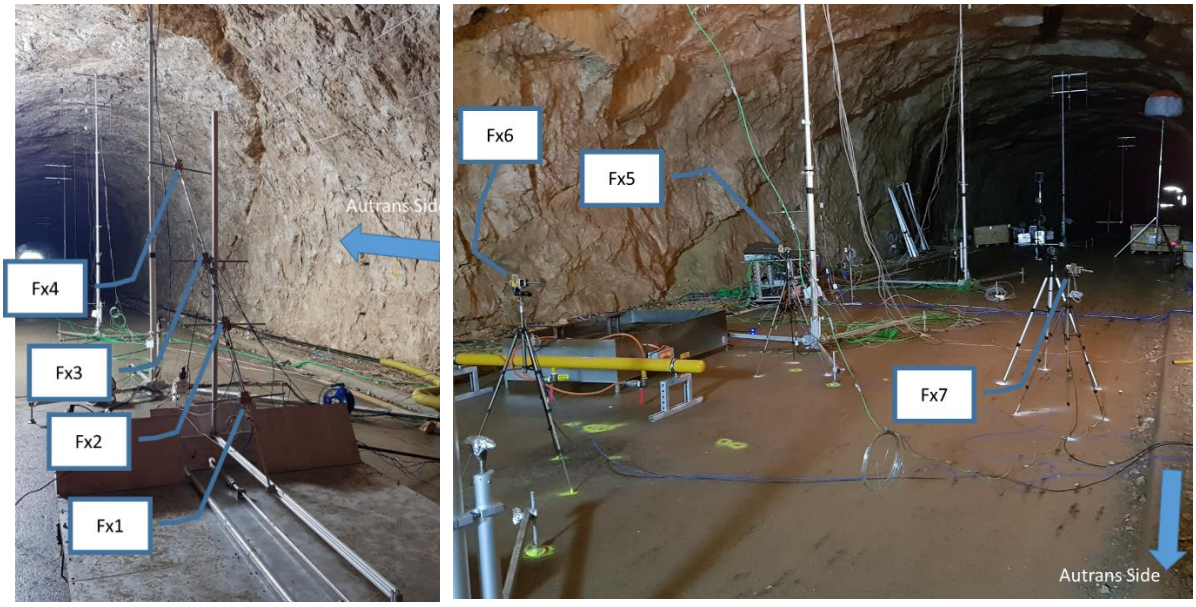

Figure 123. 2021 test series: Radiative heat flux sensors: Left – structure with 4 staggered sensors, Right – Example of single sensors arrangement (tests 08 to 010).

Table 26. 2021 test series: Radiated Heat Flux sensors positions.

Sensor	X (mm)	Y (mm)	Z (mm)	Test
Fx1	0	2600	535	All
Fx2	0	3100	895	All
Fx3	0	3600	1270	All
Fx4	0	4600	1944	All
Fx5	0	-5000	775	Test 08, 09, 010
	2000	-5000	775	Test 012 and 013 facing at a point located on the ground at (0.0, -2000, -315) Test 014 to 016 facing horizontally at the TPRD
	2000	2000	775	Test 018 facing at the impingement point of the TPRD on the ground
Fx6	0	-2000	780	Test 08, 09, 010
	2500	-2000	780	Test 012 and 013 facing at a point located on the ground at (0.0, -2000, -315) (Fx6 has been replaced by Fx9 after test 012 due to internal damage)
	2100	-2000	780	Test 014 to 016 pointed horizontally at (0,-2000,780)
	2100	0	780	Test 018 pointed horizontally at (0,0,780)
Fx7	2500	-4000	775	Test 08, 09, 010
	2000	-5000	775	Test 012 and 013 facing at a point located at (0.0, -2000, 775)
	2250	-4500	775	Test 014 to 016 pointed horizontally at the TPRD
	2000	-4000	775	Test 018 pointed horizontally at the TPRD
Fx8	2700	3000	785	Test 08, 09, 010
	2500	-2000	785	Test 012 facing at a point located at (0.0, -2000, 775) – damaged after test 012

Table 27. 2021 test series: Radiated Heat Flux sensors positions for the tests 09 and 010.

Sensor	x (mm)	y (mm)	z (mm)	Distance (mm) to a fictitious point located 2 m above TPRD
Fx1	0	2600	535	2984
Fx2	0	3100	895	3291
Fx3	0	3600	1270	3673
Fx4	0	4600	1944	4600
Fx5	0	-5000	775	5148
Fx6	0	-2000	780	2343
Fx7	2500	-4000	775	4873
Fx8	2700	3000	785	4215

4.5.3 Description of the burner

The propane burner was designed according to the principles described in Figure 124-left. It consists of two zones to simulate a localized and an engulfing fire.

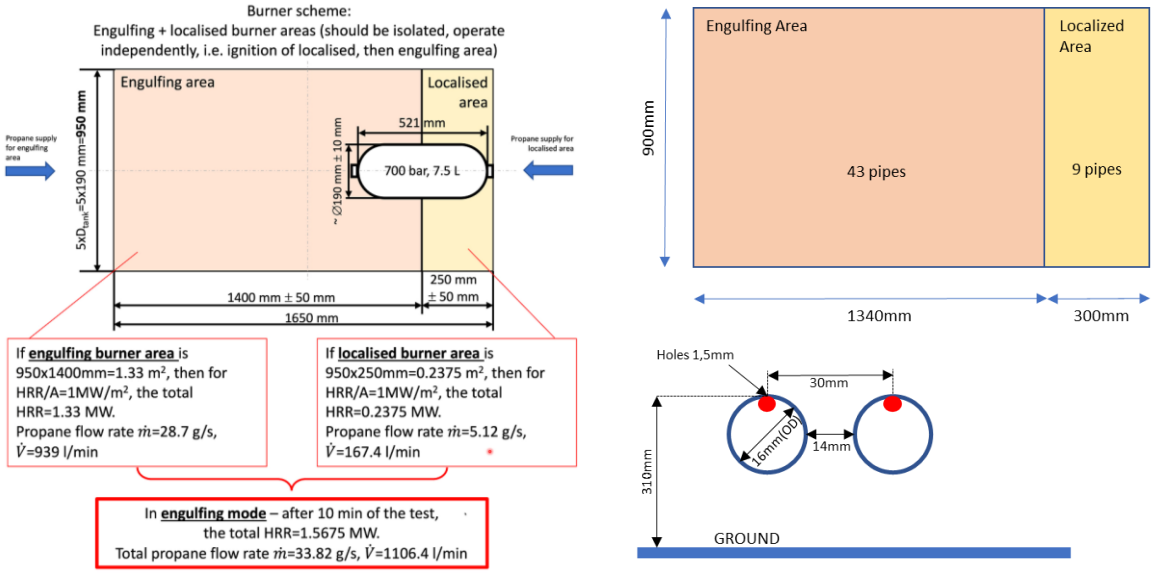

Figure 124. Schematic description of the propane burner.

The picture of the burner before the tests is provided in Figure 125.

Figure 125. Picture of the propane burner before the tests.

The dimensions of the ramps are:

- For the localized fire 300x900 mm with 9 pipes;
- For the engulfing fire 1340x900 mm with 43 pipes.

Figure 126. Picture of the two zones: left – engulfing area, right – localized area.

The pipes have an outer diameter (O.D.) of 16 mm and a thickness of 1 mm. They are made of stainless steel 304L. The spacing between pipes is 30 mm and the upper holes have a diameter of 1.5 mm and are located every 30 mm. A single tube of 21.3 mm O.D. and 1.3 mm thickness feeds each burner. The ramps are installed in a box (353 mm height for the surrounding plate and 80 mm for the 4 supporting tubes located at the four corners) and located 310 mm above the floor. The burner is fed by a propane tank with liquid extraction and evaporators. The propane flow rate during the operation of the different parts of the burner (localized, engulfing and localized+engulfing) was measured during qualification tests at different pressure levels at the supply (evaporator outlet) and with the same piping. The flow meter then failed and we do not have the time monitoring of the flow during the performed tests. However, an operator was in charge of checking the adjustment of the supply pressure during the tests to guarantee the desired flow rate to achieve a heat release rate (HRR) close to 1 MW/m². Ulster University has provided two propane mass flowrates to satisfy the requested HRR: 4.2 g/s for the localized fire and 23.4 g/s for the engulfing fire. For the interaction tests, the two sections of the burner were ignited at the maximum flowrate.

The position of the burner in the tunnel is depicted in Figure 127.

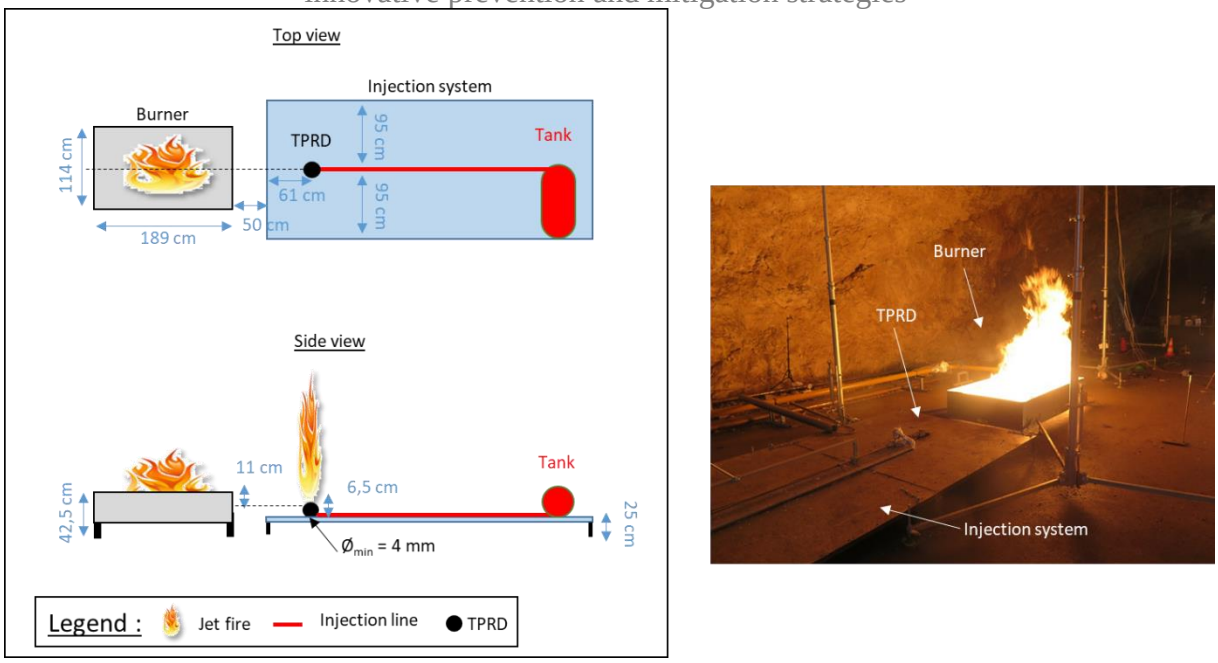

Figure 127. Position of the burner in the tunnel.

4.5.4 Test sequence and test matrix

For both test series, the test sequence is divided into several steps:

- Step 1: connection of the tank to the injection system, opening of the main tank valve to pressurize the pipe between the tank and the solenoid valve, control a leakage;
- Step 2: ignition of the pilot flame used to ignite the jet-fire;
- Step 3: ignition of the burner (if required) for several minutes;
- Step 4: opening of the solenoid valve of the tank to release hydrogen;
- Step 5: closure of the solenoid valve and continuation of the measurements.

Time zero has been set to the beginning of Step 4.

A jet fire from a TPRD initiation in a confined space may have a twofold effect on a vehicle fire consequences. The hydrogen jet fire may significantly increase the heat release rate. And, the water vapour produced by H_2-air combustion or the oxidizer depletion may counteract as an extinguisher of the fire. The interaction tests are conducted with these objectives.

The two tests' matrices are given in Table 28.

Table 28. Jet-fire and Fire/Jet-fire interaction test matrix.

Type of test	Nb of test	Volume (liter)	Pressure (bar)	Configuration	Ø TPRD (mm)	Test number
H2 jet fire (2021)	5	50 type II	200	UP	2	n°09
		78 Type IV	600 to 700	UP	2	n°10
				DW 45°	2	n°12
				DW 45°	1	n°13
				DW 90°	2	n°18
Burner (2021)	1	-	-	-	-	n°14
H2 jet fire + burner (2021)	1	78 Type IV	600 to 700	UP	2	n°15

Type of test	Nb of test	Volume (liter)	Pressure (bar)	Configuration	Ø TPRD (mm)	Test number
H2 jet fire (2020)	4	50 Type II	200	UP	0.5	n°16
				UP	2	n°17
				UP	3	n°18
				DW 90°	2	n°22
Burner (2020)	1	-	-	-	-	n°15
H2 jet fire + burner (2020)	4	50 Type II	200	UP	2	n°20
				UP	2	n°21
				UP	3	n°19
				DW 90°	2	n°23

In this document, the results of the 2021 tests are mainly described. References to the 2020 test results are given when necessary. As a reminder, these 2020 tests were performed with a type II tank and pressure limited to 200 bar and a volume of 50 liters. The first test of the 2021 campaign (Test 09) is therefore intended to reproduce a jet-fire under the conditions of 2020 (Test n°17) but under the rock vault.

Then, the comparison between the results of tests 09 and 10 (2021 series) enables to quantify the effect of the increase in storage pressure and of larger quantities. Comparison between tests 10 and 12 allows quantifying the effect of release location. For downward release, the effect of

orientation (45 or 90°) can be assessed by comparing the results of test 12 with the ones of test 18. Finally, the effect of release diameter for a downward release of 45° is investigated by comparing tests 12 and 13.

4.5.5 Test results - Reference jet-fire (200 bar, 2 mm, UP)

The reference test (test 09) is performed with a type II cylinder filled with 200 bar of hydrogen. The calibrated orifice used is 2 mm and is oriented vertically upwards. The purpose of this test is to confirm the results obtained in 2020 (test n°17) for similar conditions, except for the location in the tunnel.

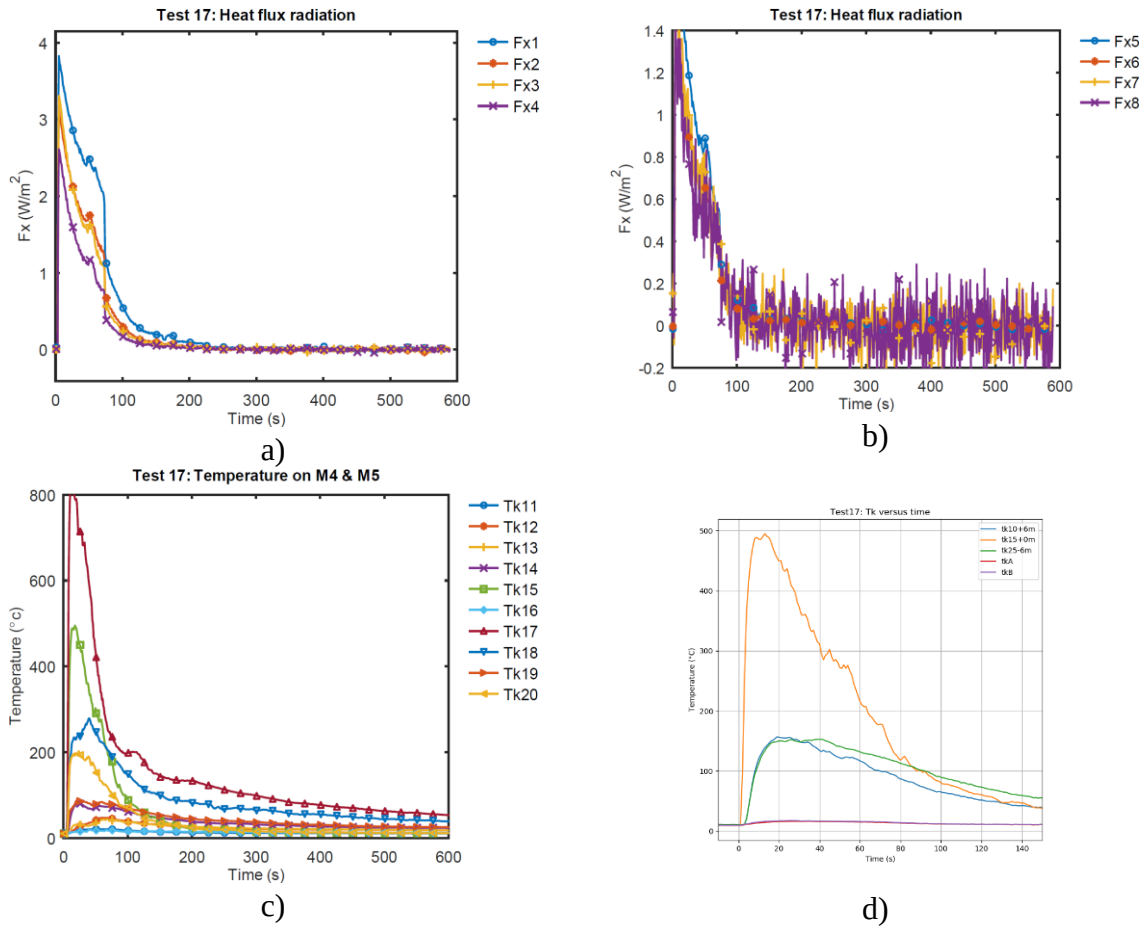

Figure 128. Results of 2020 Test 17: a) Radiated heat flux – lower part, b) Radiated heat flux – Upper part, c) Gas temperature nearby the release d) Gas temperature along the ceiling nearby the injection (TkA and TkB are located in the middle of the tunnel above the burner).

For the 2020 test (test n°17) we only have a few seconds of video of the jet-fire. However, the radiated flux and gas temperature measurements cover the total duration of the release (Figure 128). A maximum temperature of 800°C was measured above the discharge and the radial attenuation was very fast (less than 150°C measured at 6 m around the point of impact on the vault). For the fluxes, the Fx1 sensor measured up to almost 4 kW/m² for a distance of 1.3 m. This is above the threshold for irreversible effects (3 kW/m²) but below the threshold for lethal effects (5 kW/m²).

In the 2021 baseline test (Test 09), an event occurs during the discharge that affects the jet-fire. This is not a drop in flow rate at the leak and we have no explanation for this phenomenon. The

flame can be seen clearly (Figure 129) widening and decreasing in size before 10 seconds. It then returns to a more usual behavior.

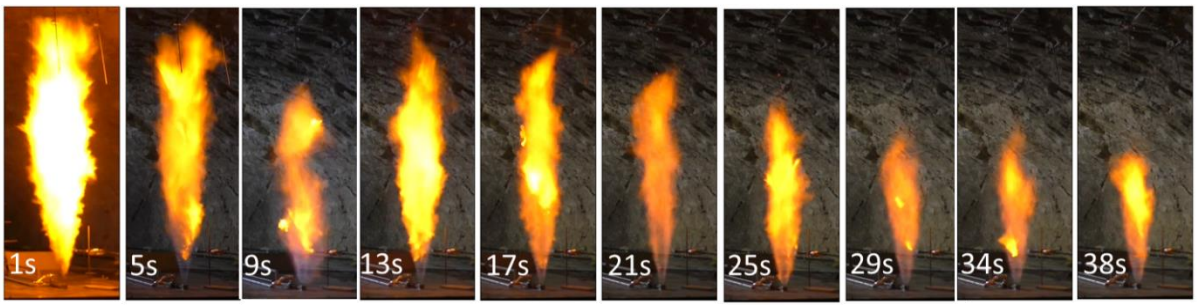

Figure 129. Test 09 Shape of the jet-fire.

The post-processing of the images clearly shows this phenomenon (Figure 130) while the theoretical analysis performed using the method described in Molkov and Saffers (2013) shows a monotonic behavior. The latter is based on properties derived from the release which does not show any abnormal behavior. Due to the unexpected experimental behavior, it is difficult to conclude on the ability of the theoretical model to predict our results. After 20 seconds, the agreement is very good.

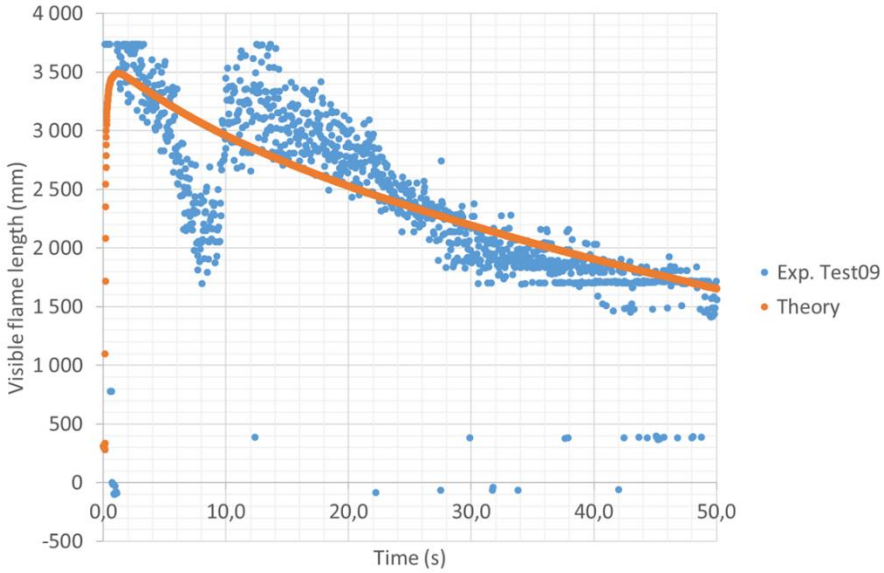

Figure 130. Test 09 Visible flame length with comparison to theory in open environment.

As the flame is affected, so are all other quantities (radiated flux and temperatures - Figure 131). The maximum flux is measured by the Fx6 flux meter which is located at a distance of about 2.3 m from the center of the flame. For the 2021 test, the measured flux is higher (2.5 kW/m²) whereas in the 2020 test at the same distance a maximum of 2 kW/m² was measured (Fx5). Then, the value of 1 kW/m² is reached after about 30 seconds which is comparable in both series of tests. Comparing the fluxes predicted by a point or multi-point radiant source method (Hankinson & Lowesmith, 2012), the values are comparable to the measurements.

Nevertheless, we notice a singular behavior for the Fx3 and Fx4 sensors located on the structure inclined at 45° in its upper part. These sensors measure larger fluxes than those predicted by theory, given their distance from the flame. It should be noted that these two sensors are placed at a height of over one meter, unlike the others.

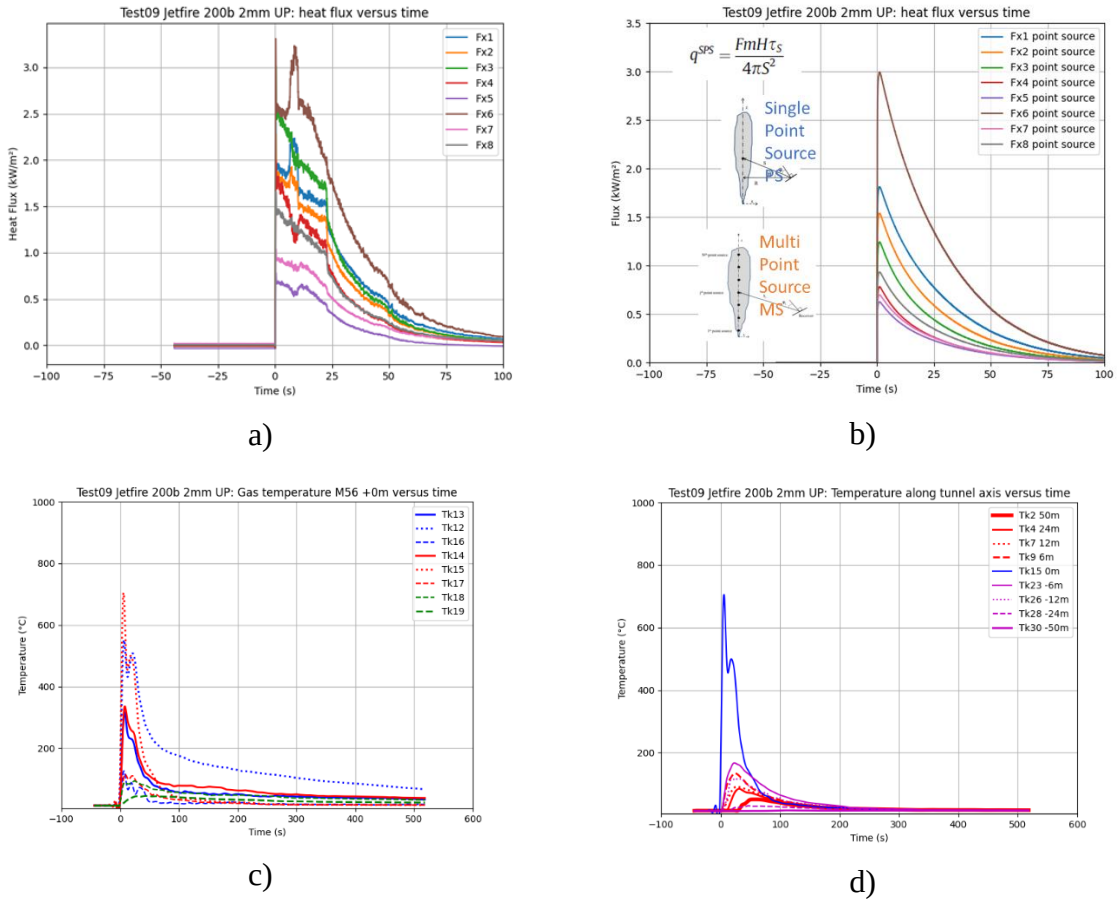

Figure 131. Test 09: a) Measured Radiated heat flux, b) Radiated heat flux computed by the point-source theory – Upper part, c) Gas temperature nearby the release d) Gas temperature along the ceiling.

For the gas temperature (Figure 131 c), we measure up to 700°C, which is comparable to the value measured in 2020. Furthermore, the lateral extension (Figure 131 d) still shows a decay below 150°C at 6 m from the impact point on each side of the tunnel. Due to the irregular rock vault, the decay is less symmetrical than it was under the concrete vault (Figure 128 d). As in the dispersion tests (Studer et al., 2021), there is a tendency for hot gases to flow towards Montaud side.

4.5.6 Effect of tank pressure for a 2 mm jet-fire

In test 010 of 2021, the initial driving pressure is now around 700 bar and the release diameter still 2 mm. The jet-fire shows a monotonic behaviour (Figure 132), which supports the hypothesis of a one-time defect in test 09.

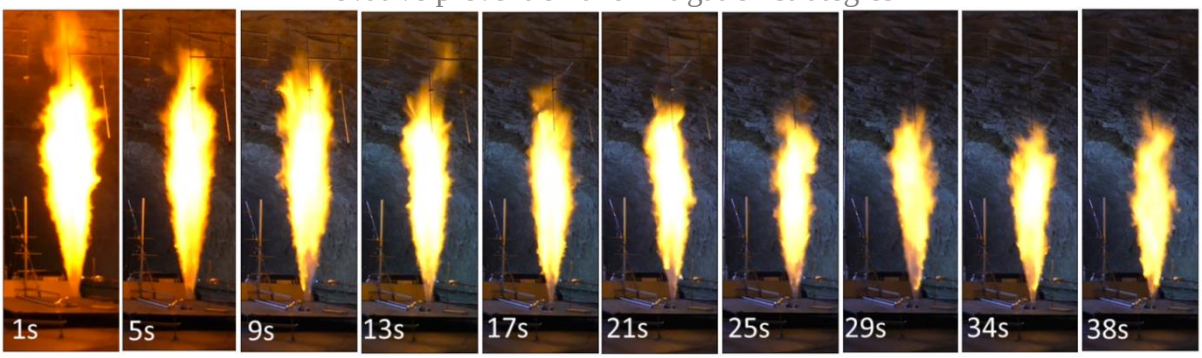

Figure 132. Test 10 Shape of the jet-fire.

The flame does not reach the vault on the images (Figure 132) and this result is confirmed by the theoretical predictions (Figure 133). The measurements and the theoretical predictions are in very good agreement (Figure 133) with a slight overestimation for the theoretical values which confirms the applicability of theory by Molkov and Saffers (2013) to hydrogen safety studies.

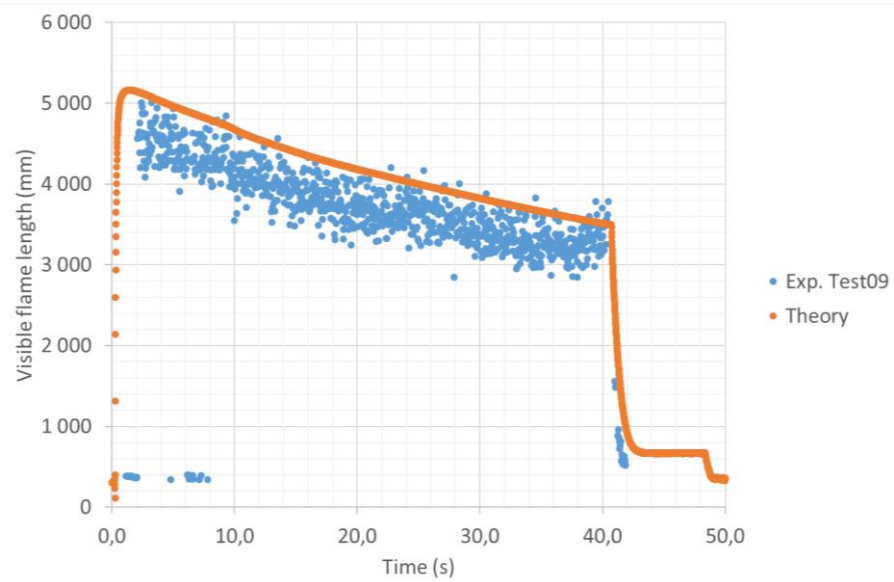

Figure 133. Test 10 Visible flame length with comparison to theory in open environment.

During the tests at 700 bar with hydrogen, the injection solenoid valve is closed when the temperature at the T_1 thermocouple reaches about -50°C, in order to avoid unexpected closure of this solenoid valve as in the dispersion tests. In this test, the initial pressure in the tank, which is about 600 bar, is about 180 bar at the switch-off which occurred about 40 seconds after the opening.

The measured radiated heat fluxes (Figure 134 a) are 0.5 kW/m² higher than those measured during the 200 bar jet-fire whereas the predicted value by the point source method reaches 1.5 kW/m² increase. Fx3 and Fx4 are still showing higher flux compared to their distance to the flame.

For gas temperatures (Figure 134 b), we now measure up to 1000°C at the tip of the flame. The hot gas temperature approach 300°C at -6 m with always the same dissymmetry. If this value is considered as a threshold value for damage to ventilation systems a safe distance of about 6 m is only available. Finally, a temperature close to 200°C is measured at 12 m on each side of the tunnel from the impingement point.

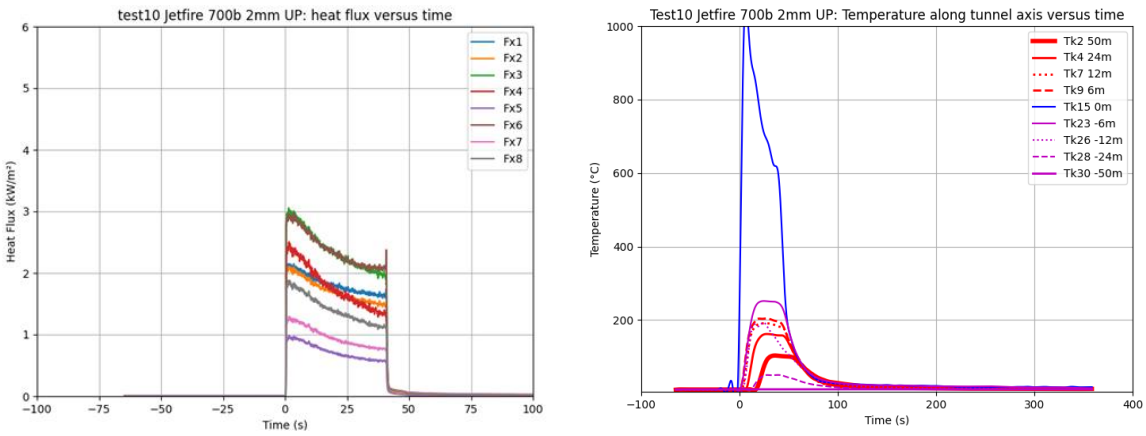

a) b)

Figure 134. Test 10: a) Measured Radiated heat flux, b) Gas temperature along the ceiling.

4.5.7 Effect of release location for a 2 mm jet fire

4.5.7.1 *Injection under the chassis*

If at the time of the accident the FCHV did not overturn, the release through the TPRD is oriented downward. In the reference situation, we still considered a jet-fire through a 2 mm hole oriented at 45° towards the rear of the vehicle (test 12).

The images (Figure 135) show that the lateral extent of the jet flame is about the size of the chassis (about 2 m). Along the rear side of the car, painted lines on the road (Figure 136) allow a rough estimation of the jet flame extension.

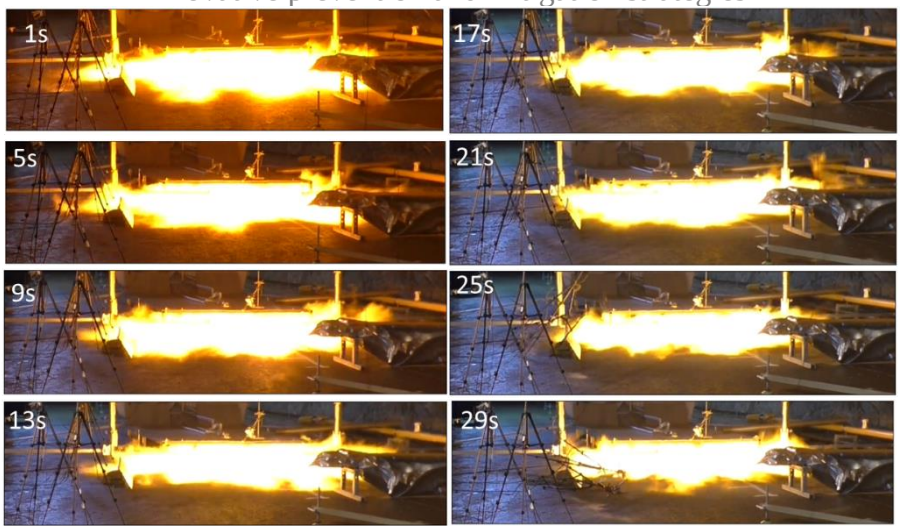

Figure 135. 2021 Test 12 2 mm DW 45°: Jet-fire shape viewed from the rear side.

Each tick is separated by 500 mm and the first one is located 1000 mm far from the release orifice. Consequently, at 1 s, the extent is about 3.5 m and it decreases to about 2.5 m at 29 s.

Figure 136. 2021 Test 12: Ground view from the side before jet-fire – the painted central line has a graduation of 0.5 m and the first one is 1.0 m far from the orifice.

Regarding radiometers measurements (Figure 137 a), the ones located on the chassis are very far from the flame and only provide values around 1 kW/m². The four radiometers installed nearby the flame show similar group behavior Fx6-Fx8 and Fx5-Fx7. The two radiometers of each group have similar positions and the only difference is their orientation: one is looking horizontally and the second one is looking to the ground where the flame is supposed to be. The results show that at these distances, the orientation is not a dominant factor. After 25 seconds, the two radiometers installed closer to the flame were damaged (destruction of supports) and fall down into the fire (see images in Figure 135).

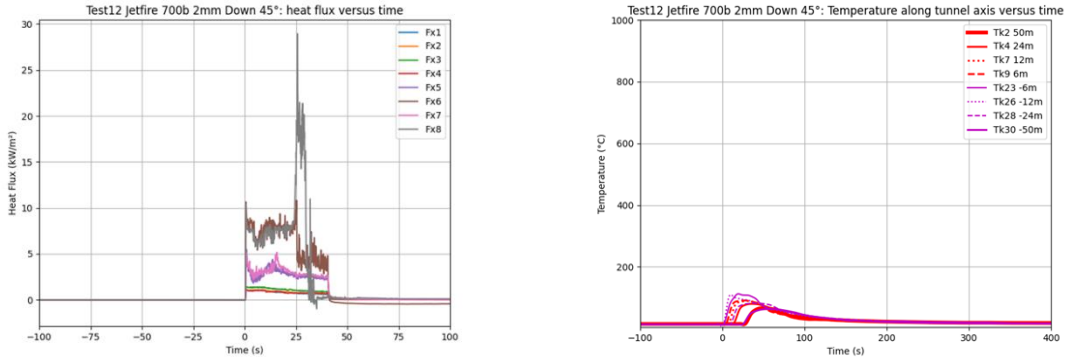

a) b)

Figure 137. Test 12: a) Measured Radiated heat flux, b) Gas temperature along the ceiling.

Finally, the hot gas temperatures (Figure 137 b) measured close to the ceiling of the tunnel were below 100°C.

4.5.7.1.1 Jet fires from TPRD with 45° downward direction: remarks on experimental and numerical studies

It may be interesting to compare these experimental results to numerical simulations performed by University of Ulster (UU) to investigate hydrogen jet fires in an underground car park environment (ST 3.2.3). Both experiments and simulations investigate jet fires from TPRD with 45° downward direction. Simulation results were reported in Section 2.3.5.3 and they recorded temperatures equal or above 300°C at the car park ceiling with height 3 m, downstream the TPRD direction for both diameter 1 and 2 mm (see Figure 47). At 16 seconds, this cloud with T≥300°C has already reached the ceiling of the parking lot (3 m height) and is located about 6 m downstream for TPRD diameter of 2 mm. In experiments, the lower thermocouple Tk20, located 4 m above the elevation of the orifice and 6 m downstream for test 12 – d= 2mm (Figure 138 a), only measured 100°C. The measured values seem well-below the computed ones. If the release diameter is decreased to 1 mm (test 13 - Figure 138 b) the maximum temperatures are the order of 75°C. In both tests, Tk21 shows smaller values because this thermocouple is protected by thin plate in order to lower the influence of radiative heat transfer. At the same time, this protection leads to a slower transient behavior.

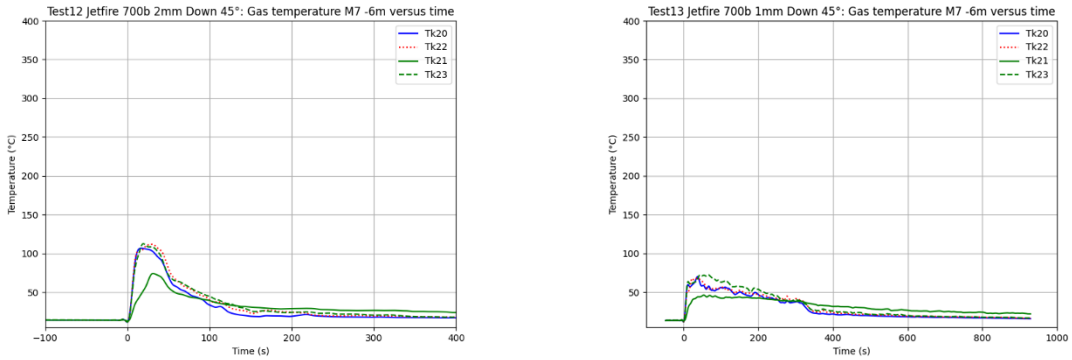

a) b)

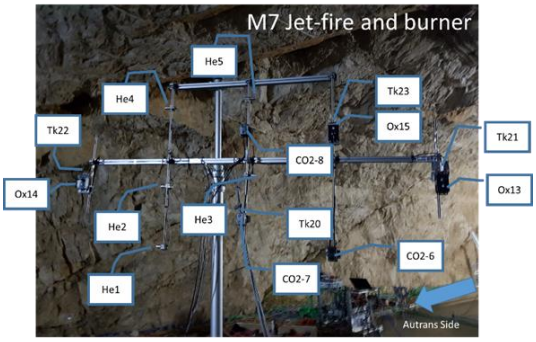

c)

Sensor	X (mm)	Y (mm)	Z (mm)
Tk20	0	-5945	4014
Tk21 protected	995	-6000	4167
Tk22	-978	-5944	4225
Tk23	460	-5962	4492

d)

Figure 138. Hot gas cloud at -6 m close to the ceiling: a) Test 12 2 mm, b) Test 13 1 mm, c) Sensors location on M7, d) Thermocouples coordinates.

It is considered that the conclusions and the results of experiments and simulations can provide complementary information and data for the two scenarios. However, the substantial differences among the two investigated scenarios prevent the performance of a direct comparison of the results. The associated differences and main considerations are listed below:

- TPRD location. In the experimental test, the TPRD was located at a height of about 20 cm from the ground, whereas in numerical simulations the TPRD was located at 30 cm. Such difference in proximity of the release may cause a significant change in the jet properties and momentum at the point of impingement on the ground, thus affecting the behaviour of the jet beyond this point and the cloud formed by the combustion products. Furthermore, in experiments the TPRD was placed towards the central axis of the chassis, whereas in simulations this was located on a side of the vehicle. It is considered that the latter may be in a more favourable position for air entrainment in the jet fire and promotion of combustion. Instead, in experiments, the presence of the 1.9 m long metal sheet above the jet fire may affect air entrainment from both sides.
- Ceiling height. The entrainment of air is proportional to the momentum flux. It is considered that in the car park scenario, the presence of the ceiling at a lower height provides a stagnation point decreasing the entrainment of fresh air into the hot products cloud, and thus increasing the recorded temperature.
- Geometry. The scenario investigated in CFD simulations involves the presence of a vehicle with maximum height of about 1.5 m within the 3 m high car park. It is considered that the presence of the vehicle would limit the entrainment of fresh air into the combustion products cloud, leading to a minor mixing and higher temperatures. On the other hand, in experimental tests, the chassis would occupy about 0.3 m over the total height of the tunnel (about 5.6 m), leaving more space for fresh air entrainment and better mixing with the combustion products cloud.
- Ground surface. In experiments the jet impinges on the ground surface characterised by a certain level of roughness and porosity, whereas in simulation the ground was considered as smooth. This further factor could affect the properties of the jet after impingement.
- Discharge coefficient (Cd). It was estimated that the discharge coefficient for the experimental test with diameter of 2 mm was approximately 0.8, whereas in simulation the conservative scenario with Cd=1 was considered. This could be the cause of the slightly larger flame length observed in simulations and as well larger hot combustion products cloud.

Further numerical works should be performed on simulation of CEA jet fire tests in a tunnel to conclude on the possible effect of the different scenarios and/or the eventual conservatism of computational analyses.

4.5.7.2 *Effect of orientation in case of 2 mm downward jet-fire*

In test 018, a downward jet-fire oriented normally to the road (90°) is performed. During this test, a loud sound was heard corresponding to an explosion at the beginning of the ignition. Unfortunately, no pressure sensors are installed to record the overpressures. The pilot flame is installed at the same location from previous tests (Test 12 and Test 13). The only difference is that the steel plate, which was installed on the road to limit the burning of the asphalted road is highly deformed by the two previous tests. A possible deflection of the jet by the plate toward the front of the car can delay the increase of hydrogen concentration nearby the pilot flame and consequently delay the ignition. However, the video taken during the test shows that 7 images (280 ms) are recorded between the beginning of the release and the fireball. The estimated injection flowrate is around 75 g/s, which leads to 21 g of hydrogen release before the ignition. Dispersion simulation may be helpful to determine the extent of the explosive atmosphere under the chassis for these conditions.

After the initial explosion, the shape of the flame is very impressive (Figure 139) and surrounds the chassis on the four sides with large flames. Despite the thermal protection installed around the high-pressure tank, it was decided to stop the release after 14 seconds.

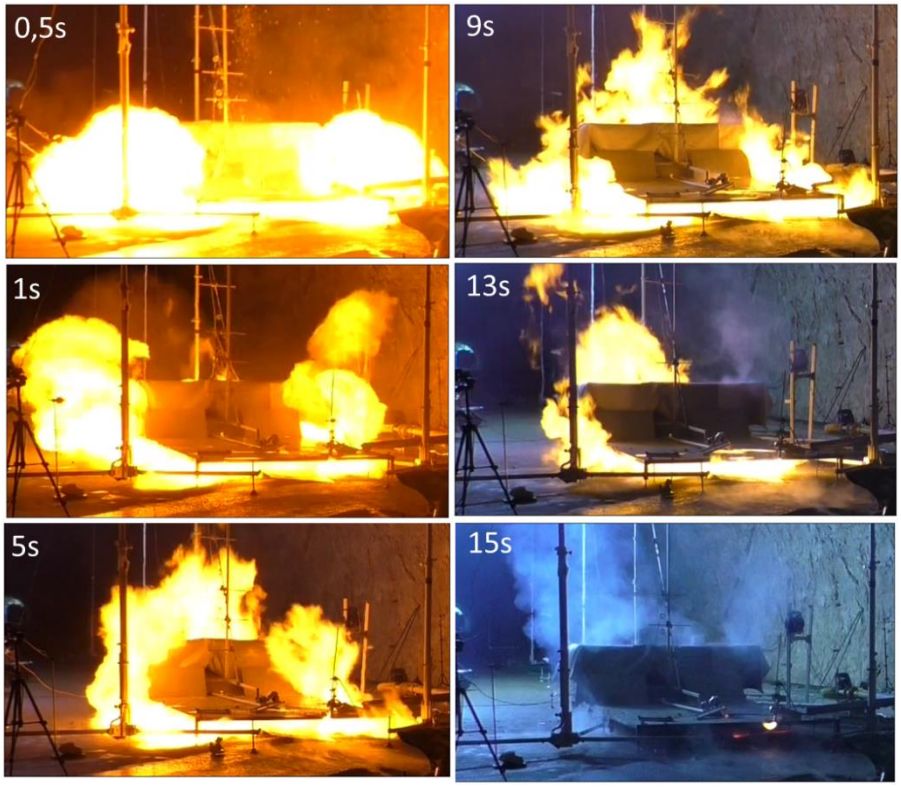

Figure 139. 2021 Test 18 2 mm DW 90°: Jet-fire shape viewed from the rear side.

The measured radiative heat fluxes (Figure 140 a) are very high at the beginning due to the fireball especially for the radiometer installed along the chassis on the side of the road (Fx5).

At the same time, a peak of temperature (Figure 140 b) is measured on the top part of the tunnel at +6 m which corresponds to the front part of the vehicle where the huge flames are observed.

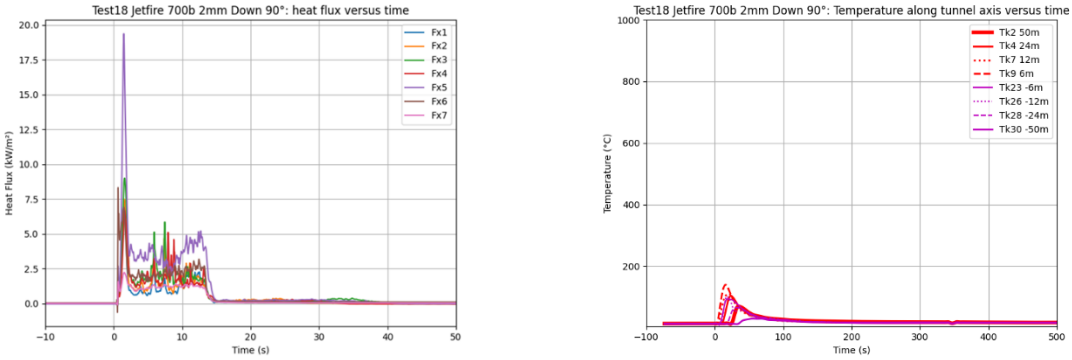

a) b)

Figure 140. Test 18: a) Measured Radiated heat flux, b) Gas temperature along the ceiling.

Finally, it is interesting to compare the shape of the flame of test 18 to the same test performed in 2020 with only 200 bar in the tank (test n°22). With only 200 bar of driving pressure the extent of the flame is completely modified (Figure 141) and the flame mostly stays under the chassis during the transient.

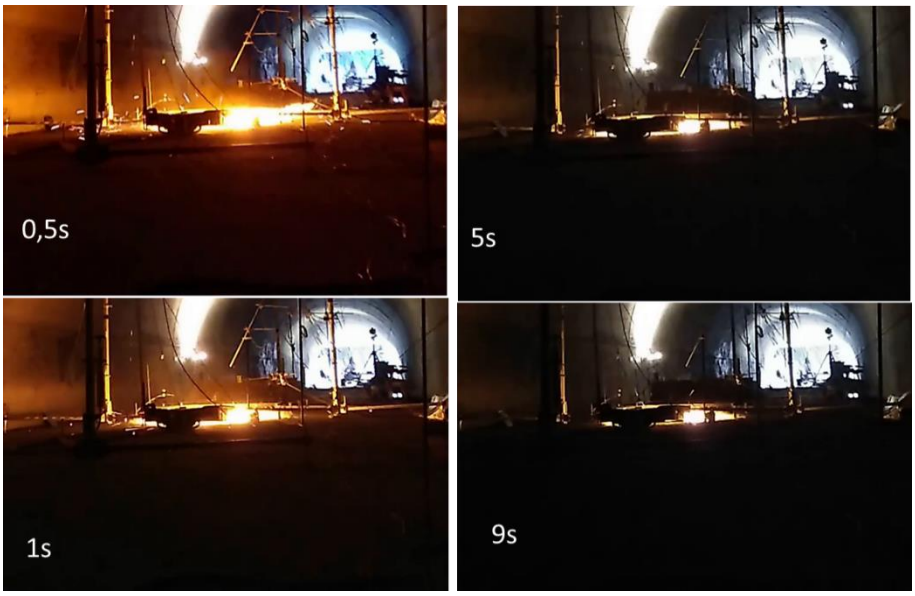

Figure 141. 2020 Test n°22 2 mm DW 90°: Jet-fire shape viewed from the rear side.

4.5.8 Effect of release diameter in case of downward 45° jet-fire

To conclude this series of jet-fire tests, the effect of the discharge orifice diameter is studied for a 45° orientation towards the rear of the vehicle. A discharge orifice of 1 mm (test 13) leads to a lower extent of the jet-flame (Figure 142). The axial extent is limited to 2.5 m and it seems to stay at this location during the first 30 seconds of the release.

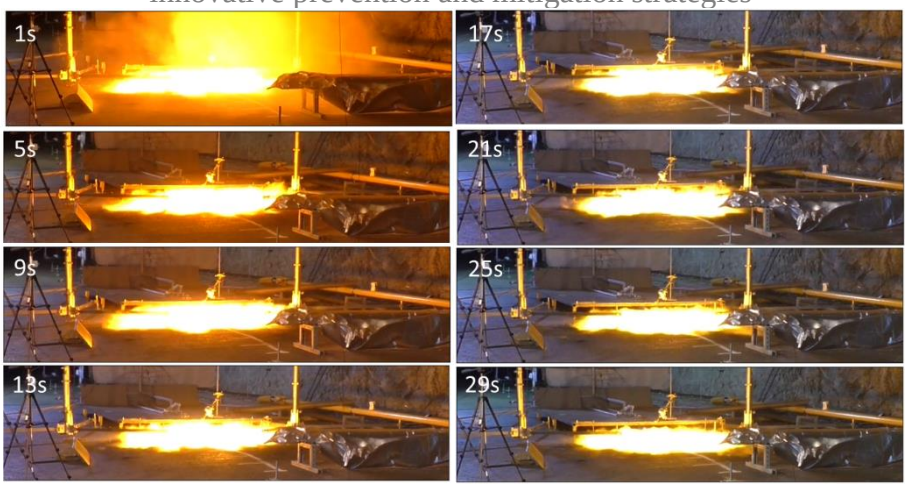

Figure 142. 2021 Test 13 1 mm DW 45°: Jet-fire shape viewed from the rear side.

A specific behavior is recorded by the radiometer located close to the jet-flame (Fx6 Figure 143 a). After a first decrease of the radiated heat flux, a sudden increase is recorded from 30 to 50 seconds. Coming back to the video, at this time the jet-flame starts to be thicker. There is no big change in the release parameters and the pressure is still above 300 bar. A possible explanation is that the asphalted road starts to release burnable products that feed the jet-fire. At the end of the release, the road was on-fire close to the impingement point. The measured gas temperature along the ceiling of the tunnel (Figure 143 b) were below 75°C.

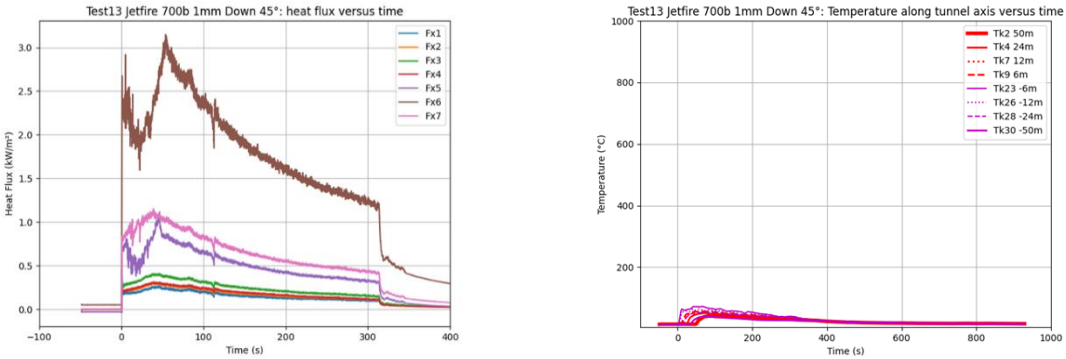

a) b)

Figure 143. Test 13: a) Measured Radiated heat flux, b) Gas temperature along the ceiling.

4.5.9 Coupling Fire/jet-fire for a 2 mm upward jet-fire

The last series of tests is dedicated to the interaction between the vehicle fire and the jet-fire. Only two tests could be performed on the subject due to the limited number of tank fills under 700 bar of hydrogen. As the discharge tests are very soliciting for the tanks, we limited the number of cycles for each of our six tanks.

In the first test (Test 15), an orifice diameter of 2 mm is chosen and the discharge is upwards. Before initiating the release, the propane burner is ignited (localized and engulfing sections) for approximately seven minutes at the maximum power to stabilize the flow conditions from this fire.

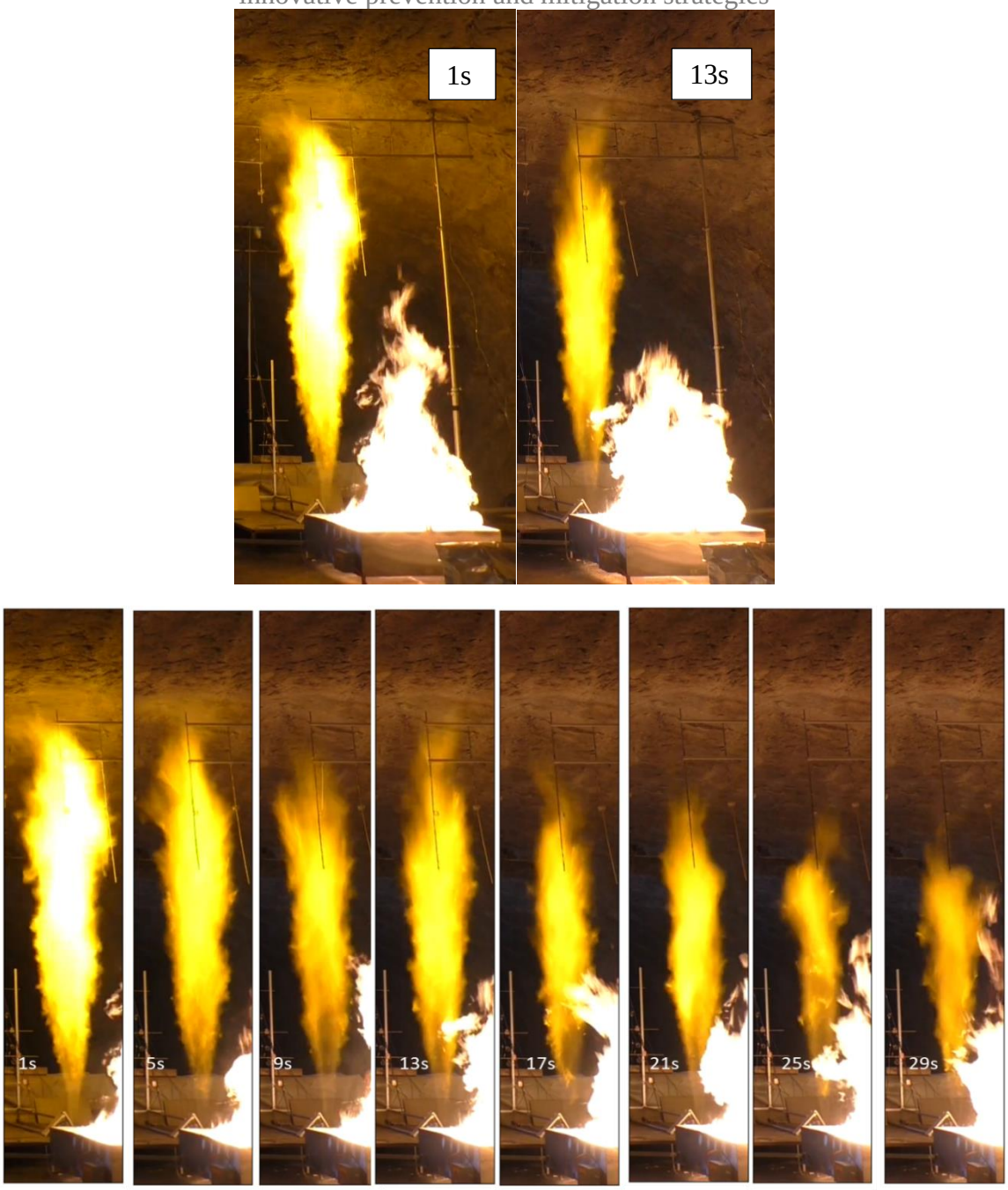

Figure 144. 2021 Test 15: Jet-fire shape viewed from the rear side.

The jet-fire remains well below the tunnel vault and decreases almost continuously (Figure 144). Post-processing of the images shows that the flame height is well below the theoretical prediction (Figure 145) but also below the values measured in the absence of fire (Test 10 Figure 133). The presence of the fire decreases the oxygen content (Figure 146 c) and increases the CO2 content to about 0.6 vol% (Figure 146 d). There is probably also a change in the ambient water vapor concentration. It should be mentioned that the result presented for the oxygen concentration has not been corrected for temperature variations, which tend to increase the measurement. It seems that these environmental conditions lead to a reduction of the vertical development of the jet-fire. Conversely, the videos and measurements do not allow us to conclude on any effect on the fire produced by the burner. Another reason for the jet fire length reduction may be the presence of air cross-flow due to entrainment of air into the burner.

The radiometers (Figure 146 a) show an increase in the radiative flux received when the jet-fire is present. The increase is more important for the radiometers located on the inclined support because the jet-fire comes between them and the fire.

The temperature of the hot gases (Figure 146 b) at the vault also highlights the effect of the jet-fire. Values close to 300°C are measured in the direction of Autrans up to +12 m.

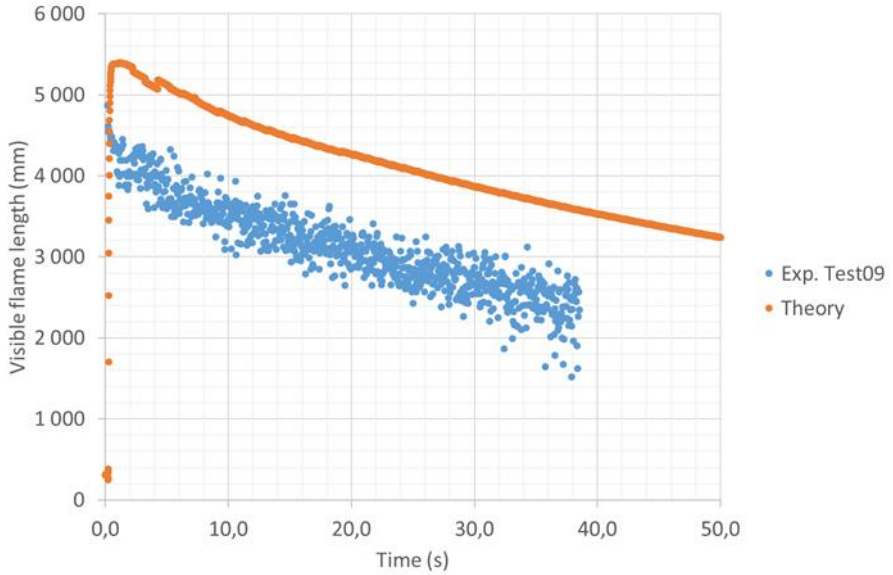

Figure 145. Test 15 Visible flame length with comparison to theory in open environment.

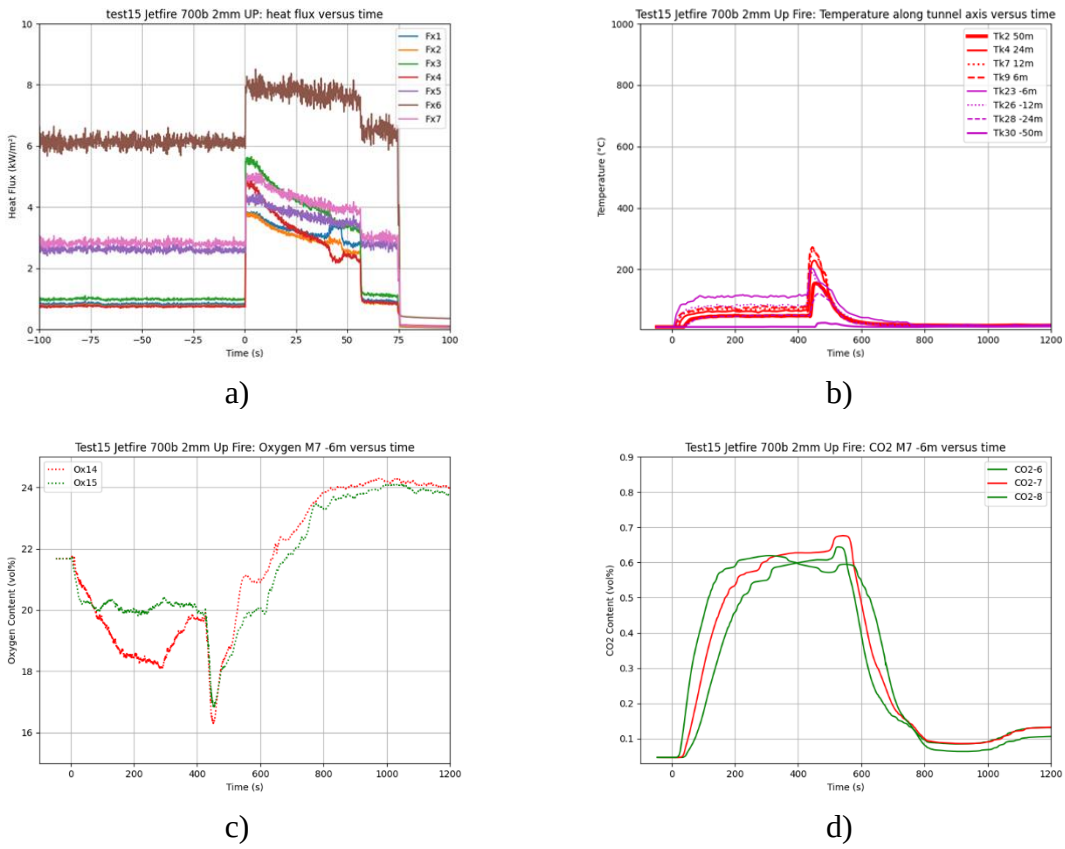

Figure 146. Test 15: a) Measured Radiated heat flux, b) Gas temperature along the ceiling, c) Oxygen content close to the ceiling at -6 m, d) CO2 content close to the ceiling at -6 m.

4.5.10 Blowdown characterization

This section summarizes how the tank blowdown was characterized. It addresses the three following concerns:

- What is the actual mass released during each test;
- What is the C_d of the CEA made TPRD (since it is not a commercial one in 2021 test campaign);
- How do perform the available blowdown models.

Full report is available in HyTunnel-CS database, see Sauzedde et al. (2021b).

Conclusions are based on 27 blowdown tests with 200 and 700 bars of different volumes and gas (helium or hydrogen). Although CEA encountered a problem with the upstream release valve on some of the tests, we could reach repeatability and use a method to consistently calculate the released mass with inaccuracy lower than 5%.

Sonic nozzle method: in this method, the temperature and pressure values from the sensors close to the TPRD are used (T2-P2 or T2-P2bis). This method uses the theoretical model "Barré de Saint Venant" to compute the mass flow for a sonic regime $Qm_{\text{sonic nozzle method}}$, which is encountered at the exit of the TPRD of the experimental setup at least during the first part of the release (if the pressure is above the critical one). The geometry and the surface quality of the release nozzle are not considered in this method and a correction is then introduced through a discharge coefficient (C_d).

$$\boldsymbol{Qm_{sonic\ nozzle\ method} = C_d \cdot S \cdot \sqrt{\gamma \cdot P \cdot \rho \times \left(\frac{2}{\gamma+1}\right)^{\frac{\gamma+1}{\gamma-1}}}}$$

During all of the tests, over the measurement range analysed, the velocity remains sonic because the pressure exceeds the critical one. The sonic nozzle calculation method is therefore valid for the duration of the tests analysed.

The coefficient C_d is introduced in the sonic nozzle method to fit the mass flow rate to the one computed using the mass balance (see Figure 147). The value of C_d is determined with the method of sum of squared residuals **SSR**. The best value of C_d that fit to the flow rate of mass balance is the one with the lowest SSR value.

$$\mathbf{SSR} = \sum((\mathbf{Qm_{mass\ balance\ method}} - \boldsymbol{Qm_{sonic\ nozzle\ method}})^2)$$

A logarithmic scale is considered in the graph shown in Figure 147 for a better understanding of the impact of C_d. We notice the mass balance is used to calculate the SSR. In this method, the data of temperature and pressure sensors located close to the OTV are used (T1-P0 or T1-P1) to compute the density variation of the gas (ρ_{gas}). The mass of the gas is then computed using the obtained density and the volume of the tank (V_{tank}). In a second step, the mass flow rate $Qm_{\text{mass balance method}}$ is computed using the first derivative of the mass balance method for the complete duration of the blowdown period.

$$\mathbf{m_{gas} = \rho_{gas} * V_{tank}} \qquad \mathbf{Qm_{mass\ balance\ method}} = {}^{\Delta \mathbf{m_{gas}}}/_{\Delta \mathbf{t}}$$

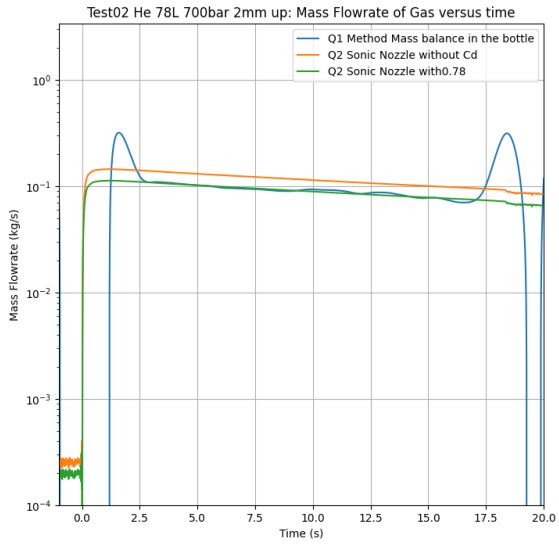

Figure 147. Helium mass flow drop with TPRD of 2mm for the test of 2021.

The value of C_d obtained from this comparison have been used for other theoretical models (e.g. flame length, radiative heat-fluxes). To summarize all our tank blowdown transient tests of 2021, their Cd values and maximum mass flow rates are given Table 29.

Table 29. Summary of 2021 tests' results – Mass flow rate.

	Test	Volume (L)	Pressure (bar)	Orifice diameter (mm)	Configuration	Cd	Maximum mass flow (g/s)
Helium dispersion	**1**	50	186	2	Up	0.74	33
	2	78	647	2	Up	0.78	119
	5	78	665	2	Dw 45°	0.84	160
	7	78	645	1	Dw 45°	0.79	54
Hydrogen jet-fire	**9**	50	177	2	Up	0.78	25
	10	78	598	2	Up	0.75	68
	12	78	635	2	Dw 45°	0.78	72
	13	78	663	1	Dw 45°	0.93	28
	15	78	661	2	Up	0.78	77
	18	78	667	2	Dw	0.85	73

These test results as well as those obtained during the 2020 campaign under 200 bar constitute a unique database for the understanding and validation of injection models.

4.5.11 Conclusions and recommendations

This document details the results obtained during jet-fire and fire/jet-fire interaction under pressure at 700 bar in the Mortier road tunnel. The releases through calibrated orifices occurred

downward or upward to simulate the opening of a TPRD with or without the rollover of the damaged car. The main results show that:

- Jet-fires up to 2 mm in release diameter have a small impact on the tunnel (height above 5 m);
- Lower release diameters e. g. 1 mm are preferable because they lead to a strong reduction of the jet-fire extend but the jet-fire stays longer, and an asphalted road can be set on fire;
- Flame length for vertical jet-fire can be predicted by correlations developed for open environment if the height under the vault is sufficient to develop it;
- The extent of downward jet-fires oriented 45° towards the rear of the car have been measured up to 3.5 m for the 2 mm diameter;
- A downward release perpendicular to the road leads to an unexpected explosion and very large flames around the chassis. Consequently, 45° orientation should be preferred.
- Hot gas cloud (T>300°C) is monitored close to the ceiling of the tunnel in the case of 4 mm release or in the case of 2 mm release with the fire;
- The presence of the car fire (1 MW/m²) prior the orifice opening lower the extend of the jet-fire;
- Hot gas cloud seems to be less extended in the experiments than in the simulations.

To summarize all our jet-fire tests, their characteristics with respect to the effect thresholds are given in Table 30. If the threshold is exceeded, the distance is given.

Table 30. Summary of 2021 tests' results – Hazard distances.

Test	**Orifice diameter (mm)**	**Jet-fire orientation**	**Fire**	**Radiated flux >3 kW/m²**	**Radiated flux >6 kW/m²**	**Radiated flux >8 kW/m²**	**Ceiling Gas Temperature >300°C**
9 (200 b)	2	UP	No	2.3 m	-	-	<6 m
10	2	UP	No	3.7 m	-	-	<6 m
12	2	DW 45°	No	5.4 m	3.2 m	3.2 m	-
13	1	DW 45°	No	3.2 m	-	-	-
18	2	DW 90°	No	2.8 m	-	-	-
15	2	UP	Yes	5.4 m	2.9 m	2.9 m	~6 m

These test results as well as those obtained during the 2020 campaign under 200 bar constitute a unique database for the understanding and validation of jet-fire and fire/jet-fire interaction models at the road tunnel scale.

4.6 Effect of water sprays on mitigation of hydrogen jet fires (ST 3.4.6, PS)

The aim of this task is to investigate the efficiency of water sprays to suppress combustion and thermal radiation from a hydrogen jet fire.

4.6.1 Facility

The experiments were performed in the safety vessel V220 (A2), as shown in Figure 148. The safety vessel with an inner diameter di = 6 m and a height h = 8 m provides a control volume of 220 m^3. It is designed for a static overpressure of 10 bar and temperatures up to 150 ^oC. The vessel is equipped with numbers of vents and ports and windows for optical access. The largest two flanges with an inner diameter di = 1890 mm are parallel and located near the bottom on the ground.

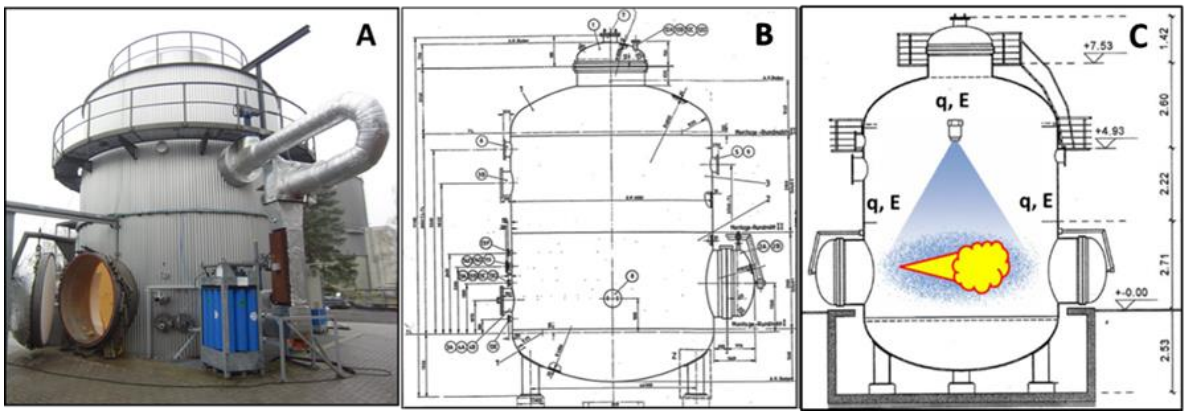

Figure 148. A) Safety vessel V220 (A2) of HYKA. B) Technical drawing. C) Sketch of the set up for suppression tests of water sprays on hydrogen jet fires.

The device of water sprinkler systems to suppress a jet fire, is placed inside the safety vessel, as shown in Figure 149-C. The jet facility is the same as described in D 2.1 "Detailed research program on unignited leaks in tunnels and confined space" (sub task 2.4.4).

Figure 149. Mist nozzle head (Danfoss SEM-SAFE® Type: HNMP-5-10-1.19-00) (left), corresponding mobile professional high-pressure water mist system (Callies GmbH) (middle) and spiral full cone spray nozzle (right).

The water spray system is characterized by the design of the release nozzle and the water supply pressure. Two different release nozzle designs were investigated in this work: a mist dominated, and a droplet dominated water spray system. Figure 150 *(left)* shows the mist nozzle head Danfoss SEM-SAFE® Type: HNMP-5-10-1.19-00 and its corresponding mobile professional high-pressure water mist system from Callies GmbH (*middle*). Figure 150 *(right)* shows the used stainless steel spiral full cone spray nozzle. This spray nozzle produces a rain

like droplet dominated spray and the water feed flow were taken directly from the test ground grid.

Figure 150. Pre-tests of a water mist spray. Left: facility to measure the quantity and uniformity of H2O-charging on the ground. Right: final design of the two nozzles head system in operation.

Pre-tests with the used spray systems were performed to quantify the H_2O-charging and its uniformity on the ground. Figure 150 shows exemplary pre-tests of a mist dominated water sprinkler system with two nozzle heads. The configured values of the system are the operation pressure of 100 bar, the water flow rate of 9 dm^3/ min per nozzle head. The distribution of the droplet size of 20 – 80 µm is given from the producer. The variables of the final mist injection design are the number of nozzle heads, the distance between the nozzle heads and the height of the nozzle heads from the jet-fire location. The values of these variables were derived from the pre-test results. The tests show that a roof above the mist nozzle head has a strong influence on the uniformity of H_2O-charging on the ground. Figure 151 shows exemplarily of the influence of a roof above a three-nozzle sprinkler system.

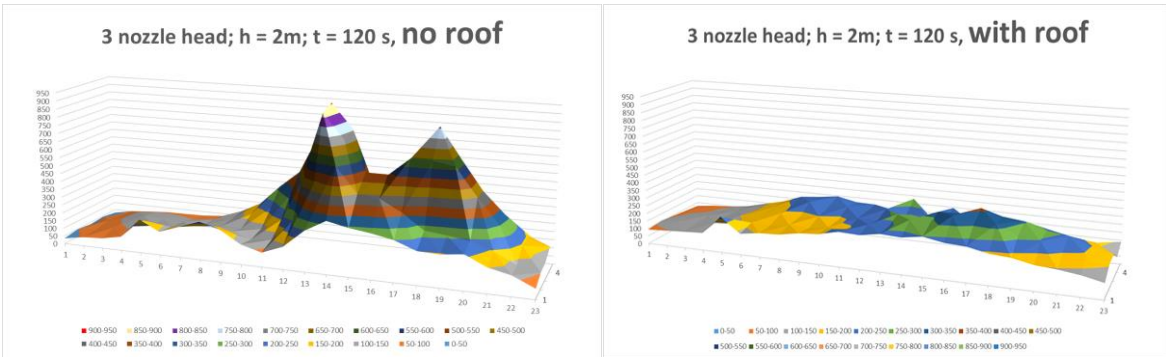

Figure 151. Example of the influence of a roof above the nozzle sprinkler system on the uniformity of H2O-charging on the ground. Left: no roof. Right: final design with roof.

The final design consists of a roof above the nozzle heads. For the variation of the water flow rate, a two and three nozzle head configuration was selected for the mist-dominated spray. For the droplet-dominated spray, one single full cone nozzle was used. In the final set-up of the mist-dominated spray, the two nozzle heads produced a release of 18 kg/min and a charging of 1 - 2 kg/m^2 per minute on the ground, respectively; the three nozzle heads produced a release of 27 kg/min and a charging of 1.5 - 3 kg/m^2 per minute on the ground, respectively. The full cone droplet nozzle releases water in a rate of 40 kg/min with a charging of 8 kg/m^2 water per minute.

Figure 152 shows the experimental set-up installed in the safety vessel V220 (A2). The nozzle heads were installed under the roof plate above the H2 jet nozzle. Two long electrodes of the spark igniter were placed on a pneumatic cylinder that removes the electrodes out of the jet fire after a successful ignition. The temperature profile of the jet-fire was measured by 11 NiCr/Ni-thermocouples that were placed perpendicular to the H2-jet axes in a fixed line. The thermocouple line can be shifted on a sleigh to different positions on the jet-axes. A special screen for optical observation was placed behind the H2-jet.

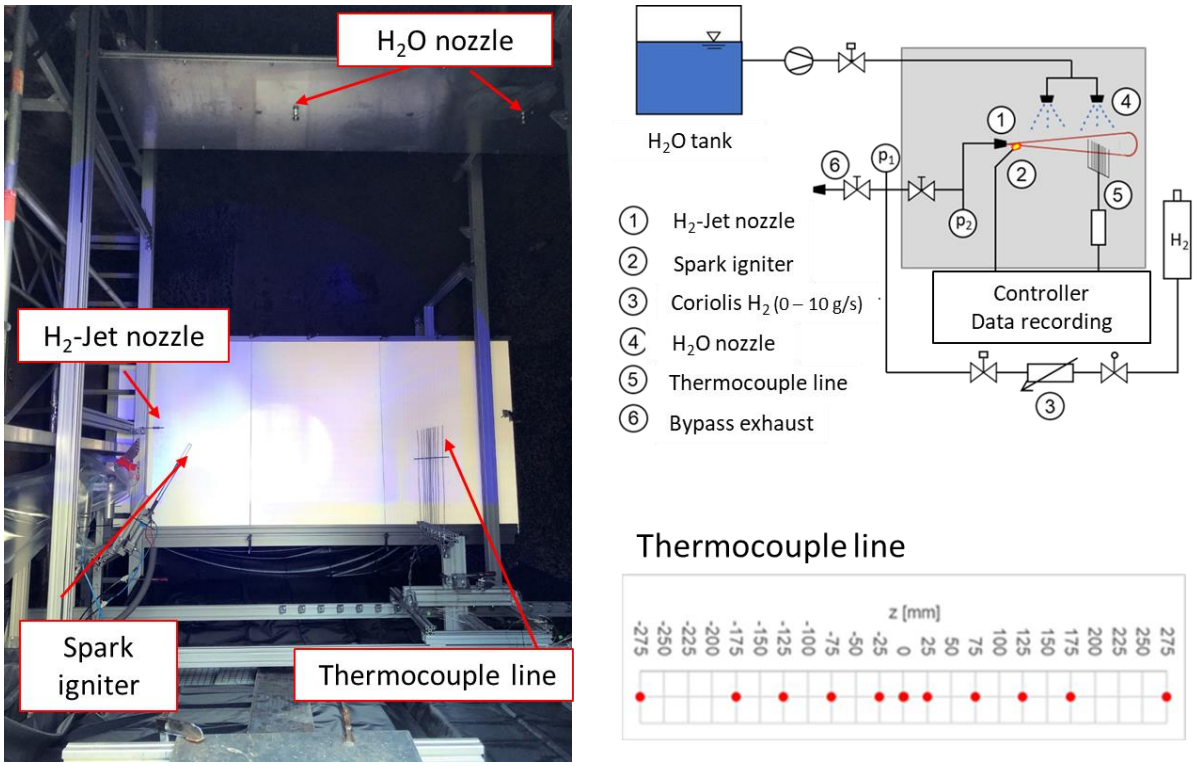

Figure 152. Experimental set-up (two mist nozzles head configuration) installed in the safety vessel V220 (A2).

The H2-jet facility is described in detail in Grune et al., 2021, where unignited jets were studied with the same mass flow rate of 1 g/s and 5 g/s released through the same nozzle diameter of 1 mm and 5 mm as in this work. In total 322 single H2-jet fire tests in 17 different configurations were performed in this work. Table 31 lists the 17 different configurations, where the variables are the jet nozzle size, H2-flow rate, water flow rate. Besides dry jet-fire tests, the two mist configurations and one droplet dominated (spray) configuration are listed too. Additionally, the influence of the ignition in dry or wet atmosphere was investigated in one selected configuration.

Table 31. Test matrix of water spray on hydrogen jet fires.

H2-jet nozzle	**1 mm**								**5 mm**							
H2-flow rate, g/s	**1**				**5**				**1**				**5**			
Dry, Mist or Spray	Dry	Mist		Spray	Dry	Mist		Spray	Dry	Mist		Spray	Dry	Mist		Spray
Water mass flow rate, kg/min	**0**	**18**	**27**	**40**	**0**	**18**	**27**	**40**	**0**	**18**	**27**	**40**	**0**	**18**	**27**	**40**
Spray starts after ignition	**1**	**2**	**3**	**4**	**5**	**6**	**7**	**8**	**9**	**10**	**11**	**12**	**13**	**14**	**15**	**16**
Spray starts before ignition											**17**					

4.6.2 Results

The efficiency of water spray to suppress the combustion of hydrogen jet fire was investigated. All scheduled experiments regarding this campaign were performed. Extinguishing of a H2-jet-fire by mist or droplet dominated water spray was not observed. Figure 153 shows an impression of the H2-jet-fire facility: the start-up of water mist injection (left), and the established water mist injection (right).

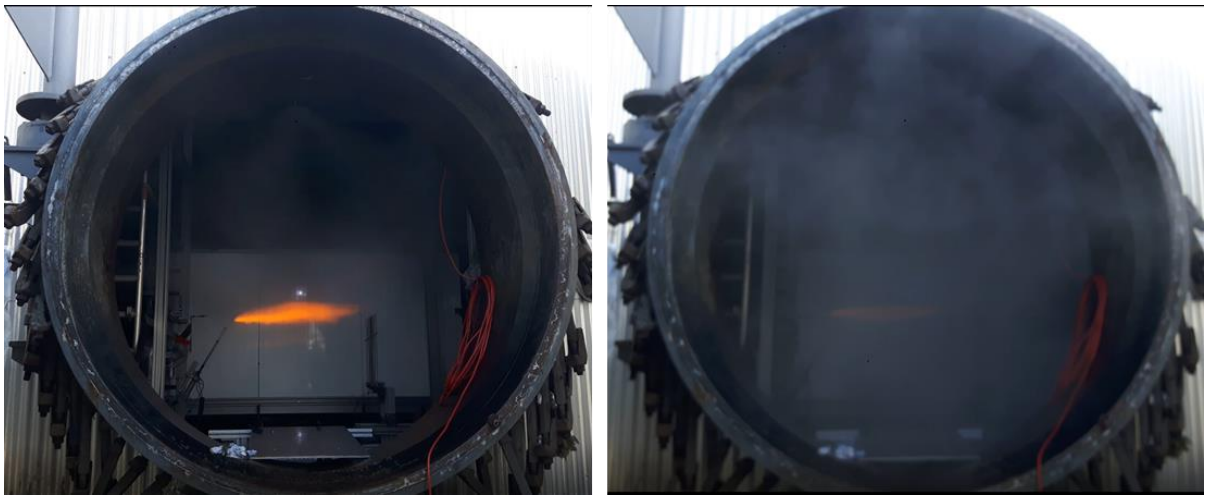

Figure 153. H2-jet-fire and water mist injection. Left: start-up of water mist injection. Right: established water mist injection.

During the start-up of the H2-release ignited in dry conditions, the water spray was initiated directly after the ignition. It needs a few seconds to establish a stable condition for the jet-fire and the water spray. The jet-fire burns for minimum 35 s per experiment. Figure 154 left shows

exemplarily the measured temperature histories of the thermocouple line in 1.5 m distance to the nozzle. The configurations in this example are: 4 mm nozzle, 5 g/s H2 flow rate und the three-nozzle head mist system with 27 kg/min water injection rate. After the ignition the temperature rises significantly after 2 s. After 22 s, it can be assumed that the water injection system runs stable, and the test area is in a steady-state spray loaded condition. The average temperature as well the maximum temperature between 22 s (t1) and 35 s(t2) were used to describe the temperature profile inside the jet fire, as shown in Figure 154 (right).

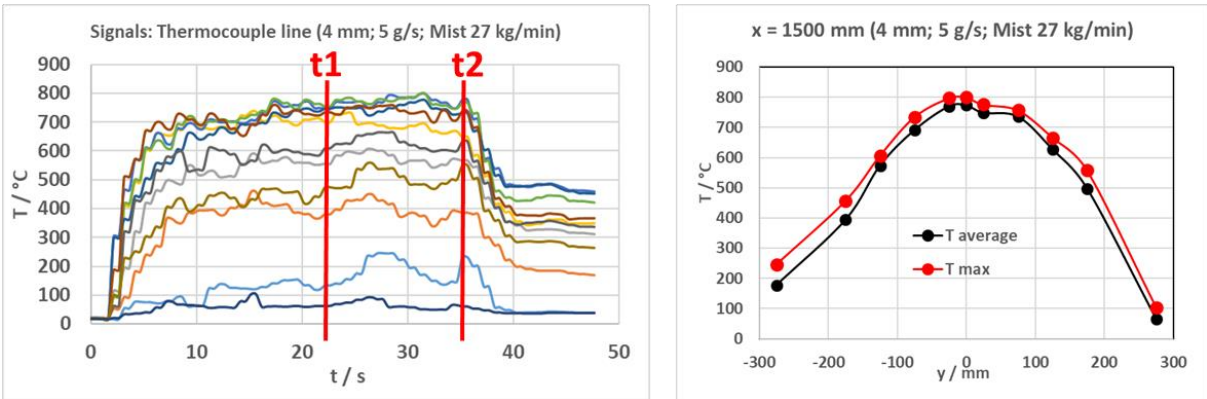

Figure 154. H2-jet-fire and water mist injection. Left: start-up of water mist injection. Right: established water mist injection.

The visible flame lengths, with and without water injection, were measured by using a high-speed (1000 f/s) imaging system. An example of a snapshot without water injection is shown in Figure 155. In the tests, a small portion of NaCl solution was added continuously near the jet nozzle to amplify the visibility of the H2 flame. It is visible that the flame does not show a buoyancy effect but the hot exhaust gases (here as shadow schlieren visible) show a strong buoyancy effect. In this example, it is visible that the hot exhaust gases do not touch the thermocouple line.

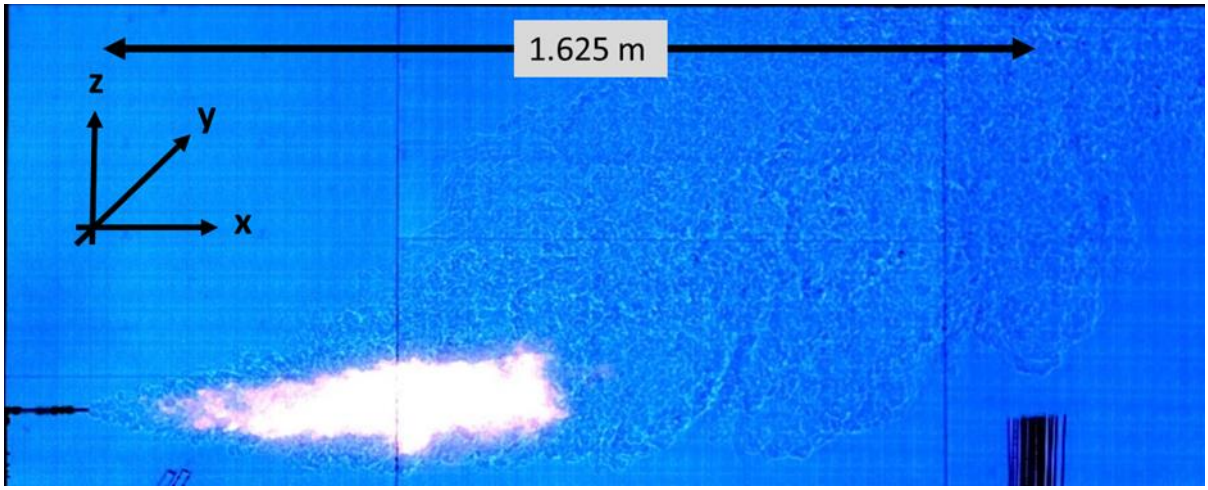

Figure 155. Snapshot from high-speed movie (Jet-fire: H2 = 1g/s. nozzle = 4 mm).

By using the high-speed imaging system, it was observed that the visible lengths of the flame have a strong oscillating nature. Figure 156 left shows a snapshot from high-speed movie (Jet-fire: H2 = 5g/s. nozzle = 1 mm, dry). Figure 156 right shows a stack montage of the visible flame length on the jet axis gained from the corresponding high-speed movie. The stack

montage demonstrates the oscillating nature of the visible flame length in a duration of 1 s with 1000 frames. The frequency looks harmonically, and the amplitude is approximately 25 % of the total flame length.

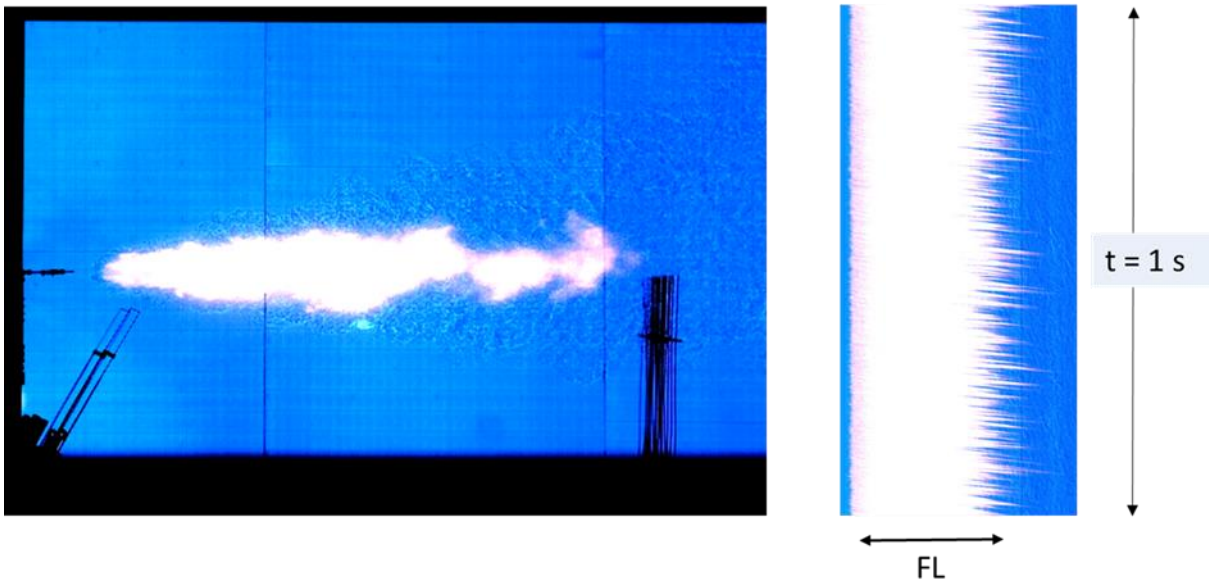

Figure 156. Left, snapshot from high-speed movie. Right, stack montage of the visible flame length on the jet axis from the corresponding high-speed movie. (Jet-fire: H2 = 5 g/s. nozzle = 1 mm; dry).

Figure 157 left shows a snapshot from high-speed movie (Jet-fire: H2 = 5g/s. nozzle = 1 mm) in the configuration with a mist injection of 18 kg/min. Compared to dry conditions the picture looks very dark, but the flame is clearly visible in this example. Also visible is the oscillating nature of the visible flame length on the stack montage as shown in Figure 157 right.

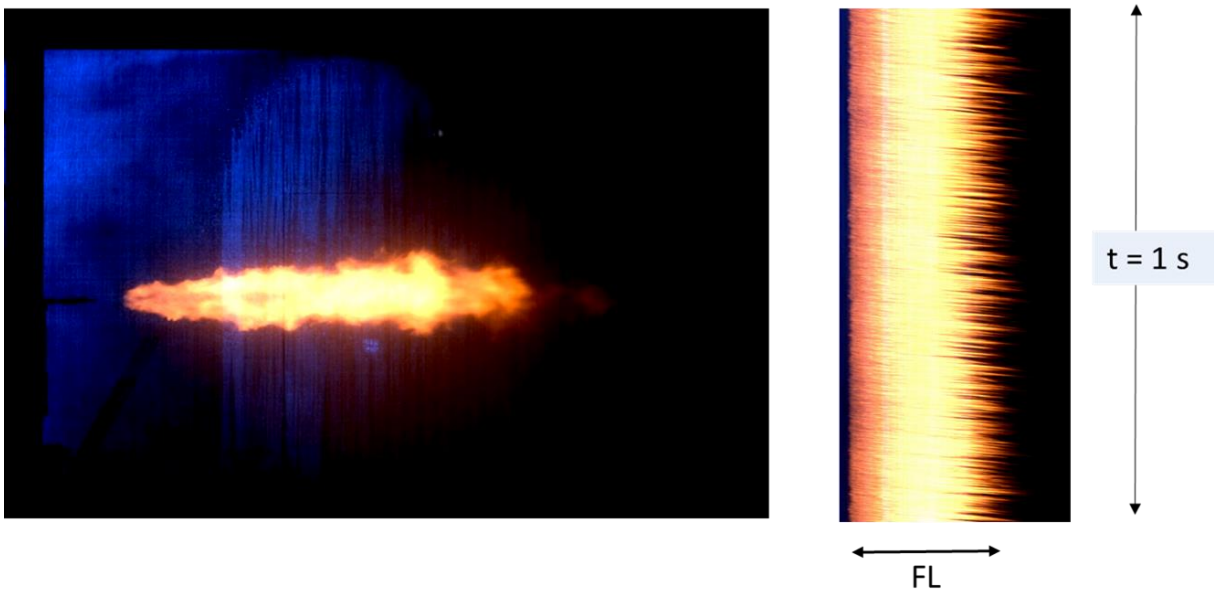

Figure 157. Left, snapshot from high-speed movie. Right, stack montage of the visible flame length on the jet axis from the corresponding high-speed movie. (Jet-fire: H2 = 5 g/s. nozzle = 1 mm; Mist 18 kg/min).

The visible flame length is quantified as the average between the maximum and minimum flame length and the jet axis for a duration of 1 s. (Right side of Figure 156 and Figure 157). The visible flame length of the jet fire was reduced due to the presence of water spray. Table 32 lists the measured visible flame length of hydrogen jet fires.

Table 32. Measured visible flame length of hydrogen jet fires.

H2 jet nozzle id	**1 mm**		**4 mm**	
H2 mass flow rate	1 g/s	5 g/s	1 g/s	5 g/s
Dry: **Visible flame length**	0.353 m	1.253 m	0.794 m	1.235 m
18 kg/min Mist **Visible flame length**	0.127 m	0.783 m	Not possible	0.815 m

In dry atmosphere, the visible flame length is clearly detectable, but a water mist load blocks the view. For the lowest investigated jet-fire (1 g/s H2; 4 mm nozzle), a detection of the visible flame length was not possible for the lower mist charge of 18 kg/s.

The temperature measurement works independently on the water load in the atmosphere. Due to the use of thermocouple of type k, the measured temperature range was limited to 1200 °C.

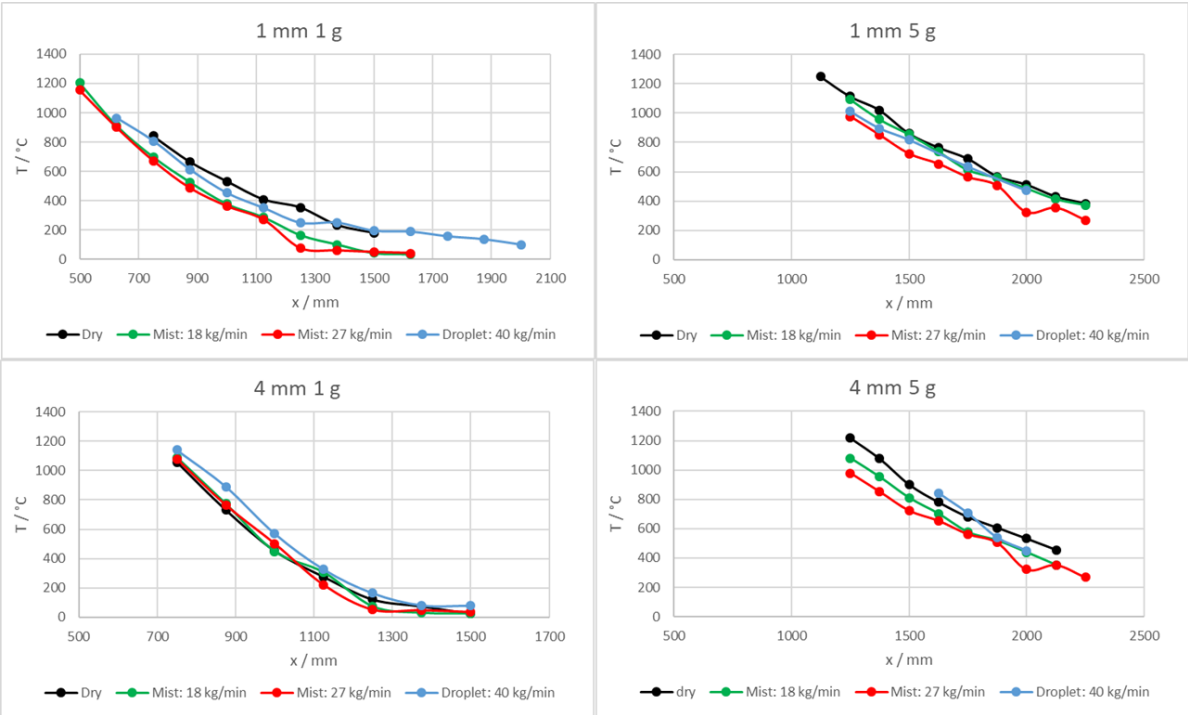

Figure 158. Average temperatures on the H2-jet-fire axis vs. distance to the nozzle.

Figure 158 shows the average temperatures on the H2-jet-axis for all investigated configurations. The highest temperatures were measured in dry atmosphere (in black). The lowest temperatures were detected in a highly charged mist atmosphere. An exemption is shown in the case with the lowest impulse jet-fire (1 g/s H2; 4 mm nozzle), where the wet atmosphere with droplet dominated water charge leads to the lowest temperatures on the jet

axis. It can be assumed that, in this configuration with the lowest impulse, buoyancy effect takes place and the H2-jet-axis lies below the jet fire centre. The main results to describe the efficiency of water injection to suppress hydrogen jet fires are the measured temperature profiles.

Figure 159 shows yz-temperature profiles perpendicular to the axis x of the jet-fire for three determined distances to the jet nozzle for the jet-fire with the lowest impulse (1 g/s H2; 4 mm nozzle). The yz zero-level in this example is located at 0.75 m, 1 m and 1.25 m distance from the nozzle. The three positions A, B, C are sketched additionally on the top of Figure 159. Due to the large number of measurement points, it is possible to present the results as temperature contour plots in a table style for dry and all wet conditions. In a distance of 0.75 m to the nozzle, the temperature profiles look circular with a hot core (> 850 °C). The centre of the hot core lies above the jet axis. With increasing distance to the jet nozzle, the distance of the hot core to the jet axis increases due to buoyancy effects. The mist atmosphere shows the stronger cooling effect compared to the dry jet fire. On the other hand, it is visible that the water droplet atmosphere shows only a minor cooling effect compared to the dry jet fire and the water droplet dominated spray (40 kg/min) supresses the buoyancy rising of the fire cloud in this example.

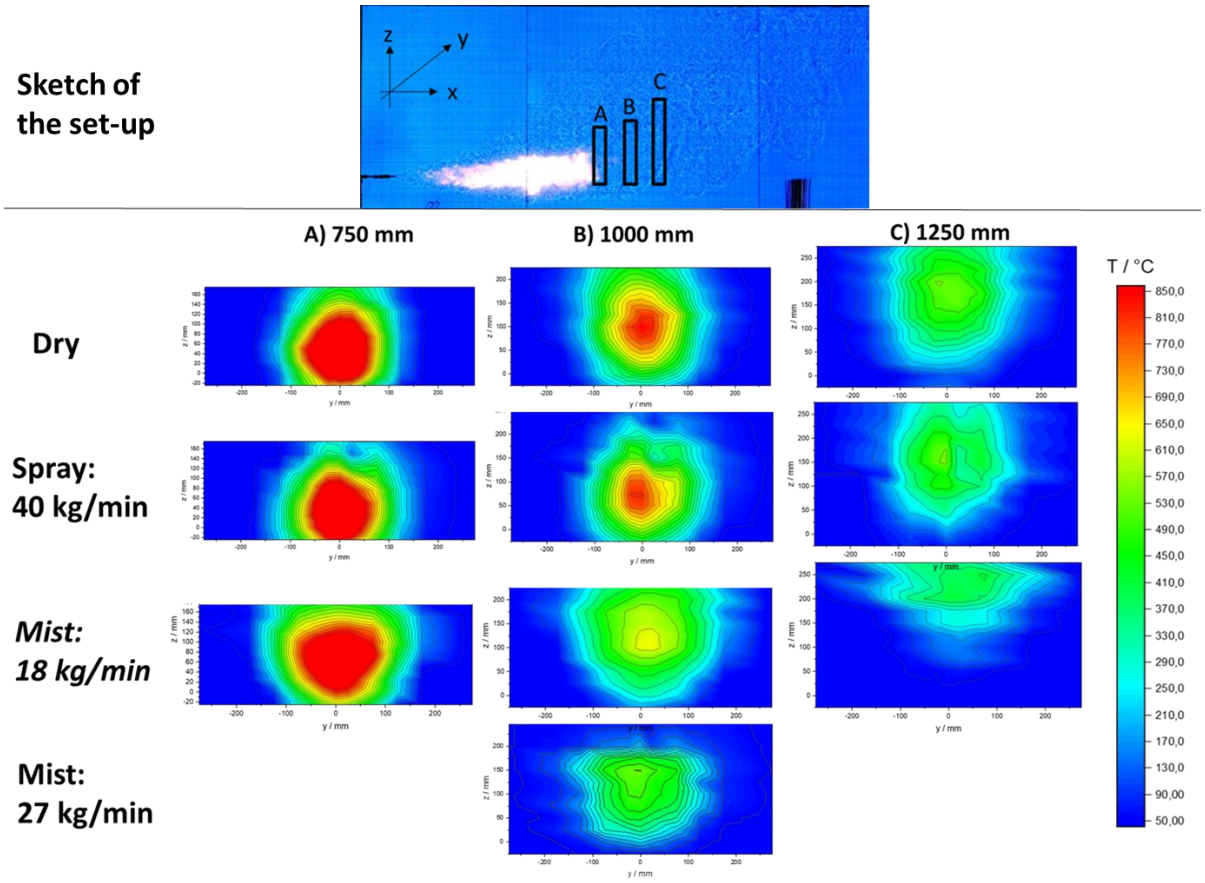

Figure 159. Temperature profiles perpendicular to the axis x of the jet-fire (H2 = 1g/s. nozzle = 4 mm) in three distances to the nozzle A) 0.75 m B) 1 m and C) 1.25 m.

The investigated H2-jet configurations with higher impulse presents only minor buoyancy effects. Figure 160 left shows temperature profiles perpendicular to the jet axis (y-direction) for different positions to the release nozzle (x-direction) for the jet configuration (1 g/s H2; 1 mm nozzle) for dry atmosphere and low mist charge (18 kg/min). The temperature profiles look like Gaussian functions with the maximum on the jet axis (y = 0). The cooling effect of the mist atmosphere is clearly visible. In a distance of 0.75 m to the nozzle, the temperature maximum is 850 °C for dry atmosphere and 700 °C in the mist atmosphere. In the mist atmosphere, it was possible to measure the temperature profile in a distance of 0.5 m to the nozzle (1200 °C) with the used type k thermocouples. It can be assumed that the thermocouples near the jet axis would be melted at this position in case of dry atmosphere.

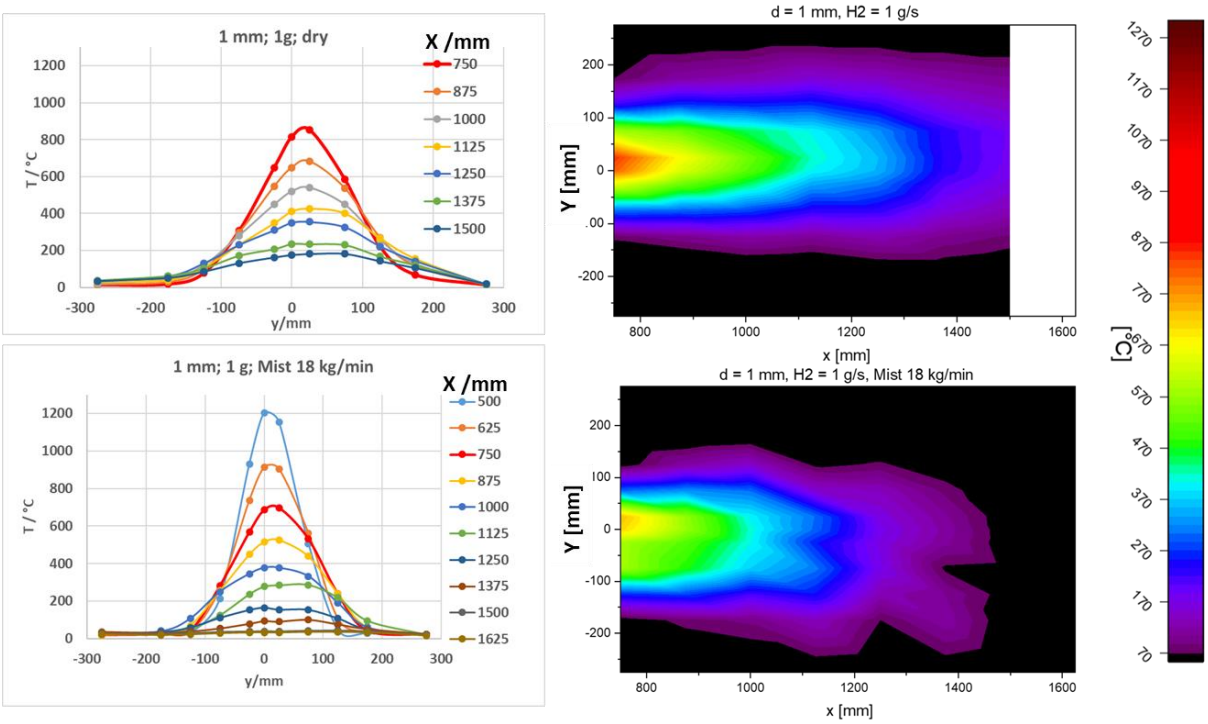

Figure 160. Left, temperature profiles perpendicular to the jet axis (y-direction) for different positions to the release nozzle (x-direction) for the jet configuration (1 g/s H2; 1 mm nozzle) for dry and mist atmospheres. Right, corresponding temperature contour plots.

The temperature contour plots on the right-hand side of Figure 160 highlight the cooling effect of a mist atmosphere on H2-jet-fire. The black colour represents the human pain threshold of 70 °C. However, it can be seen that the cooling efficiency decreases with increasing temperatures. This effect is more distinct in the 5 g/s H2-release configuration. Figure 161 shows the comparison of temperature contour plots of dry and mist atmospheres for the 5 g/s H2-release configurations. The temperature differences look minor, and the cooling efficiency of mist atmosphere is low in this domain. The hot core (> 850 °C) is in all four plots not significantly different.

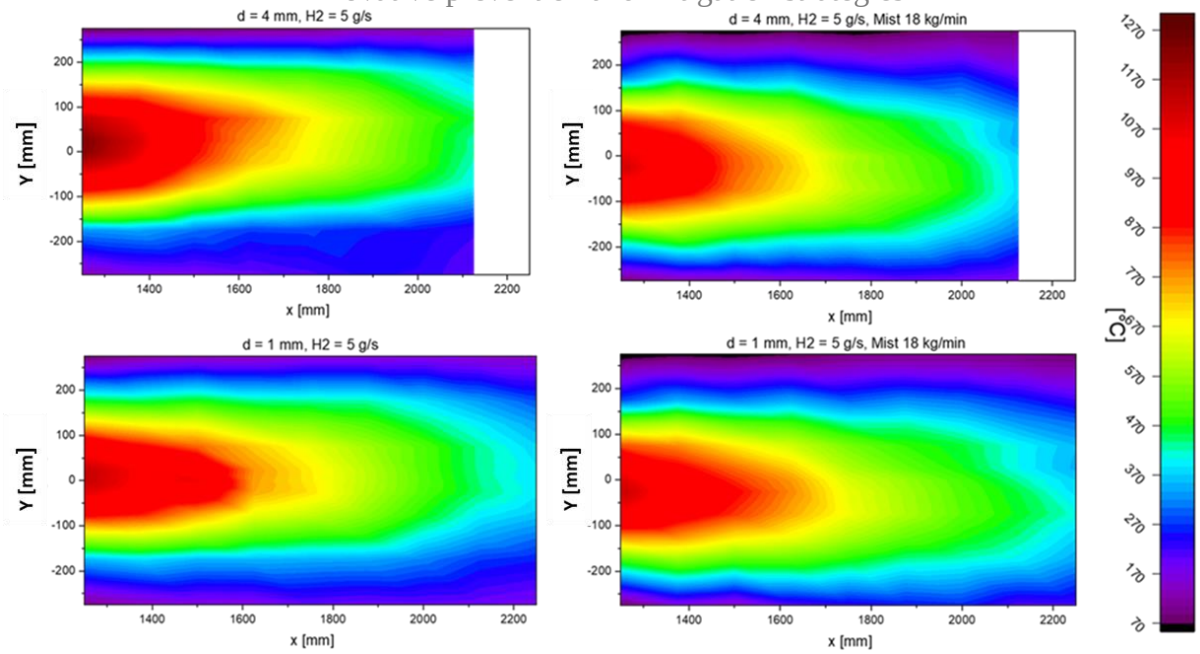

Figure 161. Comparison of temperature contour plots of for dry and mist atmospheres for the 5 g/s H2-release configurations.

4.6.3 Conclusions and recommendations

The effect of water sprays on jet fires was investigated experimentally. Two H2 release nozzles (diameters: 1 mm and 4 mm) and two H2 mass flow rates (1 g/s and 5 g/s) are the variables for H2-jet fire configurations. The influence of water sprays on the temperatures (up to ~1200 °C) in the reacting zone and the exhaust gas of H2 jet fires was studied. A droplet dominated water spray system with a capacity of 40 kg/min (~8 kg/min/m^2) and two mist dominated water sprays with low capacity, 18 kg/min, (1-2 kg/min/m^2) and high capacity, 27 kg/min (1.5 – 3 kg/min/m^2) was tested respectively. The used water spray systems are adapted to the systems commonly used in reality in terms of capacity and charging on the ground.

The study was devoted to investigate the steady state of H2-release with ignition in varying water spray conditions. No different result was observed no matter the spray starts before or after ignition.

The visibility of the H2-flame length was reduced by water injection by 34 – 64 %. The influence of view blocking due to the liquid water phase is unclear. The liquid water injection suppresses the thermal radiation.

It was shown that mist dominated water sprays have a reducing effect on the temperatures in the reacting zone and the exhaust gas of H2 jet fires. The higher the mist charging rate the higher the cooling effect. The highest cooling effect was observed on H2-jet fire (nozzle 4 mm, H2 5 g/s) in a distance of 1.25 m to the nozzle, where the temperature of the H2-jet fire in dry atmosphere is max. 1220 °C. The measured temperature in mist atmosphere was 1080 °C (low mist capacity) and 980 °C (high mist capacity). This indicates a reduction of the H2-jet fire length by only 12 cm for low mist capacity and by 20 cm for high mist capacity, respectively.

The droplet dominated water sprays have a smaller reducing effect on the temperatures in the reacting zone and the exhaust gas of H2 jet fires. For lower momentum jets (4 mm, 1g/s H2)

the high water amount (40 kg/min) suppresses the buoyancy effect of the hot gases. This effect led to higher temperatures on the jet axis under wet conditions than in dry conditions.

The general conclusion of this work on the efficiency of water sprays to suppress combustion and hazards from hydrogen jet fire is summarized as follows.

The cooling influence of water spray on the hot reaction zone (> 850 °C) of a jet fire is rather limited in the nearfield of the H2-release.

In a farther distance to the nozzle, where the temperatures are lower, the cooling influence of water spray on the hot zone of a jet fire is respectable. For the pain threshold-criteria (< 70 °C) the temperature difference due to water spray lies in the range of meters.

An extinction of a jet fire due to water spray was not observed in this study. No negative effect of water spray on hazards from hydrogen jet fire was observed in this work. A cooling and suppression effect due to water spray is present but it should be not overestimated, especially in the very hot zone (> 850 °C) near the H2-release point.

5. Main conclusions and innovations

This deliverable described the comprehensive investigations on the thermal impacts of hydrogen jet fires to e.g. structural concrete wall, mitigation due to sprinkler systems as well as pressure effects from ignited and unignited releases of hydrogen through TPRDs. Engineering and simulation models were developed and validated against the experimental tests performed within HyTunnel-CS. The extensive experimental campaigns performed in the project generated unique data for informed based recommendations and validation by modellers. The developed models and gained knowledge allow to better understand consequences from potential accidents involving hydrogen in tunnels and confined spaces, and fulfil the associated relevant knowledge gaps. A non-exhaustive list is given as follows:

- The pressure peaking phenomenon validation for garage-like enclosures for jet fires from TPRD, including reduced-order and CFD tools for the pressure peaking phenomenon prediction.
- Hydrogen non-premixed turbulent combustion in scaled underground parking, including analysis of impinging hydrogen jet fires.
- Efficiency of hydrogen fire suppression systems by water sprays and oxygen depletion.
- Assessment of TPRD design, e.g. diameter, to comply with current ventilation requirements by RCS and to reduce potential hazards for people in underground car park.
- Effect of current mechanical ventilation parameters on hydrogen jet fires in underground car parks.
- Effect of water vapour generated by hydrogen combustion from TPRD on the visibility.
- Effect of hydrogen releases to fire spread scenarios in underground transportation systems.
- Effect of hydrogen jet fire on structure integrity and concrete spalling.
- Coupled CFD+FEM modelling of the structure's reaction to fire.
- Thermal effects of hydrogen non-premixed turbulent combustion on a vehicle fire behaviour in a tunnel and similar confined spaces.

The comprehensive investigations provided many important results and outcomes. It was found that the TPRD safety device design is crucial for preventing and mitigating accidents for both tunnel and carpark accident scenarios. Hereunder the nozzle diameter is important and should be designed for vehicle on-board hydrogen tanks with a diameter as low as reasonably possible. The direction of the release was also proven to be an important factor into the production of hazards from hydrogen jet fires. From the performed analysis it seems that an inclination of 45 degree downwards to the perpendicular to the ground, in backward direction from the rear of a vehicle, showed better performance into the reduction of hazard distances for people and damage to structure. The findings suggest having more efforts on the technologies preventing or reducing hydrogen hazards, as the explosion-free in a fire tank technology developed by UU and tested by CEA.

6. References

AbdRabbo, M. F., Ayoub, A. M., Ibrahim, M. A., and Sharaf eldin A. M., 2016. The Effect of Water Mist Droplet Size and Nozzle Flow Rate on Fire Extinction in Hanger by Using FDS. J Civil Environ Eng 2016;06(02). https://doi.org/10.4172/2165-784X.1000216.

AbdRabbo, M. F., Ayoub, A. M., Ibrahim, M. A., and Sharaf eldin A. M., 2016. Study the Properties of Water Mist Droplet by Using FDS. J Civil Environ Eng 2016;6(3). https://doi.org/10.4172/2165-784X.1000224.

Anleu, G.B., Blaylock. M., LaFleur. C., 2017. Simulation of a H2 Jet Fire in a Tunnel. in: International Conference on Hydrogen Energy. Hamburg. Germany.

ArcelorMittal, 2019. Foundation Solutions Steel Sheet Piles Underground car parks Contents.

Asadi, I., Shafigh, P., Abu Hassan, Z. F. Bin, & Mahyuddin, N. B. (2018). Thermal conductivity of concrete – A review. *Journal of Building Engineering*, *20*, 81–93. https://doi.org/10.1016/j.jobe.2018.07.002

Baker, G., 1996. The effect of exposure to elevated temperatures on the fracture energy of plain concrete. Material Structures, 29(19), pp. 383-38.

Barlow, R. S. *et al.*, 1999. Nitric oxide formation in dilute hydrogen jet flames: isolation of the effects of radiation and turbulence-chemistry submodels. *Combustion and Flame*, 117(1–2), pp. 4–31. doi: 10.1016/S0010-2180(98)00071-6.

Bazant, P. & Prat, C. P., 1985. Effect of temperature and humidity on fracture energy of concrete. ACI Mater J. ACI Mater Journal, 85(4), pp. 262-271.

Birch, A., Brown, D., Dodson. M., Swaffield, F., 1984. The structure and concentration decay of high pressure jets of natural gas. Combust. Sci. Technol. 36. 249–261.

Bontempi, F. & Malerba, P., 1997. The role of softening in the numerical analysis of R.C. structures. Structural Engineering and Mechanichs, 5(6), pp. 785-801.

Brennan, S., Hussein, H.G., Makarov, D., Shentsov, V., Molkov, V., 2018. Pressure effects of an ignited release from onboard storage in a garage with a single vent. Int. J. Hydrog. Energy. https://doi.org/10.1016/j.ijhydene.2018.07.130

Brennan, S., Makarov, D., Molkov, V., 2010. Dynamics of flammable hydrogen-air mixture formation in an enclosure with a single vent. in: Proceedings of the 6th International Seminar on Fire and Explosion Hazards. Leeds.

BS 7345-7:2013. The British Standards Institution, Components for smoke and heat control systems Part 7: Code of practice on functional recommendations and calculation methods for smoke and heat control systems for covered car parks, 2013.

Cai, J. and Modest, M. F., 2016. Specular reflective boundary conditions for Discrete Ordinate Methods in Periodic or Symmetric Geometries. *Journal of Physics: Conference Series*. IOP Publishing, p. 12002.

CETU, 2010. Water mist in road tunnels, state of knowledge and provisional assessment elements regarding their use. Tunnel Study Centre (CETU), June, 2010.

Chmielewski, M., Gieras, M., 2015. Planck Mean Absorption Coefficients of H2O. CO2. CO and NO for radiation numerical modeling in combusting flows. J. Power Technol. 95. 97–104. Available at: https://papers.itc.pw.edu.pl/index.php/JPT/article/view/611 (Accessed: 18 March 2021).

Cirrone, D., Makarov, D., Lach, A.W., Gaathaug, A.V., Molkov, V. The Pressure Peaking Phenomenon for Ignited Under-Expanded Hydrogen Jets in the Storage Enclosure: Experiments and Simulations for Release Rates of up to 11.5 g/s. Energies 2022, 15, 271. https://doi.org/10.3390/en15010271

Commission Regulation (EU) No 406/2010 — European Environment Agency [WWW Document]. n.d. URL https://www.eea.europa.eu/policy-documents/commission-regulation-eu-no-406-2010 (accessed 4.22.19).

Dayan Li, Guoqing Zhu, Hui Zhu, Zhichao Yu, Yunji Gao, and Xiaohui Jiang, Flame spread and smoke temperature of full-scale fire test of car fire, Case Studies in Thermal Engineering, 10, 2017, pp. 315-324.

Deeny, S., Stratford, T., Dhakal, R., Moss, P. and Buchanan, A., 2008. Spalling of concrete: Implications for structural performance in fire. 20th Australasian Conference on Mechanics of Structure and Materials, Toowoomba, Australia. 2008.

DS/EN 1991-1-2 DK NA, 2011. Danish National Annex to Eurocode 1: Part 1-2 Actions on structures exposed to fire, Denmark: Erhvevs- og Byggestyrelsen.

EN1992.1.2004. Eurocode 2: Design of concrete structures - Part 1-2: General rules - Structural fire design.

EN1990, 2002. Eurocode 0 - Basis of structural design, Brussels, Belgium: Comité Européen de Normalisation.

EN1993-1-1: 2005, 2005. Eurocode 3: Design of Steel Structures - Part 1-1: General Rules and Rules for Buildings, Brussels, Belgium: Standard, European Committee for Standardization.

Engineers Edge. 2020. Thermal properties of metals [WWW Document].

European Industrial Gases Association. Hazards of inert gases and oxygen depletion 2009.

European Union. Minimum safety requirements for tunnels in the Trans-European Road Network; 2004

Feenstra, P. & De Borst, R., 1995. Constitutive Model for Reinforced Concrete. Journal of Engineering Mechanics, 121(1), pp. 587-595.

Fluent, A., 2016. User's guide.

Gao, W.-Y., Dai, J., Teng, J. & Chen, G., 2013. Finite element modeling of reinforced concrete beams exposed to fire. Engineering Structures 52, p. 488–501.

Gilmore, C.P., 1992. More Comfort for Your Heating Dollar. 41345th ed. Popular Science.

Glasa, J. and Valasek, L., 2014. Study on Applicability of FDS+Evac for Evacuation Modeling in Case of Road Tunnel Fire 2014(2040-7459).

Granta, G., Brenton, J., Drysdale, D., 2000. Fire suppression by water sprays.

Grosshandler, W.L., 1993. RADCAL: a narrow-band model for radiation. Calc. Combust. Environ. NIST Tech. Note 1402.

Grune, J., Sempert, K., Kuznetsov, M. et.al., 2021. Hydrogen jet structure in presence of forced co-, counter- and cross-flow ventilation. International Conference on Hydrogen Safety, 21-24th September 2021, Edinburgh, Scotland, ID41.

Han, X. and Krajnovic, S., 2013. An efficient very large eddy simulation model for simulation of turbulent flow. Int. J. Numer. Meth. Fluids 2013;71(11):1341–60.

Hankinson, G., B. J. Lowesmith, 2012. A consideration of methods of determining the radiative characteristics of jet fires. *Combust. Flame*, vol. 159, nº 3, p. 1165-1177, mars 2012, doi: 10.1016/j.combustflame.2011.09.004

Herrenknecht, 2020. *Email communication from construction equipment manufacturer*.

Hertz, K. D., 2003. Limits of spalling of fire-exposed concrete. *Fire Safety Journal*, *38*(2), 103–116. https://doi.org/10.1016/S0379-7112(02)00051-6

Hertz, K. D., 2005. Concrete Strength for Fire Safety Design. Journal of Magazine of Concrete Research, 57(8), pp. 445-453.

Hertz, K. D., & Sørensen, L. S., 2005. Test method for spalling of fire exposed concrete. *Fire Safety Journal*, *40*(5), 466–476. https://doi.org/10.1016/j.firesaf.2005.04.001

Hertz, K.D., 2018. Design of fire resistant structures, ICE Publishing, 2019

Hurley, M. J. et al., 2016. SPFE Handbook of Fire Protection Engineering, 2016, Springer-Verlag New York, New York.

Hussein, H.G., Brennan, S., Shentsov, V., Makarov, D., Molkov, V., 2018. Numerical validation of pressure peaking from an ignited hydrogen release. Int. J. Hydrog. Energy 43. 17954–17968.

Hussein, G. H., 2019, Pressure Peaking Phenomenon for hydrogen jet fires and safety considerations of indoor releases, PhD Thesis.

HyIndoor D4.4. 2014. Deliverable D4.4 Final report on analytical. numerical. and experimental studies of jet fires.

HyTunnel-CS D1.1, 2019. Deliverable D1.1 Report on assessment of effectiveness of conventional safety measures in underground transportation systems and similar confined spaces.

HyTunnel-CS D1.2, 2019. Deliverable D1.2 Report on hydrogen hazards and risks in tunnels and similar confined spaces.

HyTunnel-CS D1.3, 2019. Deliverable D1.3 Report on selection and prioritisation of scenarios.

HyTunnel-CS D2.1, 2019. Deliverable D2.1 Detailed research programme on unignited leaks in tunnels and confined space.

HyTunnel-CS D3.1, 2019. Deliverable D3.1 Detailed research programme on hydrogen fires in confined structures

HyTunnel-CS D3.2, 2020. Deliverable D3.2 Intermediate report on analytical, numerical and experimental studies on fires.

HyTunnel-CS D2.3, 2022. Deliverable D2.3 Final report on analytical, numerical and experimental studies on hydrogen dispersion in tunnels, including innovative prevention and mitigation strategies.

Jessee, J.P., Fiveland, W.A., 1997. Bounded. high-resolution differencing schemes applied to the discrete ordinates method. J. Thermophys. Heat Transf. 11. 540–548.

Kim, S. H. and Huh, K. Y., 2000. A new angular discretization scheme of the finite volume method for 3-D radiative heat transfer in absorbing, emitting and anisotropically scattering media. *International Journal of Heat and Mass Transfer*, 43(7), pp. 1233–1242. doi: 10.1016/S0017-9310(99)00211-2.

Kimley-Horn, 2016. Parking structure: design guidelines. Kma - Gesundheitswirtschaftsmagazin. https://doi.org/10.1055/s-0036-1578372

Król, M., et al, 2017. Full scale measurements of the operation of fire ventilation in a road tunnel. Tunnelling and Underground Space Technology 2017;70:204–13.

Krüger, S., Hofmann, A., Berger, A. and Gude, N., 2016. Investigation of smoke gases and temperatures during car fire-large-scale and small-scale tests and numerical investigations, Fire and Materials, 40, No.6, 2016, pp. 785-799.

Labois, M. and Lakehal, D., 2011 Very-Large Eddy Simulation (V-LES) of the flow across a tube bundle. Nuclear Engineering and Design 2011;241(6):2075–85

Lach, A.W., Gaathaug, A.V. and Vaagsaether, K., 2020. Pressure peaking phenomena: Unignited hydrogen releases in confined spaces – Large-scale experiments. Int. J. Hydrogen Energy, vol. 45, no. 56, pp. 32702–32712, 2020, doi: 10.1016/j.ijhydene.2020.08.221.

Lach, A.W. and Gaathaug, A.V., 2021a. Large scale experiments and model validation of Pressure Peaking Phenomena-ignited hydrogen releases. Int. J. Hydrogen Energy, vol. 46, no. 11, pp. 8317–8328, 2021, doi: 10.1016/j.ijhydene.2020.12.015.

Lach, A. W. and Gaathaug, A. V, 2021b. Effect of Mechanical Ventilation on Accidental Hydrogen Releases—Large-Scale Experiments. *Energies*, 14(11), p. 3008.

LaChance, J.L., 2010. Progress in risk assessment methodologies for emerging hydrogen applications. in: Sixth International Short Course and Advanced Research Workshop "Progress in Hydrogen Safety – Regulations. Codes and Standards." Belfast. Northern Ireland. UK.

Lachance, J., Tchouvelev, A., Engebo, A., 2011. Development of uniform harm criteria for use in quantitative risk analysis of the hydrogen infrastructure. Int. J. Hydrog. Energy 36. 2381–2388. https://doi.org/10.1016/j.ijhydene.2010.03.139

Leopardi, P., 2006. A partition of the unit sphere into regions of equal area and small diameter. Electron. Trans. Numer. Anal. 25. 309–327.

Liu, N., and Shih., T., 2006. Turbulence Modeling for Very Large-Eddy Simulation. AIAA Journal 2006;44(4):687–97. https://doi.org/10.2514/1.14452.

Liu, W, Riba Clascà, Markert, F. Giuliani, L., 2021. Fire Spread scenarios involving hydrogen vehicles, International conference on hydrogen safety 2021, Edinburgh, UK

Mcnamee, R. J., & Jansson, R., 2015. Fire Spalling of Concrete : Theoretical and Experimental Studies Fire Spalling of Concrete Theoretical and Experimental Studies. October 2013.

Magnussen, B., 1981. On the structure of turbulence and a generalized eddy dissipation concept for chemical reaction in turbulent flow. Am Inst Aeronaut Astronaut.

Makarov, D., Shentsov, V., Kuznetsov, M., Molkov, V., 2018. Pressure peaking phenomenon: Model validation against unignited release and jet fire experiments. Int. J. Hydrog. Energy 43. 9454–9469. https://doi.org/10.1016/j.ijhydene.2018.03.162

Mangs, J., and Keski-Rahkonen, O., 1994. Characterization of the fire behaviour of a burning passenger car. Part I: Car fire experiments. Fire Safety Journal, 23, No.1, 1994, pp.17-35.

Modest, M.F., 2013. Radiative heat transfer. Academic press.

Molkov.,V., 2012. Fundamentals of Hydrogen Safety Engineering I Download free books at Vladimir Molkov Fundamentals of Hydrogen Safety Engineering I.

Molkov, V., Makarov, V., Bragin, M. V., 2009. Physics and modelling of underexpanded jets and hydrogen dispersion in atmosphere. Phys. Extreme States Matter 146–149.

Molkov, V. and Saffers, J., 2011. The Correlation for Non-Premixed Hydrogen Jet Flame Length in Still Air. January 2011, Fire Safety Science 10:933-943 DOI: 10.3801/IAFSS.FSS.10-933.

Molkov, V. and Saffers, J., 2013. Hydrogen jet flames. International Journal of Hydrogen Energy 2013;38(19):8141–58. https://doi.org/10.1016/j.ijhydene.2012.08.106.

Momferatos, G., Venetsanos, A.G., Russo, P., 2021. Numerical investigation of thermal hazards from under-expanded hydrogen jet fires using a new scheme for the angular discretization of the radiative intensity, ebook ICHS 2021, September 21-24, 2021, 1491-1501

Murthy, J.Y., Mathur, S.R., 1998. A finite volume method for radiative heat transfer using unstructured meshes. 36th AIAA Aerosp. Sci. Meet. Exhib. M. https://doi.org/10.2514/6.1998-860

NET e-laboratory; FCH2 eductaion, https://fch2edu.eu/home/e-laboratory/; last access: 27-02-2022.

NIST (ed.). FDS_User_Guide-6. https://pages.nist.gov/fds-smv/manuals.html

Okamoto, K., Otake, T., Miyamoto, H., Honma, M., Watanabe, N., 2013. Burning behavior of minivan passenger cars. Fire Saf. J. 62. 272–280.

Peters, N., Rogg, B., 1993. Reduced kinetic mechanisms for applications in combustion systems. Berlin. Berlin.

Proust, C., Jamois, D., Studer, E., 2011. High pressure hydrogen fires. Int. J. Hydrog. Energy 36. 2367–2373. https://doi.org/10.1016/j.ijhydene.2010.04.055

Rijkswaterstaat, & Efectis Nederland. (2020). Efectis-R0695:2020 - Fire testing procedure for concrete tunnel linings and other tunnel components. 46. https://efectis.com/en/revision-rws-test-procedure-for-concrete-tunnel-linings/

Rothman, L., Gordon, I., Barber, R., Dothe, H., R., Goldman, A., Perevalov, V., Tashkun, S., Tennyson, J., 2010. HITEMP. The high-temperature molecular spectroscopic database. J. Quant. Spectrosc. Radiat. Transf. 111. 2139–2150.

Russo P., Marra F., Mazzaro M., Pilo F., Marini D., Vianello C., Pulci G., 2020, Spatial and Radiative Characteristics of Large Scale Hydrogen Jet-fires, Chemical Engineering Transactions, 82, 217-222 DOI:10.3303/CET2082037

SAE J2579. 2009. Technical information report for fuel systems in fuel cell and other hydrogen vehicles. in: SAE International. Detroit MI. U.S.

Sauzedde, F., Martin, M., Forero, D., and Studer, E., 2020. CEA Experimental devices Pre-tests of 2020. Report. HyTunnel-CS, 2020.

Sauzedde, F., Martin, M., Forero, D., and Studer, E., 2021a. CEA Experimental devices Tests of 2021. Report. HyTunnel-CS, 2021.

Sauzedde, F., Martin, M., Bouix, D., and Studer, E., 2021b. CEA tank blowdown transient test results in a full-scale tunnel. Report. HyTunnel-CS, 2021.

Schefer, R.. Houf, W., Bourne, B., Colton, J., 2006. Spatial and radiative properties of an open-flame hydrogen plume. Int. J. Hydrog. Energy 31(10). 1332–1340.

Schefer, R. W. *et al.*, 2007. Characterization of high-pressure, underexpanded hydrogen-jet flames. *International Journal of Hydrogen Energy*, 32(12), pp. 2081–2093. doi: 10.1016/j.ijhydene.2006.08.037.

Shih, T.H., Liou, W.W., Yang, A., Shabbir, Z., 1995. A new eddy-viscosity model for high Reynolds number turbulent flows—model development and validation. Comput Fluids 24. 227–238.

Shuttleworth, P., 2001. Fire Protection of Concrete Tunnel Linings. *Third International Conference on Tunnel Fires*, 157–165.

Simulia Corp., 2011. Abaqus v6.11 Documentation. RI, USA: Dassault Systèmes.

Statens Vegvesen, 2019. En stille revolusjon i norske fjorder; 2019.

Studer, E., Forero, D., Sauzedde, F. and Martin, M., 2021. CEA Helium Dispersion test results in a full-scale tunnel. Report. HyTunnel-CS, 2021.

Tamura, Y., Takabayashi, M. and Takeuchi, M., 2014. The spread of fire from adjoining vehicles to a hydrogen fuel cell vehicle', International Journal of Hydrogen Energy, 39(11), pp. 6169–6175. doi: 10.1016/j.ijhydene.2014.01.140

Thomas G.O., 2000. On the Conditions Required for Explosion Mitigation by Water Sprays. Process Safety and Environmental Protection 2000;78(5):339–54.

Thunderhead Engineering (ed.). PyroSim User Manual. https://support.thunderheadeng.com/docs/pyrosim/2020-3/user-manual/

Till R.C. and J.W. Coon. Fire Protection. Cham: Springer International Publishing; 2019.

Tunnels Study Centre of France. WATER MISTS IN ROAD TUNNELS: State of knowledge and provisional assessment elements regarding their use. Tunnels Study Centre (CETU); 2010.

Venetsanos, A.G., Baraldi, D., Adams, P., Heggem, P.S., Wilkening, H., 2008. CFD modelling of hydrogen release, dispersion and combustion for automotive scenarios. Journal of Loss Prevention in the Process Industries 2008; 21(2):162–84.

Venetsanos, A. G., Papanikolaou, E. and Bartzis, J. G., 2010. The ADREA-HF CFD code for consequence assessment of hydrogen applications. International Journal of Hydrogen Energy, 35(8), pp. 3908–3918. doi: 10.1016/j.ijhydene.2010.01.002.

Vivanni, L., 2021. Numerical modeling of the response of a tunnel concrete slab to hydrogen fire, MSc report, Civil Engineering Department, Technical University of Denmark.

Wang, Z., et al. 2016. Optimization of water mist droplet size by using CFD modeling for fire suppressions. Journal of Loss Prevention in the Process Industries 2016; 44:626–32. https://doi.org/10.1016/j.jlp.2016.04.010.

Wexler, A., 1965. Humidity and Moisture: Fundamentals and standards. A. Wexler and W.A. Wildhack, editors. Reinhold Publishing Corporation; 1965.

Wingerden, B.K., 1995. The influence of water sprays on gas explosions. Part 1: water-spray-generated turbulence.

Yamashita, A., Kondo, M., Goto, S., Ogami, N., 2015. Development of high-pressure hydrogen storage system for the Toyota “Mirai.” SAE Tech Pap SAE Int.

Zaineb, T. Experimental and numerical study of concrete exposed to rapid fire. Master Thesis, August 2020. Department of Civil Engineering, Technical University of Denmark

Zhang, B. & Bicanic, N., 2000. Residual fracture properties of normal- and high-strength concrete subject to elevated temperatures. Magazine of Concrete Research, 52(2), pp. 123-136.

Zhang, J., et al., 2019. Computational Fluid Dynamics Simulations of Hydrogen Jet Fires inside a Tunnel. Proceedings of the 2019 2nd International Conference on Sustainable Energy, Environment and Information Engineering (SEEIE 2019).